Earthquake Geology of Myanmar

Thesis by

Yu Wang

In Partial Fulfillment of the Requirements for the degree

of

Doctor of Philosophy

CALIFORNIA INSTITUTE OF TECHNOLOGY

Pasadena, California

2013

(Defended May 30, 2013)

ACKNOWLEDGEMENTS

Since there have been 300 pages in this dissertation, I should keep the acknowledgements short. However, there are so many things I want to talk about that it would be a torture if I can't. You may find the acknowledgements too long to read, but they express my most sincere feelings at the end of my PhD.

First of all, I would like to express the utmost gratitude to my advisor, Professor Kerry Sieh, for his guidance and generous support in the past several years. We have known each other for more than 10 years, since he first conducted the field work to study the active tectonics of Taiwan after the 1999 Chi-Chi earthquake. To me, he is not only a thesis advisor, but also a good friend after work hours. Although we did not have many chances to go to the field together during the past seven years, I still benefited a lot by watching how he works. I also benefited greatly from the intriguing discussions between the two of us. The topics range from science to societal issues. Although we could not always reach an agreement, these intense discussions forced me to think not only deeply, but also widely.

I also want to thank Professor Jean-Philippe Avouac for his great guidance during this period. His way of connecting geology and other different research fields really opened my eyes. His help and suggestions improved the quality of my research, especially in the discussions of fault behaviors. He showed me how to think about a geological problem from their fundamental physical properties, which is something that I have never learned before. His great perspective in geosciences is one of the most valuable things I obtained from Caltech.

Another person to mention here is Dr. J. Bruce Haote Shyu. Without his encouragement and help, this thesis would never be completed. During the last four years, we spent a lot of time in Myanmar together to work on the deformation history of Myanmar's western coast, and had a lot of great conversions about careers and families. To some degree, he is like another thesis advisor to me, but more than that, he is a mentor who always gives sincere advices at my frustrative moments. I also want to thank Bruce's wife, Shing-Lin Wang, especially for her help during my first year at Caltech. Without the two of them, my life as a graduate student at Caltech would be a lot more miserable.

My gratitude also goes to other thesis committee members, Jason Saleeby, Jean-Paul Ampuero and Joann Stock. The first class that I attended in Caltech is Jason's Ge120. Although this class is designed for undergrad students, the two weeks in the desert brought me a complete different idea about geology than what I had before in Taiwan. It was almost a cultural shock and strengthened my interest of working as a field geologist. Jean-Paul Ampuero provides me with very helpful information of what he observed from recent subduction zone earthquakes. The discussions with him help me think about the slip behavior of the ancient megathrust event. With Joann, I benefited from the discussion about the surface rupture behavior of strike-slip fault systems. I also learned a lot from her plate tectonics class, from which I applied the concepts and techniques in my research. Professor Mark Simons also helped me with the InSAR research of the 2011 Tarlay earthquake. The discussion of the shallow rupture behavior with him helped me connect the dots between the surface and the subsurface fault behaviors.

The other people that I like to mention as the “Caltech group” are Eh Tan and Wei-Ting Chen. They provided very important mental supports while I stayed in Caltech. We have been very good friends since 2007, and I believe this friendship will last for the rest of our lives. I also benefited from the discussion with Belle Philibosian and Aron Meltzer about the coral microatolls and the deformation history along the Sunda megathrust when we stay together in Pasadena and Singapore. Their help improves the quality of my research in the western Myanmar coast.

Besides the people from Pasadena, I also want to thank the scientists from Myanmar. It is impossible for me to work in Myanmar’s countryside without them. U Soe Thura Tun is the person that I worked most with. He leads a young generation of scientists from Myanmar, including Thura Aung, Soe Min, Lin Tun Aung and several others to work on the earthquake geology of Myanmar for more than seven years. It is their help that made things possible in this once-isolated country. The help from Dr. Win Swe and U Than Myint were also very essential to this thesis. Without their contributions and connections, things would not work out smoothly over these years.

I would also like to thank Dr. Hiroyuki Tsutsumi. His generous friendship helps me broaden my research in Myanmar. The good discussions we had on the earthquake geology of Myanmar and Philippines inspired me a lot when we worked together on the Sagaing fault.

I also appreciate the helps, suggestions and friendships from Younghee Kim, Yoshi Keneko, Ravi Kanda, Fan-Chi Lin, Sheng-Ji Wei, Zhong-Wen Zhan, Steve Skinner, Steve Kidder, Alan Chapman, Lisa Christiansen, Heather Steele and the Taiwanese group: Yue-Gau Chen, Hong-Wei Chiang, Chuan-Chou Shen, Kuang-Yin Lai, Ling-Ho Chung, Yu-Ting Kuo, Ray Chuang and other

YG's lab members. I also want to express my appreciation to CHUA Seok Lin (Linda), who helped me a lot while I stayed in Singapore.

I will leave the rest of this page to my families. I have been at Caltech for 7 years, and several life-changing events happened. Among them, the most important one is that I married Nina. Her role is crucial not only because of her wonderful companion during these years, but also because the great discussion we had in office and at home. While I was in Singapore and Myanmar, she needed to keep working on her own research, and to raise our two kids, Jing and Ying. Her understanding made it possible for me to work in such a distant place, and no word can express my appreciation. Now that I look back to the route that Nina and I took, it is her who pushed me to come to Caltech and who turned me from a boy to a man. We experienced laughter and tears, high and lows, shine and rains. With her next to me, I believe we can overcome whatever lies in front of us.

Last but not least, I would like to say thank you to my father, mother and my brother for their understanding and support through these years. My brother Hao Wang, and his wife Shirley Huang, gave us invaluable support with all the essentials for child raising. I also want to thank my mother in law and my sisters in law. Their mental and physical supports at Taiwan and California allow us to concentrate during the last period of the thesis work.

I leave the last line here to thank everyone who helped me in the past. THANK YOU!

ABSTRACT

This thesis describes the active structures of Myanmar and its surrounding regions, and the earthquake geology of the major active structures. Such investigation is needed urgently for this rapidly developing country that has suffered from destructive earthquakes in its long history. To archive a better understanding of the regional active tectonics and the seismic potential in the future, we utilized a global digital elevation model and optical satellite imagery to describe geomorphologic evidence for the principal neotectonic features of the western half of the Southeast Asia mainland. Our investigation shows three distinct active structural systems that accommodate the oblique convergence between the Indian plate and Southeast Asia and the extrusion of Asian territory around the eastern syntaxis of the Himalayan mountain range. Each of these active deformation belts can be further separated into several neotectonic domains, in which structures show distinctive active behaviors from one to another.

In order to better understand the behaviors of active structures, we focused on the active characteristics of the right-lateral Sagaing fault and the oblique subducting northern Sunda megathrust in the second part of this thesis. The detailed geomorphic investigations along these two major plate-interface faults revealed the recent slip behavior of these structures, and plausible recurrence intervals of major seismic events. We also documented the ground deformation of the 2011 Tarlay earthquake in remote eastern Myanmar from remote sensing datasets and post-earthquake field investigations. The field observation and the remote sensing measurements of surface ruptures of the Tarlay earthquake are the first study of this kind in the Myanmar region.

TABLE OF CONTENTS

Acknowledgements iii
Abstract vi
Table of Contents vii
List of Illustrations xii
List of Tables xvi

Chapter 1
Introduction 1

Chapter 2
Active Tectonics and Earthquake Potential of the Myanmar region 4
Abstract 4
Introduction 5
Methodology 6
Neotectonics of the Myanmar region 9
The Indoburman range 9
Coco-Delta domain 10
Ramree domain 12
Deformation front and active structures in the accretionary prism 13
Dextral strike-slip faulting in the Indoburman range 14
Active faults and folds east of the Indoburman range 15
Dhaka domain 17
Chittagong-Tripura fold belt (CTFB) 19
The high Indoburman range 23
East flank of the Indoburman range and beyond 24
Naga domain 25
The Sagaing domain 27
The southern section of the Sagaing fault 29
Bago segment 29
Pyu segment 30
Nay Pyi Taw segment 31
Meiktila segment 31
Sagaing segment 32
The Northern section of the Sagaing fault 33
Tawma and Ban Mauk segments 34
In Daw and Mawlu segments 35
Shaduzup, Kamaing and Mogang segments 36
The Shan-Sino domain 38

The left-lateral faults 39
Summary 39
Daying River, Ruili and Wanding faults 40
Nanting, Lashio and Kyaukme faults 42
Menglian, Jinghong, Wan Ha and Mengxing faults 45
Nam Ma and Mae Chan faults 48
Dien Bien Phu fault 49
The right-lateral faults 51
Summary 51
Wuliang Shan fault zone 51
Lancang fault zone 52
Kyaukkyan fault zone 53
Myint Nge segment 53
Taunggyi segment 54
Salween segment 54
Mae Ping fault zone 55
Partially reactivated faults of the Shan escarpment 55
Earthquakes past and future 55
The Indoburman range 57
Coco-Delta domain 58
Ramree domain 59
Dhaka domain. 61
Naga domain 64
The Sagaing fault 65
Shan-Sino domain 67
Conclusions 69
Acknowledgments 70
References 71

Chapter 3
Earthquakes and slip rate of the Southern Sagaing fault: insights from an offset ancient fort-wall, Lower Myanmar (Burma) 113
Abstract 113
Introduction 114
Active tectonics of the southern Sagaing fault and surrounding area 116
Structural overview of southern Myanmar 116
Southern Sagaing fault 117
1930 May Pegu earthquake and 1930 December Pyu earthquake 118
Offsets along the Pegu section 119
Offset ancient structure 120
The Payagyi ancient fortress 120
Estimation of offsets 122

Offset reconstruction 125
Paleoseismologic excavation in the ancient fortress........ 126
Sedimentary units in the trench........ 126
Fault traces on the southern trench wall. 130
Discussion 131
The age of ancient fortress 131
Late Holocene slip rate along the Southern Sagaing fault 132
Seismic potential and behavior of the southern Sagaing fault. 134
Conclusion 138
Acknowledgements 139
Reference 139

Chapter 4

Permanent upper-plate deformation in western Myanmar during the great 1762 earthquake: Implications for neotectonic behavior of the northern Sunda megathrust........ 156

Abstract........ 156
Introduction........ 157
Active tectonic context 159
Sea-level indicators 160
Biological indicators........ 161
Oysters 161
Coral microatolls and coral heads 162
Erosional coastal features 163
Shoreline angles........ 163
Sea notches 164
Wave-cut platforms........ 165
Coastal emergence 166
Ramree Island 166
Northern Ramree Island [Kyauk-Pyu area]........ 166
Central Ramree Island 168
Southern Ramree Island........ 169
Eastern Ramree Island 171
Summary of Ramree Island 172
Cheduba Island........ 173
Northwestern Cheduba Island [Ka-Ma village] 173
Southwestern Cheduba Island [Ka-I area] 175
Eastern Cheduba Island [Kan-Daing-Ok area] 177
Northeastern Cheduba Island [Man-Aung Town area]........ 179
Northwestern Cheduba Island [Taung-Yin area]........ 180
Summary of Cheduba Island........ 180
Discussion 181

Recovering co-seismic uplift from the emergence measurements 181
Non-tectonic water-level change... 181
Interseismic deformation 183
Possible later uplift events 184
The uplift pattern of the 1762 earthquake 185
The significance of the upper plate structures 185
The source of the 1762 earthquake 187
Earthquake recurrence intervals... 189
Summary and conclusions 191
Acknowledgments 192
References 193

Chapter 5
Surface Ruptures of the Mw 6.8 March 2011 Tarlay Earthquake, Eastern Myanmar 223
Abstract... 223
Introduction... 224
Field Observations 227
Logistics, scope of reconnaissance and methods 227
Field measurements 228
Kya Ku Ni.. 228
Pu Ho Mein 229
Tarlay.. 230
Eastern end of the rupture 232
Remote sensing observations 233
Kya Ku Ni and further west... 233
Discussion 235
Compilation of results... 235
The rupture length of the 2011 Tarlay earthquake 236
Preservation of offset features.. 237
Seismic potential of the rest of the Nam Ma Fault 238
Conclusions.. 239
Data and Recourses... 240
Acknowledgments 240
References 241

Chapter 6
Shallow rupture of the 2011 Tarlay earthquake (Mw 6.8), Eastern Myanmar...... 261
Abstract.. 261
Introduction.. 262
The Nam Ma Fault and the 2011 Tarlay Earthquake 263
InSAR data 264

The slip distribution of Tarlay earthquake 265
Discussion 269
  Characteristics of the surface rupture 269
  Shallow slip deficit 271
  Inferred recurrence interval on the Tarlay segment 272
Conclusions 273
Data and Resources 274
Acknowledgement 274
Reference 274

Appendix 1

Supplementary material of chapter 2 Active Tectonics and Earthquake Potential of the Myanmar region 285

Appendix 2

Supplementary material of chapter 3 Earthquakes and slip rate of the Southern Sagaing fault: insights from an offset ancient fort-wall, Lower Myanmar (Burma) 293

LIST OF ILLUSTRATIONS

Chapter 2

1. Major tectonic elements of the Myanmar region and the extreme variation in rainfall that influence preservation of tectonic landforms. 80
2. The overall neotectonic map that we mapped from various dataset and the neotectonic domains that we proposed in and around the Myanmar area....82
3. (a) Major active faults within the Coco-Delta domain. (b) Structures along the deformation front include a series of anticlinal structures very close to the trench. (c) Seindaung fault and other dextral faults along the eastern flank of the southern Indoburman range. 83
4. (a) Major active faults within the Ramree domain. (b) The detail bathymetry of the Ramree lobe, showing clear feature of imbricated faults and anticlines. (c) The marine terraces at the western side of the Cheduba Island. (d) The step-like alluvial fans north of the Ramree Island, showing the plausible periodic sea-level changes during the growth of the fan. 84
5. The fault extents and the major offset features along the Thahtay Chaung fault, within the Indoburman Range. 85
6. The active faults and anticlines of the Dhaka domain. 86
7. Geomorphological features of the Churachandpur-Mao fault at two different locations reflect clear dextral motions along the fault....87
8. Fault and drainage map in the southern part of the Kabaw valley shows no young offset features along a strike-slip element of the fault. 88
9. Map and cross sections of the Naga thrust fault system. 89
10. The fault segments and historical earthquakes along the central to southern part of the Sagaing fault. 90
11. The fault segmentation at the northern Sagaing fault 91
12. The distribution of active faults and historical earthquakes within the Shan-Sino domain between the Sagaing fault and the Red River fault. 92
13. Selected examples of the geomorphological expression of active faults of the Shan-Sino domain, ...93
14. Tectonic geomorphological expressions of select locations along the Nanting fault. 94
15. Tectonic geomorphological expressions of the Menglian, Jinghong and Mengxing faults. 95
16. Tectonic geomorphology along parts of the right-lateral Wuliang Shan fault and Lancang fault system. 96
17. Geomorphological expression of particularly informative parts of the right-lateral Kyaukkyan fault system and the Mae Ping fault zone 97
18. Schematic cross sections through two domains of the northern Sunda megathrust show the geometry of the megathrust and hangingwall structures in the Coco-Delta domain and the Ramree domain 98
19. Schematic cross sections through two domains of the northern Sunda megathrust show the geometry of the megathrust and hangingwall structures in the Dhaka domain and the Naga domain....99

20. Map of potential maximum earthquake magnitudes (Mw) associated with shallow active faults of the four domains of the northern Sunda megathrust and Indoburman range. 100
21. Map and chart of potential maximum earthquake magnitudes (Mw) associated with named segments of the Sagaing fault. 101
22. Map of total geomorphological evident offset and potential maximum earthquake magnitudes (Mw) associated with named faults of the Shan-Sino domain. 102

Chapter 3

1. Active tectonic framework and recent earthquake history of south-central Myanmar (Burma) 143
2. Landforms of the Payagyi ancient fortress, 16 km north of Bago 145
3. Survey profiles across the northern fortress wall. 146
4. Stratigraphic columns of the four pits dug through the base of the fortress wall.... 147
5. Fort-wall geometry after restoration by removal of post-fortress sedimentation and erosion 148
6. The schematic model shows the relationship of the Sagaing fault rupture to the sedimentation on the downthrown side near the northern fortress wall. 149
7. A sequential restoration of the fortress wall offset. 150
8. Map of the southern wall of Trench 1 151
9. The comparison of fault slip-rate estimations along the Sagaing fault averaged over different time spans. 152
10. Two fault-slip scenarios for the southern Sagaing fault. 153

Chapter 4

1. The map of Cheduba (Man-Aung) and Ramree Islands above the Sunda megathrust offshore the western coast of Myanmar 197
2. Natural sea-level indicators and their relationships with the tidal levels in the area of Cheduba and Ramree Islands. 199
3. The patterns of marine terraces, current drainages and tidal flats show the eastward tectonic tilting in northern Ramree Island over the past several thousand years. 200
4. Photograph and line sketch of site KPU-15 201
5. The patterns of modern drainages and marine terraces of the central-western coast of Ramree Island show an eastward tilt. 202
6. Field survey sites at the central-western Ramree coast 203
7. The different geomorphic characteristics of the southwestern and southeastern Ramree coast indicate the long-term uplift and eastward tilt of southern Ramree Island 204
8. Three topographic profiles at southwestern Ramree Island show ~1.5 m of land-level change of T1 after mid-16th century. 205

9. Photograph and line sketch of an inferred mid-Holocene wave-cut notch and wave-cut platform on the southeastern coast of Ramree Island.. 206
10. Map and a topographic profile of marine terraces near the village of Ka-Ma at the western coast of Cheduba Island 207
11. Map and a topographic profile of marine terraces near the village of Ka-I at the southern tip of Cheduba Island. 208
12. Map of the topographic profiles and sample locations on the marine terraces along the eastern coast of Cheduba Island. 209
13. Topographic profiles north and south of the village of Kan-Daing-Ok 210
14. Marine terraces at the northeastern tip of Cheduba Island and the elevation difference between the modern and uplifted beach berm. 211
15. Map and a topography profile of marine terraces in the northern part of Cheduba Island 212
16. A cartoon that shows the contributions of various processes to sea-level history of the past several hundred years 213
17. A compilation of measurements of 1762 uplift values, from our surveys and 19th-century documents 214
18. Three profiles of net post-1762 uplift drawn perpendicular to the megathrust. 215
19. A comparison of trench-perpendicular uplift patterns of several well-documented megathrust earthquakes and the 1762 event 216
20. A cartoon diagram shows the co-seismic uplift pattern and long-term deformation pattern produced by three different scenario fault ruptures. 217
21. Plausible 1762 fault-slip patterns beneath the central and southern profiles across Cheduba and Ramree Islands. 218
22. Range of nominal recurrence intervals for 1762-like earthquakes, based on the relationships between the long-term uplift rate and the interseismic subsidence rate at the southwestern corner of Cheduba Island (Ka-I area) 219

Chapter 5

1. The neotectonic context of Myanmar and adjacent regions 244
2. Map of the active faults around the Nam Ma Fault, based on geomorphological analysis of optical imagery and SRTM topography 245
3. The surface rupture distribution and the field survey locations for the 24 March 2011 Tarlay earthquake along the westernmost section of the Nam Ma Fault. 246
4. Map of the westernmost mapped fault rupture crossing paddy fields west of Kya Ku Ni village 248
5. Photographs of the fault rupture in the paddy fields southwest of Kya Ku Ni. 249
6. Map view of the area surrounding Pu Ho Mein village, showing where we documented ground failure 251
7. Photographs from three locations in the valley near Pu Ho Mein that may have experienced sinistral tectonic rupture. 252
8. Map of sites inspected in the vicinity of the Tarlay Township, showing several locations of left-lateral offset, which coincide with other ground-failure locations along the Nam Lam River. 253

9. Photographs of left-lateral displacements near Tarlay that appear to be tectonic ... 254
10. Photographs of ground cracks and fissures north of Tarlay. 255
11. Map of the sites with horizontal offsets east of Tarlay. 256
12. Photos of plausible tectonic offsets east of Tarlay. 257
13. The pre-earthquake and post-earthquake HRS image west of the Kya Ku Ni site. 258

Chapter 6

1. The location map of March 2011 Tarlay earthquake (Mw 6.8) near the Myanmar-Laos boarder.. 276
2. Detailed mapping of the Tarlay segment at the westernmost section of the Nam Ma fault, based on the 90-meter SRTM and 15-meter Landsat imagery. 277
3. ALOS L-band InSAR (a & b) and pixel-tracking analysis results (c)......................... 278
4. The range offset (RAO) for descending track 486 (a) and the prediction from our preferred finite fault model (b). (c) to (e) shows the ground deformation along three different profiles across the rupture. 279
5. The original InSAR and the pixel-tracking data, the resampled dataset, the modeled results and the residuals between observations and models 280
6. (a) The reduced chi-square plot as a function of the regularization weighting parameters. (b) to (e) Different realizations of models. 281
7. (a) Comparison between field measurements, the upper 600 m fault slip, and the near-fault deformation measured from the AZO pixel tracking analysis along the Tarlay segment. (b) The distribution of fault-slip along the Tarlay segment. (c) The comparison of the normalized slip potency from our preferred model and other earthquake events. 282

Appendix 1

S1. The coverage map of the remote sensing dataset that used in this study. 290
S2. Neotectonic map of Myanmar (Burma).. 291
S3. The plate motion vector diagram along the western Myanmar coast........................ 292

LIST OF TABLES

Chapter 2

1. Significant earthquakes within the study area since the late-19th century 103
2. Summary of maximum fault offset in the Sino-Shan domain fault system. 106
3. Scaling relationships for fault length and magnitude that used in this study. 107
4. Proposed Major Seismic Structures of Myanmar and surrounding countries 108

Chapter 3

1. Analytical results of all of the samples dated in this research. 154
2. Earthquake and damage record from different source near Bago from 875 C.E. to May-1930 C.E. 155

Chapter 4

1. Radiocarbon ages obtained in this study.. 220
2. U-Th Compositions and ^{230}Th Ages for Fossil Coral Samples of Myanmar by MC-ICP-MS.. 221
3. Net uplift in Ramree and Cheduba Islands Inferred From Sea Level Indicators 222

Chapter 5

1. Field measurements of the surface rupture of the 24 March 2011 Tarlay earthquake. 259

Chapter 6

1. ALOS PALSAR data used in this study.. 287

Appendix 1

S1. Table S1. Indian-Burma plate convergent rate along the northern Sunda megathrust from various plate rotation models 284

Appendix 2

S1. Table S1. Stories of the May 1930 earthquake from local villagers near the city of Bago (Pegu)... 294

S2. Table S2. Field photographs of small offsets along the Sagaing fault 299

S3. Table S3. Original description of the temporary palace near the Payagyi pagoda from U Kala's *Maha-ya-zawin-gyi* ("Great Chronicle") 300

Chapter 1

Introduction

Myanmar, also known as Burma, is located at the plate boundary between the Indian and Sunda plates. It is one of the most tectonically active regions in Southeast Asia. During the past several hundred years, numerous earthquakes occurred within this region, resulting from the on-going oblique convergence and extrusion processes between the Indian, Eurasian and Sunda plates.

Although Myanmar has experienced many large and destructive earthquakes throughout its long recorded history, the geology of these earthquakes was never studied in detail due to the logistic difficulty in the past several decades. None of the surface ruptures of the large earthquakes were documented in the past century, and the recurrence intervals and the slip behaviors of major active faults are poorly understood throughout the entire region.

As Myanmar gradually opens up in the past several years, the need of a better understanding of its potential seismic sources becomes urgent due to the rapid development in this once isolated country. Thus, we decided to systematically map the active structures of Myanmar and its adjacent regions, and to conduct a series of field studies to understand the active tectonics of some major active structures in this country. The following chapters are results of these investigations.

We used a global digital elevation model and optical satellite imagery, with the assistance of published geodetic, geologic and seismological analyses to produce an updated version of the regional neotectonic map of western Southeast Asia. The distribution of active structures throughout this region clearly shows that they are the products of three distinctive active deformation belts from the interaction of the Indian plate, the Burma plate, and the northern Sunda plate. Each of these deformation belts can be further separated into several neotectonic domains, in which active structures show distinctive structural behaviors from one domain to another.

In chapter 2 of this thesis, we provide an overview of the active structures in the country of Myanmar and its surrounding region based on remote sensing analysis. This systematic reconnaissance survey of active structures forms the basic framework for understanding the regional seismic potential in the future, as well as the possible sources of major earthquakes in the history. The discussion of plausible fault slip rates that derived from our geomorphic interpretations is also included in this chapter.

With the understanding of regional neotectonic textures of this area, we then focus on the active behavior of major structures, and the relationship of those structures to major earthquake events in the past. Due to the oblique plate convergence between the Indian and the Sunda plates, the dextral Sagaing fault and the northern extension of the Sunda megathrust are the two most active structures throughout this region. In order to further understand their active behaviors, we have focused on these two structures in the second part of this investigation.

In chapter 3, we provide results of field investigations of an ancient fortress that is offset by the Sagaing fault in lower Myanmar. We successfully mapped the geometry of the fortress wall across the Sagaing fault from the field survey, and thus was able to determine the amount of fault slip since the fortress was built. This study provides the first constraint on the fault slip rate of the southern portion of the Sagaing fault, and plausible earthquake scenarios in the past several hundred years.

The fourth chapter of this thesis focuses on the active behavior of the northern Sunda megathrust along the western coast of Myanmar. We analyze coastal uplift patterns during the famous 1762 Arakan earthquake at Ramree and Cheduba Islands. The analysis suggests the 1762 earthquake resulted from rupture of both the megathrust and major splay faults in the accretionary prism, similar to other splay faulting events in the sediment-rich subduction zones worldwide.

In the final part of this thesis, we focus on the ground deformations associated with a recent earthquake in remote eastern Myanmar. The Mw 6.8 Tarlay earthquake struck the Myanmar-Laos border in March 2011 and was accompanied by ~30-km long surface rupture along the westernmost Nam Ma fault. In the fifth chapter we provide the field investigation results of the surface rupture during this earthquake, with the assistance of the observations from post-earthquake high-resolution satellite imagery. We also present our InSAR analysis of the Tarlay earthquake in the sixth chapter of this thesis. Together these two chapters provide the analyses of the ground deformations and the fault slip behavior from both field-based and remote sensing observations.

Chapter 2

Active Tectonics and Earthquake Potential of the Myanmar region

Yu Wang[1,2], Kerry Sieh[2], Soe Thura Tun[3], Kuang-Yin Lai[4,5], Than Myint[3]

1. Division of Geological and Planetary Sciences, California Institute of Technology, Pasadena, U.S.A
2. Earth Observatory of Singapore, Nanyang Technological University, Singapore
3. Myanmar earthquake committee, Myanmar Engineering society, Myanmar
4. Department of Geosciences, National Taiwan University, Taiwan
5. Institute of Earth Sciences, Academia Sinica, Taiwan

Abstract

This paper describes geomorphologic evidence for the principal neotectonic features of Myanmar and its immediate surroundings. We combine this evidence with published structural, geodetic and seismic data to present an overview of the active tectonic architecture of the region and its seismic potential. Three tectonic systems accommodate oblique collision of the Indian plate with Southeast Asia and extrusion of Asian territory around the eastern syntaxis of the Himalayan mountain range. Subduction and collision associated with the Sunda megathrust beneath and within the Indoburman range and Naga Hills accommodates most of the shortening across the transpressional plate boundary. The Sagaing fault system is the predominant locus of dextral motion associated with the northward translation of India. Left-lateral faults of the northern Shan Plateau, northern Laos, Thailand and southern China facilitate extrusion of rocks around the eastern syntaxis of the Himalaya. All of these systems have produced major earthquakes within recorded history and continue to present major seismic hazards in the region.

Introduction

In the context of plate tectonics, the eastern margin of the Indian Ocean is a right-lateral convergent plate boundary (Fig. 1a). Along the entire plate boundary, the Sunda megathrust accommodates eastward subduction of oceanic under predominantly continental lithosphere. Right-lateral strike-slip faults traverse the entire margin, from Sumatra in the south to Myanmar in the north. The Sumatran fault accommodates most of the right-lateral component of oblique convergence along the 2000-km length of Sumatra (Fitch, 1972; Sieh and Natawidjaja, 2000; Chlieh et al., 2007; McCaffrey, 2009). An en-echelon spreading center carries a large component of the dextral component of deformation beneath the Andaman Sea (Curray, 2005). Farther north, the Sagaing fault plays a significant dextral-slip role along a 1400-km span centered on Myanmar (e.g., Win Swe, 1970; Vigny et al., 2003; Curray, 2005). Both the Sunda megathrust and the Sagaing fault systems terminate northward into the eastern Himalayan syntaxis.

The 1000- to 1300-km wide terrane bisected by the Sagaing fault is tectonically complex. On the west is the subducting oceanic Indian plate, and on the east are the predominantly continental Yangtze and Sunda blocks (Fig. 1b). Between the Indian plate and the Sagaing fault is an elongate tectonic block that is commonly called the Burma plate or the Burma sliver (Curray, 1979). Between the Sagaing fault and the Yangtze and Sunda blocks is a terrane that includes the Shan Plateau, characterized by a plexus of dextral and sinistral strike-slip faults (e.g., Lacassin et al., 1998).

Geodetic measurements show that the motion of the Indian plate relative to the Sunda block ranges from 2.7 to 4.3 cm/yr at the latitude of Myanmar (Sella et al., 2002; Prawirodirdjo and Bock, 2004; Kreemer et al., 2003; Socquet et al., 2006; DeMets et al., 2010). Geodetic and geologic measurements indicate that the Sagaing fault accommodates only about 2 cm/yr of the north component of this relative motion (Bertrand et al., 1998; Vigny et al., 2003; Socquet et al., 2006;

Maurin et al., 2010; Wang et al., 2011). The megathrust and related upper-plate structures also absorb some of the relative strike-slip plate motion (e.g., Nielsen et al., 2004; Socquet et al., 2006); the rest of the strike-slip motion may be partitioned into the interior of the Burma plate (e.g., Socquet et al., 2006). Except under southernmost Myanmar, the geometry of the subducting slab is well established from hypocenters of an east-dipping Wadati-Benioff zone (e.g., Ni, 1989; Richards et al., 2007). The 60-km isobath runs approximately beneath the eastern flank of the Indoburman range.

Historical records demonstrate that great and destructive earthquakes have occurred throughout much of the region (Fig. 2). These reports are sparse but informative (e.g., Halstead, 1842; Oldham, 1883; Milne, 1911; Brown, 1917; Brown et al., 1931 and 1933; Chhibber, 1934; Win Swe, 2006; Martin and Szeliga, 2010). Although they provide important information about the general locations and approximate sizes of the earthquakes, they reveal little or nothing about the character of the causative faults. In fact, until 2011, no post-earthquake investigations had involved mapping the surface trace of an active fault in the region. For example, only the pattern of seismic intensities (Oldham, 1883) supports the contention that the Mandalay earthquake of 1839, which killed more than 500 people in central Myanmar, resulted from rupture of a section of the Sagaing fault west of Mandalay (Le Dain et al., 1984 and Win Swe, 2006). A far more mysterious example is the earthquake of 1927, which was felt most strongly north of Yangon (Brown, 1930; Chhibber, 1934). Potential seismic sources in this region remain speculative, even though the earthquake was close to the region's largest city, which is home to more than four million people and continues to grow rapidly.

Methodology

The aforementioned geological, seismological and geodetic investigations do not constitute a systematic assessment of the neotectonic architecture of the Myanmar region and its seismic potential. Here we present a new synthesis of regional kinematics that relies principally on a modern geomorphologic analysis of tectonic landforms. The last such geomorphological study appeared three decades ago (Le Dain et al., 1984). That study relied upon Landsat satellite imagery, whereas our principal data are from shaded-relief digital-elevation imagery. In recent years, modern geomorphologic analyses founded upon the use of digital elevation models and high-quality imagery have substantially improved understanding of the kinematics and seismic potential of many other regions. A few examples include work in Sumatra (Sieh and Natawijaya, 2000), Taiwan (Shyu et al., 2005), and the eastern Tibetan plateau (Densmore et al., 2007).

In this paper, we describe the geomorphologic expression of active faults and folds within and around Myanmar. We then discuss the implications of this analysis for understanding the active tectonics of the area, drawing also on geodetic analyses, local structural studies, historical earthquake accounts and other seismological data. Our goal is to construct a view of the neotectonic architecture of the region that provides a clear framework for understanding of the recent seismic activity and the potential for future large earthquakes.

Our geomorphologic analysis relies heavily on terrestrial shaded-relief maps constructed from the Shuttle Topography Radar Mission (SRTM version 2 to version 4 at 90-m resolution) (e.g., Jarvis et al., 2008) and offshore shaded-relief maps derived from ETOPO-1 (Amante and Eakins, 2009). We also use stereoscopic imagery constructed from the Advanced Spaceborne Thermal Emission and Reflection Radiometer (ASTER VNIR L1B at 15-m resolution) (an index appears in the Appendix-1 as Fig. S1). Together these data resolve topographic features far better than non-stereoscopic imagery and enable a broad but detailed survey of the region.

In places of particular interest, we also use aerial photographs at scales of about 1:50,000 and 1:25,000. Fig. S1 in Appendix-1 shows the coverage we used. Where available, we integrate the high-resolution bathymetric data and structural geologic maps published by others to inform our interpretations.

Our reliance on geomorphic expression of tectonic landforms implies that our analysis is limited by their expression and preservation, which varies, of course, as a function of the type of deformation (Yeats et al., 1997, Burbank and Anderson, 2012). Strike-slip faults have a vastly different geomorphic expression than thrust faults and normal faults, and fast-slipping faults show up in the landscape more clearly than slow-slipping faults.

Modulating these expressions of active structures in the landscape is the degree of interaction of the solid earth with the atmosphere and hydrosphere. In particular, variations in rainfall play a major role in the variable expression of tectonic landforms. Figure 1c shows that average annual rainfall across the region varies by at least a factor of five. Rainfall in Bangladesh and the western Myanmar coast is two to three times greater than in the central Burma basin and farther east (Rudolf and Schneider, 2005; Rudolf et al., 2010). All else being equal then, erosion would reduce a young tectonic structure in the central or eastern regions less than if the same active feature were on the western flank of the Indoburma Range or in Bangladesh.

Another variable in the expression of tectonic landforms is the youthfulness of the landscape (Yeats et al., 1997). For example, the expression of active faults and folds on the young prograding river deltas of southern Myanmar will be limited to very youthful features not buried by rapid sedimentation. Older and more prominent tectonic landforms would be evident only on older landscapes.

For these two reasons, we must expect that our analysis of active tectonic features will not be uniformly sensitive to rates of activity across the entire region. Active features along the western coasts and on the southern deltas are less likely to be clearly expressed than features elsewhere in the region.

Neotectonics of the Myanmar region

Figure 2 is a simplified version of our neotectonic mapping of the Myanmar region, drafted at a scale of about 1:10,000,000. This scale is far smaller than the 1:50,000 to 200,000 scales at which we mapped structures using the SRTM and other topographic data and GIS software. We provide a more detailed neotectonic map in Appendix 1 (Fig. S2).

Figure 2 shows the division of Myanmar's three principal tectonic regimes into six domains, each defined by its particular geomorphological and structural expressions of tectonic activity. In the Indoburman range, along-strike variations in expression of convergence vary appreciably, so we have divided this system into four distinct structural domains. In the next section, we discuss each of these four domains separately, beginning in the south and ending in the north.

The Indoburman range

In its grand, arcuate northward sweep from southern Myanmar toward the Himalaya, the Indoburman range of western Myanmar evolves from narrow, low hills at 16°N to a very broad and high range near 24°N (Fig. 2). Farther north, on the south side of India's Assam valley, the mountains swing toward the east-northeast and narrow considerably.

In the far south, highly oblique convergence dominates within what we term the Coco-Delta domain. Its northern neighbor, the Ramree domain, represents a transition from oblique subduction to nearly orthogonal subduction that involves a thin accretionary wedge of sediment. The broadest portion of the Indoburman range comprises the Dhaka domain, in which a very wide belt of folded and faulted sediment mantles a very low-angle subduction megathrust. East of the Shillong plateau is the Naga domain, where the northern edge of the Burma plate overrides India's Assam block.

Coco-Delta domain

The 500-km span of the Sunda megathrust between the Andaman islands and the southern end of the Indoburman range trends decidedly more easterly than adjacent sections (Figs 1 and 2). In fact, the trend of the deformation front between about 14.2°N and 17°N is nearly parallel (within the uncertainties) to the direction of relative motion between the Indian plate and the Burma sliver plate (see Appendix-1 Fig S3 last column of row 5; Appendix-1 Table S1). This implies that subduction and accretion should be very slow here and that relative motion across the boundary should be predominantly right-lateral at a rate between about 8 and 28 mm/yr (see Appendix-1 Table S1). The lack of a Wadati- Benioff zone down dip of the deformation front between about 14°N and 17.8°N (Ni, 1989; Richards et al., 2007) lends further support to this thought. Other areas of highly oblique subduction are similar in this regard (for example, the Scotia arc and the Queen Charlotte Islands (e.g. Aristeo et al., 1989; Mazzotti et al., 2003; Bustin et al., 2007). Additional support for low rates of convergence across the Coco-Delta domain comes from seismic tomography, which shows only weak evidence of a slab extending downdip (Li et al., 2008).

The low relief of both the Indoburman range and the fore-arc in this region and their narrow (70- to 90-km) width imply low rates of uplift and little total accretion. The small sizes of Coco and Preparis Islands relative to the Andaman islands farther south also likely reflect lower rates of uplift and accretion (Fig 2 and 3). Between Preparis Island and the southern tip of the Indoburman range, rates of uplift are so low that erosion and sedimentation on the Ayerawaddy (Irrawaddy) Delta have kept pace with any ground rising above wave base (Fig. 3a). Additional support for low rates of uplift and scant accretion in the Coco-Delta domain is the fact that the Indoburman range is far narrower and lower in the Coco-Delta domain than in the next domain to the north. The precise coincidence of the southward diminishment of the Indoburman range with the northeastward extrapolation of the Coco-Delta section of the plate margin argues for an abrupt and sustained drop off of the uplift that has created the Indoburman ranges. This is clear evidence that the abrupt bend in the plate margin at the northeastern end of the Coco-Delta domain coincides with a sharp and major change in accretion and uplift rates.

Despite the abovementioned evidence for minimal vertical deformation, bathymetry along the steep escarpment of the plate margin shows clearly that there is a convergent component to deformation within the Coco-Delta domain. Swath mapping of Nielsen et al. (2004) shows that the 2-km high slope rising from the flat floor of the Indian Ocean is much steeper than is typical for accreting sedimentary prisms but very similar to the slopes of highly oblique convergent margins. The right-stepping en echelon character of both the deformation front and of some anticlines just upslope prove that the sense of slip along the section from 14° to 15.5°N is dextral-reverse rather than purely dextral (Fig. 3b).

Strike-slip faults within the thin tail of the Indoburman range conform to the dextral-reverse nature of the Coco-Delta domain. Breaking the low topography of its eastern portion are several linear features that strike roughly parallel to the range front and to the nearby plate margin (Fig. 3a and Fig. 3c). One outlying block, partially surrounded by sediments of the Ayeyarwady River appears to have shifted right-laterally about ten km from the main body of the range along the Seindaung fault. Unfortunately, the resolution of the SRTM imagery is too coarse to tell whether or not the faults laterally offset small channels and ridges there, so we do not venture an opinion as to whether or not these faults are currently active. Their sharp geomorphic expression does, however, suggest that they have been active within the Quaternary Period. Farther north, where the Indoburman range widens and transitions to the next domain, drainages are larger and more developed. Some of these display right-lateral offsets of about 10 km. We discuss these further in the next section.

Coseismic and post-seismic displacements of the great 2004 Aceh-Andaman earthquake confirm and illuminate the dextral-reverse nature of slip across the Coco-Delta domain. Meltzner et al. (2006) show that several decimeters of uplift occurred on Coco Island and that Preparis may have risen 20 to 30 cm. Horizontal deformations were measured as far north as about 13.5° (Chlieh et al., 2007). Whereas horizontal motions farther south along the arc were nearly perpendicular to the plate margin, the five stations on the Andaman Islands (between 12 and 13.5°N) experienced a marked dextral component as well. Their coseismic and post-seismic motions are nearly parallel to the strike of the Coco-Delta domain plate margin and imply up to 5 meters of purely dextral slip at the very southern end of the Coco-Delta domain and equal parts of dextral and thrust motion on the megathrust beneath the rest of the Andaman Islands.

Ramree domain

The Ramree domain is the northern neighbor of the Coco-Delta domain (Fig. 2). Sustained convergence and accretion along this 450-km section of the plate margin have produced a belt of deformation that increases in width from about 170 km in the south to about 250 km in the north (Fig. 4a). Further evidence of northward-increasing convergence through the Ramree domain is the pronounced rise in height of the Indoburman range, from less than 1000 m in the south to more than 2000 m in the north. Seismicity of the subducting Indian plate also becomes more pronounced from south to north. In the south, the deepest hypocenters of the Wadati-Benioff zone are about 70 km deep and 140 km east of the deformation front, whereas in the north, hypocenters reach depths of about 120 km and extend to about 300 km from the deformation front (NEIC catalog, 1976 to 2010).

Plate-vector diagrams that relate motion of the Indian plate to that of the Sunda block and ascribe about 20 mm/yr of dextral slip to the Sagaing fault imply dextral-oblique convergence rates between 7 and 23 mm/yr across this domain (see Appendix-1, Fig. S3, last row of columns 3 and 4). Taking the vector diagram at face value, one would expect the ratio of convergence to dextral slip to be as large as about 3:2.

With these broad attributes of the Ramree domain in mind, we now discuss geomorphologic evidence of recent neotectonic activity, moving from west to east, from the offshore and coastal regions to the interior of the Indoburman range and then to the plains east of the mountains. We begin with bathymetric evidence for the nature of deformation at the deformation front offshore and then proceed to document bathymetric and topographic evidence for activity on thrust faults within the accretionary prism nearer the coast. We then present evidence for an important dextral strike-slip fault within the mountains and a backthrust along the eastern flank of the mountains. Finally, we describe thin-skinned folds and faults to the east.

Deformation front and active structures in the accretionary prism

High-resolution bathymetry between 17° and 18.5°N displays clear evidence of tectonic shortening at and adjacent to the deformation front along the southern half of the domain (Nielson et al., 2004). Accretion of sediment is particularly clear along the salient that they call the Ramree lobe, between 17°40’ and 18°N (Fig. 4b).

East of the deformation front, along the coast, is abundant evidence for youthful folding. Flights of uplifted coastal terraces are clear even in non-stereographic, high-resolution satellite imagery, because vegetational differences differentiate flat terrace treads from steep terrace risers (Figs. 4c and 4d). Figure 4a shows that the number of terraces visible in this imagery varies throughout the region.

Thus far, Cheduba and Ramree Island, which appear to have the largest number of marine terraces, have yielded the most definitive data on uplift patterns and timing. Shishikura et al. (2009) and Aung et al. (2008) showed that these two islands and coastlines up to 100 km farther northwest have been rising incrementally throughout the late Holocene, presumably in association with large earthquakes. They also report that the terraces on the islands northwest of Ramree Island tilt northeastward.

Wang et al. (2013a) added substantial detail to this story. They demonstrated that the islands are the subaerial expressions of two doubly plunging antiforms. The long axes of these antiforms run parallel to the deformation front for more than a hundred km (Fig. 4a) and their southwestern flanks are far steeper than their northeastern flanks. They also demonstrate from field measurements and radiometric dating of mid- to late-Holocene terraces that each of the islands is tilting progressively and independently toward the mainland coast, rising most rapidly along their southwestern coasts. The pattern of uplift implies that the two asymmetric antiforms are rising on the backs of two contemporaneously active northeast-dipping faults (splay faults) within the accretionary prism.

Eyewitness accounts collected by a British survey team 80 years after the great Arakan earthquake suggest that the lowest terrace on Cheduba and Flat Island rose out of the sea during the great 1762 Arakan earthquake (Halsted, 1842; Mallet, 1878; Oldham, 1883). Wang et al. (2013a) demonstrate via U-Th disequilibrium dating of coral microatolls that the most recent large uplift of both Ramree and Cheduba Island did, indeed, occur during the great Arakan earthquake of 1762.

Dextral strike-slip faulting in the Indoburman range

Clear evidence for a 160-km long right-lateral strike-slip fault exists within the Indoburman range, from about 17.75° to 19°N (Fig. 4). All major rivers flowing to the southwestern coast exhibit sharp dextral deflections of many km along the trace of this structure, which we call the Thahtay Chaung fault (labeled TCf in Fig. 4), after one of the large river channels that it offsets (Fig. 5). Between 17.75°N and 18.5°N, the best fitting offsets for the major stream canyons are predominantly between 10.3 and 11.3 km. From 18.5°N to 19°N, the best-fit offsets diminish from about 11 to about 5 km. The fault may splay northwestward into two or more obscure structures before dying out, but the geomorphological evidence for this is not at all compelling.

The acute angle between the nearly north-south strike of the Thahtay Chaung fault and the northwesterly trends of the large offset streams suggest substantial dextral warping associated with dextral slip on the fault. Such dextral warping is especially clear within several kilometers near fault, where major channels are constantly flowing northwestward at the western flank of the Indoburman range.

We can speculate about the age of the cumulative ~10-km offsets and about the ratio of dextral slip to convergence across the Ramree domain. It is reasonable to assume that the Thahtay Chaung fault began to develop river-channel offsets once the turbidites of the regional bedrock rose above the sea and fluvial channels began to incise. The time of this emergence must substantially post-date the age of the beds, which are shown on the geological map of Brunnschweiler (1966) to be Miocene flysch. If the drainage system began to develop around 5 Ma in this part of Indoburman range, we then expect the average slip rate of the Thahtay Chaung fault would be about 2 mm/yr, given by the ~10-km offset of river channels. This would be about an order of magnitude less than the rate of convergence across the entire domain.

The Thahtay Chaung fault is the only active strike-slip fault that we could recognize from the SRTM topography. Even though the southwestern flank of the Indoburman range is remarkably straight between about 18.75° and 20°, and between 20° and 21°N a notably linear valley extends northwestward from the mountainfront, these features do not appear to reflect active strike-slip faulting. Careful inspection of these and other, lesser lineations in the Ramree domain revealed very little evidence for other young strike-slip faulting. We conclude that the Thahtay Chaung fault is the only clear manifestation of strike-slip faulting in the Ramree domain.

Active faults and folds east of the Indoburman range

The eastern flank of the Indoburman range is an impressive escarpment along the entire length of the Ramree domain, averaging slopes of ~ 3° from the crest of the range to the mountainfront.

This is far steeper than the average ~1° slope of the southwestern flank of the range. The morphology of the mountainfront suggests that it is rising along an active, west-dipping reverse fault. Along most of its length, however, there is scant evidence (at least at the resolution of the SRTM imagery) for fault scarps that would indicate a young fault breaking to the surface.

A more plausible explanation is that the escarpment has been produced by flexure. Bedding orientations and dips along the mountainfront would help us infer the underlying structure, but bedding is cryptic in the SRTM imagery, and few published works address this section of the range. Structural sections from Brunnschweiler (1966) and Bender (1983) suggest steep eastward dips of the bedrock along the escarpment, and that these beds have been overridden by the east-dipping thrust faults of the Central Basin. Our guess is that the mountainfront is mainly a fold scarp due to slip on a ramp beneath the mountain range that ruptures to the surface only locally, if at all. If this is the case, then young folds ten to a hundred km to the east, in Myanmar's Central Basin and the floodplain of the Ayeyarwady River (Fig. 4), may result from a décollement that emanates from the top of this blind structure and traverses eastward at shallow depth to a position beneath them.

Several short scarps and folds in the central valley are topographically obvious, and we propose that they are active. For example, near 18°N we observe a series of highly dissected lateritic terraces 10 to 20 km east of the mountain front that are 20 to 30 meters higher than the active floodplain of the Ayerawaddy. Many of these have fan shapes that suggest they represent alluvium originating from the Indoburman range. The linearity of the eastern edge of these terraces suggests that these are fault scarps rather than cuts into alluvial fans by a laterally migrating Ayeyarwady River. We do not see scarps on younger, unlaterized fluvial or alluvial deposits in the coarse SRTM imagery, so we have no clear evidence for latest Pleistocene or Holocene rupture.

Several other reverse faults east of the Indoburman range also have mild geomorphologic expressions that might indicate current activity in the central Burma basin. All of these are in the hundred km or so east of the Indoburman range and most are associated with anticlinal folding. The West Bogo-Yoma fault (WBf, Fig. 4) and the Paungde Fault (PDf, Fig. 4) are two east-dipping reverse faults that show clear activity during the late-Quaternary Period. At least two of these folds and reverse faults cross the Ayerwaddy River, but the coarseness of the 90-m SRTM and 15-meter ASTER imagery preclude recognition of small river terraces that would confirm young anticlinal deformation.

Eyewitness accounts of a phenomenon associated with the Prome earthquake of 1858 support the hypothesis that this field of folds and faults is seismically active. The strongest shaking of this widely felt large earthquake was reported from the reach of the Ayerwaddy valley that encompasses the cities of Prome and Thayet-Myo (Fig. 4). Eyewitnesses report that in the several hours following the earthquake, the Ayerawaddy near Thayet-Myo flowed upstream (Oldham 1883). This could be explained by sudden uplift across the 30-km long, 10-km wide anticline that crosses the Ayerwaddy about 20 km downstream from the city. The river drops about 2 m between Thayet-Myo and the anticline, so if incremental uplift of a few meters occurred during the earthquake, the river gradient might have been impeded enough to cause the river surface to be instantaneously tilted upstream. A considerable amount of time would have been necessary for the river surface to re-equilibrate to an appropriate gradient. This explanation is identical to that advanced for the retrograde flow of the Mississippi river in the hours following the New Madrid earthquake of Feb-1812. During that event, a six-meter uplift of the Tiptonville dome, an anticline astride the river, caused the river to flow upstream and overflow its banks (Penick, 1981).

Dhaka domain

North of the Ramree domain, the Burma sliver plate collides with the thickest part of the great Ganges-Brahmaputra delta. The effect of this collision with a 20-km thick pile of Eocene to Holocene sediment (Fig. 1a) has been the formation and rapid westward growth of a great fold and thrust belt within the sediments of the eastern side of the delta (Fig. 6a). The total width of this Chittagong-Tripura fold belt (CTFB) and the higher part of the Indoburman range approaches 400 km at 23°N. The crest of the Indoburman range increases in height northward from the Ramree domain to nearly 3000 m at 21.3°N, and retains a height of more than 2000 m for many hundreds of km northward. We refer to this ~500-km long section as the Dhaka domain, after the largest city within the fold and thrust belt.

In marked contrast to domains to the south and north, a well-expressed Wadati-Benioff zone illuminates the subducting Indian oceanic lithosphere in the Dhaka domain (e.g. Ni, 1989; Satayabala, 1998; Guzman-Speziale and Ni, 2000). Hypocenters occur as deep as 200 km and up to 450 km from the deformation front. Few of the focal mechanisms are consistent with either strike-slip or dip-slip on the megathrust; most reveal steeply dipping strike-slip and normal faulting associated with internal deformation of the down-going slab (e.g., Satyabala, 1998; Purnachandra and Kalpna, 2005). Beneath the Chittagong-Tripura fold belt, several moderate earthquakes show dextral or reverse faulting in the shallow part of the crust; however, their hypocenters are not well constrained by the global seismic network. The seismic silence of the megathrust raises an important question: Does the megathrust in the Dhaka domain slip only aseismically or is it capable of generating great megathrust earthquakes?

GPS-based vector diagrams suggest that modern relative motions between the Indian plate and the Burma plate at the latitudes of the Dhaka domain are similar to relative motions across the Ramree domain (Appendix-1, Fig. S3, rows 1 and 2). Relative motion between the Indian plate and Sunda plate, with 18-22 mm/yr of right-lateral slip on the Sagaing fault removed, yields oblique convergence between the Indian plate and Burma plate. At 21.25°N, estimated motions of 6 to 25 mm/yr are predominantly perpendicular to the deformation front, with a small component of dextral strike-slip. Further north, at 23.5°N, the dextral strike-slip motion increases significantly due to the change of megathrust fault's orientation. Relative motion of a station within the fold belt

(Aizawi, Fig. 6a) is about 10 mm/yr eastward toward Dhaka (Jade et al., 2007; Banerjee et al., 2008). Although GPS stations are too sparse to fully map strain accumulation across the Burma plate at this latitude, this measurement is consistent with a predominance of convergence and a minimal oblique component. Farther north and east, Imphal is converging southwestward toward Dhaka at between 11 and 20 mm/yr. This implies significant active right-lateral strike-slip faulting or clockwise rotations at this latitude.

With these broad attributes of the Dhaka domain in mind, we now discuss stratigraphic, geomorphologic, and seismic evidence of recent neotectonic activity, moving from west to east, as we did for the Ramree domain. We begin with a discussion of the history of deformation within the Chittagong-Tripura fold belt (CTFB) on the eastern flank of the Ganges-Brahmaputra delta. We then proceed to document topographic evidence for activity on faults within the higher parts of the Indoburman range. Finally, we discuss the significance of the steep eastern flank of the range and evidence for and against active faulting in the lowlands farther east.

Chittagong-Tripura fold belt (CTFB)

Relevant to our neotectonic analysis is a large body of work on the geological architecture and history of the Ganges-Brahmaputra delta and the CTFB. We begin with a summary of salient information.

The Ganges-Brahmaputra delta rests on lithosphere that is transitional between thick, buoyant Indian continental lithosphere on the west and north and dense Indian oceanic lithosphere on the east. (e.g., Alam, 1989; Curray, 1991). Sediment contributions to the delta began to arrive from the Himalaya and Indoburman range around the early Oligocene epoch (~35 Ma) and have been prograding southward to the present day (e.g., Curiale et al., 2002; Curray et al., 2003). The arriving mass of these sediments loaded and depressed the underlying lithosphere, leading to the creation of additional accommodation space for deltaic sediment. Additional lithospheric depression and accommodation space has resulted from the southward thrusting of the Shillong Plateau over the delta through the past 5 million years and from the westward thrusting of the Indoburman ranges toward the delta (e.g., Johnson and Alam, 1991). Altogether, current thicknesses of the deltaic sediment now range from about 12 to 21 km on the western flank of the Dhaka domain (Curray, 1991; Brune et al., 1992).

The Chittagong-Tripura fold belt has developed within the upper parts of this thick deltaic sequence. Many folds are clearly visible in the SRTM imagery as north-northwest-striking anticlinal and synclinal hills (Fig. 6a). Through construction of a balanced cross section across the CTFB, Maurin and Rangin (2009) estimated a total east-west shortening of about 11 km in the past 2 million years, which implies a long-term shortening rate of about 5 mm/yr.

Various stratigraphic and structural studies show that the CTFB has not developed synchronously. In general the fold belt has grown progressively westward, toward the deformation front (Johnson and Alam, 1991; Uddin et al., 1999; Steckler et al., 2008; Maurin and Rangin, 2009). Many of the folds in the west have been active only from the late Pliocene or later. Many of the folds in the eastern part of the CTFB appear to no longer be active, even though they are clearly evident on the SRTM imagery. The rate of propagation of the deformation front has been about 100 mm/yr in the past 2 million years (Maurin and Rangin, 2009), far greater than the current rate of convergence across the fold belt.

This rapid propagation of the deformation front helps to explain the broad curvature of the CTFB between 24°N and the Shillong plateau. As the fold belt has propagated into the basin over the past 2 million years, it has not been able to propagate over the continental crust of the Shillong plateau, which has been rising and thrusting southward out over the basin through the past five million years. The sweep of the fold belt thus reflects the impediment to westward propagation imposed by the Shillong plateau.

Figure 6 shows in black those anticlines and related faults that do not appear to have been active recently. Those anticlines and related faults mapped in red have evidence for recent activity. In the case of the faults, evidence for activity consists of unusually steep flanks on the related anticline, which suggests that a fault has propagated to, or close to, the surface. In the following paragraphs we describe the evidence for recent activity of some of the anticlines.

Published seismic reflection profiles across several anticlines reveal growth strata that constrain the initiation of folding. In some places the age of the growth strata constrain the initiation of anticlinal growth to Pliocene or younger. The initiation of the Sylhet, Habiganj, Patiya, Jaldi, and two offshore anticlines (labeled S, H, P, and J in Fig. 6a) are so constrained (Johnson et al., 1991; Steckler et al., 2008; Maurin and Rangin, 2009).

Evidence of even more youthful activity exists for a few other folds. These include the Maheshkhali anticline, whose upper surface formed during the Last Glacial Maximum, when the fluvial plain extended many kilometers out onto the current seafloor but now sits far above the modern floodplain (M, Fig. 6a). Khan et al. (2005) interpret this to indicate uplift in the past 18,000 years. Possible support for activity of this anticline is a report of extensional cracks that developed atop this anticline during a small (mb 5.2) earthquake in 1999 (Ansary et al., 2000). Steckler et al. (2009) plausibly interpret these as an indication of "coseismic slip on a blind ramp-flat fault with extension in the hangingwall block as it moved through the kink." Khan et al. (2005) also propose that the nearby Jaldi anticline is active, as evidenced by the young age of the soil on its crest. Their luminescence date from the crestal surface of the anticline implies a rise in fluvial baselevel in the past 35,000 years.

Other clear evidence of youthful vertical deformation along the western portion of the CTFB is resolvable from the SRTM 90-meter digital elevation model and from optical satellite imagery. Sandwip Island, at the mouth of the Ganges is a good example (SW, Fig. 6a). A nearby radiocarbon date (Goodbred and Kuehl, 1999) suggests to us that its upper surface is about 7,000 years old or younger. That surface displays an anticlinal warp of ~5 meters above sea level (Fig. 6b). This is likely representative of the entire Comilla Tract immediately to the north. The surface of this large tract at the front of the modern delta is three to four meters above the modern surface of the delta (Steckler et al., 2008) and appears to be very gently folded (CT, Fig. 6a). Another tract of the delta, Madhupur tract north of Dhaka (MT, Fig. 6a), sits well above the surrounding modern delta plain (Morgan and Mclntire, 1959, Coates and Alam, 1990; Steckler et al., 2008). Its westward slope raises the possibility that a fault has recently propagated beneath it and may even break the surface at its western edge (e.g., Steckler et al., 2008). The existence of both the Comilla and Madhupur Tracts suggest that the active deformation front has propagated as far west as the Ganges River.

Other evidence from SRTM topography and optical imagery are two uplifts farther south. The anticline at the southern tip of Bangladesh (Dakhinpara) uplifts a terrace ~ 5 to 10 meters above the current fluvial and coastal plain (Da, Fig. 6a). Farther south, St. Martin Island sports at least two marine terraces, which imply incremental uplift since the mid-Holocene (SM, Fig. 6a, and Fig. 4).

Although the earthquake history is mostly unclear throughout the Chittagong-Tripura fold belt, large, destructive earthquakes are well known and frequent in this area. One of the recent large events is the Srimangal Earthquake of 1918 (M ~7.5), during which the northwestern part of the CTFB and the adjacent Ganges-Brahmaputra delta were shaken strongly. Stuart's (1920) isoseismal map shows clearly that the highest intensity occurred just east of the Rashidpur anticline (R, Fig. 6a), where most of the buildings were leveled to the ground. The distribution of high intensities during the Srimangal Earthquake suggests the earthquake was caused by a fault beneath the northwestern fold belt, perhaps most likely the fault that is associated with uplift of the Rashidpur anticline.

Other large earthquakes within the Chittagong-Tripura fold belt may have resulted from slip on the megathrust itself. The area of Chittagong was so badly damaged by the Arakan earthquake of 1762 that some have suggested that the megathrust ruptured from the Ramree domain through the southern portion of the Dhaka domain (e.g., Cummins, 2007; Gupta and Gahalaut, 2009). Another earthquake in 1548 also wreaked havoc across nearly the entire Dhaka domain. Based on its widespread high seismic intensities, Steckler et al. (2008) suggests this earthquake resulted from rupture of the megathrust north of the 1762 rupture patch. However, paleoseismological investigations along the southern flank of the Shillong Plateau suggest that the earthquake was caused by slip on the north-dipping Dauki fault (Morino et al., 2011).

The high Indoburman range

A ~170-km long right-lateral oblique-slip fault is clearly evident in the topography of the high Indoburman range near Imphal (Fig. 6a). Along the western flank of the Imphal basin, many of the eastward flowing rivers and basins exhibit dextral deflections and warping along the Churachandpur-Mao fault (Fig. 6). This NNE-SSW-striking fault also shows a clear vertical component in the SRTM topography, as the range rises up steeply more than 1000 m from the basin floor to the mountain crest. We find the largest dextral geomorphic offset is about 3 km along the fault trace, whereas the vertical offset is likely more than 1.5 km (Fig. 7a and 7b). Both the vertical and right-lateral offsets diminish northward and southward, and the geomorphological evidence becomes less compelling north and south of the basin.

The latitudinal span of the Churachandpur-Mao fault is almost perfectly coincident with the span over which the CTFB narrows from south to north. This spatial correlation suggests that the fault resulted from the impediment posed by the Shillong block to westward motion of the Indoburman range. If the high Indoburman range is not moving westward as fast in the north as it is in the south, then a dextral-slip fault with the orientation of the Churachandpur-Mao fault could be a consequence and manifestation of that differential motion.

This neotectonic scenario also suggests the initiation of the Churachandpur-Mao fault would have been much later than the formation of the high Indoburman range. Geomorphic features within the Imphal basin support this hypothesis. For example, wind gaps along the western flank of the basin suggest that the drainage basins west of the Imphal basin originally extended east into the basin. Moreover, the burial of highly eroded ridges in the eastern part of the basin indicates that it became the depositional center after formation of these ridges. Both of these observations support the hypothesis that initiation of the Churachandpur-Mao fault occurred long after initiation of uplift and erosion of the high Indoburman range.

We can speculate that lifetime-averaged slip rate of the fault is about 2 mm/yr, if we assume that the fault initiated about 2 Myr ago and that its total maximum offset is represented by the 3-km dextral and 1.5-km vertical geomorphic offset. This very long-term guess is much lower than the differential motion seen in geodetic measurements across the high Indoburman range. GPS vectors suggest modern motion across the Churachandpur-Mao fault is an order of magnitude higher and the horizontal motion is almost purely dextral (i.e., 1 to 1.6 cm/yr; Jade et al., 2007; Kumar et al., 2011; Gahalaut et al., 2013). This disparity implies that our calculation of a long-term rate may be grossly in error. It could be correct, however, if either the rate of slip has accelerated by nearly an order of magnitude or permanent dextral deformation across the high Indoburman range is distributed across a wider deformation belt rather than localized along the Churachandpur-Mao fault.

East flank of the Indoburman range and beyond

The tectonic morphology of the eastern flank of the Indoburman range in the Dhaka domain is very different than that throughout the Ramree domain. In addition to an impressive east-facing escarpment, the eastern flank includes the basin of the Kabaw valley, which is flanked on the east by a narrow range of low hills (Fig. 6a). This implies that the east-dipping fault that traverses the eastern side of the Kabaw valley is raising the hills faster than sediment streaming out of the Indoburman range can bury the hangingwall block of the fault.

We call this the Kabaw fault system, as originally proposed by Win Swe et al. (1972). Others have used this name in reference to west-dipping thrust faults along the entire eastern flank of the Indoburman range (e.g., Hla Maung, 1987; Curray, 2005). In this work, we conform to the original use of the name.

The youthful appearance on SRTM and ASTER images of the eastern flank of the Kabaw valley between 22˚N and 24.8˚N suggests that the Kabaw fault system is active. Closer inspection of the southern half of the valley with 1:25,000-scale aerial photographs revealed no evidence for offset of an elevated erosion surface along a steeply dipping strike-slip fault in the center of the valley (Fig. 8). Moreover, evidence of thrust-fault scarps on the eastern side of the low hills was equivocal. We therefore believe that if the Kabaw fault system is currently active, its rate of slip is equal to, or lower than rates of sedimentation and erosion in this N-S running narrow basin.

Naga domain

A fundamental change in the Indian-Burma collision occurs at 25˚N, where the Dauki thrust intersects the western flank of the Indoburman range (Fig.1). As the folds of the Chittagong-Tripura fold belt approach the Dauki thrust from the south, they swing eastward and the width of the belt narrows from about 240 to about 160 km (Fig. 6a). North of the Dauki fault the CTFB is absent, and in its place along the steep western flank of the Naga Hills is a fold and thrust belt that is an order of magnitude narrower (Fig. 9a). We refer to this segment of the Indo-Burman collision as the Naga domain, after the eponymous mountains that span the 430-km distance between the Shillong plateau and the Himalayan syntaxis.

This dramatic change in the structural and topographic expression of collision at 25°N reflects the dramatic change in nature of the footwall block across the Dauki fault. As we have just described, collision south of the Dauki fault in the Dhaka domain is extending rapidly westward, out into the thick pile of Gangetic delta sediments that rest atop transitional and foundering oceanic crust (Fig. 1). North of the Dauki fault the Naga Hills override a very different footwall – recently uplifted continental crust of the Shillong Plateau and (farther east) the narrow continental shelf of the Assam block (e.g., Verma et al., 1976; Clark and Biham, 2008).

The stark geomorphologic contrast between Chittagong and Naga domains appears to reflect shallow crustal differences in collision rather than deep-seated ones. The nature of the higher Indoburman range does not change markedly across the domain boundary. Nor do isobaths drawn on the top of Wadati-Benioff zone beneath the mountains show any clear bend or tear across the domain boundary below depths of ~60 km. The narrower width of the shallow portions of the Wadati-Benioff zone beneath the Naga Hills is consistent with the lack of a wide, CTFB-like fold and thrust belt and underlying décollement.

Beneath the Naga Hills, the Wadati-Benioff zone extends to depths of ~160 km, as far as 150 km from the mountainfront. This implies subduction of at least a couple hundred km of oceanic lithosphere before the thrust faults of the Naga hills began to ramp up onto the continental shelf of the Assam block in the early Miocene (Kent et al., 2002).

The Naga Hills reflect convergence of the Burma plate and the Assam block across the 430 km that separate the Shillong Plateau from the Himalayan syntaxis. The narrowing of the hills from about 170 km in the southwest to 90 km in the northeast (Fig. 9a) may imply a northeastward diminishment in total shortening across the range.

Geomorphological expression of the Naga thrust is very clear along the front of the Naga Hills, and its presence there is well known from geological and geophysical surveys (e.g., Mathur and

Evans, 1964; Berger et al., 1983; Ranga Rao and Samanta, 1987). The fault trace appears as several arcuate lobes along the range front. Along its southwestern 100 km, a linear scarp clearly marks the location of the fault. An anticline and 5-km wide piggyback basin sit on the hanging-wall block, and nested terraces imply incremental uplift. The highest terrace projects ~200 m above the range front, suggesting late-Quaternary uplift of at least that amount (Fig. 9b). Younger terraces display uplifts ranging from 20 to 50 m.

Geological mapping and seismic reflection lines at ~95.5°E illuminate the nature of the fault system. The fault dips moderately to steeply and breaks the surface at the position shown on Figure 9a. It thrusts folded lower Miocene rocks over undeformed upper Pliocene to Quaternary beds (Kent et al., 2002). The geometry of the anticlinal fold implies that it developed as a fault-propagation fold that was eventually breached by propagation of the fault to the surface. The clear geomorphological expression of the anticline implies that it is still active and that the dip of the thrust fault decreases at depth (Fig. 9c).

The Naga thrust system terminates at 96° E where it appears to be cut by a NW-striking thrust fault and associated anticlines. This short fault appears to be the westernmost element in a system of thrust faults associated with westward thrusting of the Eastern Himalayan syntaxis over the Assam valley and Naga Hills. We infer from the topographic profile of the crest of the Naga Hills that slip on the Naga thrust dies out over ~100 km as it approaches this termination.

The Sagaing domain

The Sagaing fault system performs the classic role of a ridge-trench transform fault as it traverses the 1400-km distance between the Andaman Sea spreading center in the south and the eastern Himalayan syntaxis in the north (Fig. 1) (Yeats et al., 1997). Total dextral offsets since the Miocene, estimated from bedrock matches, river offsets across the fault and the total opening of the Andaman Sea, range from about 203 to 460 km (e.g., Mitchell, 1977; Myint Thein, 1981; Curray et al., 1982; Hla Maung, 1987; Armijo et al., 1989). The central and the southern part of the Sagaing fault also approximated the western boundary of the Sunda block during its eastward and southward extrusion in an early (~34 to ~17 Ma) phase of the Indian-Asian collision (e.g., Leloup et al., 2007). It is recognized as the region's major tectonic divide, separating disparate rocks of the Burma plate from those of the Sunda plate (e.g., Mitchell, 1977; Curray et al., 1982).

Seismicity and both geomorphologic and structural evidence confirm that it is a dextral-slip fault system (e.g., Myint Thein, 1991; Hla Maung, 1987; Guzman-Speziale and Ni, 1993). Its recent slip rate, assessed from an offset Pleistocene basalt and from GPS measurements, is about 20 mm/yr (Bertrand et al., 1998; Vigny et al., 2002, Socquet et al., 2006, Maurin and Rangin 2010). Given its high slip rate, it is no surprise that the fault is well expressed geomorphically – the most notable exception being where it traverses the rapidly aggrading and prograding young delta north of and beneath the Andaman Sea. Isoseismal maps and seismic analyses of historical earthquakes show that about half of the Sagaing fault has ruptured during many large earthquakes over the past nine decades (e.g., Brown and Leicester, 1933; Hurukawa and Phyo Maung Maung, 2011, Table 1).

Like the San Andreas Fault, but in contrast to the Sumatran fault, the Sagaing fault system is unbroken by large stepovers or complications along most of its length. This unbroken geometry is probably due to the fault's large accumulation of slip. The northern 400 km of the fault system, however, is very complex. It comprises several distinct faults arranged in a complex horsetail pattern that fans out northward to a width of about 100 km. This complex geometry likely reflects both the lengthening of the fault system to accommodate India's northwards motion and the extrusion of Asia around the eastern Himalayan syntaxis.

Between about 18˚N and the Himalayan syntaxis, the Sagaing fault forms a broad concave-eastward arc (Fig. 1). The fact that the arc mimics the curvature of the eastern flank of the Indoburman range to the west and coincides with the belt of sinistral-slip faults to the east intimates a shared cause – likely the westward extrusion of the Sichuan-Yunnan block around the syntaxis. The fast slip rate of the Sagaing fault overwhelms erosional and depositional activity along most of its trace, so abundant tectonic landforms enable us to map and characterize most of the fault well. This geomorphic evidence, in addition to historical seismicity, inspires us to divide the fault into various segments. We begin with segments along the southern subaerially exposed and relatively simple portion of the fault and then proceed to the complex horsetail of the northern few hundred km.

The southern section of the Sagaing fault

Although a synoptic view of most of the Sagaing fault leads one to think that its geometry is simple, careful geomorphic mapping justifies its division into five distinct segments between 16.5˚ and 23.5°N (Fig. 10). What distinguishes these segments are bends, splays and distinct secondary features, as well as the terminations of historical ruptures.

Bago segment

The Bago segment extends northward at least 170 km from the Myanmar coast, across the young, southward-propagating delta of the Sitong River (Tsutsumi and Sato, 2009, Wang et al., 2011). We do not know how much further it extends southward on the submarine portion of the Sitong River delta. However, regional structural maps show that the Bago segment connects to a series of E-W running normal faults several tens of km south of the current coastline (e.g., Replumaz, 1999; Pubellier et al., 2008). Its northern limit coincides with an abrupt 10˚ westward bend at 18˚N (Fig. 10). Tsutsumi and Sato (2009) and Wang et al. (2011) mapped in detail the tectonic landforms of this segment, from the aerial photos and satellite imagery. The last major earthquake produced by the Bago segment was the Mw 7.2 Pegu earthquake of May 1930 (Table 1; Pacheco and Sykes, 1992). Measurement of small offsets led Tsutsumi and Sato (2009) to suggest that the maximum offset during this earthquake was at least 3 meters. Wang et al. (2011) suggest a rupture length of about 100 km, extending from the southern coastline to ~20 km north of Bago city, based on the field investigations and their interpretation of isoseismals published by Brown et al. (1931). Measurements of an offset ancient wall and related paleoseismic work north of Bago led Wang et al. (2011) to propose an earthquake recurrence scenario for the Bago segment.

Pyu segment

The Pyu segment extends ~130 km, from the sharp bend at 18°N to a bifurcation at 19.1°N. Along this reach, the main trace of the Sagaing fault skirts the base of the escarpment of the Bago-Yoma range (Fig. 10). SRTM imagery clearly shows that most fluvial channels and alluvial fans from the Bago-Yoma range are offset right-laterally at the mountain front (for details see Appendix-1 Fig. S2). Close to the central part of this segment, an elongate terrace borders the Pyu segment on the east. The terrace is rising on the hangingwall block of a west-dipping reverse fault that crops out on the east flank of the ridge (Replumaz et al., 1999). This reverse fault and the escarpment are manifestations of a minor component of transpressional shortening across the Pyu segment (Replumaz et al., 1999; Wang et al., 2011). This transpression is consistent with the 10˚ counterclockwise deviation of this section of the Sagaing fault from its overall more northerly strike.

The last major earthquake generated by the Pyu segment is the Mw 7.3 Pyu earthquake, which occurred in Dec 1930, just a few months after the similar-sized rupture of the Bago segment to the south (Table 1). The relocated epicenter of the Pyu earthquake is close to the segment's southern boundary (Hurukawa and Phyo Maung Maung, 2011). The isoseismals drawn by Brown and Leicester (1933) clearly show that the highest intensities of the earthquake span the entire Pyu segment. Thus it is appears that the entire Pyu segment ruptured during the Dec 1930 earthquake.

Nay Pyi Taw segment

At 19.1°N the Sagaing fault splays into two parallel fault traces that span the entire ~70 km length of the Nay Pyi Taw segment (Fig. 10). The relief across the fault along this segment is much more subdued than it is along the Pyu segment. This indicates lesser vertical motion during the Quaternary Period. Both traces of the Nay Pyi Taw segment offset channels and alluvial fans, so slip is significantly partitioned between these two branches. In the north, both traces traverse the ~30 km long basin in which the new capital, Nay Pyi Taw, was established in 2005. The western trace cuts through the eastern edge of the new capital, and sports a ~5-m high east-facing scarp.

This segment does not appear to have produced a large earthquake in recent times. The moderate Swa earthquake of August 1929 (Table 1) severely damaged the railroad and bridges about 40 km south of the new city (Brown, 1932; Chhibber, 1934). The highest intensities of the earthquake occurred along the eastern branch of the Nay Pyi Taw segment south of Myanmar's new capital city (Brown, 1932). But because the earthquake does not appear in the early global seismic catalog and was only felt in a limited area, we believe its magnitude is likely not to have been larger than Mw 7.

Meiktila segment

The Meiktila segment traverses a ~220 km reach of the fault between Nay Pyi Taw and Mandalay. Its very simple trace runs almost uninterrupted from just north of Nay Pyi Taw to the southern side of the Irrawaddy river. Our choice for the northern boundary of the Meiktila segment is a bit arbitrary, but is coincident with a greater prominence of transpressional secondary features north of the river.

Unlike the Pyu and the Nay Pyi Taw segments, the Meiktila segment does not run along the eastern base of the Bago-Yoma Range; instead it traverses a broad valley (Fig. 10; Appendix-1 Fig. S2). Narrow linear ridges are common along the fault trace as it traverses the fluvial valley fill.

These probably reflect shallow shear dilatation of the faulted sands and gravels of the floodplain (e.g., Gomberg et al., 1995). The utter lack of elevation differences across the fault shows that along this segment the Sagaing fault has no vertical component of slip. The largest clear right-lateral offset is ~2.4 km across a channel at 20°N.

There is no clear historical record of rupture of the Meiktila segment. The most recent plausible such event would be the Ava earthquake of 1839, so named for the ancient capital that straddles the fault on the southern bank of the Ayeyarwady River. Records written by British officers in nearby Mandalay indicate that the earthquake caused catastrophic damage and liquefaction east and south of the Ayeyarwady River, especially in Ava (Oldham, 1883, Chhibber, 1934).

Sagaing segment

The namesake of the Sagaing segment is a small city on the fault just north of the Ayeyarwady River. It is the tectonic morphology of this section of the fault that led to the fault's discovery by Win Swe (1970). The northern limit of the Sagaing segment is at 23.5˚N, where the fault steps left approximately 2 km from the eastern bank to the western bank of the Ayeyarwady River (Fig. 10; Fig. S2). The northern limit of the Sagaing segment also marks the location where the fault splays into multiple traces. Further to the south, in the low Sagaing hills, east of the fault and north of the Ayeyarwady crossing are the southernmost outcrops of metamorphic rocks on the eastern flank of the fault.

Like the Meiktila segment, the Sagaing segment is relatively straight and simple. However, along its southern extent, the elongate ridges that comprise the Sagaing hills are larger than the ridges in the young fluvial sediments of the Meiktila segment and display more structural relief. Perhaps this greater relief is an indication that the formation of the Sagaing hills began well before the fault-zone ridges to the south, where they involve disruption only of young sediment and rocks.

Between 21.9˚N to 22.6˚N, the Sagaing segment runs along the western bank of the Irrawaddy River and offsets a series of post-Pliocene alluvial fans along a 20-km reach (Myint Thain et al., 1991).

North of the Singu basalt, SRTM topography suggests that the Sagaing fault comprises two parallel fault traces, west and east of the Ayeyarwady River. Farther north, the western trace becomes what we term the Tawma segment, after it splits to two northward-diverging faults. A 5- to 10-meter high east-facing scarp on a fluvial surface attests to the recent activity of the eastern trace.

The northern two-thirds of the Sagaing segment may have produced the magnitude 7.6 earthquake of September 1946 (Fig. 10; Table 1). The relocated epicenter of the earthquake implies that the event initiated south of the Singu basalt (Hurukawa and Phyo Maung Maung, 2011) (Fig. 10). A field investigation after the Shwebo earthquake of 11 November 2012 located ground cracks along the youthful-looking small scarps that we mapped from SRTM (Soe Thura Tun, personal communication). We therefore suggest that that part of the fault may have ruptured during both the September 1946 earthquake and the most recent event. The southern third of the segment may have ruptured during a smaller, Ms 7.0 earthquake in July 1956, which caused severe building damage in the Sagaing-Mandalay area (Win Swe, 2006). Unfortunately, no field investigations were conducted or isoseismal maps made after the 1946 or 1956 events. Based on the historical records of shaking, however, we speculate that the part of the Sagaing segment that runs along the western flank of Sagaing hills ruptured during the 1956 Sagaing earthquake.

The Northern section of the Sagaing fault

Beginning at 23.5˚N, the Sagaing fault system fans northward as four distinct active fault zones that terminate sequentially from west to east between about 25˚ and 27˚N (Fig. 11). Geomorphological evidence for the westernmost fault zone ceases at about 25˚N, whereas evidence for the easternmost one extends as far north as ~27˚N and nearly connects to active structures between the Sagaing fault system and the Naga thrust. Because slip is distributed among these four sub-parallel fault traces, their geomorphic expressions are not as clear as those of the southern strands. The four fault zones of the northern Sagaing fault system comprise six discrete segments, distinguished by their geometries and discontinuities. In the paragraphs below, we describe each, starting with the southern and western ones and moving north and east.

Tawma and Ban Mauk segments

The Tawma segment extends northward from a complex of faults at 23.5°N (TMs in Fig. 11). The Tawma segment is the northward continuation of the western fault trace of the northern part of the Sagaing segment (see Fig. S2 for details). The Tawma segment strikes northward nearly along the base of an east-facing escarpment. Some of the drainages flowing across the escarpment show right-lateral deflections across the fault.

The geomorphic expression of the segment disappears at ~24°N, at a left stepover to the Ban Mauk segment, which is 10 km farther west (BMs, Fig. 11). The stepover between the two segments is complicated. SRTM imagery shows an array of NE-SW striking faults across a 10-km wide transpressional ridge. Some of these faults may have a normal component of slip. The lengths of these secondary faults are mostly less than 20 km, and their subtle expression suggests they have low slip rates, compared to the rates of the main traces of the Sagaing fault.

A Mw 6.9 earthquake in 1991 may have resulted from rupture of the Tawma segment. Its relocated epicenter is near the segment's southern termination (Hurukawa and Phyo Maung Maung, 2011) (Fig. 11). The CMT solution is consistent with dextral slip on a nearly N-S striking fault. This orientation is more consistent with the strike of the Tawma segment than the strike of the active In Daw segment to the east (IDs in Fig. 11). Moreover, the length of the Tawma segment is comparable to typical rupture lengths for an earthquake of this magnitude (Wells and Coppersmith, 1994).

The Ban Mauk segment extends ~150 km northward from approximately 23.8˚N (BMs in Fig. 11). It separates Neogene volcanic rocks on the west from Miocene sedimentary rocks on the east (Bender, 1983). Geomorphological expression of the Ban Mauk segment is more muted than along segments to the south and east; clear geomorphic evidence, such as offset channels and offset drainage basins are rare. Thus, we posit that the right-lateral slip rate of the Ban Mauk segment is significantly lower than the rates of neighboring faults. The northern terminus of the Ban Mauk segment is east of Taungthonton volcano, at 25˚N. It appears that the fault trace there is covered by the apron of clastic deposits from Taungthonton volcano. This is another indication of the low rate of slip of the Ban Mauk segment at least through the late Quaternary period.

The scant evidence of youthful activity along the Ban Mauk and Tawma segments is consistent with recent analysis of geodetic data, which implies that most strain across the Sagaing fault system is accumulated on fault segments farther east (Maurin et al., 2010).

In Daw and Mawlu segments

The In Daw and Mawlu segments extend northnortheastward 170 km from the Sagaing segment. They form the eastern boundary of the fault system between ~24˚ and ~25˚N (Fig. 11). The In Daw segment separates from Tawma segment on the northern bank of Ayeyarwady River at 23.7°N, striking 7˚ more easterly than the Tawma segment. Farther north, at 24.25°N, a 3-km wide pull-apart basin, holding In Daw Lake, separates the In Daw segment from the Mawlu segment, which continues northnorthwestward another 90 km. The northern limit of the Mawlu segment coincides with several fault traces that cut Cretaceous to Eocene ultramafic rocks.

The InDaw and Mawlu segments are much more clearly expressed geomorphically than their western neighbors, the Tawma and Ban Mauk segments. We find the largest dextral geomorphologic offset across the In Daw/Mawlu segments to be about 4 km, four to five times larger than the largest geomorphologic offset across the Tawma and Ban Mauk segments. Furthermore, recent geodetic analysis implies strain accumulation equivalent to ~2 cm/yr of dextral slip across the InDaw and Mawlu segments (Maurin et al., 2010). These two independent observations imply that the slip rate across these eastern segments has been substantially higher than the slip rates of the western segments through at least the past few thousand years.

Although their epicenters were separated by 200 km, the In Daw segment produced a Mw7.3 foreshock three minutes before the Sagaing segment's Mw 7.7 earthquake of September 1946 (Pacheco and Sykes, 1992; Table 1; Figs. 10 & 11). The size of the 7.3 earthquake is consistent with the 80-km length of the In Daw segment, so we suspect that the entire In Daw segment ruptured during this foreshock.

Shaduzup, Kamaing and Mogang segments

The northern termination of the Mawlu segment is at ~ 24.8°N, where the fault system trifurcates and fans northward in the shape of a horse's tail (Fig. 11). From west to east, we call these strands of the horse's tail the Shaduzup, Kamaing and Mogang segments (SZs, KMs and MGs in Fig. 11).

The obscurity of geomorphic evidence for activity along the westernmost of these suggests that it accommodates less strain than its two neighbors. Although the Shaduzup segment truncates Tertiary geological units and structure, we did not find clear evidence of drainages offset across the fault. The northern termination of the Shaduzup segment is not well defined in the coarse SRTM topography north of 26°N, so it appears that its total length is no more than 120 km.

The Kamaing segment traverses the western flank of a ridge composed of Precambrian and Miocene rocks (Bender, 1983) and displays clear geomorphologic evidence of youthful activity along its middle reach. The Kamaing segment extends much farther north than the Shaduzup segment, well into the eastern border of the Naga Hills, north of 26.7°N. Several drainages along the eastern side of the Naga Hills show clear dextral offset near the northern termination of the Kamaing segment. Farther northwest, the northwestern extension of the Kamaing segment connects to the thrust fault system that bounds the eastern margin of the Assam valley (Fig. 11).

The Kamaing segment has been seismically active over the past four decades, but no earthquakes larger than M 6 appear in the global catalogue. A cluster of moderate (M 5 to 6) earthquakes forms a lineation parallel and almost beneath the fault trace between 26˚ and 27.4˚N. Another set of earthquakes clusters along it around 25.4˚N. If generated by this segment, these clusters may indicate partial decoupling of this reach of the Kamaing segment, a notion supported by a modern geodetic analysis that implies very shallow locking of this segment (Maurin et al., 2010).

The easternmost of the active horsetail faults is the Mogang segment. It extends in a broad arc from ~24.8˚N to ~26.8˚N. Northward from 24.8˚N, it forms an arcuate boundary between hills of Precambrian and Miocene rocks on the west and a broad valley on the east. Along the eastern flank of the hills, deflections of a series of drainages that incise the Miocene formation suggest up to 10 km of dextral offset. This implies that the Mogang segment has also been active during the late Quaternary Period. The Mogang segment terminates at 26.8°N, east of the Naga domain, along strike of a NW-SE running thrust fault that bounds Precambrian and Cretaceous units of the eastern Himalayan syntaxis (Fig. 11).

Unlike the Kamaing segment, the Mogang segment has been seismically silent in the past several decades. The last major earthquake to originate near these segments is the Ms 7.5 earthquake of January 1931 (Pacheco and Sykes, 1992; Table 1). Its relocated epicenter is within kilometers of the arcuate Mogang segment (Table 1). The magnitude of the earthquake suggests a surface rupture of about 100 km, short enough to be associated with either the Mogang or the

Kamaing segment (Fig. 11). The lack of a reliable isoseismal map for this earthquake precludes us from confident assignment of the earthquake to either of the two segments. We favor the Kamaing segment as the source, however, because earthquake intensities were higher near the Kamaing segment than along the Mogang segment (Chhibber, 1934). However, we cannot rule out the possibility of a Mogang source of this event, as the seismic intensity records were sparse for this event.

The Shan-Sino domain

The Shan-Sino domain embodies a plexus of active predominantly left- and right-lateral faults between the Sagaing and Red River faults (Fig. 2). North- to north-northwest-striking dextral-slip faults dominate the western and central eastern parts of the domain. West- to northeast-striking sinistral-slip faults dominate the central corridor of the domain, from its northwestern corner, near the northern Sagaing fault, to the arcuate Dien Bien Phu fault, about 750 km to the southeast (Fig. 1). The geometry of these faults and GPS vectors drawn relative to the Sunda block (e.g., Simons et al., 2007) show that these faults accommodate southwestward rotational extrusion of the northern part of the Sunda block at rates that increase northwestward, toward the eastern Himalayan syntaxis. This extrusion appears to be driven by the ongoing extrusion of eastern Tibet's Sichuan-Yunnan block, which is bounded on the east by the Xiaojiang fault system (see Tapponnier et al., 1982) (Fig. 1). In the past 4 to 5 million years, the Xiaojiang fault has experienced about 60 km of left-lateral motion, which is consistent with the broad 40- to 60-km bend of the Red River fault (e.g., Allen et al., 1984; Wang et al., 1998). The presence of significant dextral-slip faults and a few normal faults within the region southwest of the Red River fault imply that the Shan-Sino domain is also extending slightly in an east-west direction (Fig. 12).

The Sunda block has an earlier Cenozoic tectonic history involving its eastward and southward extrusion during an earlier phase of collision of India into Asia (e.g., Tapponnier et al., 1982; Leloup et al., 2007). Many of the structures related to this earlier collision remain visible in the topography of the Shan-Sino domain, but by and large appear to be inactive. Some of these earlier structures served as dextral-slip faults in the earlier phase of extrusion, but have been moving left-laterally throughout at least the past 5 million years (Lacassin et al., 1998).

In the paragraphs below we describe evidence for activity of the faults of the Shan-Sino domain, beginning with the larger left-lateral faults and then the larger right-lateral fault systems.

The left-lateral faults

Summary

The large left-lateral faults form the core of the Shan-Sino domain (Fig. 12). In general, these left-lateral faults (like the GPS vectors) arc around a pivot point near the eastern Himalayan syntaxis, with fault curvature decreasing away from the syntaxis.

Many of these left-lateral faults distinctly offset the major river courses of Southeast Asia, including the Salween and Mekong Rivers and their tributaries. These sharp offsets imply a long and ongoing history. Some of these offsets have a hairpin shape that implies a regional reversal of slip from right- to left-lateral sometime between 5 and 20 Ma (Lacassin et al., 1996).

To facilitate a structured discussion, we separate these left-lateral faults into four geographical subgroups. The first group including the Daying River, Ruili, Wanding and nearby smaller faults slice through the northwestern corner of the Shan-Sino domain. These exhibit left-lateral shear and have associated west-northwest normal faults. The second group includes the Nanting, Lashio and Kyaukme faults, which are farther southeast and show almost purely westward left-lateral motion. The third group is still farther southeast and much shorter. The southeastern limit of the domain is defined by the long Dien Bien Phu fault zone.

Daying River, Ruili and Wanding faults

The Daying River fault, Ruili fault and Wanding fault cut the northwesternmost portion of the Sunda plate (Fig. 12). Two common characteristics are that each connects to a N-S striking normal-dextral fault in the northeast and that each has a clear normal-slip component in the southwest. These characteristics show that this corner of the Shan-Sino domain is extending roughly east-west.

The **Daying River fault** is the northwesternmost of these three principal left-lateral faults. It courses southwestward about 135 km from the Tengchong Volcanic field in Yunnan (TCV, Fig. 12) to the western escarpment of the Shan plateau in northern Myanmar. Along its traverse of the southeastern margin of the Yingjiang basin, it shows well-developed triangular facets indicative of a normal-slip component and clear left-lateral channel deflections (Fig. 13a).

A field survey along the Daying River fault that enabled thermoluminescence (TL) dating determination of 10 and 20 ka ages for alluvial surfaces showed that left lateral slip rates are ~1.2 to 1.6 mm/yr (e.g., Guo et al., 1999a; Chang et al., 2011).

A Mw 5.5 earthquake that struck the region in March 2007 also indicates that the Daying River fault is active (Table 1). Both the focal mechanism and relocated aftershocks are consistent with the strike and sense of slip on the Daying River fault (Lei et al., 2012). Judging from the lateral extent of the aftershock sequence, the 2007 earthquake may have resulted from rupture of an approximately 12-km long section of the fault.

The **Ruili fault** (aka Longling-Ruili fault) parallels the Daying River fault to the south. It roughly follows the highly sheared Gaoligong metamorphic belt and extends more than 140 km from Yunnan to northeastern Myanmar (Fig. 12; Socquet and Pubellier, 2005; Wang et al., 2008; Huang et al., 2010). We map the fault splitting in the east into several northward-striking faults and connecting to N-S striking normal-dextral faults (Fig. 12; Fig. S2). The Ruili fault merges southwestward with the E-W striking Wanding fault.

Figure 13b illustrates some of the complexity of the Ruili fault in the east, at the north margin of the Luxi basin. There the fault comprises at least two major active fault traces. These parallel faults cut the highly sheared Goligong metamorphic belt and offset a series of incised drainages that are separated by wind or water gaps (W, Fig. 13b). Left-lateral channel deflections along the southern of the two faults range from 2 to 3.6 km, but the wind and water gaps along the trace allow for a plausible offset as large as 11 km. The northern of the two faults could accommodate an additional km of slip and a lesser fault nearer the mountain front could have slipped 0.5 km. The down-to-the-southeast steps across these faults implies a normal-slip component to the fault zone here, as well.

The geomorphic features in the west are not as clear as those in the east. Perhaps slip is transferred to a normal fault at the left step of the fault across the Ruili basin. This 60-km long normal and left-lateral Namkham fault (NKf, Fig. 12) forms the southern margin of the Ruili basin and dies out near the western escarpment of the Shan plateau.

An alluvial fan surface offset near the eastern end of the Ruili fault and shown to be 33 kyr old by luminescence dating has been offset about 70 m (Huang et al., 2010). This and a nearby channel deflection of about 20 m on a 10-kyr old alluvial fan suggest the left-lateral slip rate of approximately 2 mm/yr.

The 170-km long **Wanding fault** is southeast of the Ruili fault. It bends northward near its eastern end and terminates at a N-S striking normal fault. The Wanding fault connects with the Ruili fault at its western end. Topographic relief across the Wanding fault is small, perhaps because its strike is not oblique to the direction of regional extension.

Lacassin et al. (1998) and Wang et al. (1998) report 9- and 10-km left-lateral offsets of the Salween River across the Wanding fault. Tributaries of the Salween River are offset similar amounts (Figure 13c). This observation indicates the horizontal displacement along the entire Wanding fault is roughly constant.

Field investigations and a survey of aerial photography shows that the Wanding fault offsets a series young fluvial terraces of the Salween River (Chang et al., 2012). They derive an average left-lateral slip rate of about 2 mm/yr based on the thermoluminescence (TL) ages from the offset sediments. This confirms the earlier estimate of Lacassin et al. (1998), which was based upon the assumed age of incision of the Salween River.

On May 29, 1976, two Mw 6.7 and Mw 6.6 earthquakes struck the region between the Ruili and Wanding fault in quick succession, causing severe destruction in local villages (Table 1; Fig. 12). Focal mechanisms match the strike of the Ruili fault, but no fault surface ruptures were found along the fault trace. An isoseismal map of the second earthquake centers on the intersection of the Ruili fault and a normal fault (Compilation Group of China Seismic Intensity Zoning Map SSB, 1979). We speculate that the Mw 6.6 event resulted from rupture of the easternmost portion of the Ruili fault. The isoseismal contours of the first earthquake focus close to the Wanding fault. One of the high intensity is coincident with a secondary normal and left-lateral fault of the Wanding fault system, so we suspect it to be the cause of this earlier event.

Nanting, Lashio and Kyaukme faults

These faults comprise an arcuate 400-km long system of left-lateral faults that cuts across nearly the entire width of the Shan plateau. SRTM topography and LANDSAT imagery show that this system terminates near, but slightly east of the western escarpment of the plateau. The fault traces sport geomorphological features typical of strike-slip faults without a large component of dip slip: linear ridges, narrow and localized pull-apart basins, laterally offset stream channels and alluvial fans and the like (Yeats et al., 1997).

The longest of these faults, in fact the longest within the entire Shan-Sino domain, is the **Nanting (Nan Tinghe) fault**. An abundance of offset features demarcate its trace. Within the Yunnan area, two traces mark the eastern section of the fault. Both traces clearly exhibit large channel offsets. The southeastern of the two is the less linear, less continuous and shorter of the two, which indicates that the northwestern branch is structurally more mature; that is to say that it has accommodated more slip. This is supported by the fact that most of the young depositional basins align along the northwestern trace (Zhu et al., 1994). Along the western margin of the Shan Plateau, geomorphically obvious fabric within the Mogok metamorphic belt shows clear sinistral warping near the termination of the Nanting fault, indicating its left-lateral fault slip has been accommodated by diffuse deformation within the metamorphic belt, and that the fault does not extend as far west as the Sagaing fault.

The geomorphic evidence for recent activity of the Nanting fault has been long recognized (e.g., Zhu et al., 1994; Wang and Burchfiel, 1997; Lacassin et al., 1998; Wang et al., 1998; Socquet and Pubellier, 2005; Wang et al., 2006), but the total slip across the Nanting fault is not agreed upon. Lacassin et al. (1998) suggest that left-lateral offset is greater than 8 km, based on the offset of the channel of the Salween River. Wang and Burchfiel (1997) suggest the northeastern part of Nanting fault offsets the Mengliang ophiolitic suture about 40 to 50 km, five to six times greater than the Salween River offset along the central section of the fault. A later study from Wang et al. (1998) suggests that the southern branch of the Nanting fault may accommodate 17 km of left-lateral offset, based on the left-lateral warping of a major river.

In an attempt to resolve the dispute between the proponents of the 8-km and the 40-km offsets, we re-examined the geomorphic evidence for offset of the Salween River. We note that a wide wind gap east of the 8-km measurement would permit an offset as great as at least 15 km (Fig. 14a). This wind gap is wide enough to have accommodated the Salween River before it migrated to its current channel south of the fault. Moreover, a plausible restoration of channels at the eastern end of the fault implies a left-lateral offset as large as 21 km across the Nanting fault (Fig. 14b and c). This 21-km offset estimation magnitude of left-lateral offset could also apply to the Salween River offset. Nonetheless, this value would still be no more than half the 40- to 50-km bedrock offset suggested by Wang and Burchfiel (1997).

The last major earthquake in the vicinity of the Nanting fault is a M ~7 event in May 1941 (Figure 12; Table 1). The eastern part of the Nanting fault intersects the zone of highest intensities (Compilation Group of China Seismic Intensity Zoning Map SSB, 1979). Wang et al. (2006) argue from the historical earthquake reports that surface rupture of an at least 12-km long section of the fault is plausible. No other sections of the 370-km long fault can be associated with large earthquakes of the 20th century. Indeed, for that eastern part of the fault within Yunnan province, Chinese historical data reveal no other destructive events in their written history (Wang et al., 2006), which for this region extends at least prior to the Qing dynasty (~17th century).

South of and parallel to the western part of the Nanting fault are the left-lateral Lashio and Kyaukme faults. The two faults also exhibit clear geomorphic evidence of activity, but not to the degree that the Nanting fault does. This comparison suggests comparatively lower slip rates.

The 85-km long **Lashio fault** lies 30 km south of the Nanting fault (Fig. 12). The match of bedrock ridges, channel deflections and the width of a transtensional basin suggest a plausible total left-lateral offset of about 6.5 km. The eastern part of this E-W fault curves to the northeast and splits into a group of southeast-dipping normal faults. Along the Lashio fault's western span, geomorphic evidence of horizontal displacement gradually diminishes westward, which suggests that left-lateral slip may disperse into secondary faults that we cannot identify in the SRTM and ASTER imagery.

The Kyaukme and Nanting fault have an en echelon relationship to each other, whereby the former runs parallel to, but lies to the south and west of the latter (Fig. 12). Like the shorter Lashio fault, the Kyaukme fault curves northward along its eastern part.

The approximately 210-km long **Kyaukme fault** does not show any clear horizontal deflection of the current channel of the Salween River, although the river does have a gentle left-curving channel south of an ~300-m high fault scarp. A series of small beheaded channels at the base of this scarp suggests left-lateral offsets greater than one km. The western portion of the fault traverses the northern margin of two large basins and there shows left-lateral deflections of rivers flowing into the basins. The largest geomorphic offset that we see in SRTM topography is approximately 2.5 km, along the central and western parts of the fault (for locations see Table 2).

With one possible exception, both the Lashio and the Kyaukme fault were seismically quiet throughout the 20th century. An Mw 7.2 earthquake on June 22, 1923 may have resulted from failure of one of these faults, as the epicenter from global earthquake catalog falls southeast of the Kyaukme fault (Fig. 12; Table 1). However, the lack of an isoseismal map or a damage report impedes assignment of a likely source.

Menglian, Jinghong, Wan Ha and Mengxing faults

Still farther southeast, a group of left-lateral faults occupies the central part of the Shan-Sino domain (Fig. 12). The most prominent of these are the Menglian, Jinghong, Wan Ha, Mengxing, Nam Ma and the Mae Chan faults. All of these faults are more limited in their eastern and western extent that the large fault systems just discussed. Three features in common are that they strike NE-SW, their lengths range from roughly 100 to about 200 km, and they terminate to the northwest just shy of a prominent NW-SE striking fault. In this section, we will discuss together the geomorphic evidence for the Menglian, Jinghong, Wan Ha and Mengxing faults, the smaller of the six.

The 120-km long **Menglian fault** straddles the border between China and Myanmar and shows clear geomorphic evidence for activity (Mf; Fig. 12). On the east, it terminates before reaching the major NW-SE running dextral Lancang fault. On the west, the fault ends near where it crosses the Salween River.

The total left-lateral offset of the Menglian fault is approximately 5 km. Lacassin et al. (1998) suggest that it offsets the Nam Hka River about 2.5 km at the hairpin loop that led them to propose an earlier 5 km offset as well (Fig. 15a). However, a tributary of Nam Hka River, west of the Nam Hka's hairpin, shows a left-lateral deflection of about 5 km (Fig. 15a). At the eastern part of the Menglian fault, a tributary of the Nam Loi River (Nanlei River) shows approximately 5.5 km left-lateral deflection (for location see Table. 2). Smaller left-lateral deflections and warps are also evident in the drainage networks traversed by the fault.

The Menglian fault is the likely source of an Mw 5.9 foreshock and Mw 6.8 earthquake mainshock in the Chinese-Myanmar border region in July 1995. Both epicenters and the aftershock cluster are ~20 km south of the Menglian fault. Both focal mechanisms are consistent with left-lateral slip on the Menglian fault. The mapped region of highest intensity roughly coincides with the fault near the border (Chen et al., 2002). Thus, we suggest the western part of the Menglian fault produced the mainshock.

Eighty km southwest of the Menglian fault is a very similar structure, the 110-km long **Jinghong fault**. As with the Menglian fault, the Jinghong fault terminates just before reaching the dextral-slip Lancang fault (Fig. 12). Coincident with the intersection of these two active faults is a triangular shaped basin. Beyond the Jinghong's western termination is a normal fault that may relate to the termination of the Jinghong fault.

The Jinghong's largest geomorphic disruption is an 11-km sinistral deflection along its central part. There the Taluo River, which flows along the China-Myanmar border, bends left-laterally along the fault (Fig. 15b). Both upstream and downstream, its channel is deeply incised into bedrock, so this likely represents an offset. Further support for this hypothesis is the fact that a nearby contact between granitic intrusive rocks and Paleozoic rocks displays a left-lateral offset that is similar to that of the nearby river (Bureau of Geology and Mineral Resources of Yunnan, 1993). Smaller offsets of fans and channels indicate that the Jinghong fault continues to be active.

A Mw 7.1 earthquake on Feb 2, 1950 was most likely caused by rupture of the Jinghong fault. The epicenter of mainshock is very close the central part of the fault and several Chinese cities north of the Jinghong fault were damaged (Xie and Tasi, 1983). Unfortunately, though, Chinese intensity data are too sparse to enable construction of an isoseismal map that might confirm the source. Two more recent and more moderate earthquakes (Mw 5.6 and Mw 5.4) on June 23, 2007, may also have resulted from failure of the Jinghong Fault. Their GCMT focal mechanisms are consistent with the fault's strike.

Further southeast, the Wan Ha and Mengxing faults form a complicated left-lateral fault system. They come within about 10 km of each other in their central reaches, but diverge toward the southwest (Wf & MXf; Fig. 12). Both curve southward near their southwestern termini and transform into southeast-striking normal faults. To the northwest, the nexus of these and the dextral-slip Lancang fault zone are series of extensional basins.

Two major river channels that flow across the ~140-km long **Wan Ha fault** show left-lateral deflections of several km. Lacassin et al. (1998) suggest that the Nam Loi River, which flows across the central part of the Wan Ha fault, is left-laterally offset about 5 km. Farther east, the Mekong River has a similar sized left-lateral curve along the easternmost trace of the fault (Fig.

15c). Matching the shape of these two river channels and the crest of a bedrock ridge, we derive a 5- to 6-km geomorphological left-lateral offset of the Wan Ha fault. Along its northeastern part, where the Wan Ha fault strikes nearly NNE-SSW along the eastern margin of a transtensional basin, SRTM topography shows clear left-lateral bends and deflections of channels. These small tectonic landforms imply activity of the fault during the Quaternary period.

The **Mengxing fault** traverses more than 180 km from near the Lancang fault to the Myanmar-Thailand border region, where both the Mekong and Nam Loi Rivers display a large left-lateral offset (Fig. 15c). Lacassin et al. (1998) noted the hairpin shape of the Nam Loi River and suggested that the sense of slip reversed from right- to left-lateral about 20 to 5 Myr ago. We estimate the left-lateral deflection of the Mekong River to be between 7 and 11 km and that of a small tributary just to the southwest to be ~11 km. This small tributary and the Mekong River are separated by a wind gap at the Mengxing fault (Fig. 15c). The Nam Loi River hairpin loop, however, shows 23 to 24 km of left-lateral deflection 56 km farther southwest. Both upstream and the downstream sections of the Nam Loi River are deeply incised into bedrock, so it is reasonable to surmise that the river has had little space to meander from its ancient to its current course. Moreover, there seems to be little possibility for this deflection to have been caused by river capture. The 23- to 24-km bend may be the largest geomorphological left-lateral offset on the Mengxing fault. This would imply that the smaller 11-km offset of the Mekong River and its tributary result from river capture after the initiation of left-lateral slip.

Nam Ma and Mae Chan faults

We now consider two larger left-lateral faults farther to the southeast in the central Shan-Sino domain (Fig. 12). The **Nam Ma fault** appears as a narrow 215-km long fault zone in the region of the Lao-Myanmar border, with a 12-14 km left-lateral offset of the Mekong River channel at the central part of the fault (Lacassin et al., 1998). The hairpin geometry of the Mekong River channel here implies that a larger 30-km right-lateral offset preceded this left-lateral phase (Lacassin et al., 1998). Left-lateral offset across the 310-km long Mae Chan fault is smaller; landforms visible in SRTM topography suggest an offset of about 4 km (Table 2).

The Nam Ma fault terminates on both ends in transtensional basins. Consistent with the fault's left-lateral sense of slip, the basin at the northeastern terminus is in the block north of the fault, whereas the basin at the southeastern terminus is in the block to the south.

Two-hundred to 400-m left-lateral deflections of small river channels crossing the fault that we identify from SRTM and LANDSAT imagery imply that the fault is still active. Rupture of the westernmost 30 km of the fault during the Mw 6.8 Tarlay earthquake in March 2011 proved that the fault is still active (chapter 5 and 6).

Tectonic landforms along the **Mae Chan fault** are less clear than those along the Nam Ma fault. Perhaps this implies that the fault is slipping at a lower rate, as its smaller total geomorphic offset also implies. SRTM topography suggests that the fault has multiple traces west and south of the Mekong River. Farther west, the fault cuts through a Quaternary basin, within which it exhibits a ~50-m high north-facing scarp.

The epicenter of the Mw 6.3 earthquake of May 16th, 2007 is mid-way along the Mae Chan Fault, and the focal mechanism of the earthquake is consistent with the strike of the fault. A larger, M 6.8 earthquake in 1925 may have resulted from rupture of the eastern part of the Mae Chan fault (Table 1). However, neither an isoseismal map nor earthquake reports are available to constrain better the 1925 earthquake source.

Dien Bien Phu fault

The Dien Bien Phu fault forms the southeastern boundary of the Shan-Sino domain (Fig. 2 and Fig. 12). It is the southeasternmost active left-lateral fault between the right-lateral Red River and Sagaing faults. The fault is nearly but not quite co-linear with the left-lateral Xiaojiang fault system on the opposite (north) side of the Red River fault and is southeast of the 40- to 60-km left-lateral bend of the Red River fault that has resulted from extrusion of the Sichuan-Yunnan block (e.g., Wang et al., 1998). Along its southern reaches, the Dien Bien Phu fault exists within the much older (Triassic) Nan Suture zone and multiple linear valleys imply that it fans into multiple left-lateral faults within a wide deformation belt.

Tectonic landforms are prominent along the southwestern and northern thirds of the 370-km long Dien Bien Phu fault. The central section of the fault may, in fact, not be active. SRTM topography along the northern (Vietnam) segment and the southern (Mekong) segment clearly shows river channel and alluvial fan offsets. The largest left-lateral geomorphological offset along the Vietnam segment is about 12.5 km (Lai et al., 2012). Numerous kinks in the Mekong River canyon parallel the Mekong River segment and may indicate large left-lateral offsets there as well. However, we are not confident that these left-lateral bends reflect left-lateral motion because we cannot restore small drainages and regional geomorphic or bedrock patterns in any consistent way.

The central (Nam Hou) segment of the Dien Bien Phu fault separates the Vietnam and Mekong segments by a 110 km stretch, along which evidence of young fault activity is weak. Young fluvial landscapes dominate the low-relief topography and the best evidence for the fault seems to be contrasts of bedrock. We find only weak geomorphic evidence of fault activity. Moreover, the Nam Hou River shows no evidence for tectonic warping where it crosses the fault. We suggest that the Nam Hou segment has experienced only very small left-lateral motions and that what deformation has occurred is distributed across a wide zone.

Some historical earthquakes may have been caused by the Dien Bien Phu fault. The Mw 6.8 earthquake of Nov 1935 occurred near the southern end of the Vietnam segment (Figure 12). Moreover, the Mw 6.2 earthquake of June 24, 1983, has a focal mechanism that is consistent with the strike of the fault.

The right-lateral faults

Summary

Two right-lateral fault systems define the western and northeastern flanks of the Shan-Sino domain (Fig. 2; Fig. 12). The western of these systems is nearly parallel to the Sagaing fault and extends about 200 km into the Shan-Sino domain (Fig 10). The northeastern set of faults is subparallel to the Red River fault and extends nearly 300 km into the Shan-Sino domain. These systems extend along most of the western and northeastern flank of the domain, but notably terminate northward near the Nanting fault system (Fig. 12).

Wuliang Shan fault zone

The Wuliang Shan fault zone is a diffuse, dextral shear zone 50 to 100 km southwest of the Red River fault. It extends nearly the entire 400-km length between the Nanting and Dien Bien Phu fault zones as a set of discontinuous dextral and normal faults. The strand that courses along the eastern flank of the Wuliang Shan range shows very large and significant dextral offset of the river channels. Dextral offsets there range from 300 m to more than 3 km. The largest dextral offset in SRTM topography is approximately 6 km, along the central part of the fault (Fig. 16a). Field investigations and interpretations of aerial photography supports our observation, suggesting right-lateral offsets of several hundred meters on several NNW-running faults within the Wuliang Shan fault zone (e.g., Guo, et al., 1999b).

The Wuliang Shan fault zone was very active in the 20th century. The last of five moderate earthquakes along the fault zone was an Mw 6.1 on June 2, 2007, near the city of Ning’er (Table. 1). Both the GCMT focal mechanism of the mainshock and the distribution of the relocated aftershocks (Lu and Zhou, 2011) are consistent with the general strike of and sense of slip on the Wuliang Shan faults. Other recent earthquakes, such as the Mw 6.0 of March 15, 1979 and the Mw

5.6 of January 26, 1993, also show GCMT focal mechanisms that are consistent with the strike and the slip sense of the Wuliang Shan fault.

Lancang fault zone

The right-lateral Lancang fault zone traverses a distance of about 210 km, between the left-lateral Nanting and Mengxing faults (Fig. 12). It forms the boundary between set of left-lateral and right-lateral faults. The fault is a simple strand in the north but a complex set of anastomosing faults in the south. Although a regional geological map shows that the Lancang fault offsets the Lincang batholiths 30 km left-laterally (e.g., Wang and Burchfiel, 1997), geomorphic offsets are clearly right-lateral. This implies a history of slip inversion as previously hypothesized for currently left-lateral faults in this region (Lacassin et al., 1998).

We estimate right-lateral slip across the Lancang fault system to be about 17 km, based on a series of right-lateral bends of the Nanguo River valley (Fig. 16b). If this offset began to accrue around 5 Ma, in concert with initiation of right-lateral slip on the Red River fault and left-lateral slip on the Xiaojiang fault (e.g., Lacassin et al., 1998; Wang et al., 1998; Leloup et al., 2007), then the average fault slip rate of the Lancang fault system is approximately 3.4 mm/yr. This rate is close to the higher bound of the 2 ± 2 mm/yr dextral rate estimated in the geodetic study of Shen et al., (2005).

The best seismic confirmation of the activity of the Lancang fault is a Mw 7.0 earthquake that occurred on Nov 6, 1988 (Table 1). An approximately 45-km long rupture occurred along the northern part of the fault accompanied the earthquake (Yu et al., 1991). A post-earthquake field survey found clear dextral slip at least at two locations along the main trace of the fault. At one of these locations, offset reached 1.4 m (Yu et al., 1991; Wang et al., 1991).

Kyaukkyan fault zone

The Kyaukkyan fault zone is a complex 500-km long right-lateral fault zone that lies within the western Shan plateau between ~18˚ and 22.5˚N, 100 to 150 km east of the Sagaing fault (Fig. 10). Its northern terminus nearly coincides with the western terminus of the left-lateral Kyaukme fault. The fault zone includes a 40-km wide right step with prominent active normal faults in the vicinity of Taunggyi. At 18˚N it intersects the Mae Ping fault zone, which arcs southeastward into Thailand (e.g., Morley et al., 2007). We separate the Kyaukkyan fault zone into three distinct segments, based primarily on its stepovers and geomorphic expression.

Myint Nge segment

The northern 160 km of the Kyaukkyun fault is east of Mandalay and north of Taunggyi, the capital of the Shan states (Le Dain et al., 1984). Tectonic landforms along this reach demonstrate clearly that it is an active dextral-slip fault (Fig. 17; Fig. S2). The largest of these is the offset of the Myint Nge River (Fig. 17a). This deeply incised river flows westward from the Shan plateau and down the Shan escarpment. At the fault crossing, it has a hairpin geometry that implies initial sinistral motion of 8 to 10 km followed by dextral offset of approximately 5 km (Fig. 17a & b).

The Northern segment of the Kyaukkyun fault produced one of the largest earthquakes in Myanmar's history on 23 May 1912 (Brown, 1917; Chhibber, 1934). Earlier reports assign it a magnitude of 8 (Gutenberg and Richter, 1954), but later studies re-assess its magnitude and revise it downward to Ms 7.7 to 7.6 (e.g., Abe and Noguchi, 1983; Pacheco and Sykes, 1992). The area of highest intensities encompasses the entirety of the Northern segment but does not extend close to Taunggyi (Brown, 1917; Wang et al., 2009; Fig. S4). The distribution of highest intensities and the size of the earthquake are consistent with rupture of the entire northern segment.

Taunggyi segment

Geomorphological expression of the Kyaukkyun fault zone becomes obscure as it extends southward toward Taunggyi, likely because it splays into several less-rapidly slipping traces (Fig. 10; Fig. 12). From 21.5°N the fault zone widens into several obscure strands that extend southward into a 50-km wide transtensional basin. This basin extends 100 km from north to south, to 20.3°N. The most obvious active faults associated with the basin are the two normal faults that bound it – the Pindaya fault on the west and the Taunggyi fault on the east.

Both of these two bounding normal faults show clear, youthful vertical displacements. The steep limestone escarpment of the east-facing Pindaya fault is at least 350 m high and the west-facing Taunggyi escarpment is about 400 m near the city of Taunggyi. Farther south, Inle Lake shows an asymmetric geometry that suggests eastward tilt of the basin associated with motion of the Taungyi fault. The western side of the lake is significant shallower than the eastern side (Fig 17c).

Although the limestone escarpment that extends from Taunggyi to Inle Lake is steep and rugged, we were unable in the field to find any small scarps along its base that might have indicated rupture within the past few centuries or millennia. Nonetheless, triangular facets and faulted alluvium indicate activity in the late Quaternary Period (Fig. 17c).

Salween segment

The Southern segment of the Kyaukkyun fault extends from the southern end of the transtensional basin southward ~220 km to the Mae Ping fault zone at the Salween River (Fig. 10). The maximum offset we found at this segment is ~4.7 km from the offset bedrock ridge and ~5.4 km from the offset Salween River, almost identical to the maximum offset we found at the northern segment of the Kyaukkyan fault. The major fault trace passes through the western bank of the Moybe dam (Fig. 10) and was covered by the young fluvial deposits south of the reservoir. Further south, the fault trace bends nearly 20° westward at 19.2°N, and create a narrow transtentional basin along the Salween River. The southern segment of the Kyaukkyan fault connects to the Mae Ping fault zone at about 18.2°N. After merge with the Mae Ping fault zone, it continues runs ~170 km southeastward along the Thai-Myanmar border and may later entering the Mekong basin north of the Bangkok (e.g., Morley et al., 2007).

Mae Ping fault zone

We also find clear geomorphic evidence along the northwestern part Mae Ping fault that suggests the dextral slip along its fault trace. However, comparing to the Sagaing fault and the Kyaukkyan fault, the amount of dextral motion is smaller based on the maximum channel offsets we found along its fault trace. Between the Sagaing fault and the southern Kyaukkyan fault, we only find ~1.2 km dextral offset along the Mae Ping fault from the SRTM data. East of 97.5°N, the maximum dextral offset on the Mae Ping fault is ~2.5 km after the southern Kyaukkyan fault connects the Mae Ping fault system (Fig. 17d).

Partially reactivated faults of the Shan escarpment

A dramatic linear valley that parallels and lies between the Sagaing fault and the Kyaukkyun fault within the Shan escarpment, suggests the presence of a large strike-slip faults there (Fig. 10). The question for us is whether or not this large fault is active. The lack of disruption of small landforms along most of its trace implies that most of it is inactive. Perhaps it was an active element of the early to mid-Cenozoic extrusion of the Sunda block. In those few places where small drainages show right-lateral deflections, we show the fault as active on Figure 10.

Earthquakes past and future

The two principal motivations of our neotectonic study of Myanmar have been to understand the past occurrences of and future potential for large earthquakes in the Myanmar region.

Throughout the previous pages, we have accomplished the former by constructing a new neotectonic map that helps to make sense of many of the large earthquakes of the past century or so.

Looking to the future, public seismic safety will depend to a large extent on understanding the potential for other large earthquakes throughout this region. Our neotectonic map assists in this goal, as well. Many of the active faults within the region have not produced large earthquakes during the past century or more of human record-keeping, so what is their potential for the future?

Although what we have presented is by no means complete, our geomorphologic mapping augmented by seismic, geodetic and other relevant geological data, provides a fundamental basis for a simple evaluation of the predominant seismic sources for each of the three active tectonic domains of Myanmar and its neighboring countries. In this section we utilize our neotectonic understanding of these active faults to assess their potential for future rupture. The current scarcity of published structural information, high-quality seismological and geodetic data and paleoseismological information limits this effort to a pretty basic level. Nonetheless, we provide below a synoptic, first-order estimate of plausible earthquake scenarios within each domain.

Wells and Coppersmith (1994) (W&C) provide equations that relate rupture length to earthquake magnitude. Blaser et al., (2010) improved upon these scaling relationships by using a enlarged historical earthquake database. They also incorporated thrust fault ruptures in subduction environments, thus enabling better estimates of earthquake magnitude for such faults. Length-magnitude scaling relationships for subduction megathrusts have also been given by Strasser et al. (2010). These two independent scaling relationships help us to estimate the uncertainties in estimation of maximum earthquake magnitude produced by the megathrust along the western Myanmar coast. Table 3 lists the parameters that we used to calculate potential earthquake magnitude.

Although we used structural discontinuities, jogs and kinks to define structural segments and assumed that these segment boundaries delimit plausible future fault ruptures, we are well aware that fault ruptures sometimes propagate through such structural complications and thus produce larger earthquakes (e.g., Wesnousky, 2006). Currently, however, paleoseismological and historical documentation of rupture lengths in the Myanmar region are too sparse to warrant a sophisticated consideration of multiple–segment ruptures. In this first effort, we simply estimate magnitudes associated with single-segment rupture for the mapped faults. In some cases, we also use estimates of fault slip rate and published geodetic analyses to offer plausible average earthquake recurrence-times for these full-segment ruptures. These simplistic average recurrence intervals provide a useful starting point for future hazard analyses.

Table 4 summarizes the potential earthquake magnitudes we have calculated for all of the major structures. Below, we explain these results for the faults of each domain, starting in the west with the four domains of the Indoburman range and ending in the east with the Shan-Sino domain.

The Indoburman range

We will assess the seismic potential of the four domains of the Indoburman range from south to north, in the same order that we described them in the preceding section. In addition to the surface manifestation of these domains that appear in the maps of Figures 3a, 4a, 6 and 9a, we utilize four schematic cross-sections (Fig. 18 and 19), based upon available geological and seismicity data. Together the maps and cross-sections allow us to estimate the preliminary three-dimensional geometry of the megathrust and its relationship to large secondary structures. At this stage of our understanding of the geometries and kinematics of the region’s active faults, it seems unwarranted to conduct a statistical analysis of plausible rupture areas, widths and slip amounts. We attempt here merely a crude first cut at assessing earthquake potential of the region. So for example, we do not attempt to include the range of uncertainty in the depth of down-dip rupture limits for the megathrust; instead, we mainly use the length of fault mapped from the surface to assess the plausible maximum earthquake magnitude on the subduction zone interface.

Coco-Delta domain

We have described above a Coco-Delta domain dominated by a highly oblique plate interface that dips about 20° to 30° eastward (Dasgupta et al., 2003) (Fig. 18a). The orientation of this section of the megathrust (early parallel to the vector of relative plate motion), its steep dip and secondary features imply predominantly right-lateral slip across this oblique-reverse fault. A predominance of dextral slip within the domain, on the very northern part of the 2004 megathrust rupture (Chlieh et al., 2007), is consistent with this interpretation. The down-dip limit of its seismic rupture is likely shallower than the ~50-km down-dip limit of the adjacent megathrust farther south (Chlieh et al., 2007; Heurent et al., 2011), as its motion contains a large component of strike slip. However, the down-dip limit of the locked patch may still extend to about 20 or even 30 km, as the subducting oceanic lithosphere here is old and cold (> 80 Ma; Müller et al., 1997). We use the reverse fault and megathrust equations from both Blaser et al. (2010) and Strasser et al. (2010) of to estimate a Mw 8.6 to 8.9 range for the maximum earthquake that could be produced by this 480-km long segment (Table 4).

The fact that the southernmost part of this domain ruptured during the great 2004 earthquake (Meltzner et al., 2006), supports the suspicion that this section of the megathrust can accumulate tectonic strain and slip seismically. Moreover, large submarine landslides mapped by Nielsen et al., (2004) within this domain could well be evidence that the megathrust has produced high ground accelerations in the past. However, a complete rupture of the Coco domain megathrust segment would be very rare, because the ten or more meters of slip during such an event would take a millennium or longer to accumulate at the average slip rate of the fault, which could well be lower than 1 cm/yr.

In addition to the megathrust, we suggest that at least three other structures along the eastern flank of the Indoburman range may be capable of generating significant earthquakes (Table 4; Fig. 2 and Fig. 20). From their lengths, we estimate that Mw 7.6 to 7.7 earthquakes are plausible. Lacking reliable estimations of their fault slip rate, however, it would be speculative to estimate average return periods of such earthquakes.

Ramree domain

The Arakan earthquake of 1762 may represent the maximum earthquake within the Ramree domain, because it appears to have resulted from failure of the megathrust in combination with large splay faults in the upper plate (Wang et al., 2013a). If the megathrust ruptured across the entire length of the domain, from near Fouls Island to Chittagong (Figure 4), as Cummins (2007) suggests, then the magnitude would likely have been within the range Mw 8.5 and 8.8, based on the average coseismic fault slip on the megathrust fault plane (Wang et al., 2013a). This range of magnitudes is consistent with our estimation of the maximum earthquake magnitude based upon fault length (Blaser et al., 2010 and Strasser et al., 2010; Table 4).

Terrace- and coral-uplift records yield recurrence intervals ranging between about 400 to 1000 years for earthquakes that involve uplift of Ramree and Cheduba Islands (Shishikura et al., 2009; Wang et al., 2013a). This range is about twice as long as the 190- or 550-year recurrence interval calculated for Mw 8.6 to 8.8 earthquakes if the 23 mm/yr oblique plate convergence is fully taken up by slip on the 450-km long megathrust. This discrepancy implies either that the megathrust is not fully coupled or that the oblique Indian-Burman plate motion is partitioned between the megathrust and upper plate faults, such as the Thahtay Chaung fault within the Indoburman Range.

Upper-plate structures may fail separately from the megathrust and generate smaller, but nonetheless destructive earthquakes along the western Myanmar coast. The 1848 earthquake of northern Ramree Island (Oldham, 1883) may be one of these events. It caused moderate damage to the city of Kyaukpyu, but the felt area was much more limited than that of the 1762 earthquake.

The great length of the right-lateral strike-slip Thahtay Chaung fault, within the Indoburman Range (Fig. 4a and 5) implies that this fault could generate the earthquake as large as Mw 7.6 (Wells and Coppersmith, 1994; Blaser et al., 2010). The lack of reliable written history in this mountainous region precludes knowing whether such an event has happened within the past 250 years. Moreover, a lack of constraints on the slip rate of the fault precludes us from saying anything meaningful about an average recurrence interval. Nevertheless, the existence of this large strike-slip fault within the Indoburman range gives good reason to hypothesize that large, destructive shallow earthquakes are plausible within the range.

The lengths of the west-dipping East Limb faults that crop out along the eastern flank of the Indoburman Range (Fig. 4a and 18b) imply that they are capable of generating Mw 7.8 and 7.3 earthquakes (Table 4). It is likely that these two faults may be connected in the subsurface by a blind thrust. If so, combined rupture could generate an even greater earthquake. The average recurrence interval of such an event along the eastern Indoburman Range would be greater than a thousand years, though, as GPS analysis shows the shortening rate across the eastern Indoburman Range and the central Burma basin is < 9 mm/yr (Socquet et al., 2006).

Several active reverse faults between Thayet-Myo and Yangon could generate large earthquakes along the floodplain of the Ayerawaddy River. Within the Ramree domain, the southernmost of these is the West Bogo-Yoma fault, on the eastern flank of the Ayerawaddy flood plain. The fault is likely a high-angle reverse fault that dips northeastward beneath the western flank of the Bago-Yoma Range. The length of the western Bogo-Yoma fault implies a maximum magnitude of Mw 7.2 to 7.3 for earthquakes near the Ayerwaddy flood plain north of Yangon. The Paungde fault, farther north along the Ayerwaddy flood plain, is longer, so we estimate that it is capable of producing a Mw 7.3 to 7.4 earthquake in the vicinity of Prome. A related fault farther north likely produced the earthquake of 1858 and may have disrupted temporarily the flow of the Ayeyarwady River.

Before we leave the discussion of the Ramree domain, we should also note that rupture of faults within the downgoing slab could also produce damaging earthquakes in the region. Such hidden faults would not be manifest in our mapping of surface features, so we can say little more than that the existence of these should be contemplated in making a comprehensive seismic assessment of the region. The mb 6.5 Bagan earthquake of 1975 was an event of this type. Its hypocentral depth was about 120 km (Engdahl and Villasenor, 2002). The earthquake ruined several temples in the ancient capital of Burma that are believed to have been built in about the 12th century.

Dhaka domain.

The Dhaka domain is defined by the length and width of the broad belt of folds of the Chittagong-Tripura fold belt. As such it extends nearly 600 km along strike from south to north and more than 200 km from west to east. If the blind megathrust underlying this entire domain were to fail at once, the resulting earthquake would likely have a magnitude of about Mw 8.9 (Blaser et al., 2010; Table. 4).

Whether such a large event is plausible is currently a matter of some debate. Recent GPS studies above the megathrust show that the Indoburman Range is moving westward at least 5 mm/yr relative to the Indian plate (Steckler et al., 2012; Gahalaut et al., 2013). Whether this E-W shortening is reflects aseismic creep on or strain accumulation across the megathrust remains unclear. Gahalaut et al. (2013) argue the seismic risk from the underlying plate interface event is low because the E-W shortening on the N-S running megathrust is so low and they find no earthquakes in the history were sourced from the plate-interface. Steckler et al. (2008) argue from comparison with other megathrusts with sediment-rich accretionary prisms that this section of the megathrust may well be capable of producing large earthquakes, even through the prism's internal strength and basal friction are weak.

The lack of large historical earthquakes in the past 400 to 500 years for this portion of the megathrust does not mean the risk of such large megathrust event is low. In fact, if elastic E-W shortening is indeed only 5 mm/yr, it would take nearly 1000 years to accumulate enough slip potency for an Mw 8.9 earthquake on a fully coupled 520-km long and 350-km wide megathrust. If the megathrust is semi-coupled, as many megathrusts are (e.g. Chlieh et al., 2008; Hsu et al., 2012), the recurrence interval of such events would be even longer.

Regardless of whether the megathrust/décollement is capable of producing a giant earthquake, many upper-plate structures associated with actively growing young anticlines (Fig. 6) are undoubtedly capable of producing earthquakes, either in association with failure of the megathrust or individually. Using the lengths of young anticlines as indicators of the lengths of the underlying faults, we calculate plausible maximum earthquake magnitudes ranging from Mw 6.3 to 7.7 (Table 4). The 1918 Mw 7.5 earthquake near the Rashidpur anticline may be an example of such an event. The 1999 mb 5.2 earthquake near the Maheshkhali anticline may be an example of partial failure of one of these faults.

Several other moderate but destructive earthquakes have struck within the fold belt during the pre-instrumental historical period. From the records of shaking alone, however, one cannot be certain that these were produced by failure of secondary structures above the megathrust. They could also have been caused by rupture of faults within the descending plate, beneath the décollement. Speculating about the recurrence intervals of these earthquake sources is not particularly useful because so little is known about the rate of slip on these structures or how their ruptures relate to ruptures of the subjacent megathrust/decollement.

Ruptures of faults within the down-going Indian Ocean lithosphere farther east are another plausible source of destructive earthquakes. One example is the Ms 7.4 earthquake of 1954, which struck east of the Indoburman Range. Its hypocentral depth is 180 km (Engdashi and Villasenor, 2002), clearly within the Wadati-Benioff zone of the downgoing slab. Fortunately, sources deeper than about 50 km within the Wadati-Benioff zone pose relatively low seismic hazard, because such ruptures are far from human infrastructure at the Earth's surface. Shallower sources, however, within the subducting Indian Ocean lithosphere west of the crest of the Indoburman range, could cause destructive earthquakes within the populated regions of Bangladesh. Destructive earthquakes in Bangladesh in 1842 and 1885, for example, are reasonable intraslab candidates, as there is no geomorphic evidence of surface deformation near their proposed epicenters.

As in the Ramree domain to the south, the Dhaka domain has seismic faults within and east of the high Indoburman range. The Churachandpur-Mao fault is the most prominent of these. Judging by its 170-km length, wholesale failure of this right-lateral fault could produce an Mw 7.6 earthquake. The geodetic analysis of Gahalaut et al. (2013) suggests, however, the fault may be slipping aseismically. Aseismic slip along active strike-slip faults is usually associated with minor to moderate earthquakes (Lienkaemper et al., 1991). However, we did not find any historical events that could be related to the Churachandpur-Mao fault in the earthquake catalog of Szeliga et al. (2010), nor does the instrument catalog show a high level of seismic activity along the fault.

The ~280-km length of the eastward dipping Kabaw fault implies that it could generate an Mw 8.4 earthquake if it were to fail all at once (Table 4). The average interval between such earthquakes would be a millennium or longer, since geodetic analysis suggests the fault slip rate must be lower than 9 mm/yr (Socquet et al., 2006).

Naga domain

The southeastward-dipping Naga thrust fault is the principal seismic source within the Naga domain (Fig 9). The 400-km length of the fault implies a maximum earthquake of Mw 8.5 to 8.7 (Table 4). The structural cross section from Kent (2002) suggests the dip of the Naga thrust fault is about 23°, higher than the dip angle of the megathrust of the Dhaka and Ramree domains. In addition to being distinguished by a steeper dip, the fault is also distinguished by the fact that it is the interface between two pieces of continental lithospheres (Fig. 19b; Fig. 1a), rather than the convergent boundary between oceanic lithosphere and the continental lithosphere.

Using the equations from Blaser et al. (2010) and Strasser et al. (2010), we estimate that the Naga thrust fault is capable of producing an Mw 8.5 to 8.7 earthquake, similar in size to the great Assam earthquake of 1950, which resulted from rupture of the Himalayan Frontal Thrust, just to the north. On the other hand, it is plausible that each of the three 100- to 150-km long arcuate lobes we have mapped commonly fail individually. In such a case, the magnitude of the largest Naga thrust earthquakes would be in the Mw 7.7 to Mw 8 range.

The slip rate of the Naga thrust fault is constrained neither by GPS vectors spanning the fault nor by vectors from plate-motion models. GPS vectors on either side of the western part of the Naga thrust are similar, so it appears that there is no shortening across this thrust fault system (Jade et al., 2007; Maurin et al., 2010). This ostensibly conflicts with recent field investigations that show the Naga thrust overrides Quaternary alluvium at the mountain front (Aier et al., 2011). Clearly, additional work will be needed to resolve this important question about the seismic potential of the fault.

Although we did not find any evidence of active faults along the southeastern flank of or within the northern Indoburman range (Fig. 9a), some intraslab earthquakes occur within the down-going Indian plate beneath the range. Although the intraslab events in the Naga domain were not as frequent as those in the Dhaka domain, failure of faults within the subducting plate poses a potential hazard within the Naga domain. In addition, several earthquakes greater than magnitude 6 have occurred along the southeastern margin of the northern Indoburman range. These include a magnitude 7 earthquake in 1932 and an Mw 7.2 earthquake in 1988 (Engdashi and Villasenor, 2002). Both of these two events originated at depths greater than 90 km. Although their hypocenters are deep, the 1988 earthquake still caused some damages to the nearly regions.

The Sagaing fault

The 60- to 260-km range of segment lengths along the right-lateral Sagaing fault imply a range of maximum magnitudes from Mw 7 to 8 (Table 4; Fig. 20). This is consistent with the observation that during the first half of the 20th century, more than half of the fault appears to have ruptured in several earthquakes with magnitudes in the mid-7 range (Brown and Leicester, 1933; Hurukawa and Phyo Maung Maung, 2011) (Fig. 21). This historical behavior of the Sagaing fault appears quite similar to that of the more-highly segmented Sumatran fault through the first half of the 20th century (Daryono et al., 2012). The early-20th century clustering of large ruptures is also similar to the behavior of the North Anatolian fault, which produced several low- to high-7 earthquakes in the 20th century (e.g., Stein et al., 1997).

One notably (and perhaps ominously) quiet section of the fault is the 220-km long Meiktila segment, between the large city of Mandalay and the new capital of Naw Pyi Daw. This long quiet section separates the southern set of ruptures of 1929 and 1930 from the northern set of ruptures between 1931 and 2012. The length of the Meiktila segment implies it is capable of producing an earthquake as large as Mw 7.8 to 7.9, if it ruptures all at once (Wells and Coppersmith, 1994; Blaser et al., 2010; Table 4).

We speculate, on the basis of sparse historical records of shaking, that the 1839 Ava earthquake may have resulted from the failure of Meiktila segment, in conjunction with the Sagaing segment, its neighbor on the north. If the Meiktila segment has been dormant since then, and the fault is fully coupled down to 12 to 15 km at depth, as Vigny et al. (2003) and Socquet et al. (2006) suggest, then we estimate the slip potency that has accumulated on the Meiktila segment to be enough to generate a Mw 7.6 earthquake.

We further estimate the average interval of an Mw 7.8 to 7.9 earthquake on the Meiktila segment to be about 330 to 460 years, based on the 18 mm/yr slip accumulation rate on a 220-km long vertical fault that is locked to 15 km at depth, as modeled from GPS data by Vigny et al. (2003). The estimated recurrence intervals of the Pyu and Bago segments, farther south, are much shorter, no more than 200 to 300 years, because slip per event for these shorter segments is much less. Paleoseismological investigations along the southern Sagaing fault suggest even shorter recurrence intervals, just 100 to 150 years (Tsutsumi and Sato, 2009; Wang et al., 2011). This even lower range of intervals results from even shorter rupture lengths (e.g., Wells and Coppersmith, 1994; Blasser et al., 2010).

The earthquake histories and complicated fault geometry of the northern half of the Sagaing fault imply a more complex behavior than that of the southern half of the fault. The segment lengths of the northern half of the fault yields a range of maximum earthquake magnitudes from about Mw 7.0 to 8.0 (Table 4; Fig. 21). These estimates may be high, however, because a recent geodetic analysis suggests the locking depth of the northern Sagaing fault is just ~5 to 7 km (Maurin et al., 2010), far more shallow than for most of the faults used in the global length-magnitude scaling relationships.

We have chosen in our analysis of plausible earthquakes to assume that each segment will rupture completely during future earthquakes. Nonetheless, it is clear that this is not always the case. The recent earthquake of a short portion of the Sagaing segment in November 2012 is an example of the partial failure of a segment. This Mw 6.8 earthquake took place along just part of a segment that most likely ruptured wholly during a larger Mw 7.7 earthquake in 1946 (Fig. 21). Perhaps coincidentally, the slip potency accumulated on the 40-km long 2012 fault-rupture in the years between 1946 and 2012 roughly equals the potency of the 2012 event, if the rupture extended to 12 km. The 180-km long Sagaing segment illustrates well that our assumption of whole-segment rupture is a gross simplification of reality. One could calculate return periods of just decades for Mw 6.8 to Mw 7.0 partial failure events or Mw 7.7 whole-segment failures about every 350 years.

The historical record of the northern half of the Sagaing fault may illustrate another complexity as well – multi-segment rupture. One plausible example of this is the combined rupture of Meiktila and the Sagaing segment during the great 1839 earthquake. The boundary between these two segments is less well defined than other segment boundaries along the fault, so it may be that our assignment of that segment boundary is a bit tenuous. If the fault rupture propagates through both the Meiktila and the Sagaing segment, its length would be about 400 km. The earthquake produced by such a long rupture could have a magnitude between Mw 8.1 and 8.3 (Wells and Coppersmith, 1994; Blaser et al., 2010). The slip associated with such a long rupture would be so large that its return time would be longer than 500 to 1000 years.

Shan-Sino domain

We have identified 27 active faults systems within the Shan-Sino domain. The lengths of these faults range from about 30 to more than 480 km (Table 2). Our mapping suggests that maximum geomorphically expressed offsets range from approximately one to more than 20 km for these strike-slip fault systems (Table 2; Fig. 22).

From length-magnitude relationships, we estimate maximum earthquake magnitudes that range from about Mw 6.5 to 8.4 (Wells and Coppersmith, 1994; Blaser et al., 2010 Table 4; Fig. 22). For comparison, the earthquake catalogue for the past century shows the largest magnitude is 5.5 to

7.7 (Table 1; Table 4; Fig. 12). The difference between the estimated and actual maximum magnitudes suggests that most historical events involved partial failure of the fault.

The 1988 Mw 7.0 Lancang earthquake is one example of partial failure. The highest intensities (MMI ≥ VIII) and a ~45-km long surface rupture occurred along the northwestern part of the 200-km long dextral-slip fault (Yu et al., 1991; Fig. 12).

The 2011 Mw 6.8 Tarlay earthquake is another example of partial failure of one of these strike-slip faults. Measurements of the surface rupture from satellite imagery and field measurements show clearly that only the westernmost 30 km of the Nam Ma fault ruptured during this earthquake. The rupture spanned the entire length of a segment of the fault that terminates eastward in a pull-apart basin (Wang et al., 2013b). Other examples include partial failures of the Kyaukkyun fault during the 1912 Mw 7.7 earthquake and of Nanting fault during a magnitude 7 earthquake in 1941. Although the surface ruptures of these early 20th-century earthquakes were not mapped in the field, isoseismal maps in both cases imply that rupture of the faults was partial (Brown, 1917; Compilation Group of China Seismic Intensity Zoning Map SSB, 1979; Fig. 12). These examples and the commonly moderate size of earthquakes along the strike-slip faults of the Shan-Sino domain show that partial rupture of these faults is typical.

We now use the maximum geomorphically expressed offset and estimated ~5 Ma age of these offsets (Lacassin et al., 1998; Wang et al., 1998) to calculate fault-slip rates for the strike-slip faults of the Shan-Sino domain. These first-order slip rate estimations (Table 4) allow us to speculate about the average frequency of whole-fault or partial ruptures by estimating the seismic moment accumulation rate on the given fault plane. Most of the average fault-slip rates are lower than 4 mm/yr. Two exceptions are the 4 to 5 mm/yr rates of the Nanting fault and the Menglian fault. These estimated low fault slip rates imply recurrence interval > 1000 years for each of the slower-slipping faults. For example, we estimate an average recurrence interval of 3000 years for the maximum (Mw 7.5) earthquake on the Daying River fault. The 180-km long Mengxing fault is one of the fastest moving faults, but its maximum (Mw 7.7) earthquake would recur only about every 1300 years.

Although the low fault-slip rates of these faults means long recurrence intervals for complete rupture of any one fault, the large number of faults and their common partial rupture mean that earthquakes are still very frequent throughout the domain. In fact, about 14 moderate to strong (Mw 6.7 to Mw 7.7) earthquakes occurred within the Shan-Sino domain during the past century – on average about one every eight years. If we assume that an average partial failure of these faults produces a Mw 7.0 earthquake, which is slightly smaller than the averaged earthquake magnitude of these 14 destructive earthquakes in the past century, we calculate a recurrence of about 15 years for the whole domain.. This recurrence interval is, however, about half the average interval of the past century. This implies that throughout the past century the Shan-Sino domain has been experiencing an episode of activity than is higher than its average level over the millennia. This speculation is supported by the observation that total seismic moment released during these historical earthquakes is about three times higher than the seismic moment that would have been accumulated based on their fault slip rates.

Conclusions

Geomorphologically evident active faults and folds of the Myanmar region comprise three majors systems, which accommodate the northward translation of the Indian plate into the Eurasian plate and the extrusion of crust around the eastern syntaxis of the Himalaya. The western of these three systems comprises four distinct neotectonic domains, each distinguished by a unique geometry of the Sunda subduction/collision megathrust. Distinct active hangingwall structures within each of these four domains include large strike-slip faults and both blind and surface-rupturing thrust faults. The Sagaing fault comprises the second of the three systems.

Second-order structural characteristics of this ~1200-km long domain suggest division into 12 segments. Historical seismicity confirms that to a large degree these structurally defined segments constrain seismic ruptures. The third of the neotectonic systems is the Shan-Sino domain, a large region of conjugate left- and right-lateral active faults that accommodate extrusion of material around the eastern Himalayan syntaxis.

Empirical global relationships between fault length and earthquake magnitude allow us to estimate maximum magnitudes for the active faults in each of these domains. The lengths of these structures imply that most are capable of generating events greater than Mw 7.0. However, the historical and instrumental records show that smaller earthquakes are common during partial rupture of these faults. Each of the four megathrust segments are capable of producing an earthquake of Mw 8.5 or greater, but only one has done so in the period of historical record. Estimates of slip rates for the faults of the Shan-Sino domain and empirical relationships between fault length and magnitude suggest that recurrence intervals for complete rupture of these faults are typically several thousand years. Seismic moment release in this domain during the past century may have been greater the millennially averaged rate. In contrast, empirical relationships and historical seismicity show that ruptures of each segment of the Sunda megathrust and the Sagaing fault should rupture on average every several hundred years.

Our analysis of these active, seismogenic faults serve provide a foundation for more formal evaluations of seismic hazard, risk and exposure of the Myanmar region.

Acknowledgments

We have benefited greatly from discussions with Win Swe and other friends in Myanmar during our stay in Yangon. We also appreciate assistance from members of the Myanmar

Geosciences Society (MGS), the Department of Meteorology and Hydrology (DMH) of Myanmar since 2006.

References

Abe, K. and S. Noguchi (1983) Revision of magnitudes of large shallow earthquakes, 1897 – 1912, Phys. Earth Planet. Int. 33, 1-11.

Aier, I, K. Luirei, S.S. Bhakuni, G. T. Thong, G. C. Kothyari (2011) Geomorphic evolution of Medziphema intermontane basin and Quaternary deformation in the schuppen belt, Nagaland, NE India, Zeitschrift für Geomorphologie, 55(2), 247-265.

Alam, M., 1989. Geology and depositional history of Cenozoic sediments of the Bengal Basin of Bangladesh. Palaeogeography, Palaeoclimatology, Palaeoecology 69, 125–139.

Allen, T. I., K. D. Marano, P. S. Earle, and D. J. Wald (2009), PAGER-CAT: A composite earthquake catalog for calibrating global fatality models, Seismol. Res. Lett., 80, 57–62, doi:10.1785/gssrl.80.1.57.

Amante, C. and B. W. Eakins (2009) ETOPO1 1 Arc-Minute Global Relief Model: Procedures, Data Sources and Analysis. NOAA Technical Memorandum NESDIS NGDC-24, 19 pp, March 2009.

Ansary, M.A., Al-Hussaini, T.M.and Sharfuddin, M. (2000), Damage Assessment of July 22, 1999 Moheshkhali Earthquake, Bangladesh, Proc., PMC-2000, 8th ASCE Specialty Conference on Probabilistic Mechanics & Structural Reliability, Indiana, USA.

Armijo, R., P. Tapponnier, P., H. Tonglin (1989), Late Cenozoic right-lateral strike-slip faulting in southern Tibet. J. Geophys. Res. 94, 2787 – 2838.

Banerjee, P., R. Bürgmann, B. Nagarajan, and E. Apel (2008), Intraplate deformation of the Indian subcontinent, Geophys. Res. Lett., 35, L18301, doi:10.1029/2008GL035468.

Bender, F. (1983), Geology of Burma, 293, Gebruder Borntraeger, Berlin.

Berger, P., et al., (1983), Assam–Arakan basin: Schlumberger Well Evaluation Conference India, 1134–1170.

Bertrand, G., et al. (1998), The Singu basalts (Myanmar): New constraints for the amount of recent offset on the Sagaing Fault, C. R. Acad. Sci., Ser. IIa, 327, 479–484.

Blaser, L., F. Krüger, M. Ohrnberger & F. Scherbaum (2010), Scaling relations of earthquake source parameter estimates with special focus on subduction environment, Bull. seism. Soc. Am., 100(6), 2914–2926.

Brown C (1929), The Rangoon earthquakes of September and December 1927. Rec Geol. Surv. India LXII p.258.

Brown C (1932), A note on the Swa earthquake of August 8th, 1929. Rec Geol. Surv. India LXVI p.244.

Brown, C. (1917), The Burma earthquake of May 1912, Memoirs of the Geological Survey of India, 42(1), 1–147.

Brown, C.J., P. Leicester, and H.L. Chhibber (1931), A preliminary note on the Pegu earthquake of May 5th, 1930, Rec. Geol. Surv. India, 65, 221–284.

Brown, J.C. and P. Leicester (1933), The Pyu earthquake of 3rd and 4th December, 1930 and subsequent Burma earthquakes up to January 1932. Memoirs of the Geological Survey of India, 42, 1-140.

Brune, J. N., J. Curray, L. Dorman, R. Raitt (1992), A proposed super-thick sedimentary basin, Bay of Bengal, Geophys. Res. Lett., 12, 565–568.

Brunnschweiler, R. O. (1966), On the geology of the Indo-Burma ranges, J. Geol. Soc. Aust., 13, 127–194.

Bureau of Geology and Mineral Resources of Yunnan (1993). Geological map of Yunnan, scale 1:500,000.

Bustin, A. M. M., R. D. Hyndman, H. Kao, and J. F. Cassidy (2007), Evidence for underthrusting beneath the Queen Charlotte margin, British Columbia, from teleseismic receiver function analysis, Geophys. J. Int., 171, 1198–1211, doi:10.1111/j.1365-246X.2007.03583.x.

Chang, Z.F., G. Chen and J.Q. Yu (2011), Geological evidence of Activity Along the Dayyingjiang fault since late Pleistocene, Seismology and Geology, 33(4), 877 – 888. DOI: 10.3969/j.issn.0253-4967.2011.04.012 (Chinese with English abstract).

Chang, Z.F., X.W. An, Y.F. Zhang (2012). Study on late-Quaternary Activity and Displacement of drainage systems along the Wanding fault. Seismology and Geology, 34(2), 228 – 239. doi:10.3969/j.issn.0253-4967.2012.02.00.

Chen Q F ed-in-chief (2002). Earthquake Cases in China (1995–1996). Seismological Press, Beijing, 1–488 (in Chinese).

Chhibber H.L., 1934, Geology of Burma: London, McMillan, 538 p.

Chlieh, M., et al. (2007), Coseismic slip and afterslip of the great (Mw 9.15) Sumatra-Andaman earthquake of 2004, Bull. Seismol. Soc. Am., 97, S152–S173, doi:10.1785/0120050631.

Chlieh, M., J. P. Avouac, K. Sieh, D. H. Natawidjaja, and J. Galetzka (2008), Heterogeneous coupling of the Sumatran megathrust constrained by geodetic and paleogeodetic measurements, J. Geophys. Res., 113, B05305, doi:10.1029/2007JB004981.

Clark, M. K., and R. Bilham (2008), Miocene rise of the Shillong Plateau and the beginning of the end for the Eastern Himalaya, Earth Planet. Sci. Lett., 269, 336–350.

Coates, D.A., A.K.M.K. Alam (1990), The Mymensingh Terrace: evidence of Holocene deformation in the delta of the Brahmaputra river, central Bangladesh. Geol. Soc. Amer. Bull. 22, 310 Abstracts with Program.

Compilation Group of China Seismic Intensity Zoning Map SSB (1979): Atlas of Chinese Earthquake Isoseismals, Seismological Press, Beijing. (in Chinese).

Cummins, P. R. (2007), The potential for giant tsunamigenic earthquakes in the northern Bay of Bengal, Nature, 449, 75–78.

Curiale, J.A., G.H. Covington, A.H.M. Shamsuddin, J.A. Morelos, and A.K.M. Shamsuddin (2002), Origin of petroleum in Bangladesh: AAPG Bulletin, 86(4), 625-652.

Curray, J. R. (2005), Tectonics and history of the Andaman Sea region, J. Asian Earth Sci., 25, 187–228.

Curray, J. R., F. J. Emmel, D. G. Moore (2003), The Bengal fan: morphology, geometry, stratigraphy, history and processes, Mar. Pet. Geol., 19, 1191–1223.

Curray, J. R., (1991), Possible greenschist metamorphism at the base of a 22-km sedimentary section, Bay of Bengal, Geology, 19, 1097–1100.

Curray, J.R., D.G. Moore, L.A. Lawver, F.J. Emmel, R.W. Raitt, M. Henry & R. Kieckhefer (1979). Tectonics of the Andaman Sea and Burma, Am. Assoc. Petrol. Geol. Mem., 29, 189–198.

Curray, J.R., F.J. Emmel, D.G. Moore, R.W. Raitt (1982). Structure, tectonics and geological history of the northeastern Indian Ocean. In: Nairn, A.E.M., Stehli, F.G. (Eds.), The Ocean Basins and Margins. The Indian Ocean, vol. 6. Plenum Press, New York, pp. 399–450.

Dahlen, F. A., J. Suppe, and D. Davis (1984), Mechanics of fold-and-thrust belts and accretionary wedges: Cohesive Coulomb Theory, J. Geophys. Res., 89(B12), 10087–10101, doi:10.1029/JB089iB12p10087.

Daryono, M., D.H. Natawidjaja, K. Sieh, (2012), Twin-Surface Ruptures of the March 2007 M > 6 Earthquake Doublet on the Sumatran Fault, Bull. Seismol. Soc. Am., 102(6), 2356-2367, doi: 10.1785/0120110220.

Dasgupta, S., et al. (2003), The geometry of the Burmese-Andaman subducting lithosphere, J. Seismol., 7, 155–174.

Davis, D., J. Suppe, and F. A. Dahlen (1983), Mechanics of fold-and-thrust belts and accretionary wedges, J. Geophys. Res., 88(B2), 1153–1172, doi:10.1029/JB088iB02p01153.

DeMets, C., R.G. Gordon, and D.F. Argus (2010), Geologically current plate motions, Geophys. J. Int., 181(1), 1-80, doi: 10.1111/j.1365-246X.2009.04491.x.

Densmore, A. L., M. A. Ellis, Y. Li, R. Zhou, G. S. Hancock, and N. Richardson (2007), Active tectonics of the Beichuan and Pengguan faults at the eastern margin of the Tibetan Plateau, Tectonics, 26, TC4005, doi:10.1029/2006TC001987.

Engdahl, E.R. & A. Villaseñor (2002), Global Seismicity: 1900–1999, International Handbook of Earthquake and Engineering Seismology, v. 81A, Elsevier Science Ltd., Amsterdam, The Netherlands, 665–690.

Fitch, T. J. (1972), Plate convergence, transcurrent faults, and internal deformation adjacent to southeast Asia and the western Pacific, J. Geophys. Res., 77, 4432–4457.

Frankel, K.L. et al. (2008), Active tectonics of the eastern California shear zone, in Field Guide to Plutons, Volcanoes, Reefs, Dinosaurs, and Possible Glaciation in Selected Areas of Arizona, California, and Nevada, Geol. Soc. Am. Field Guide, 11, pp. 43–81, eds E.M. Duebendorfer & E.I. Smith, Geological Society of America, Boulder , CO , doi:10.1130/2008.fld011(03).

Gahalaut VK, Kundu B, Laishram SS, Catherine JK, Kumar A, Devchandra M, Tiwari RP, Chadha RK, Samanta SK, Ambikapathy A, Mahesh P, Bansal A, Narsaiah M (2013) Aseismic plate boundary in the Indo-Burmese wedge, northwest Sunda Arc. Geology 41:235–238. doi:10.1130/G33771.1.

Gomberg, J., P. Bodin, W. Savage, and M. E. Jackson (1995), Landslide faults and tectonic faults, Analogs?—The slumgullion earthflow, Colorado, Geology, 23, 41–44.

Goodbred, S.L. Jr., S.A. Kuehl (1999), Holocene and modern sediment budget for the Ganges–Brahmaputra river system: evidence for highstand dispersal to flood-plain, shelf, and deep-sea depocenters. Geology 27, 559–562.

Guo, S.M., H.F. Xiang, X.W. Xu et al., (1999a) The preliminary study on late Quatrnary activity of Dayingjiang fault zone, western Yunnan Province. In: Institute of Geology, CEA(ed). Research on Active fault (7). Seismological Press, Beijing (in Chinese).

Guo, S.M., Y. Wang, F.J. Ji., (1999b) Tectonic mechanism of moderate-strong swarms in Yunnan's Simao-Pu'er region. J. Seism. Res., 22(2), 105-115 (in Chinese with English abstract).

Gupta, H. and V. Gahalaut (2009), Is the Northern Bay of Bengal Tsunamigenic? Bull. Seism. Soc. Am., 99(6), 3496–3501.

Gutenberg, B. and C.F. Richter (1954), Seismicity of the earth and Associate Phenomena, Princeton University Press, Princeton.

Guzman-Speziale, M., and J. F. Ni (1993), The opening of the Andaman Sea: Where is the short-term displacement being taken up, Geophys. Res. Lett., 20, 2949– 2952.

Halsted, E. P. (1841), Report on the Island of Chedooba, J. Asiatic Soc. Bengal, 114, New Series No. 27, 419–436.

Heuret, A., S. Lallemand, F. Funiciello, C. Piromallo, and C. Faccenna (2011), Physical characteristics of subduction interface type seismogenic zones revisited, Geochem. Geophys. Geosyst., 12, Q01004, doi:10.1029/2010GC003230.

Hla Maung (1987), Transcurrent movements in the Burma-Andaman Sea region, Geology, 15, 911 –912.

Hsu, Y.-J., S.-B. Yu, T.-R. Song, T. Bacolcol, (2012). Plate coupling along the Manila subduction zone between Taiwan and northern Luzon, J. Asian Earth Sci. 51(2), 98-108.

Huang, X.M., Y. Du, S.B. Shu and F.R. Xie (2010). Study of the Late Quaternary Slip Rate Along the Northern Segment on the south branch of the Longling-Ruili fault. Earthquake Research in China, 24(4), 456-466.

Hurukawa, N., and P. Maung Maung (2011), Two seismic gaps on the Sagaing Fault, Myanmar, derived from relocation of historical earthquakes since 1918, Geophys. Res. Lett., 38, L01310, doi:10.1029/2010GL046099.

Hutchinson, C. S.(1989), Geological Evolution of SE Asia, Oxford Monographs on Geology and Geophysics, 3, 368, Clarendon, Oxford, England.

Jade, S., M. Mukul, I. A. Parvez, M. B. Ananda, P. D. Kumar, and V. K. Gaur (2002), Estimates of coseismic displacement and post-seismic deformation using Global Positioning System geodesy for the Bhuj earthquake of 26 January 2001, Curr. Sci., 82, 748–752.

Jarvis, A., H.I. Reuter, A. Nelson, E. Guevara, (2008), Hole-filled SRTM for the globe Version 4, available from the CGIAR-CSI SRTM 90m Database (http://srtm.csi.cgiar.org).

Johnson, S. Y., and N. Alam (1991), Sedimentation and tectonics of the Sylhet Trough, Bangladesh, Geol. Soc. Am. Bull., 103, 1512–1527.

Kent, W.N., R.G. Hickman & U. Dasgupta (2002), Application of a ramp/flat-fault model to interpretation of the Naga thrust and possible implications for petroleum exploration along the Naga thrust front, AAPG Bull., 86, 2023–2045.

Khan, M.S.H., B. Parkash, S. Kumar (2005), Soil-landform development of a part of the fold belt along the eastern coast of Bangladesh. Geomorphology 71, 310-327.

Kreemer, C., W.E. Holt, and A.J. Haines (2003), An integrated global model of present-day plate motions and plate boundary deformation. Geophys. J. Int., 154: 8–34. doi: 10.1046/j.1365-246X.2003.01917.x.

Kumar, A., M. Sanoujam, L. Sunil, T. Dolendro (2011), Active Deformations at the Churachandpur Mao Fault (CMF) in Indo Burma Ranges: Multidisciplinary Evidences, Int. J. Geosci, 2, 597-609, doi:10.4236/ijg.2011.24062.

Lacassin, R., A. Replumaz, and P. H. Leloup (1998), Hairpin river loops and slip-sense inversion on southeast Asian strike-slip faults, Geology, 26, 703–706.

Lai, K.Y., Y.G. Chen, D.Đ. Lâm (2012) Pliocene to present morphotectonics of the Dien Bien Phu fault in northwest Vietnam. Geomorphology, 173-174, 52-68. DOI:10.1016/j.geomorph.2012.05.026.

Le Dain, A. Y., P. Tapponnier, and P. Molnar (1984), Active faulting and tectonics of Burma and surrounding regions, J. Geophys. Res., 89, 453–472.

Lei, J., G. Zhang, F. Xie, Y. Li, Y. Su, L. Liu, H. Ma and J. Zhang, (2012), Relocation of the 10 March 2011 Yingjiang, China, earthquake sequence and its tectonic implications, Earthq Sci, 25, 103-110. doi:10.1007/s11589-012-0836-4.

Leloup, P.H., P. Tapponnier, and R. Lacassin, (2007), Discussion on the role of the Red River shear zone, Yunnan and Vietnam, in the continental extrusion of SE Asia. J. Geol. Soc., 164: 1253–1260.

Li, C., R. van der Hilst, A. S. Meltzer, and E. R. Engdahl (2008), Subduction of the Indian lithosphere beneath the Tibetan Plateau and Burma, Earth Planet. Sci. Lett., 274, 157–168, doi:10.1016/j.epsl.2008.07.016.

Lienkaemper, J. J., G. Borchardt, *and* M. Lisowski (1991), Historic creep rate and potential for seismic slip along the Hayward Fault, California, J. Geophys. Res., *96*(B11), 18261–18283, *doi:*10.1029/91JB01589.

Lu, X. and L.Q. Zhou, (2011), Accurate location of the 2007 Ms 6.4 Ning’er, Yunnan, earthquake sequence, Seism. Geol., 33(3), 560-567. doi:10.3969/j.issn.0253-4967.2011.03.006.

Mallet, F. R. (1878), The Mud volcanoes of Ramri and Cheduba, Geol. Surv. India Rec., 11, part 2, 188–207.

Martin, S., and W. Szeliga (2010), A catalog of felt intensity data for 570 earthquakes in India from 1636 to 2009, Bull. Seismol. Soc. Am., 100(2), 562–569.

Mathur, L. P., and P. Evans (1964), Oil in India: 22nd Session International Geological Congress Proceedings, p. 7–52.

Maurin, T., and C. Rangin (2009), Structure and kinematics of the Indo-Burmese Wedge: Recent and fast growth of the outer wedge, Tectonics, 28, TC2010, doi:10.1029/2008TC002276.

Maurin, T., F. Masson, C. Rangin, U. T. Min, and P. Collard (2010), First Global Positioning System results in northern Myanmar: Constant and localized slip rate along the Sagaing fault, Geology, 38(7), 591–594, doi:10.1130/G30872.1.

Mazzotti, S., H. Dragert, J. Henton, M. Schmidt, R. Hyndman, T. James, Y. Lu and M. Craymer (2003), Current tectonics of northern Cascadia from a decade of GPS measurements. J. Geophys. Res. 108(B12): doi: 10.1029/2003JB002653. issn: 0148-0227.

McCaffrey, R., (2009), The tectonic framework of the Sumatran subduction zone, Annual Reviews of Earth and Planetary Sciences, 37, 345-366,

Meltzner, A. J., K. Sieh, M. Abrams, D. C. Agnew, K. W. Hudnut, J.-P. Avouac, and D. H. Natawidjaja (2006), Uplift and subsidence associated with the great Aceh-Andaman earthquake of 2004, J. Geophys. Res., 111, B02407, doi:10.1029/2005JB003891.

Milne, J. (1911). A Catalogue of Destructive Earthquakes A. D. 7 to A. D. 1899, BAAS, London.

Mitchell, A.H.G., (1977), Tectonic settings for emplacement of southeast Asian tin granites. Geological Society of Malaysia, Bulletin 6, 123–140.

Morgan, J. P., and W. Mclntire (1959), Quaternary Geology of the Bengal Basin, East Pakistan and India: Bull. Geol. Soc. America, 70, 319-342.

Morino M., A.S.M. M. Kamalb, D. Muslimc, R.E. Alid, M.A. Kamald, Z. Rahmane, F. Kanekoa (2011) Seismic event of the Dauki Fault in 16th century confirmed by trench investigation at Gabrakhari Village, Haluaghat, Mymensingh, Bangladesh, J. Asian Earth Sci., 42(2) 492-498.

Morley, C. K., M. Smith, A. Carter, P. Charusiri, and S. Chantraprasert (2007), Evolution of deformation styles at a major restraining bend, constraints from cooling histories, Mae Ping Fault zone, western Thailand, in Tectonics of Restraining and Releasing Bends, edited by D. Cunningham, and P. Mann, Geol. Soc. Spec. Publ., 290, 325–349.

Müller, R. D., W. R. Roest, J.-Y. Royer, L. M. Gahagan, and J. G. Sclater (1997), Digital isochrons of the world's ocean floor, J. Geophys. Res., 102(B2), 3211–3214, doi:10.1029/96JB01781.

Myint Thein, Kyaw Tint, Aye Ko Aung, (1981), On the lateral displacement of the Sagaing Fault. Georeports 1(1). University of Mandalay, Burma.

Ni, J. F., M. Guzman-Speziale, M. Bevis, W. E. Holt, T. C. Wallace, W. R. Seager, (1989), Accretionary tectonics of Burma and the three-dimensional geometry of the Burma subduction zone, Geology, 17, 68–71.

Nielsen, C., et al. (2004), From partial to full strain partitioning along the Indo-Burmese hyper-oblique subduction, Mar. Geol., 209, 303–327, doi:10.1016/j.margeo.2004.05.001.

Oldham, T. (1883), Catalogue of Indian Earthquakes, Mem. Geol. Surv. India, 19(3), 170 pp.

Pacheco, J.F. & L.R. Sykes, (1992). Seismic moment catalog of large shallow earthquakes, 1900 to 1989, Bull. seism. Soc. Am., 82, 1306–1349.

Pelayo, A. M., and D. A. Wiens (1989), Seismotectonics and relative plate motions in the Scotia Sea region, J. Geophys. Res., 94(B6), 7293–7320, doi:10.1029/JB094iB06p07293.

Peltzer, G., F. Crampe, S. Hensley, and P. Rosen (2001), Transient strain accumulation and fault interaction in the eastern California shear zone, Geology, 29, 975–978.

Penick, J. L., Jr. (1981) The New Madrid Earthquakes Rev. ed., Univ. of Mo. Press, Columbia.

Prawirodirdjo, L. and Y. Bock, (2004), Instantaneous global plate motion model from 12 years of continuous GPS observations, J. Geophys. Res., 109, B08405, doi:10.1029/2003JB002944.

Pubellier M. et al. (2008). Structural Map of Eastern Eurasia, Commission for the Geological Map of the World, 1:12.500.000 scale.

Ranga Rao, A., and M. K. Samanta, (1987), Structural style of the Naga overthrust belt and its implication on exploration: Bulletin of the Oil and Natural Gas Commission, v. 24, p. 69–109.

Rao, N. P., and Kalpna (2005), Deformation of the subducted Indian lithospheric slab in the Burmese arc, Geophys. Res. Lett., 32, L05301, doi:10.1029/2004GL022034.

Replumaz, A., (1999). Reconstruction de la zone de collision Inde-Asie. Étude centrée sur l'Indochine. PhD thesis, Université de Paris 7-IPG, Paris, 230 pp.

Richards, S., G. Lister, and B. Kennett (2007), A slab in depth: Three-dimensional geometry and evolution of the Indo-Australian plate, Geochem. Geophys. Geosyst., 8, Q12003, doi:10.1029/2007GC001657.

Rudolf, B. and U. Schneider (2005): Calculation of Gridded Precipitation Data for the Global Land-Surface using in-situ Gauge Observations, Proceedings of the 2nd Workshop of the International Precipitation Working Group IPWG, Monterey October 2004, EUMETSAT, ISBN 92-9110-070-6, ISSN 1727-432X, 231-247.

Satyabala, S. P. (1998), Subduction in the Indo-Burma region: Is it still active? Geophys. Res. Lett., 25, 3189–3192.

Sella, G. F., T. H. Dixon, and A. Mao (2002), REVEL: A model for recent plate velocities from space geodesy, J. Geophys. Res., 107(B4), 2081, doi:10.1029/2000JB000033.

Shen, Z.-K., J. Lu, M. Wang, and R. Burgmann (2005), Contemporary crustal deformation around the southeast borderland of the Tibetan Plateau, J. Geophys. Res., 110, B11409, doi:10.1029/2004JB003421.

Shishikura, M., et al. (2009), Geomorphological evidence of great Holocene earthquakes of western Myanmar, Proceedings of the International Workshop on Tsunami and Storm Surge Hazard Assessment and Management for Bangladesh, CDMP, 35–40.

Shyu, J. B. H., K. Sieh, Y.-G. Chen, and C.-S. Liu (2005), Neotectonic architecture of Taiwan and its implications for future large earthquakes, J. Geophys. Res., 110, B08402, doi:10.1029/2004JB003251.

Sieh, K., and D. Natawidjaja (2000), Neotectonics of the Sumatran fault, Indonesia, J. Geophys. Res., 105(B12), 28295–28326, doi:10.1029/2000JB900120.

Simons, W. J. F., et al. (2007), A decade of GPS in Southeast Asia: Resolving Sundaland motion and boundaries, J. Geophys. Res., 112, B06420, doi:10.1029/2005JB003868.

Smith, G., L. McNeill, T. J. Henstock, and J. Bull (2012), The structure and fault activity of the Makran accretionary prism, J. Geophys. Res., 117, B07407, doi:10.1029/2012JB009312.

Socquet, A., and M. Pubellier (2005), Cenozoic deformation in western Yunnan (China-Myanmar border), J. Asian Earth Sci., 24, 495–515.

Socquet, A., C. Vigny, N. Chamot-Rooke, W. Simons, C. Rangin, and B. Ambrosius (2006), India and Sunda plates motion and deformation along their boundary in Myanmar determined by GPS, J. Geophys. Res., 111, B05406, doi:10.1029/2005JB003877.

Soe Thura Tun, Saw Ngwe Khaing, Y. Wang, Myo Thant, Nyunt Htay, Yin Myo, Min Htwe, Than Myint, K. Sieh (2013) Surface Ruptures of the 2011 Tarlay Earthquake and Their Relationship to the Active Tectonics of Eastern Myanmar, in preparation.

Steckler, M.S., Akhter, S.H. & Seeber, L., (2008), Collision of the Ganges–Brahmaputra Delta with the Burma Arc: implications for earthquake hazard, Earth planet Sci. Lett., 273, 367–378.

Steckler et al. (2012), GPS Velocities and Structure Across the Burma Accretionary Prism and Shillong Anticline in Bangladesh, American Geophysical Union, Fall Meeting 2012, abstract # T51F-2667

Stein, R. S., Barka, A. A. and Dieterich, J. H. (1997), Progressive failure on the North Anatolian fault since 1939 by earthquake stress triggering. Geophysical Journal International, 128: 594–604. doi: 10.1111/j.1365-246X.1997.tb05321.x

Strasser, F.O., M.C. Arango and J.J. Bommer (2010), Scaling of the source dimensions of interface and intraslab subduction-zone earthquakes with moment magnitude, Seism. Res. Lett., 81(6), 941–950.

Stuart, M. (1920), The Srimangal earthquake of 8th July 1918, Memoirs of the Geological Survey of India, 46(1).

Szeliga, W., et al. (2010), Intensity, magnitude, location, and attenuation in India for felt earthquakes since 1762, Bull. Seismol. Soc. Am., 100(2), 570–584.

Tapponnier, P., G. Peltzer, A.Y. Le Dain, R. Armijo & P. Cobbold (1982), Propagating extrusion tectonics in Asia: new insights from simple experiments with plasticine, Geology, 10, 611–616.

Than Tin Aung, K. Satake, Y. Okamura, M. Shishikura, Win Swe, Hla Saw, Tint Lwin Swe, Soe Thura Tun, and Thura Aung (2008), Geologic evidence for three great earthquakes in the past 3400?years off Myanmar, J. Earthquake Tsunami, 2, 259–265.

Tsutsumi, H., and T. Sato (2009), Tectonic geomorphology of the southernmost Sagaing Fault and surface rupture associated with the May 1930 Pegu (Bago) earthquake, Myanmar, Bull. Seismol. Soc. Am., 99, 2155–2168, doi:10.1785/0120080113.

Uddin, A., and N. Lundberg (1999), A paleo-Brahmaputra? Subsurface lithofacies analysis of Miocene deltaic sediments in the Himalyan-Bengal system, Bangladesh, Sediment. Geol., 123, 239–254.

Verma, R. K., and M. Mukhopadhyay (1977), An analysis of the gravity field in northeastern India, Tectonophysics, 42, 283–317.

Vigny, C., A. Socquet, C. Rangin, N. Chamot-Rooke, M. Pubellier, M. Bouin, G. Bertrand, and M. Becker (2003), Present-day crustal deformation around Sagaing fault, Myanmar, J. Geophys. Res., 108(B11), 2533, doi:10.1029/2002JB001999.

Wang, E. and B. C. Burchfiel, (1997), Interpretation of Cenozoic tectonics in the right-lateral accomodation zone between the Ailao Shan shear zone and the eastern Himalayan syntaxis, Int. Geol. Rev., 39, 191–219

Wang, E., B. C. Burchfiel, L. H. Royden, L. Chen, J. Chen, W. Li, (1998), Late Cenozoic Xianshuihe-Xiaojiang and Red River fault systems of southwestern Sichuan and central Yunnan, China, Spec. Pap. Geol. Soc. Am., 327, 108.

Wang, G., J. Wan, E. Wang, D. Zheng, and F. Li (2008), Late Cenozoic to recent transtensional deformation across the Southern part of the Gaoligong shear zone between the Indian plate and SE margin of the Tibetan Plateau and its tectonic origin, Tectonophysics, 460, 1–20, doi:10.1016/j.tecto.2008.04.007.

Wang, H., Z.J. Qiang, Z.Z. Yuan, Y.L. Wang, H. Zhang, X. Zhao, (1991), The Distribution of seismic intensities and surface rupture in the Lancang-Gengma (Yunnan Province, China) earthquakes of November 6, 1988. Acta Seismologica Sinica, 13(3), 344 – 353. (in Chinese with English abstract).

Wang, J.N., Y.L. Wang, X.W. An, X.D. Yang (2006), Analysis of Latest Activity on NE-segment of West Branch of Nantinghe Fault, Journal of seismological research, 29(3), 264 – 268.

Wang, Y., E. Wang, Z. Shen, M. Wang, W. Gan, X. Qian, G. Meng, T. Li, W. Tao, Y. Yang, J. Cheng, and P. Li (2008), GPS-constrained inversion of present-day slip rates along major faults of the Sichuan-Yunnan region, China, Sci. China D, 51, 1267–1283.

Wang, Y. K, Sieh, Soe Min, Saw Ngwe Khaing, Soe Thura Tun (2009), Smoking gun of the May-1912 Burma earthquake? Neotectonics of the Kyaukkyan fault system, Eastern Burma (Myanmar). American Geophysical Union, Fall Meeting 2009, abstract #T33B-1912.

Wang, Y., Sieh, K., Aung, T., Min, S., Khaing, S. N. and Tun, S. T. (2011), Earthquakes and slip rate of the southern Sagaing fault: insights from an offset ancient fort wall, lower Burma (Myanmar). Geophysical Journal International, 185:49–64. doi:10.1111/j.1365-246X.2010.04918.x

Wang, Y. et al. (2013a), Permanent upper plate deformation in western Myanmar during the great 1762 earthquake: Implications for neotectonic behavior of the northern Sunda megathrust, J. Geophys. Res. Solid Earth, 118, doi:10.1002/jgrb.50121.

Wang, Y., Y.N. Lin, M. Simons, Soe Thura Tun (2013b) Shallow rupture of the 2011 Tarlay earthquake (Mw 6.8), Eastern Myanmar. BSSA, in review.

Wells, D.L. & K.J. Coppersmith (1994), New empirical relationships among magnitude, rupture length, rupture width, rupture area, and surface displacement, Bull. seism. Soc. Am., 84(4), 974–1002.

Wesnousky, S. (2006), Predicting the endpoints of earthquake ruptures, Nature, 444, 358–360, doi:10.1038/nature05275.

Wesnousky, S. (2008), Displacement and geometrical characteristics of earthquake surface ruptures: Issues and implications for seismic-hazard analysis and the process of earthquake rupture, Bull. Seismol. Soc. Am., 98, 1609–1632, doi:10.1785/0120070111.

Win Swe, (1970), Rift-features at the Sagaing-Tagaung ridge, in Proc. 5th Burma Research Congress, Rangoon.

Win Swe, C. Thacpaw, Nay Thaung Thaung, Kyaw Nyunt (1972), Geology of part of the Chindwin basin of the central belt, Burma, Department of Geology, Arts and Science University, Mandalay. 34p.

Win Swe, (2006), Earthquake hazard potentials in Myanmar: a science to public welfare outlook, in Symp. Tectonics, Seismotectonics, and Earthquake Hazard Mitigation and Management of Myanmar, Yangon, Abstract.

Xie, Y.S. and M.B. Tsai (Chief Eds). (1983), Compilation of historical materials of Chinese Earthquakes, Vol. X, Science Press, Beijing (in Chinese).

Yeats, R. S., K. Sieh, and C. R. Allen, (1997), The Geology of Earthquakes, Oxford Univ. Press, New York.

Yu, W.X., T.J. Cai, X.Y. Hou, (1991), Deformation zone of M = 7.6 Lancang earthquake, Seismology and Geology, 13(4), 343- 352 (in Chinese with English abstract).

Zhu Y.X., P. Li, J.W. Ren (1994), Activity of Nandinghe fault zone and its paleoearthquake events, Earthquake Research in China, 10(4), 347-356. (in Chinese with English abstract)

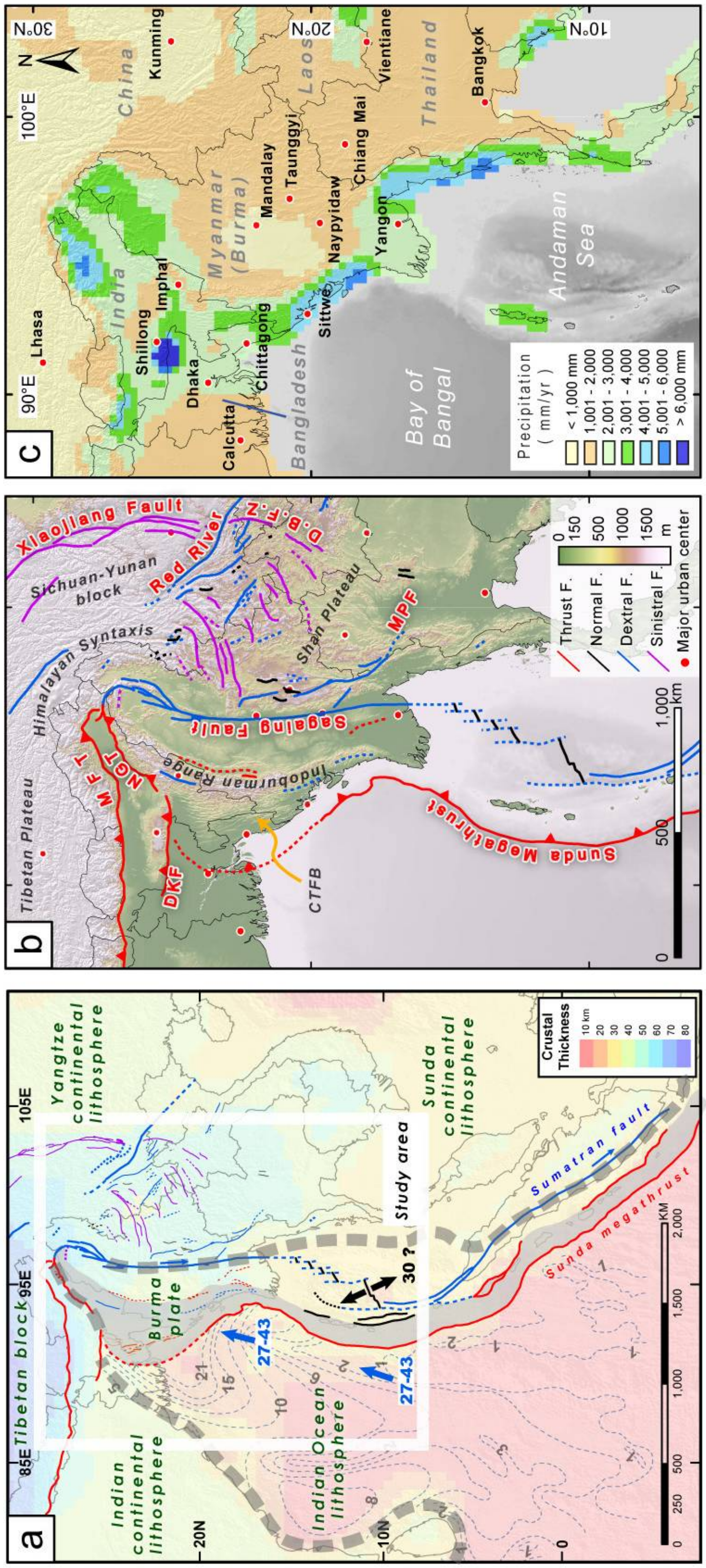
a
Tibetan block
85E
95E
105E
20N
10N
0
Indian continental lithosphere
Indian Ocean lithosphere
Burma plate
27-43
27-43
30 ?
Study area
Yangtze continental lithosphere
Sunda continental lithosphere
Sumatran fault
Sunda megathrust
Crustal Thickness
10 km
20
30
40
50
60
70
80
0 250 500 1,000 1,500 2,000 KM
b
Tibetan Plateau
Himalayan Syntaxis
Sichuan-Yunan block
Xiaojiang Fault
Red River
D.B.F.Z
M F T
NGT
DKF
CTFB
Indoburman Range
Sagaing Fault
Shan Plateau
MPF
Sunda Megathrust
Thrust F.
Normal F.
Dextral F.
Sinistral F.
Major urban center
0 150 500 1000 1500 m
0 500 1,000 km
c
90°E
100°E
30°N
20°N
10°N
Lhasa
Kunming
China
India
Shillong
Imphal
Dhaka
Calcutta
Chittagong
Bangladesh
Myanmar (Burma)
Mandalay
Taunggyi
Laos
Naypyidaw
Chiang Mai
Vientiane
Thailand
Sittwe
Yangon
Bangkok
Bay of Bangal
Andaman Sea
Precipitation (mm/yr)
< 1,000 mm
1,001 - 2,000
2,001 - 3,000
3,001 - 4,000
4,001 - 5,000
5,001 - 6,000
> 6,000 mm

Figure 1 Major tectonic elements of the Myanmar region and the extreme variation in rainfall that influence the preservation of tectonic landforms. (a) Crustal thickness associated with the major plates and tectonic blocks of the region. The pale-blue arrow shows the direction of Indian plate motion relative to Sunda plate (e.g., Socquet et al., 2006). The black arrow shows the opening direction of the Central Andaman spreading center. The velocity is in mm/yr. (b) Two major fault systems accommodate the northward translation of the Indian plate into Eurasia. These are the northern extension of the Sunda megathrust and the Sagaing fault system, which form the western and eastern margin of the Burma Plate. Conjugate right- and left-lateral faults of the Shan plateau and southern China accommodate southwestward extrusion of the Sichuan-Yunnan block around the eastern Himalayan syntaxis. (c) Extreme variations in annual rainfall across the region result in extreme variations in preservation of tectonic landforms. The precipitation data is from GPCC global data (Rudolf and Schneider, 2005).

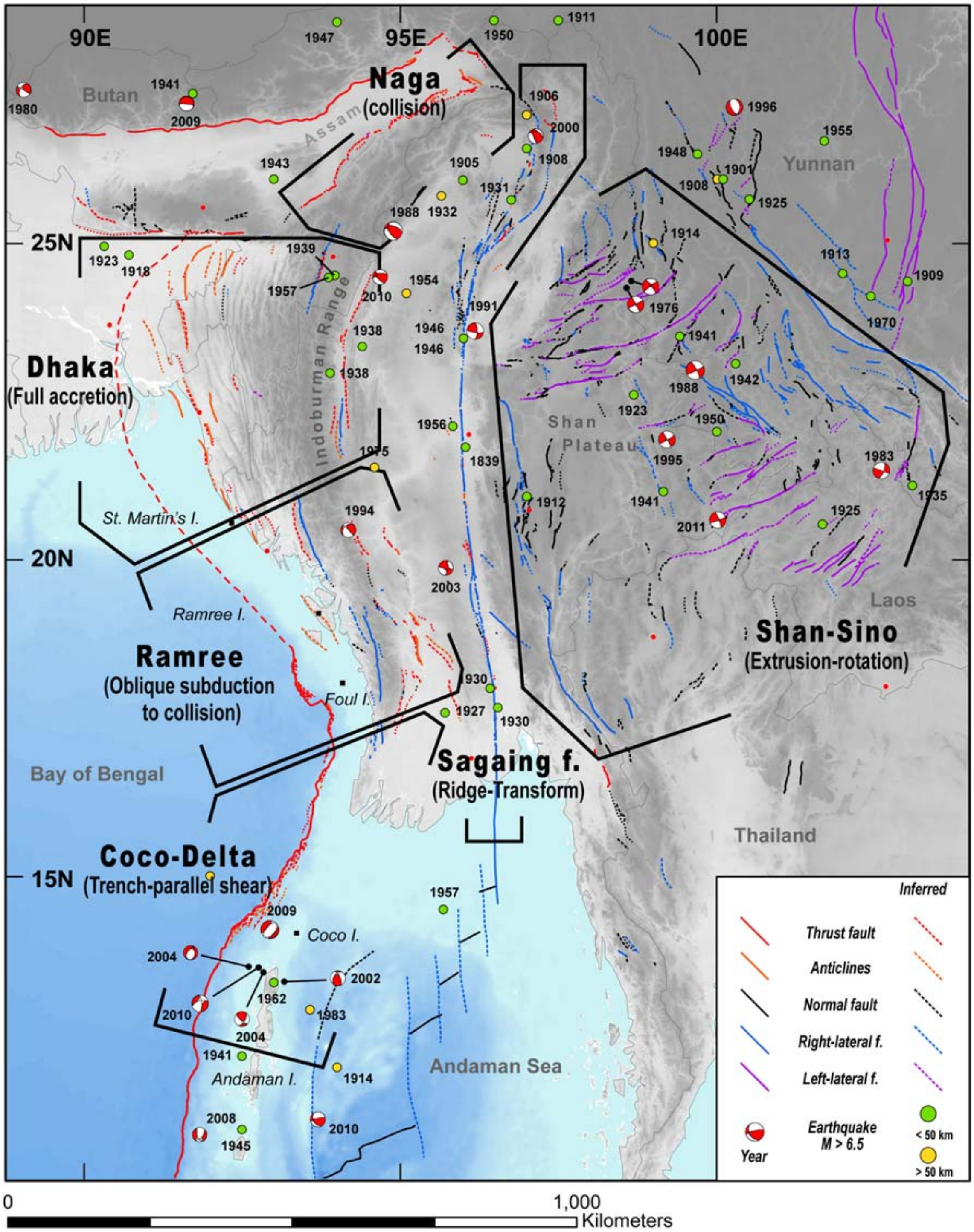

Figure 2 Simplified neotectonic map of the Myanmar region. Black lines encompass the six neotectonic domains that we have defined. Green and Yellow dots show epicenters of the major 20th-century earthquakes (source: Engdahl and Villaseñor, 2002). Red and white beachballs are focal mechanisms of significant modern earthquakes (source: GCMT database since 1976). A more detailed, high-resolution map, from which is this figure was derived, appears in the Appendix 1 Fig. S2.

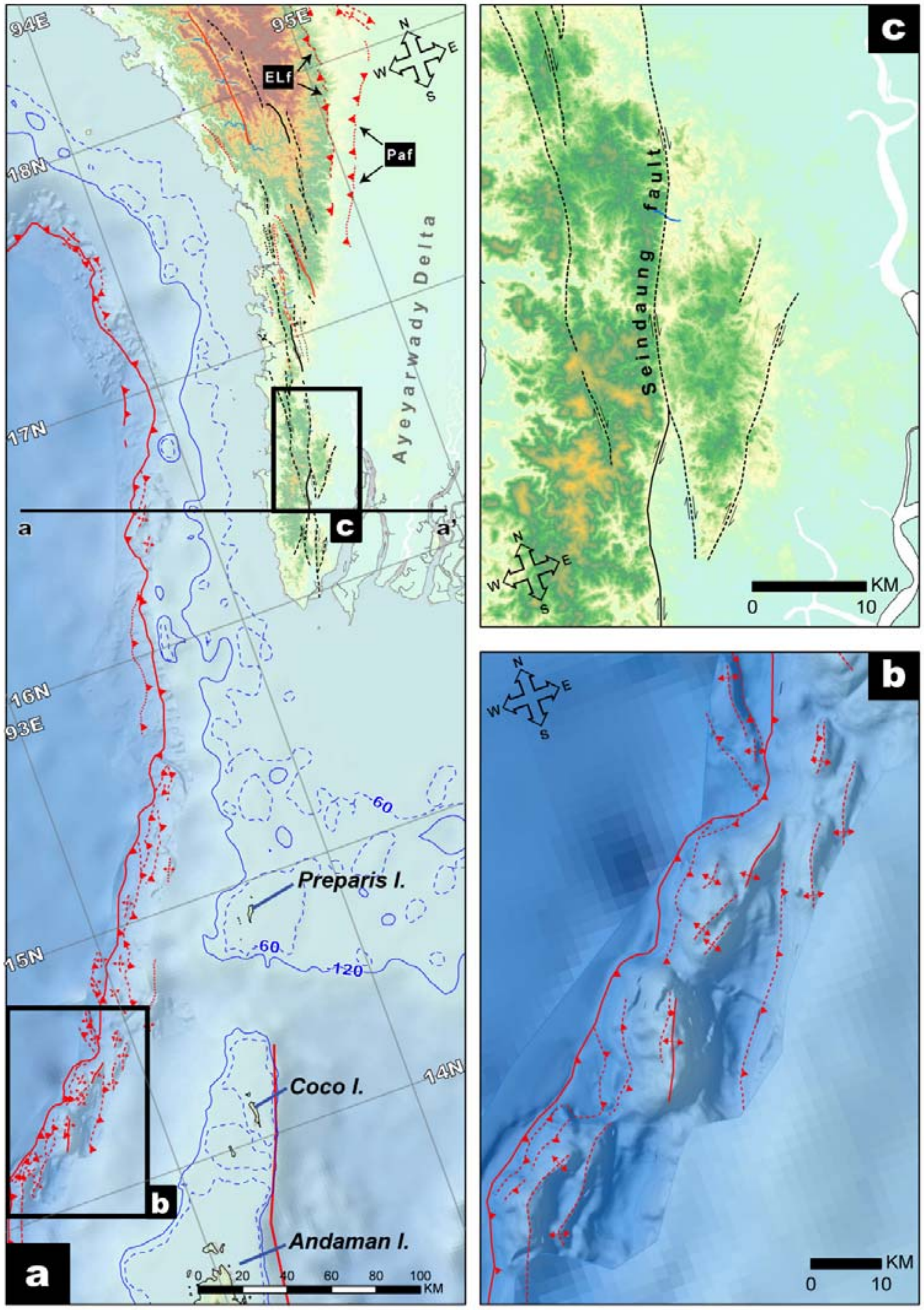

Figure 3 (a) Major active faults within the Coco-Delta domain. (b) Structures along the deformation front include a series of anticlinal structures very close to the trench. Detailed inset bathymetry is from Nielsen et al. (2004). (c) Seindaung fault and other dextral-slip faults along the eastern flank of the southern Indoburman range. Although these faults are clearly expressed in the topography, we cannot identify any obvious young offset features.

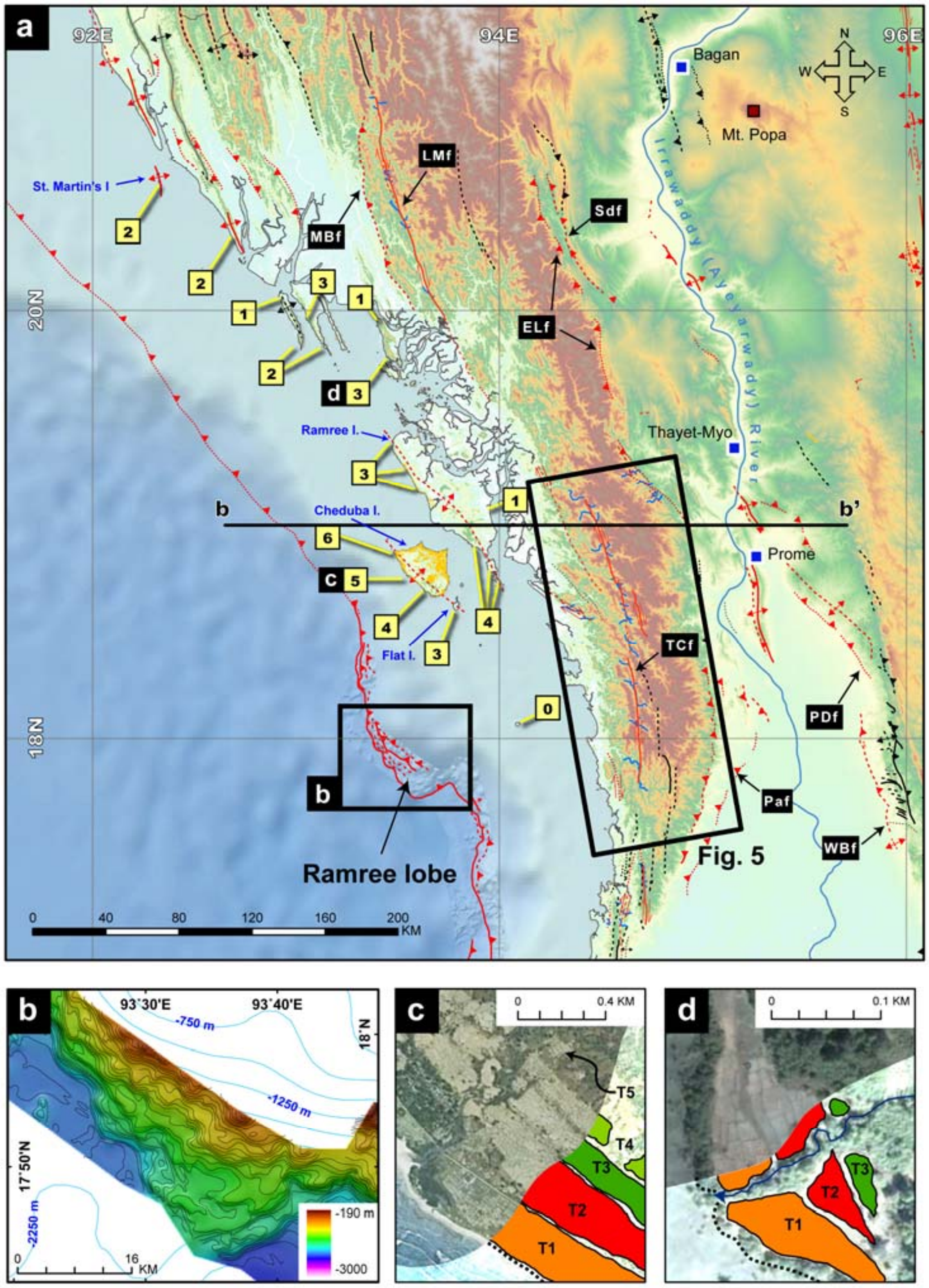

Figure 4 (a) Major active faults within the Ramree domain (Name abbreviations in black boxes). Numbers in yellow boxes indicate number of marine terraces visible in high-resolution satellite imagery. (b) Detailed bathymetry of the Ramree lobe shows clear geomorphic expression of imbricated faults and anticlines, which imply active shortening near the deformation front. (c) Marine terraces on the western side of Cheduba Island (colored patches) from satellite imagery. (d) Nested alluvial fan surfaces north of Ramree Island show episodic uplift during the seaward growth of the fan.

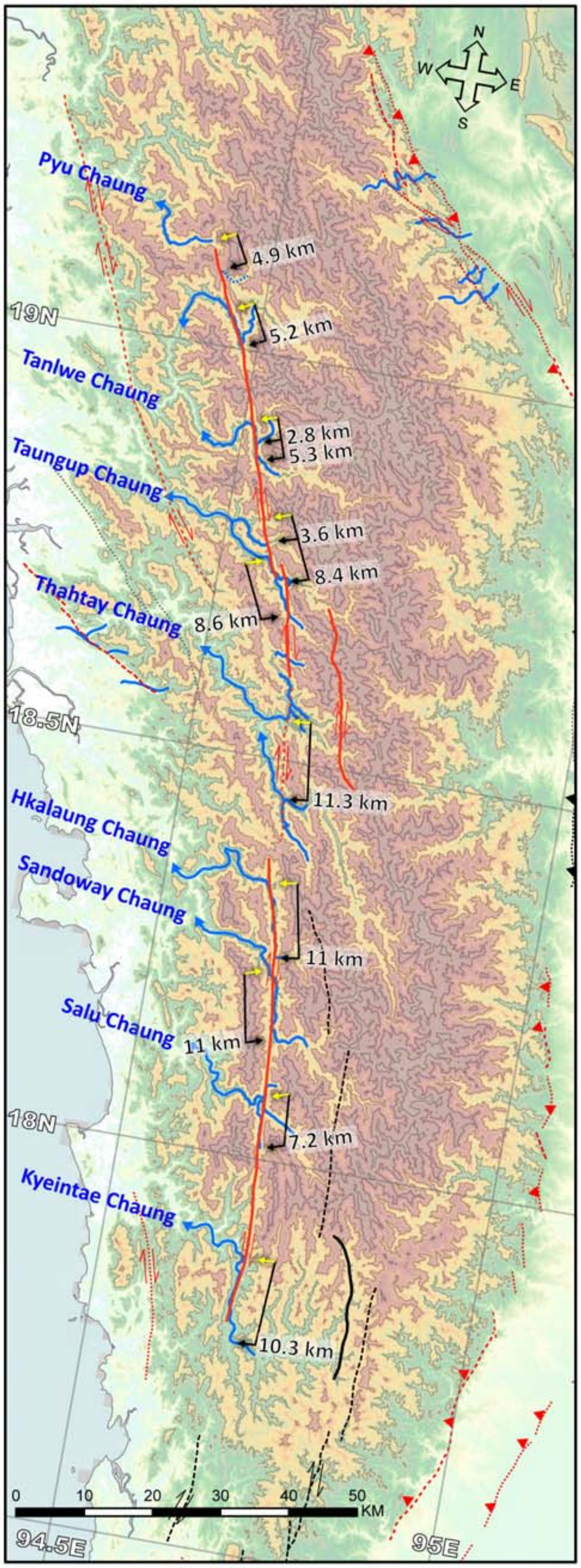

Figure 5 Right-lateral offset of river channels along the Thahtay Chaung fault, within the Indoburman Range. The maximum geomorphic offset is about 10.3 km, close to the southern limit of the fault.

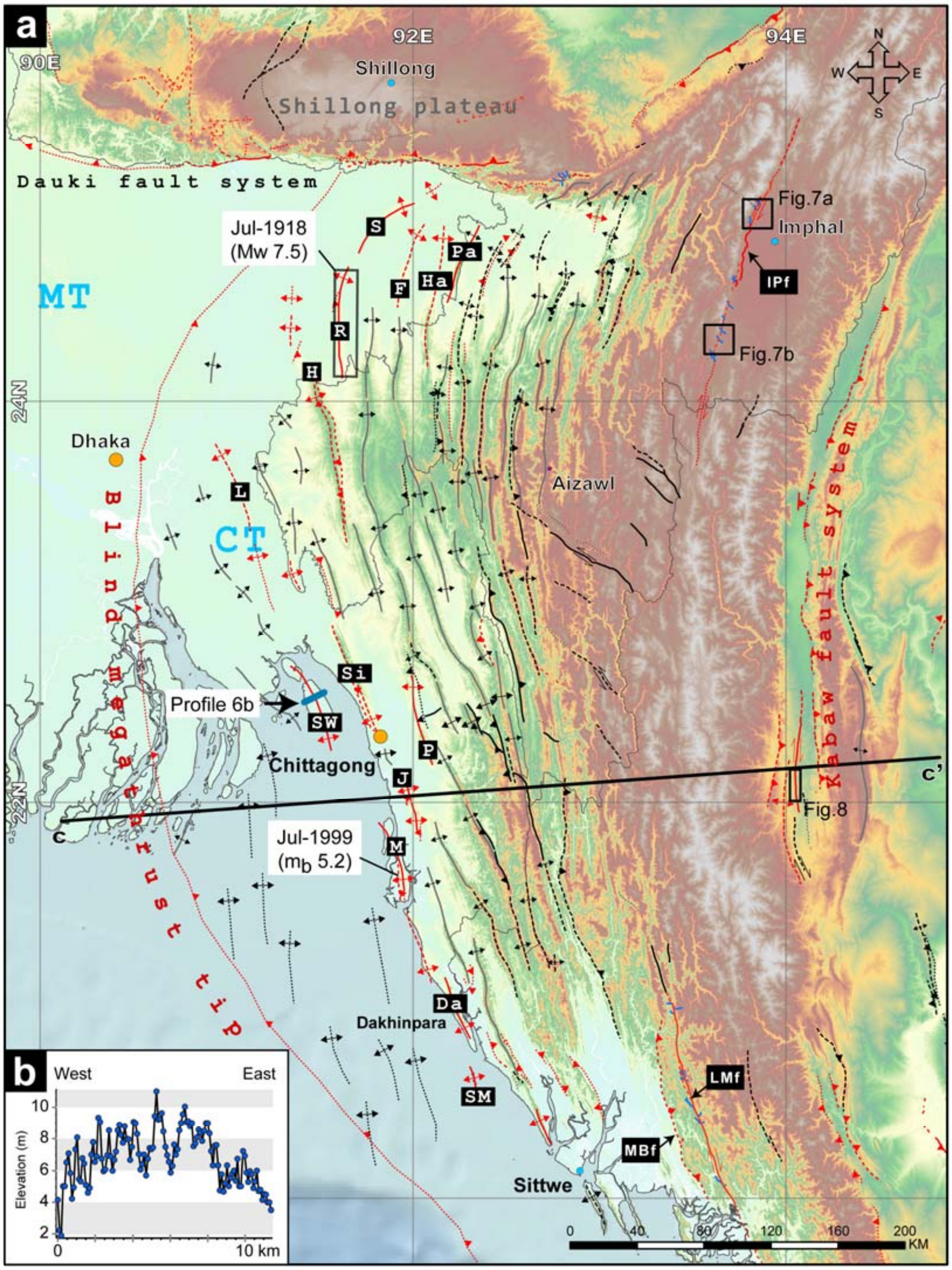

Figure 6 (a) Active faults and anticlines of the Dhaka domain superimposed on SRTM topography. Most of the active anticlines lie within 120 km of the deformation front. CT = Comilla Tract, MT = Madhupur tract. White boxes contain the dates and magnitudes of earthquakes mentioned in the text. (b) Profile from SRTM topography of Sandwip Island. Cross-section CC' appears in Figure 19.

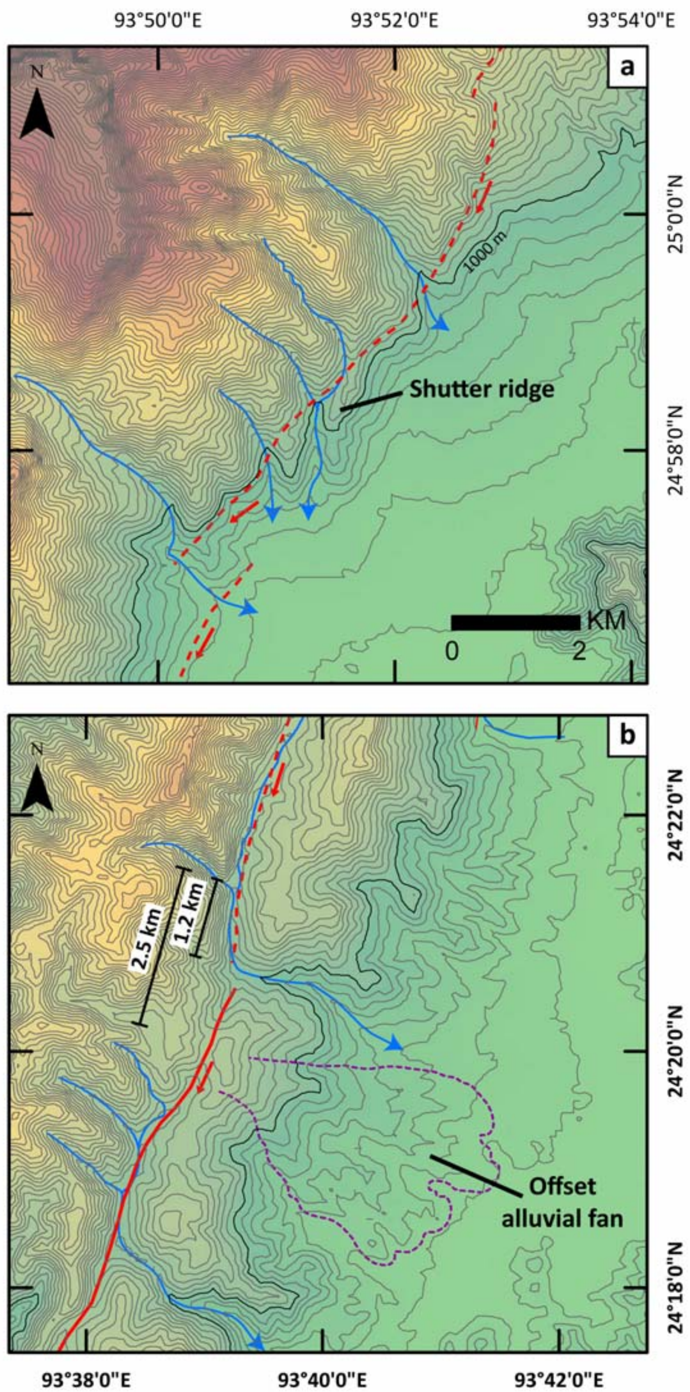

Figure 7 Geomorphological features of the Churachandpur-Mao fault at two different locations reflect clear dextral motions along the fault. (a) Clear right-lateral channel deflections on the 25-meter contour map from SRTM topography along the northwestern margin of the Imphal basin. (b) Eroded and beheaded alluvial fan and nearest plausible source basin about 2.5 krn to the northeast along the fault.

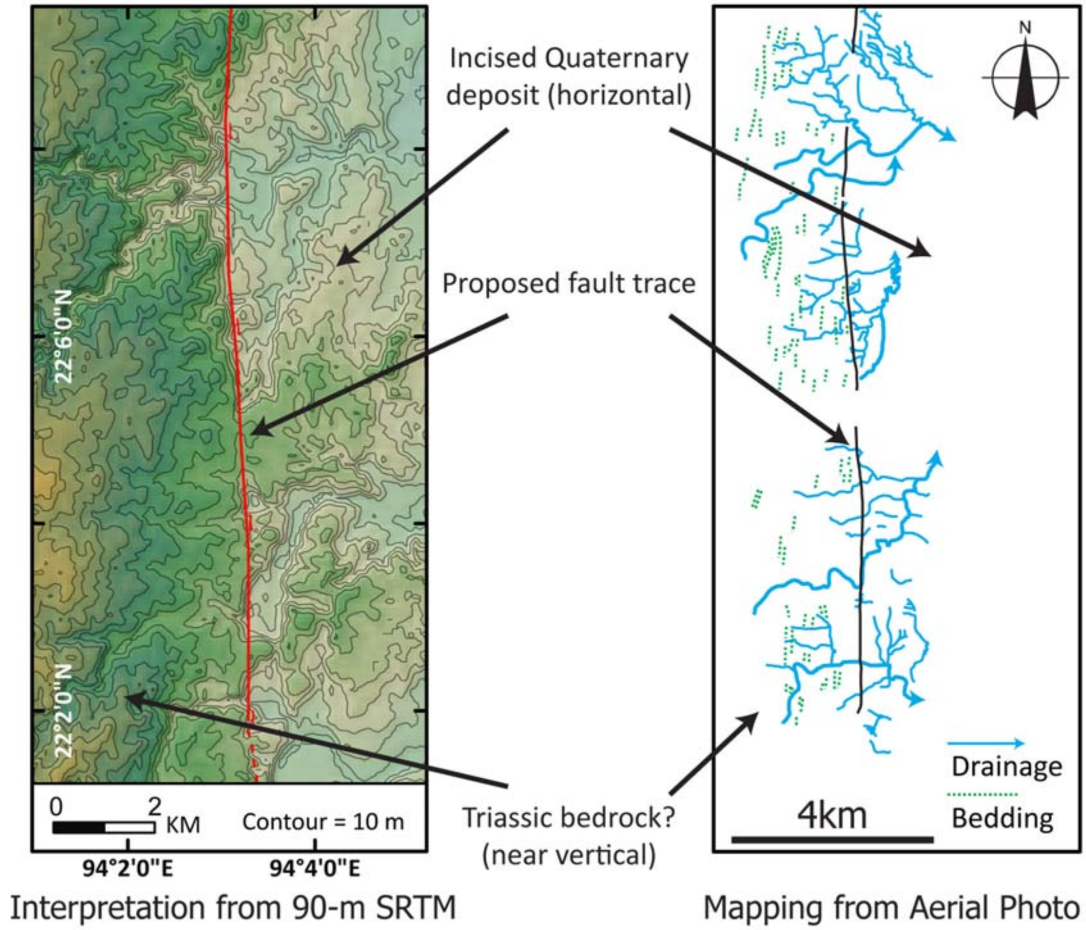

Figure 8 Fault and drainage map in the southern part of the Kabaw valley shows no young offset features along a strike-slip element of the fault.

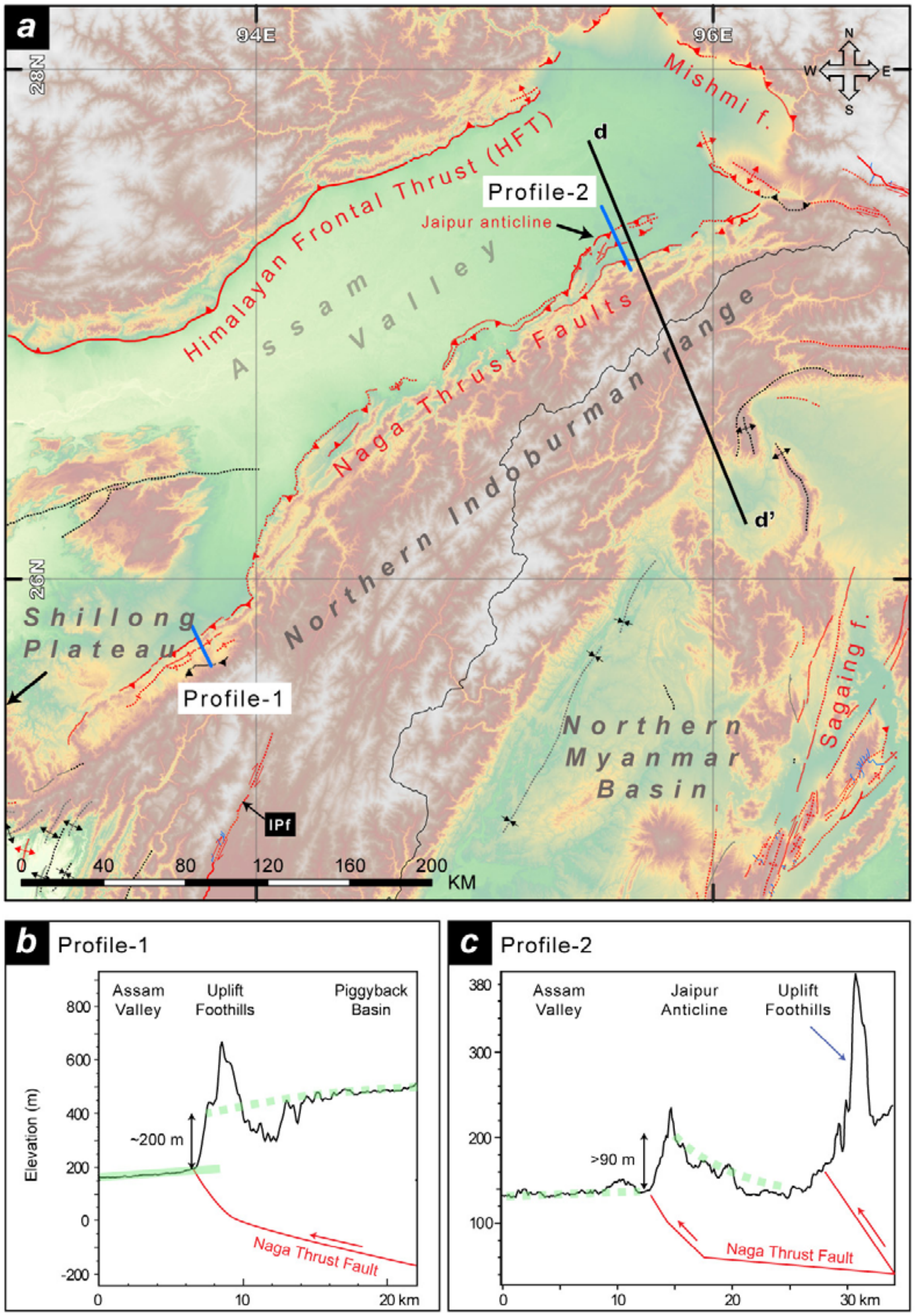

Figure 9 Map and cross sections of the Naga thrust fault system. (a) Map of traces of the fault visible in SRTM imagery shows three distinct lobes along its ~400-km length. The geomorphic profiles in (b) and (c) show the thrust fault system deforms late-Quaternary depositional surfaces and offsets them vertically by more than 90 m. Cross section DD’ appears in Figure 19. The scale at depth is not equal to the scale of topographic profiles.

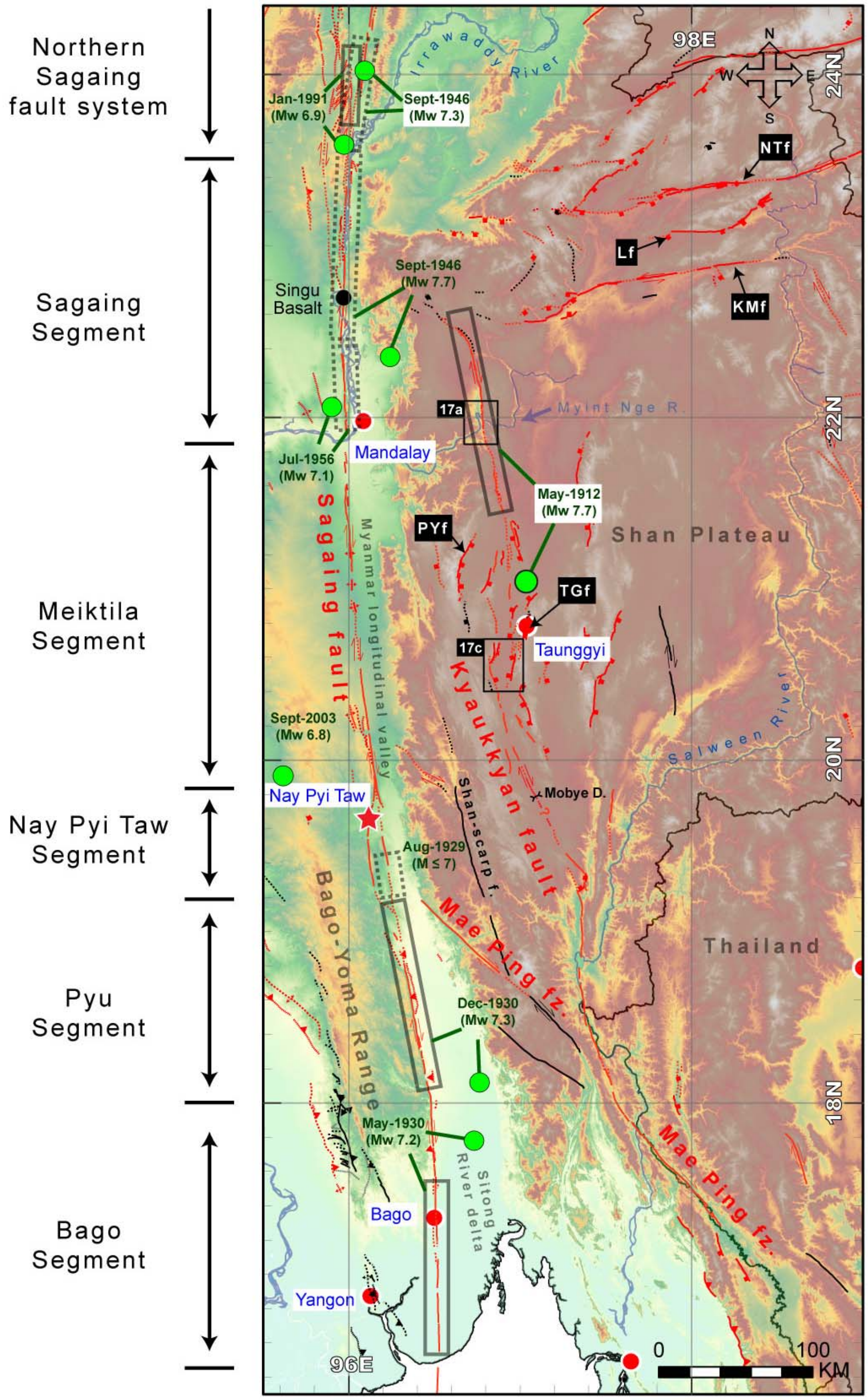

Figure 10 Fault segments and historical earthquakes along the central and southern parts of the Sagaing fault. Green dots show relocated epicenters from Hurukawa and Phyo Maung Maung (2011). Dashed and solid gray boxes surround segments of the fault that ruptured in historical events.

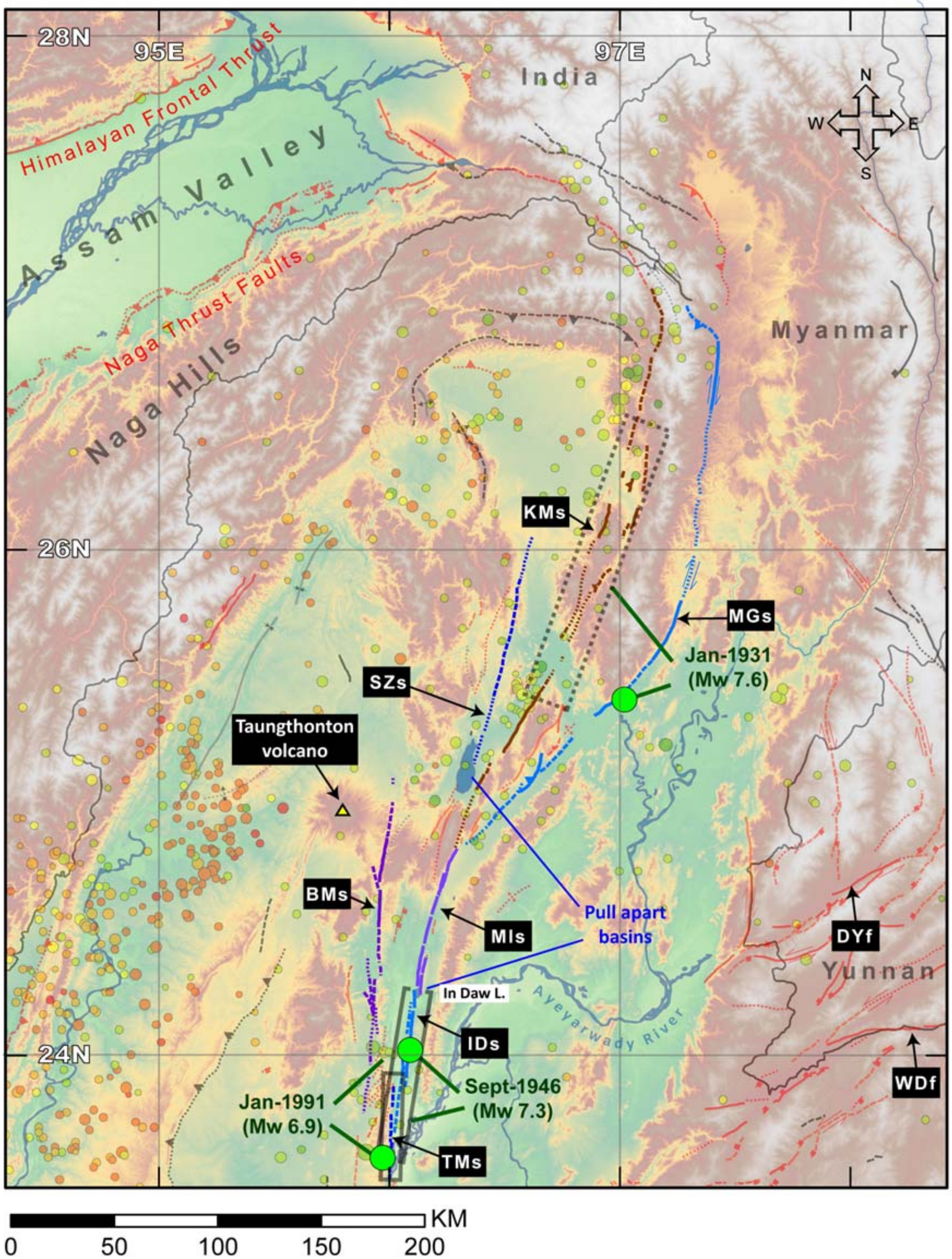

Figure 11 Fault segments of the northern Sagaing fault, differentiated by purple, blue and brown colors. Lettering in black boxes show the abbreviated names of the segments. Green dots are relocated epicenters of major earthquakes from Hurukawa and Phyo Maung Maung (2011). Gray boxes show inferred rupture patches during these earthquakes.

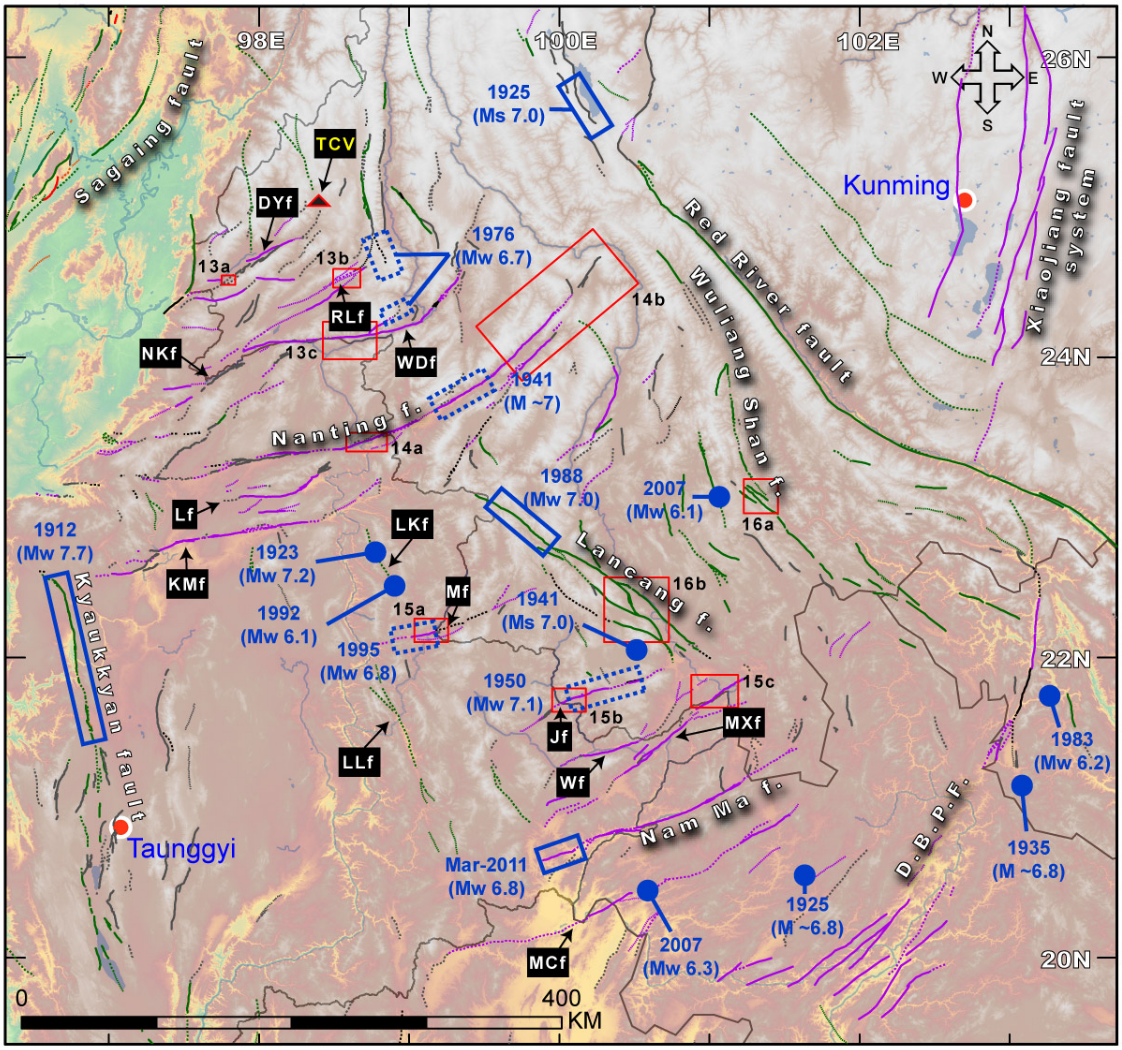

Figure 12 Active faults and associated historical earthquakes within the Shan-Sino domain. Purple = left-lateral faults. Green = right-lateral faults. Gray = normal faults. Blue dots and boxes show locations of earthquake and ruptures of the past century. Red boxes are the locations of coming up figures. TCV = Tengchong Volcano; DYf = Da Yingjiang fault; RLf = Ruili fault; WDf = Wanding fault; NKf = Namkham fault; Lf = Lashio fault; KMf = Kyaukme fault; LKf = Loi Kwi fault; Mf = Menglian fault; LLf = Loi Lung fault; Jf = Jinghong fault; Wf = Wan Ha fault; MXf = Mengxing fault.

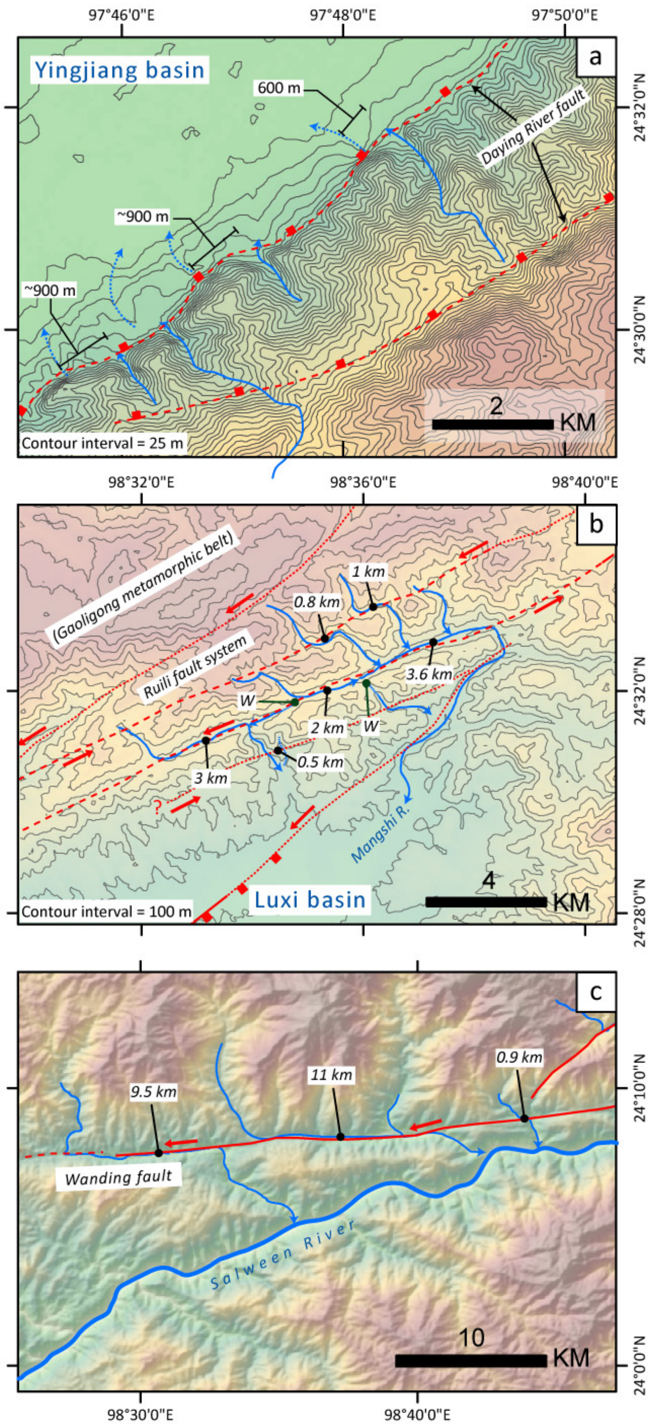

Figure 13 Selected examples of the geomorphological expression of active faults of the Shan-Sino domain, from SRTM topography and LANDSAT imagery. Blue lines = streams. Red lines = fault traces. (a) The Daying River fault appears as a trace with large vertical displacements within the mountain range and a trace with left-lateral displacements at the mountainfront. (b) Offsets along multiple strands of the left-lateral Ruili fault total 10 to 11 km. W = wind gap. (c) Matches of tributaries of the Salween River suggest left-lateral offsets of ~11 km along the Wanding fault.

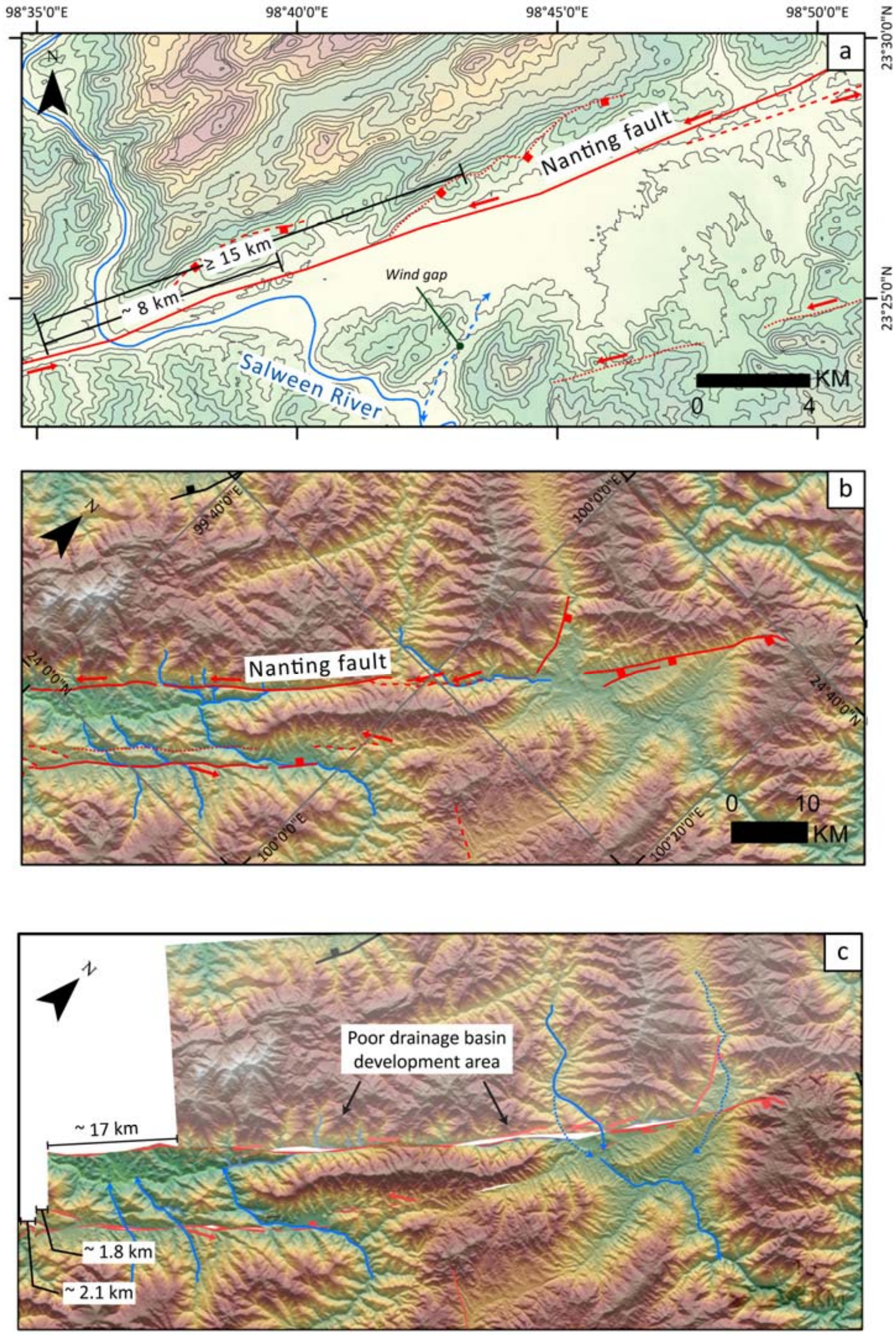

Figure 14 Tectonic geomorphological expressions of select locations along the Nanting fault. Conventions same as in previous figures. (a) Plausible 15-km offset along the central part of the Nanting fault, based upon recognition of a wind gap between the fault and the Salween River. (b and c) Current and restored stream-channel patterns along the northeastern reach of the Nanting fault suggest a 20-km offset.

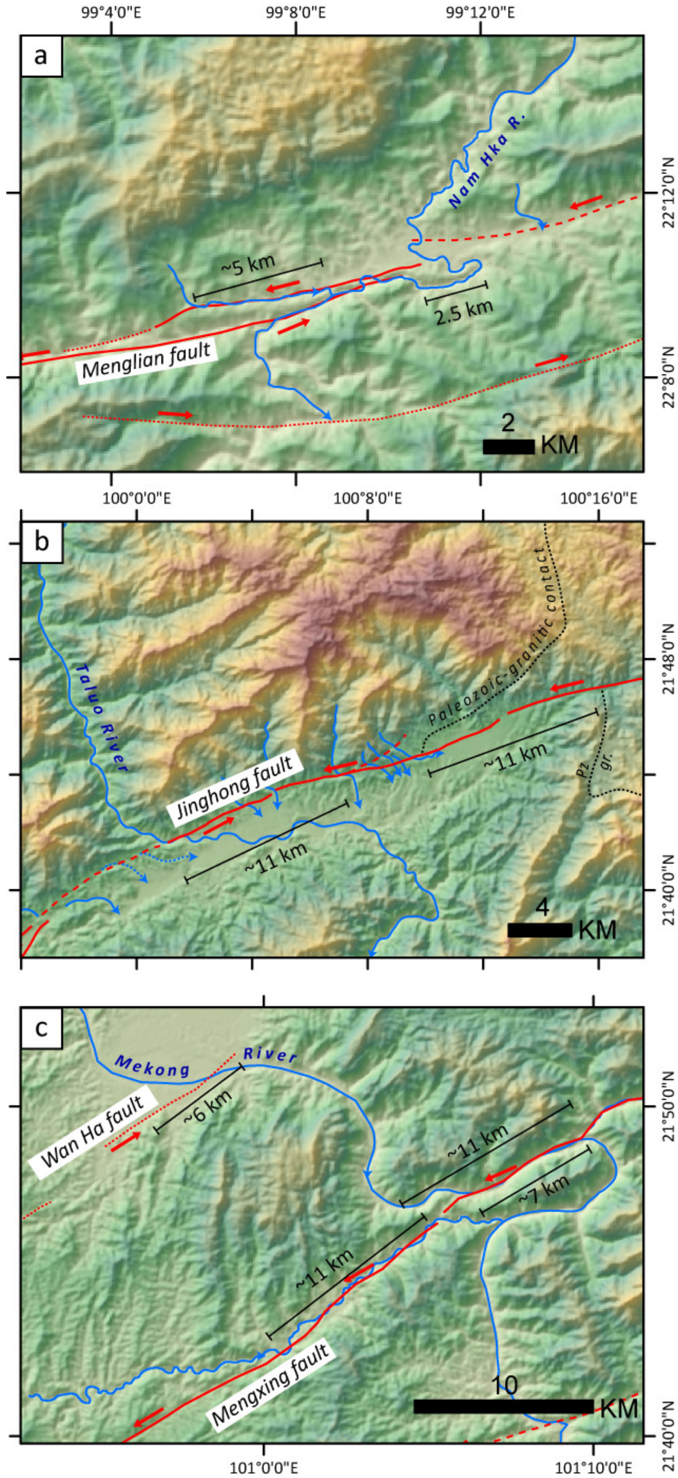

Figure 15 Tectonic geomorphological expressions of the Menglian, Jinghong and Mengxing faults. (a) Deflections of the Nam Hka River and a tributary imply 2.5- and 5-km left-lateral offsets along the Menlian fault. (b) Deflections of the Taluo river imply an 11 km left-lateral offset along the Jinghong fault, which roughly matches the 11 km left-lateral offset of a bedrock contact. (c) Left-lateral deflections of the Mekong river and a tributary imply an 11-km offset by the Menxing fault.

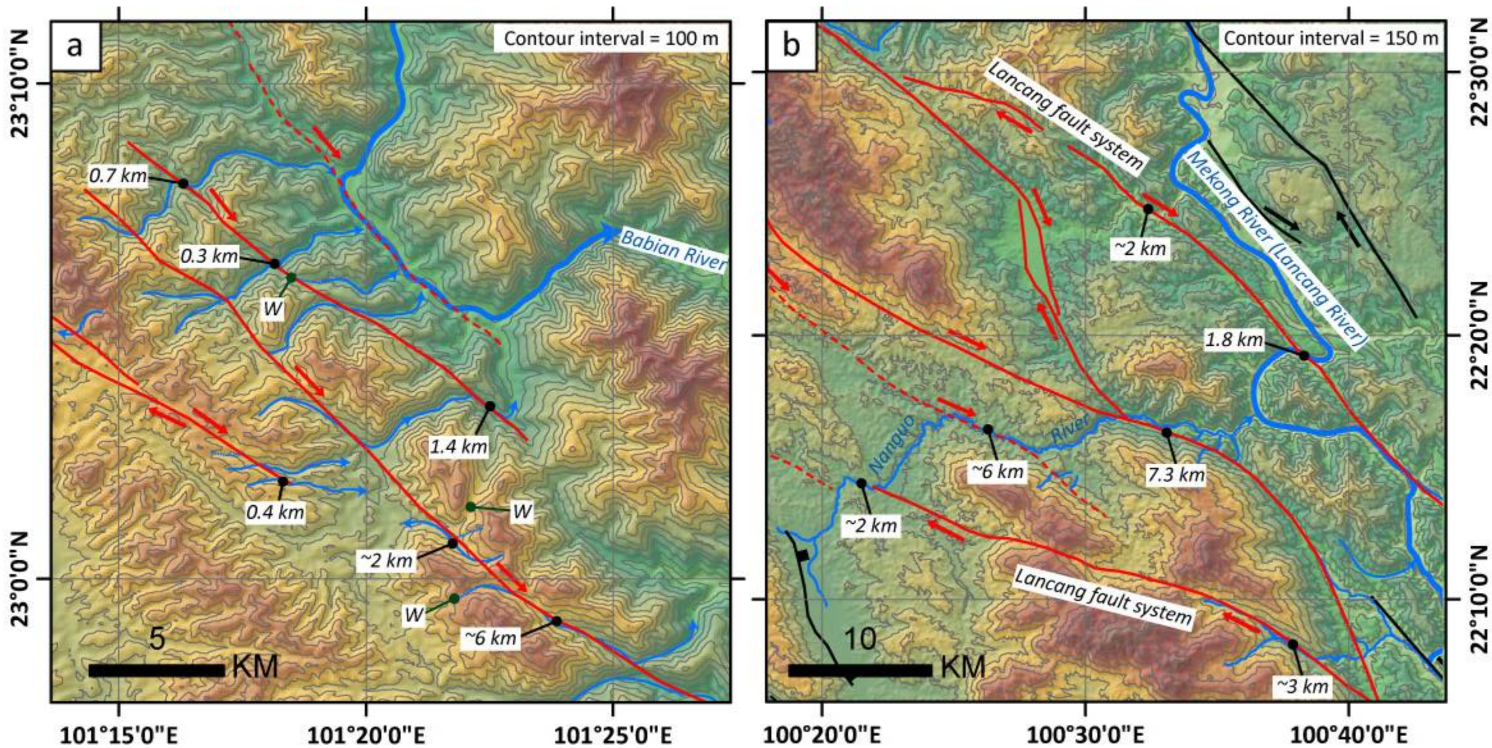

Figure 16 Tectonic geomorphology along parts of the right-lateral Wuliang Shan fault and Lancang fault system. (a) Maximum deflections of drainages across the Wuliang Shan fault zone is about 6 km here. (b) Deflections of the Nanguo river across a complicated set of faults suggests ~ 17 km of dextral offset across the Lancang fault system here.

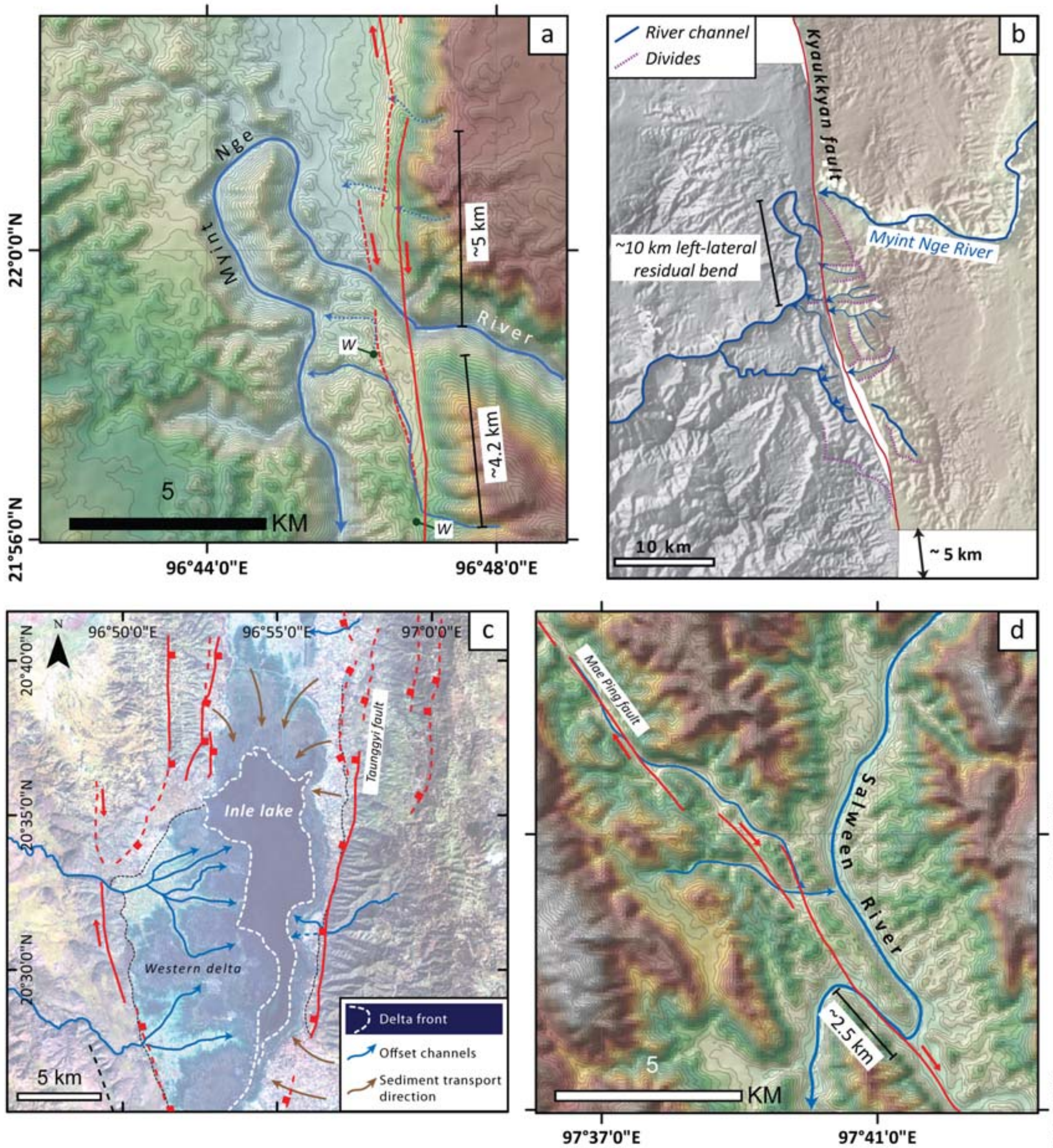

Figure 17 Geomorphological expression of particularly informative parts of the right-lateral Kyaukkyan fault system. (a) The hairpin geometry of the Myint Nge river channel, along the northern reach of the Kyaukkyan fault shows clear evidence for normal and dextral displacement along the fault. (b) Restoration of a 5-km recent right-lateral component of slip leaves a remaining, earlier 10-km left-lateral bend. (c) LANDSAT imagery of the Inle lake region showing the complex geometry of Taunggyi normal fault. (d) The Mae Ping fault zone offsets the Salween river channel and tributaries about 2.5 km.

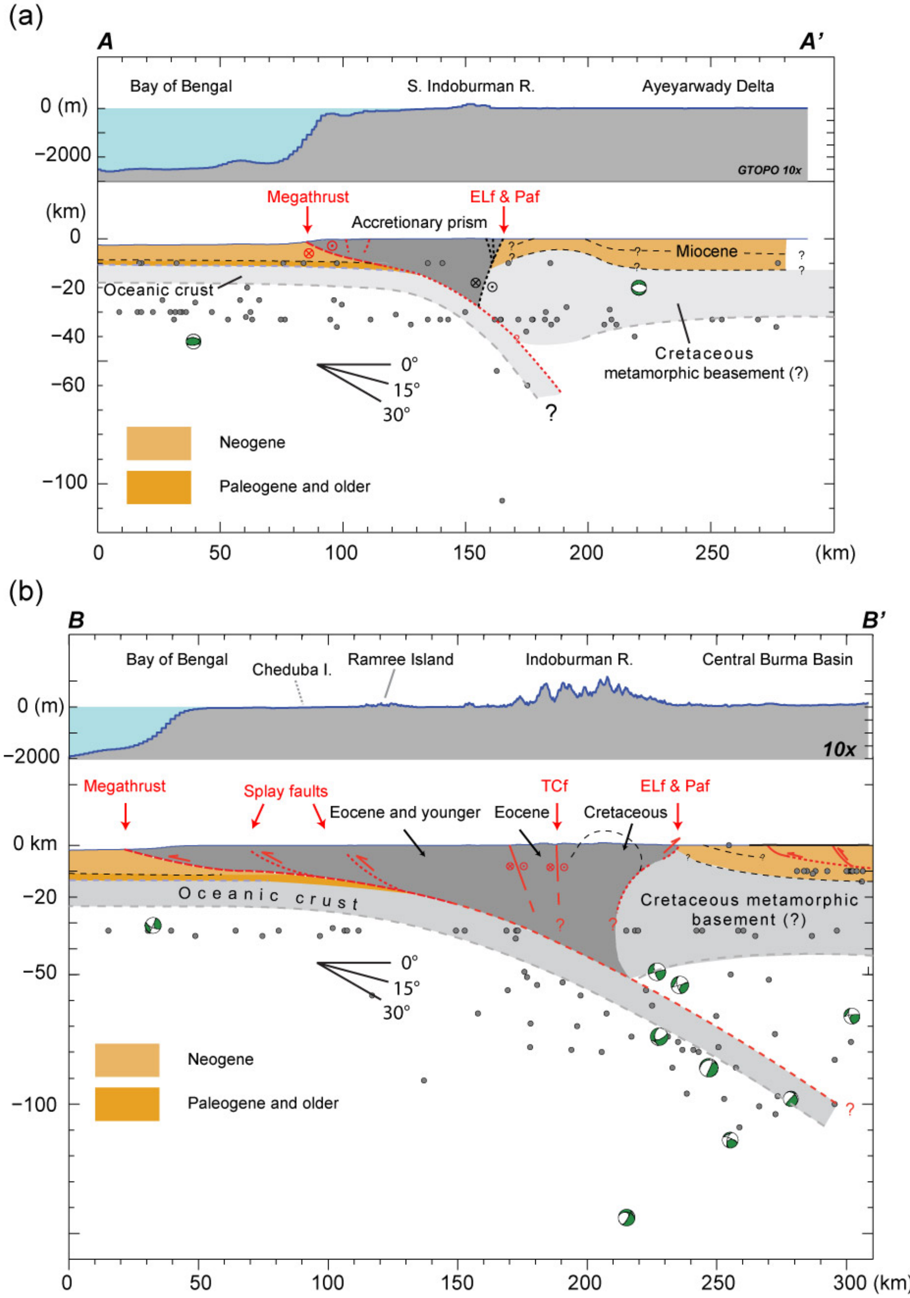

Figure 18 Schematic cross sections through two domains of the northern Sunda megathrust show the geometry of the megathrust and hangingwall structures. Grey dots the hypocenter locations from NEIC catalog since 1976. Green and white focal mechanisms are from GCMT database. (a) The megathrust along the Coco-Delta domain dips moderately and has secondary active structures near the deformation front. See Figure 3 map for profile location. (b) The megathrust along the Ramree domain dips shallowly and is associated with splay thrust faults and strike-slip faults within the hangingwall block. See Figure 4 map for location of the profile.

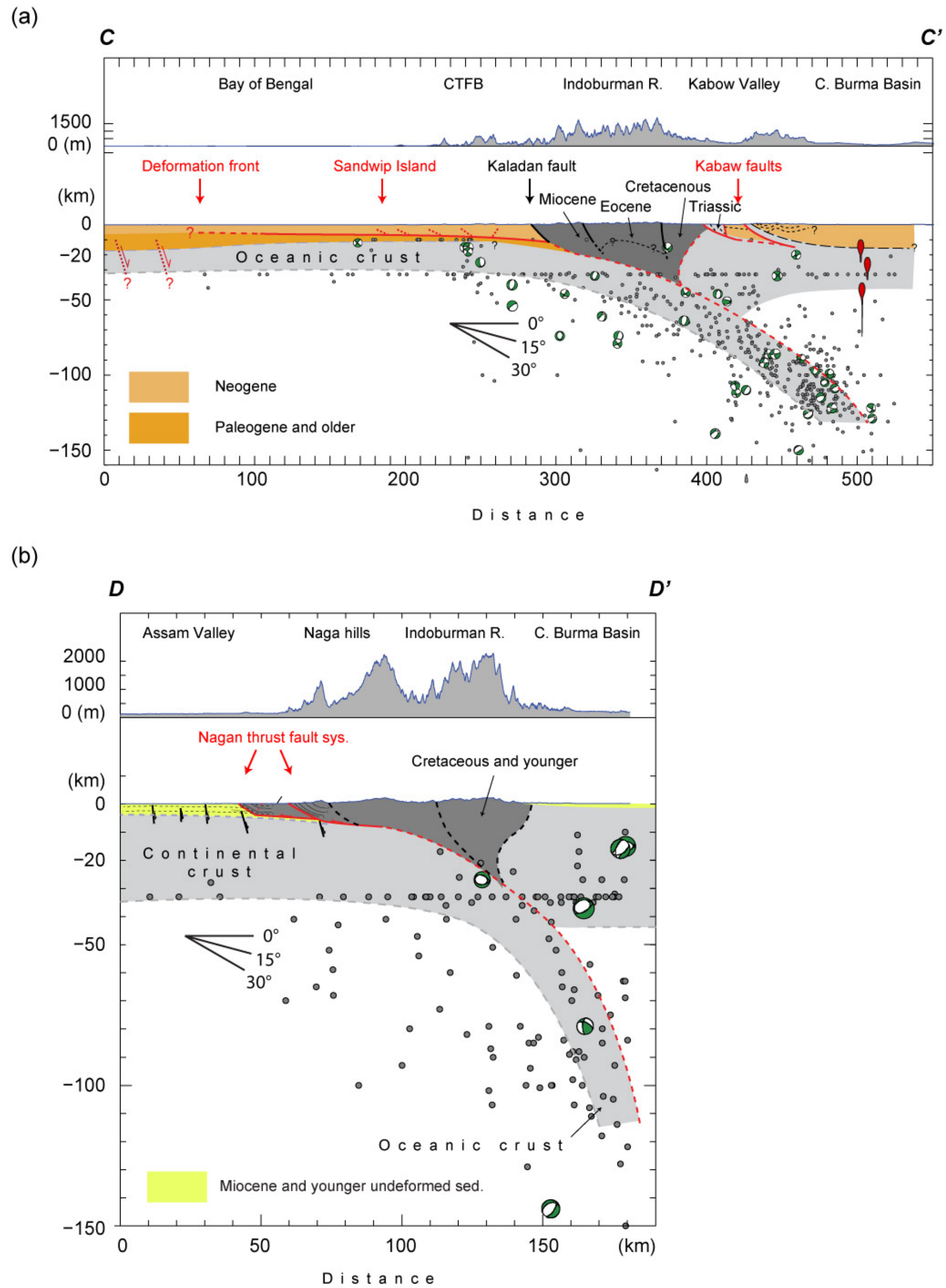

Figure 19 Schematic cross sections through two domains of the northern Sunda megathrust show the geometry of the megathrust and hangingwall structures. Symbols as in Figure 18. (a) The megathrust along the Dhaka domain dips very shallowly and has secondary active thrust faults within 120 km of the deformation front. See Figure 6 map for profile location. (b) The megathrust along the Naga domain dips moderately and juxtaposes continental against continental crust, but still has an attached subducting slab of Indian-plate oceanic crust. See Figure 9 map for profile location.

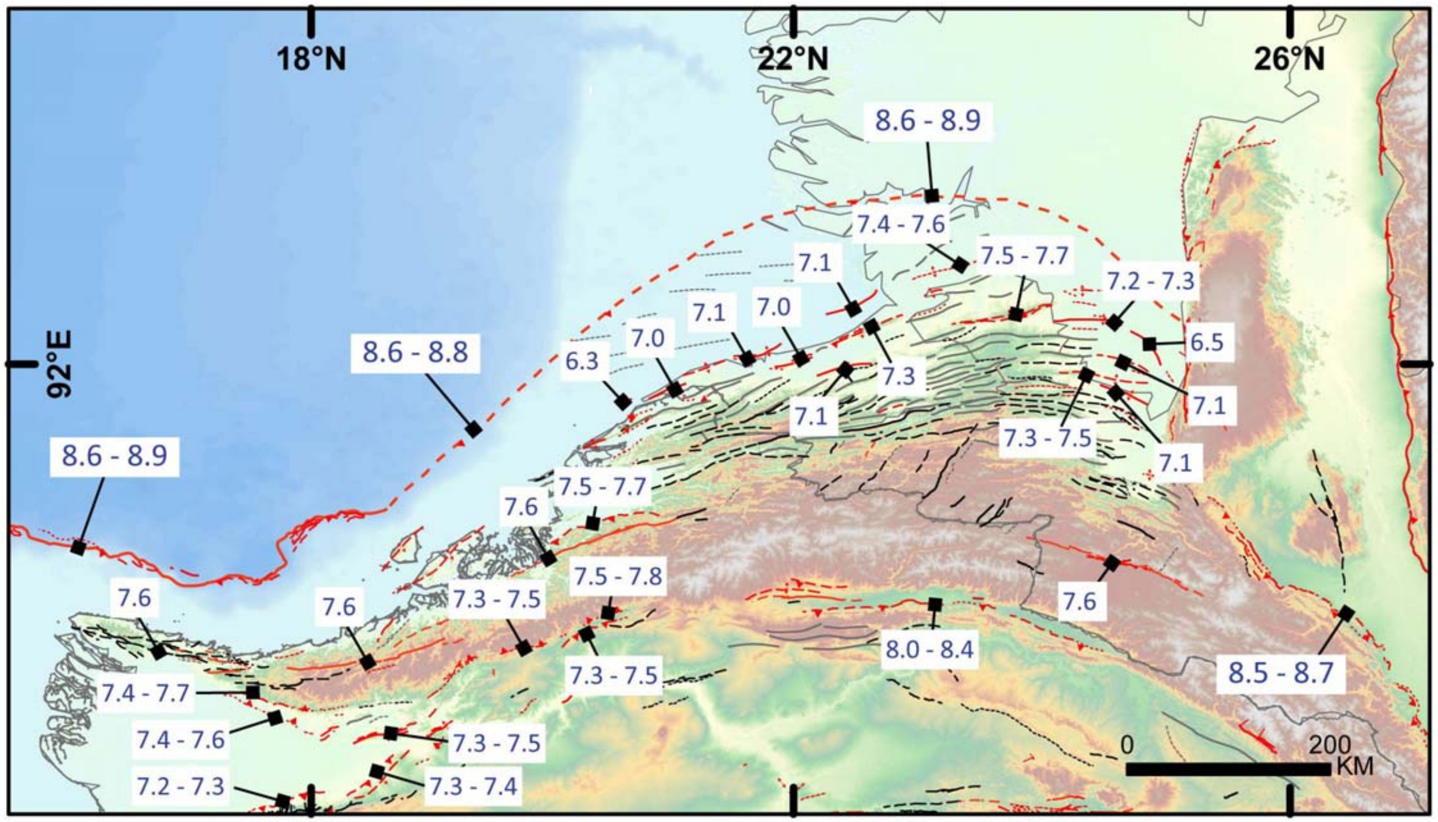

Figure 20. Map of potential maximum earthquake magnitudes (Mw) associated with shallow active faults of the four domains of the northern Sunda megathrust and Indoburman range. Blue numbers show earthquake magnitudes assuming complete rupture of each fault along its entire strike length. Red lines show the active structures mapped from digital elevation model and satellite imagery. Black lines show structures that we interpret to be inactive.

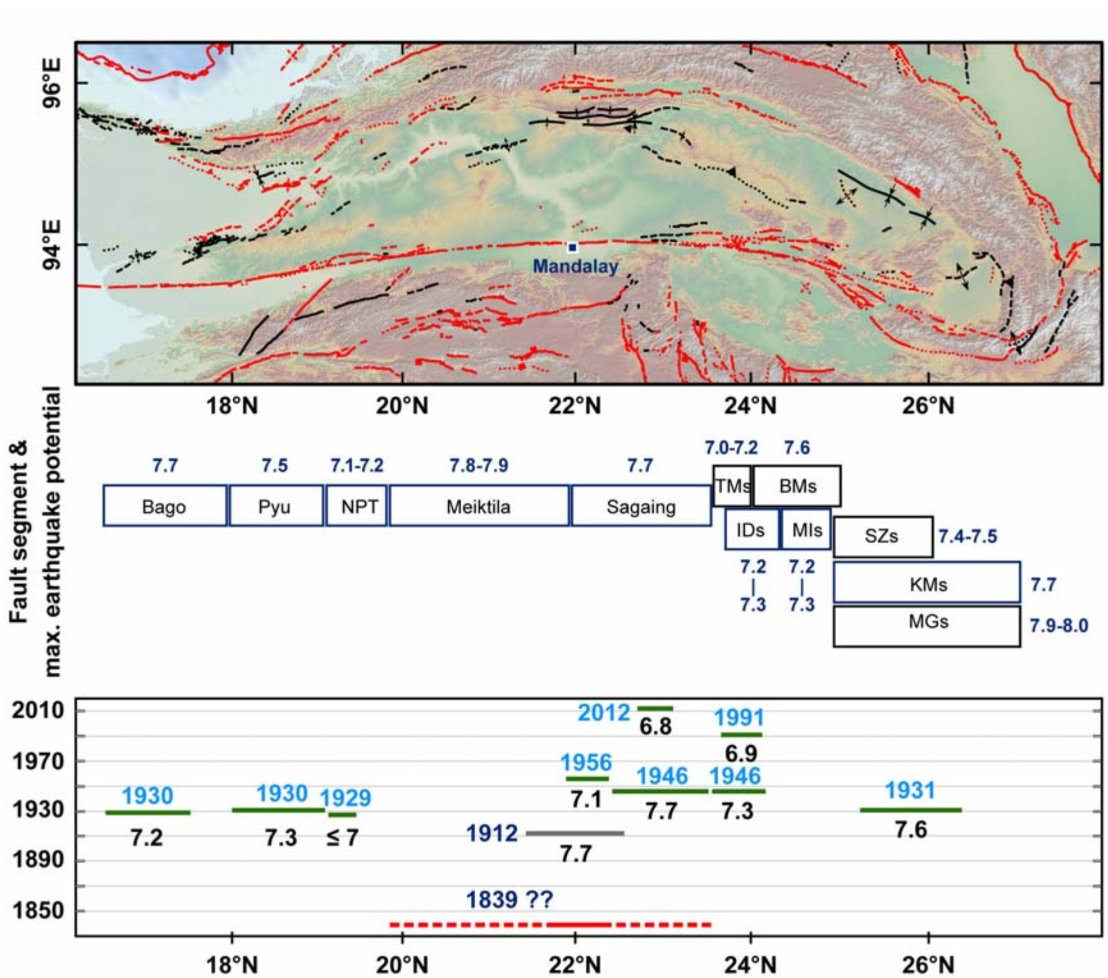

Figure 21 Map and chart of potential maximum earthquake magnitudes (Mw) associated with named segments of the Sagaing fault. Ruptures of the past century appear in the lower box

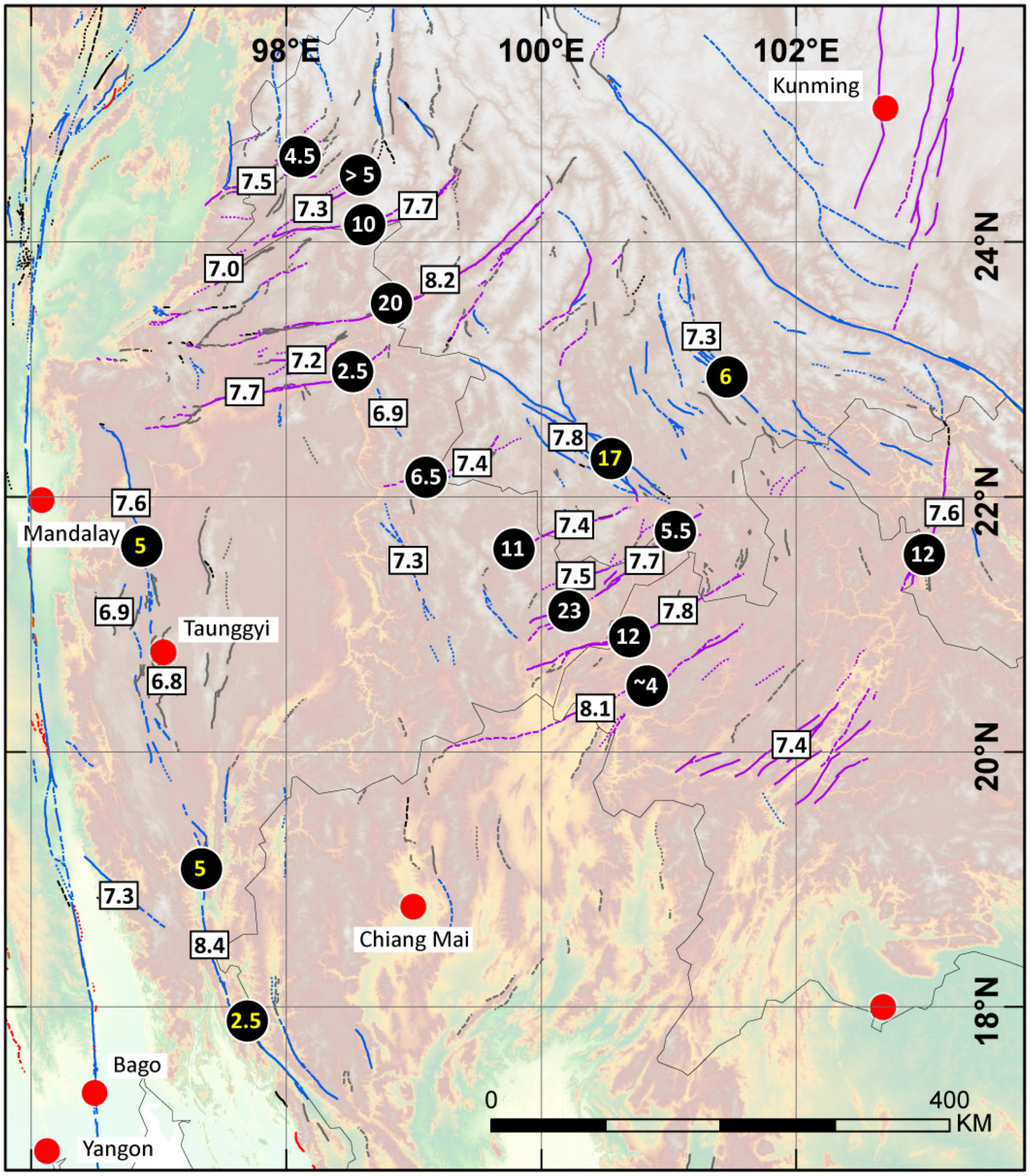

Figure 22 Map of total geomorphological evident offset (black dots) and potential maximum earthquake magnitudes (Mw) (White rectangles) associated with named faults of the Shan-Sino domain. The maximum earthquake magnitudes are based on the assumption that each fault will rupture along its entire length. Purple, blue and gray lines represent left-lateral, right-lateral and normal faults, respectively.

Table 1. Significant earthquakes within the study area since the late-19th century

Date (YYYY-MM-DD)	Lat	Lon	M	M_{type} ‡	Location	Type of records	Reference
Indoburman Range and central Burma basin							
1762/4/2	19	93.5	> 8.5	M_{fault}	Sunda megathrust	Int + G	H; O; W1
1858/3/23	19.3	95	7.7	M_{int}	Central Burma basin	Int	O; A&D;
1906/6/24	15	92	7.3	M_{unk}	Near megathrust	S	A
1918/7/8	24.5	91	7.5	Mw	Bangladesh	Int + S	S; E&V
1927/12/17	17.5	95.5	~ 6?	M	North of Yangon	Int	Brown, 1929
1943/10/23	26	93	7.1	Mw	Assam Valley	S	E&V
Sagaing fault							
1839/3/23	22	96	> 7	M	Near Mandalay	Int	O
1929/8/8	19.2	96.2	~7	M	Near Taungoo	Int	B2
1930/5/5	17.78	96.73	7.2	Mw	Bago	Int + S	Brown et al., 1931; E&V; H&P
1930/12/3	18.12	96.76	7.3	Mw	Pyu	Int + S	Brown et al., 1933; E&V; H&P
1931/1/27	25.41	97.02	7.6	Mw	Kamaing	Int + S	Chhibber, 1934; E&V; H&P
1946/9/12	24.02	96.09	7.3	Mw	Sagaing fault	S	E&V; H&P
1946/9/12	22.35	96.24	7.7	Mw	Sagaing fault	S	E&V; H&P
1956/7/16	22.06	95.9	7.1	Mw	Sagaing	S + Int	E&V; H&P

Table 1. (Continue)

Date (YYYY-MM-DD)	Lat	Lon	M	M_{type} ‡	Location	Type of records	Reference
1991/1/5	23.59	95.97	6.9	Mw	Tagaung	S	E&V; H&P; GCMT
2003/9/21	19.91	95.63	6.6	Mw	Taungdwingyi	S	E&V; H&P; GCMT
2012/11/11	22.755	95.708	6.8	Mw	Singu	S + G	NEIC; GCMT;
Shan-Sino domain							
1912/5/23	21	97	7.7	Mw	Kyaukkyan fault	Int + S	Brown, 1917; E&V
1923/6/22	22.589	98.681	7.2	Mw	Eastern Myanmar	S	E&V
1925/12/22	20.538	101.667	6.8	M_{unk}	Mae Chan fault ?	S	A
1935/11/1	21.148	103.082	6.8	M_{unk}	close to DBPF	S	E&V
1941/5/16	23.7	99.4	6.9	Ms	Nanting fault	S + Int + G	Lee and Wang, 1978; GNSIZM, 1979; E&V
1941/12/26*	21.08 ?	99.14 ?	7	Ms	Yunnan-Myanmar	Int + S	GNSIZM, 1979; E&V
1942/2/1	23.1	100.3	6.8	M_{unk}	Yunnan	Int + S	X; A
1950/2/2	21.758	99.97	7.1	Mw	Jinghong fault ?	Int + S	X; A
1976/5/29	24.509	98.913	6.7	Mw	Yunnan	Int + S	GNSIZM, 1979; A; GCMT
1976/5/29	24.52	98.502	6.6	Mw	Yunnan	Int + S	GNSIZM, 1979; A; GCMT
1983/6/24	21.721	103.265	6.2	Mw	close to DBPF	Int + S	Trieu et al., 2008; A; GCMT
1988/11/6	22.869	99.571	7	Mw	Lancang fault	Int + S + G	Yu et al., 1991; A; GCMT

Table 1. (Continue)

Date (YYYY-MM-DD)	Lat	Lon	M	M_{type} ‡	Location	Type of records	Reference
1992/4/23	22.422	98.887	6.1	Mw	Myanmar	S	A; GCMT
1992/4/23	22.41	98.821	6.1	Mw	Myanmar	S	A; GCMT
1995/7/11	21.89	99.22	6.8	Mw	Myanmar-Yunnan, Menglian fault ?	Int + S	Chen et al., 2002; A; GCMT
2007/3/10	24.727	97.597	5.5	Mw	Myanmar-Yunnan, Daying River fault	S	NEIC; GCMT; Lei et al., 2012
2007/6/2	23.02	101.01	6.1	Mw	Yunnan, Wuliang Shan fault	S	A; GCMT
2007/5/16	20.47	100.69	6.3	Mw	Laos, Mae Chan fault	S	A; GCMT
2011/3/24	20.62	100.02	6.8	Mw	Myanmar, Nam Ma fault	S + G	Wang et al., 2013b; GCMT

‡ M_{fault}: calculated from the fault slip model; **M_{int}**: Calculated from the seismic intensity record; **M_{unk}**: Instrument record, with unknow type of magnitude. **M:** speculation from the intensity records in history

$ Type of records: **Int:** Intensity; **S:** Instrument; **G:** Ground deformation

***** The epicenter location is inconsistence to the isoseismal map

Reference: **A:** Allen et al., 2009; **A&D:** Ambraseys and Douglas, 2004**; E&V:** Engdahl and Villaseñor, 2002; **H:** Halsted, 1842; **H&P:** Hurukawa and Phyo Maung Maung, 2011; **O:** Oldham, 1883; **S:** Stuart, 1920; **W1**: Wang et al., 2013; **X:** Xie and Tasi, 1983;

Table 2. Summary of maximum fault offset in the Sino-Shan domain fault system.

Fault name	Fault length (KM)	Fault type[a]	Location[b] Lon	Lat	Type of offset	Max. offset (KM)	Ref.[c]	Note
Daying River Fault	135	L + N	97.95	24.65	River channel	4		Min. offset
Huna Fault	60	L + N	97.65	24.38	River channel	5		
Manda fault	> 30	L	98.09	24.52	Ridge crest	4.5		
Ruili fault (Eastern)	100	L + N	98.57	24.43	River channel	≤13		> 5 km
Ruili fault (Western)	40	L + N	97.76	23.98		> 1.7		
Namkham fault	60	L + N	97.47	23.79	River channel	> 0.6		
Wanding fault	170	L	98.63	24.14	Salween River system	10 ± 1	LAC	
Nanting fault	380	L	100.17	24.52	Ridge crests & rivers	20		
Lashio fault	85	L	97.99	23.07	Ridge crest & basin	6.5?		> 2.5 km
Kyaukme fault	> 200	L	98.13	22.88	River channel	2.5		
Menglian fault	120	L	99.53	22.32	River channel	5.5 ± 0.5		
Jinghong fault	110	L	100.05	21.7	River channel	~11		
Wan Ha fault	140	L	100.18	21.34	Nam Loi River	5.5 ± 0.5	LAC	
Mengxing fault	180	L	100.63	21.38	Nam Loi River	23.5 ± 0.5	LAC	
Nam Ma fault	215	L	100.58	20.88	Mekong River	13 ± 1	LAC	
Mae Chan fault	310	L	100.71	20.508	Ridge crest and channels	~4		
Dien Bien Phu fault	150	L	103.15	20.02	River channel	12.5	LAI	Single fault
Dien Bien Phu fault	~110	L	101.6	19.9	Mekong River	< 60		Multi. faults
Wiliang Shan Fault	~400	R	101.4	22.98	Mekong River sys.	~6		
Lancang fault	210	R	100.52	22.28	Nanguo River	~17		
Northern Kyaukkyan	~160	R	99.77	21.99	Myint Nge River	~5		

a. N = Normal fault; L = Left-lateral fault; R = Right-lateral fault;
b. The location is roughly the center point of the offset feature along the fault
c. LAC = Lacassin et al., 1998; LAI = Lai et al., 2012

Table 3. Scaling relationships for fault length and magnitude that used in this study.

Equation	Reference	Note
Reverse/Thrust fault		
Mw = 4.16 + 1.75 * log10(L)	Blaser et al., 2010	
M = 5.00 + 1.22 * log10(SRL)	Wells and Coppersmith, 1994	
M = 4.49 + 1.49 * log10(RLD)	Wells and Coppersmith, 1994	For blind structure
Mw = 4.868 + 1.392 * log10(L)	Strasser et al., 2010	For subduction interface
Normal fault		
Mw = 3.67 + 1.92 * log10(L)	Blaser et al., 2010	
M = 4.86 + 1.32 * log10(SRL)	Wells and Coppersmith, 1994	
M = 4.34 + 1.54 * log10(RLD)	Wells and Coppersmith, 1994	For blind structure
Strike-slip fault		
Mw = 4.20 + 1.56 * log10(L)	Blaser et al., 2010	
M = 5.16 +1.12 * log10(SRL)	Wells and Coppersmith, 1994	
M = 4.33 +1.49 * log10(RLD)	Wells and Coppersmith, 1994	For blind structure

Table 4. Proposed Major Seismic Structures of Myanmar and surrounding countries.

Code	Name	Type‡	Length (km)	Slip rate mm/yr	Strike	Dip	$M_{W\&C}$ [length]	M_{Blaser} [length]	$M_{Strasser}$ [length]	Last known earthquake		
										Year	M	Partial / Entire
Coco-Delta domain												
	Sunda megathrust (Coco-delta section)	SS + R	480	8 to 28 [A]	N20E	20	8.3	**8.9**	**8.6**			
Paf	Pathein fault	R	95	< 12 [B]	N20E	45	**7.4**	**7.6**				
Elf[S]	East-limb fault (Southern section)	R	100	< 12 [B]	N20E	45	**7.4**	**7.7**				
	Seidaung fault	SS	>160	< 5 ?	N20E	90	**7.6**	**7.6**				
Ramree domain												
	Sunda megathrust (Ramree section)	R	450	< 23 [B]	N35W	16	8.2	**8.8**	**8.6**	1762	8.5 to 8.8	Entire
WBf	Weest Bogo-Yoma fault	R	65	> 0.4 [C]	N20W	45	**7.2**	**7.3**		1927?	~6?	Partial?
PDf	Paungde Fault	R	70	> 0.4 [C]	N45W	45	**7.3**	**7.4**				
MBf	Minbya Fault	R	105	--	N20W	45	**7.5**	**7.7**				
LMf	Laymyo Fault	SS	175	~ 0.6 [D]	N20W	90	**7.7**	**7.6**				
TCf	Thahtay Chaung fault	SS	>150	~ 2 [D]	N15W	90	**7.6**	**7.6**				
Elf[C]	East-Limb fault (central section)	R	60	< 9 [B]	N45W	45	**7.2**	**7.3**				
Elf[N]	East-Limb fault (northern section)	R	~120	< 9 [B]	N25W	45	**7.5**	**7.8**				
Sdf	Sidoktaya Fault	R	70	< 9 [B]	N25W	45	**7.3**	**7.4**				
PTf	Pato fault	R	30	--	N45W	45	**6.8**	**6.7**		1858?	7.7	Entire?
Pyf	Pyay fault	R	80	--	N15W	45	**7.3**	**7.5**				

Table 4. Proposed Major Seismic Structures of Myanmar and surrounding countries (Continued).

Code	Name	Type‡	Length (km)	Slip rate mm/yr	Strike	Dip	$M_{W\&C}$ [length]	M_{Blaser} [length]	$M_{Strasser}$ [length]	Last known earthquake		
										Year	M	Partial / Entire
Dahaka and Naga domains												
	Blinded Sunda megathrust (Dhaka section)	R	520	> 6[A]	N15W	5	8.3	**8.9**	**8.6**			
IPf	Churachandpur-Mao fault	SS	≧170	16[E]	N10E	90	**7.6**	**7.6**				
	Kabaw fault	R	~280	< 9[B]	N-S	45	**8.0**	**8.4**				
SM	St. Martin’s Island	A	>16	1 to 3[F]	N10W	--	**6.3**	**6.3**				
Da	Dakshin Nila	A	40	1 to 3[F]	N30W	--	**6.9**	**7.0**				
M	Maheshkhali	A	50	1 to 3[F]	N20W	--	**7.0**	**7.1**		1999	5.2	Partial
J	Jaldi	A	40	1 to 3[F]	N20W	--	**6.9**	**7.0**				
P	Patiya	A	50	1 to 3[F]	N20W	--	**7.0**	**7.1**				
Si	Sitakund	A	65	1 to 3[F]	N25W	--	**7.2**	**7.3**				
SW	Sandwip	A	50	1 to 3[F]	N25W	--	**7.0**	**7.1**				
L	Lalmai	A	90	1 to 3[F]	N15W	--	**7.4**	**7.6**				
H	Habiganj	A	105	1 to 3[F]	N15W	--	**7.5**	**7.7**				
R	Rashidpur	A	62	1 to 3[F]	N5W	--	**7.2**	**7.3**		1918	7.5	Entire
S	Sylhet	A	22	1 to 3[F]	N70E	--	**6.5**	**6.5**				
F	Fenchunganj	A	45	1 to 3[F]	N10W	--	**7.0**	**7.1**				
Ha	Hararganj	A	80	1 to 3[F]	N15W	--	**7.3**	**7.5**				
Pa	Patharia	A	46	1 to 3[F]	N15W	--	**7.0**	**7.1**				
	Naga thrust fault	R	400	< 5[G]	N48E	23	8.2	**8.7**	**8.5**			

Table 4. Proposed Major Seismic Structures of Myanmar and surrounding countries (Continued).

Code	Name	Type‡	Length (km)	Slip rate mm/yr	Strike	Dip	$M_{W\&C}$ [length]	M_{Blaser} [length]	$M_{Strasser}$ [length]	Last known earthquake		
										Year	M	Partial / Entire
Sagaing domain												
	Bago	SS	>170	18[H]	N-S	90	**7.7**	**7.7**		1930	7.2	Partial
	Pyu	SS	130	18[H]	N10W	90	**7.5**	**7.5**		1930	7.3	Entire
	Nay Pyi Taw	SS	70	18[H]	N10W	90	**7.2**	**7.1**		1929	~7	Partial
	Meiktila	SS	220	18[H]	N5W	90	**7.8**	**7.9**		1839?		Entire?
	Sagaing	SS	180	18[H]	N-S	90	**7.7**	**7.7**		1946/1956	7.6/7.0	Partial
BMs	Ban Mauk	SS	150	<< 20[I]	N5E	90	**7.6**	**7.6**				
TMs	Tawma	SS	60	<< 20[I]	N-S	90	**7.2**	**7.0**		1991	6.9	Entire
IDs	In Daw	SS	80	~20[I]	N10E	90	**7.3**	**7.2**		1946	7.3	Entire
Mls	Mawlu	SS	90	~20[I]	N10E	90	**7.3**	**7.2**				
Szs	Shaduzup	SS	120	< 20[I]	N10E	90	**7.5**	**7.4**				
Kms	Kamaing	SS	170	~20[I]	N15W	90	**7.7**	**7.7**		1931	7.5	Partial?
Mgs	Mogang	SS	260	< 20[I]	N10W	90	**7.9**	**8.0**				
Shan-Sino domain												
DYf	Daying River Fault	SS + N	135	1.4 ± 0.2[J]	N50E	90	**7.5**	**7.5**		2007	5.5	Partial
	Huna Fault	SS + N	60	~1[K]	N70E	90	**7.2**	**7.0**				
	Manda fault	SS	> 30	~0.9[K]	E-W	90	**6.8**	**6.5**				
RLf	Ruili fault (Eastern)	SS + N	100	~2[L]	N50E	90	**7.4**	**7.3**				
RLf	Ruili fault (Western)	SS + N	40	< 2[L]	N50E	90	**7.0**	**6.7**				

Table 4. Proposed Major Seismic Structures of Myanmar and surrounding countries (Continued).

Code	Name	Type[‡]	Length (km)	Slip rate mm/yr	Strike	Dip	$M_{W\&C}$ [length]	M_{Blaser} [length]	$M_{Strasser}$ [length]	Last known earthquake		
										Year	M	Partial / Entire
NKf	Namkham fault	SS + N	60	?	N50E	90	**7.2**	**7.0**				
Wdf	Wanding fault	SS	170	~2[M]	N40E - E-W	90	**7.7**	**7.7**				
NTf	Nanting fault	SS	380	4.2[K]	N50E-N80 E	90	**8.0**	**8.2**		1941	7	Partial
Lf	Lashio fault	SS	85	1.3[K]	E-W	90	**7.3**	**7.2**				
KMf	Kyaukme fault	SS	165	~0.5[K]	N80E	90	**7.6**	**7.7**				
Mf	Menglian fault	SS	120	~1[K]	N70E	90	**7.5**	**7.4**		1995	6.8	Partial
Jf	Jinghong fault	SS	110	~2.2[K]	N70E	90	**7.4**	**7.4**		1950	7.1	Partial
Wf	Wan Ha fualt	SS	140	~1[K]	N70E	90	**7.6**	**7.5**				
MXf	Mengxing fault	SS	180	~4.8K	N50E	90	**7.7**	**7.7**				
MNf	Nam Ma fault	SS	215	~2.6[K]	N70E	90	**7.8**	**7.8**		2011	6.8	Partial
MCf	Mae Chan fault	SS	310	~1[K]	N70E	90	**8.0**	**8.1**		2007	6.3	Partial
DBPf-V	Dien Bien Phu fault (Vietnam segment)	SS	150	2.5[K]	N10E	90	**7.6**	**7.6**		1935/198 3	6.8/6.2	Partial
DBPf-M	Dien Bien Phu fault (Mekong segment)	SS	110	2.5[K]	N45E	90	**7.4**	**7.4**				
LKf	Loi Kwi fault	SS	50	~0.8[K]	N25W	90	**7.1**	**6.9**		1992	6.1	Partial
LLf	Loi Lung fault	SS	95	~0.7[K]	N20W	90	**7.4**	**7.3**				

Table 4. Proposed Major Seismic Structures of Myanmar and surrounding countries (Continued).

Code	Name	Type‡	Length (km)	Slip rate mm/yr	Strike	Dip	$M_{W\&C}$ [length]	M_{Blaser} [length]	$M_{Strasser}$ [length]	Last known earthquake		
										Year	M	Partial / Entire
KKF	Kyaukkyan fault (Myint Nge segment)	SS	160	~1[K]	N10W	90	**7.6**	**7.6**		1912	7.7	Entire
PYf	Pingdaya fault	SS	50	--	N10E	60	**7.1**	**6.9**				
TGf	Taunggyi fault	SS	45	--	N10E	60	**7.0**	**6.8**				
KKF	Kyaukkyan fault (Salween segment)	SS	480	~1[K]	N10W	90	**8.2**	**8.4**				
WLSf	Wuliang Shan fault zone	SS	105[#]	> 1.2[K]	N10W-N50W	90	**7.4**	**7.4**		2007	6.1	Partial
LCf	Lancang fault	SS	200	> 3.4[K]	N50W	90	**7.7**	**7.8**		1988	7	Partial
MPf	Mae Ping fault	SS	100	~0.5[K]	N45W	90	**7.4**	**7.3**				

ǂ R: Reverse fault; N: Normal fault; SS: Strike-slip fault; A: Anticline with unknown type of blind faulting.
The longest dextral fault trace within the Wuliang Shan fault zone.
A: The rate is estimated from the Indian, the Burma and the Sunda plate motion vectors (See Appendix-1 Table S1).
B: Inferred from the Socquet et al., 2006.
C: We assume the age of 30-m high uplift surface is ~100 ka.
D: We assume the strike slip begin to active in 5 Ma.
E: The rate is from Gahalaut et al., 2013.
F: speculate from the anticline uplift rates in this region.
G: speculate from the uncertainity of geodetic analysis.
H: Slip rate is from Vigny et al., 2003.
I: Slip rate is from Maurin et al., 2010.
J: Average fault slip rate is from Chang et al., 2011.
K: Rate = maximum offset / 5 Ma. We assume the fault slip began in 5 Ma, based on the regional tectonic history.
L: Average fault slip rate is from Huang et al., 2010.
M: Average fault slip rate is from Chang et al., 2012.

Chapter 3

Earthquakes and slip rate of the Southern Sagaing fault: insights from an offset ancient fort-wall, Lower Myanmar (Burma)

Originally published in Wang, Y., Sieh, K., Aung, T., Min, S., Khaing, S. N. and Tun, S. T. (2011), Earthquakes and slip rate of the southern Sagaing fault: insights from an offset ancient fort wall, lower Burma (Myanmar). Geophysical Journal International, 185: 49–64. doi: 10.1111/j.1365-246X.2010.04918.x.

Abstract

Field investigations of an ancient fortress wall in southern Myanmar reveal an offset of ~6 m across the Sagaing fault, the major right-lateral fault between the Sunda and Burma plates. The fault slip rate implied by offset of this 16th-century fortress is between 11 and 18 mm/yr. A paleoseismological excavation within the fortress reveals at least 2 major fault ruptures since its construction. The slip rate we obtained is comparable to geodetic and geological estimates farther north, but is only 50% of the spreading rate (38 mm/yr) at the Andaman Sea spreading center. This disparity suggests that other structures may be accommodating deformation within the Burma plate. We propose two fault-slip scenarios to explain the earthquake-rupture history of the southern Sagaing fault. Using both small offset features along the fault trace and historical records, we speculate that the southern Sagaing fault exhibits a uniform-fault-slip behavior and that one section of the fault could generate a M7+ earthquake within the next few decades.

Introduction

The long, partially preserved record of civilization in Myanmar (Burma) provides an unusual opportunity to understand the recent behavior of some of its active faults. In particular, inscriptions on some Buddhist religious shrines (pagodas) record damages and renovations through about the past two thousand years (Win Swe, 2006). These could give paleoseismologists a great advantage in determining the timing and recurrence intervals of historical earthquakes, especially if they can determine the seismic sources for these historical events.

Thus, we initiated paleoseismic work in Myanmar with the hope that the precise timing of pagoda destructions would provide exceptional constraints on the recurrence characteristics of large seismic events on the 1200-km-long strike-slip Sagaing fault.

The Sagaing fault is one of the great strike-slip faults of Southeast Asia, bisecting Myanmar from north to south (Fig.1a) (Curray et al., 1979 and Le Dain et al, 1984). The fault is the principal right-lateral boundary between the Sunda and Burma plates (Curray et al., 1979; Bird, 2003; Curray, 2005). Its southern terminus is at the Andaman Sea spreading system, and its northern end fans out toward the Eastern Himalayan syntaxis (Curray, 2005). Like the San Andreas fault in California but in contrast to the great Sumatran fault in Indonesia (Sieh and Natawidjaja, 2000), its trace is remarkably smooth and continuous (Le Dain et al., 1984). This smooth geometry likely reflects very large total offsets.

Brown and Chhibber (Brown et al., 1931; Brown and Leicester, 1933; Chhibber, 1934) were the first to write about the Sagaing fault. It was the alignment of several moderate to strong earthquakes from southern to north-central Myanmar in the early 20th century that attracted their attention and led them to suggest the existence of a long active fault cutting across the active fluvial plains of central Burma. Nonetheless, the fault trace itself was not recognized and mapped until decades later (Win Swe, 1970). This initial delineation of the fault trace was based on field mapping guided by aerial photography. Subsequently more details of its geometry have been revealed through various field investigations and remote sensing studies (Le Dain et al., 1984; Myint Thein et al., 1991; Replumaz, 1999; Tsutsumi and Sato, 2009).

The proximity of the Sagaing fault to several major cities and towns means that large numbers of people are at risk. In the south these cities include the Myanmar's new capital, Nay Pyi Daw, and the ancient capitals of Taungoo and Bago (previously called Pegu). Yangon, the biggest city and largest economic center in Myanmar, and until recently the country's capital, is only 36 km west of the fault trace. These cities have suffered significant seismic damage within the past thousand years (Thawbita, 1976). The high degree of activity of the fault and its proximity to large populations makes the southern reach of the Sagaing fault a prime target for modern neotectonic, paleoseismologic, seismologic and geodetic study.

Another important aspect of the Sagaing fault is its slip rate. Estimates vary by a factor of two. Curray et al. (1982) inferred a long-term slip rate of 35.4 mm/yr, based upon spreading of 460 km in 13 Ma across the Andaman Sea spreading center. Myint Thein et al. (1991) suggested just half that value, 18.5 mm/yr, assuming a later (11 Ma) initiation of rifting and a 203 km offset of a metamorphic belt near Mandalay. Bertrand et al. (1998) calculated a slip rate of between 10±1 and 23±3 mm/yr, from a 2.7-6.5 km offset of a 0.25 to 0.31 million-year old basalt flow in central Myanmar. Vigny et al. (2003) used two years of GPS observations to estimate 18 mm/yr of elastic deformation across the central Sagaing fault. Meade (2007) estimated the rate using GPS observations in a block model for the Indian and Southeast Asian plates. His model suggests that the strike-slip rate between the Indian and Southeast Asian plate is 17 and 49 mm/yr at across the central and northern Sagaing fault, respectively. His estimation represents the maximum value for the Sagaing fault if all of the strike-slip motions between the Indian and Southeast Asian plate are concentrated along this single fault. Liu and Bird (2008) predicted a rate of 22-35 mm/yr on the

Sagaing fault by using their kinematic model to fit the regional geodetic velocities, geological fault slip rates and stress directions.

Comparison of these slip-rate estimates shows that estimates for the central Sagaing fault (Vigny et al., 2003, Bertrand et al., 1998 and Myint Thein et al., 1991) are slower than estimates from simplified tectonic models (Curray, 1982; Meade, 2007; Liu and Bird, 2008), even if these models consider the slip partitioning between Indo-Burma Range and Sagaing fault (Liu and Bird, 2008). Also, the rate seems to vary geographically. Rates across the central Sagaing fault are slower than the Andaman Sea spreading rate (Curray et al., 1982 and Kamesh Raju et al., 2004). This ostensible northward decrease in rate implies that about 2 cm/yr of the opening rate across the Andaman Sea spreading center has been partitioned between the Sagaing fault and one or more other structures.

In this study, we reconstruct the offset and estimate the construction date of an ancient fortress, thereby enabling an evaluation of both the earthquake history and slip rate of the southern Sagaing fault. We further refine the fault's recent history through a paleoseismological study within the fortress. This rate, averaged over just a few centuries, fills a gap in rates between geologic rates averaged over more than a million years and geodetic rates spanning just a few years.

Active tectonics of the southern Sagaing fault and surrounding area

Structural overview of southern Myanmar

Figure 1b shows active tectonic features in southern Myanmar. This map includes primarily tectonic geomorphologic features deduced from analysis of 90-meter-resolution SRTM and

15-meter stereo ASTER VNIR images. Aerial photography at 1:25000 and 1:50000 scales also aided in our mapping along the western and eastern flanks of the Pegu-Yoma range.

The distribution of active structures indicates that tectonic strain is accommodated not only by the Sagaing fault, but also by other structures in southern Myanmar. These active structures occur in three regions: The western and eastern edges of the Pegu-Yoma range and the western Shan plateau.

Along the western edge of the Pegu-Yoma range, west-facing scarps and slightly warped lateritic terraces suggest the existence of active contractional structures. These structures are mostly NNW trending, oblique to the orientation of regional compressional stress (Gahalaut and Gahalaut, 2007), as would be expected in a transpressional regime. The lack of active strike-slip structures along the western side of the Pegu-Yoma range suggests that mostly contraction perpendicular to the Sagaing fault is occurring there.

On the other side of the Sagaing fault, on the western Shan plateau, offset drainages along the major intraplate Mae Ping fault (Morley, 2002) suggest recent strike-slip activity. Clear geomorphic evidence of recent activity occurs only along that section of the Mae Ping fault closest to the Sagaing fault. The youthful geomorphic expression of the Mae Ping fault implies that the Sagaing fault is not the only locus of strike-slip motion, and that strain partitioning is not as simple as it appears to be farther south, in Sumatra (Fitch, 1972; McCaffrey, 1991; Sieh and Natawidjaja, 2000; Genrich et.al., 2000; Chlieh et. al., 2007).

Southern Sagaing fault

The southern Sagaing fault shows clear evidence of right-lateral offset, along the eastern edge of the Pegu-Yoma range. The fault forms a remarkably straight boundary between the Miocene-to-Pleistocene sediments of the Pegu-Yoma range and Holocene sediments of the fluvial plain. South of 18.5°N, the fault's geomorphology varies markedly along strike. Between

18.5°N and 17.5°N, well-aligned offset stream channels, linear valleys and linear scarps dominate. Right-lateral channel separations range from ~500 m to 4 km. The length of these separations implies a long history of offset recorded by the landforms. South of 17.5°N, the fault trace traverses predominantly the active fluvial plain of the Sittaung and Bago Rivers, whose deltas are still prograding southward. Meandering river landforms dominate tectonic landforms. In this region of very low and young topographical relief, the Sagaing fault's trace is marked intermittently by small west-facing scarps and N-S trending tectonic ridges. The rapid construction of this fluvial landscape and the fact that fluvial features are nearly parallel to tectonic landforms make it difficult to identify clear tectonic landforms.

The trace of the Sagaing fault changes strike by about 10° at 18°N. This sharp kink results in a local transpressional environment, as evidenced by minor contraction structures on the eastern fluvial plain.

The NEIC/USGS global earthquake catalog (magnitudes greater than 4 since 1973) shows a non-uniform distribution of background seismicity along the southern Sagaing fault. Epicenters cluster around the kink at 18°N. Global CMT solutions suggest that the fault plane strikes ~355° south of and 335° north of the fault bend, which is consistent with the change of fault orientation at the surface. Moderate earthquakes north and south of the kink are rare in the catalogue; thus the cluster of recent activity may mark highly coupled sections to the north and south.

1930 May Pegu earthquake and 1930 December Pyu earthquake

Two major earthquakes occurred in rapid succession along the southern Sagaing fault in the 20th century. The Pegu earthquake, which shook the region violently on 5 May 1930, had an estimated magnitude (Ms) of 7.2 (Pacheco and Sykes, 1992). The Pyu earthquake, which occurred just 6 months later on 3 December 1930, had a similar magnitude (Ms 7.3), but was most severe farther north. Grey dashed lines in Fig. 1b surround the regions of highest intensity (Rossi-Forel

VIII to IX) (Brown et al., 1931 and Brown and Leicester, 1933). This corresponds to Modified Mercalli intensities of VII to IX (Wood and Neumann, 1931).

For both earthquakes, Rossi-Forel intensity IX extends about 60 km along the Sagaing fault. The Rossi-Forel intensity VIII zones are also parallel to the trend of the fault. The southern (Pegu) earthquake has a smaller and narrower region of intensity VIII than the northern (Pyu) earthquake. Also, the northern and southern terminations of the intensity VII zone are close to the edge of intensity-IX zone, which shows the rapid northward and southward decaying of the seismic intensity during the Pegu earthquake.

Study of recent earthquakes suggests the distribution of Modified Mercalli intensities >VIII coincides with the length of the seismic surface rupture (i.e. Sokolov and Wald, 2002). Hence, we believe the high intensities of the Pegu and Pyu earthquakes likely represent the maximum lengths of their fault ruptures.

Although most of the southern Sagaing fault experienced high intensities during these two events, a section of lower intensity exists between 17.5°N and 18°N. This implies that at least a 50-km section of the fault between the two events of 1930 did not rupture during either of these two earthquakes.

Offsets along the Pegu section

From April 2008 to March 2009, we conducted a series of field investigations to map the trace of the southern Sagaing fault and the possible surface rupture during the Pegu earthquake. We focused on the area between 17.5°N to 17.2°N, where the intensity of the Pegu earthquake decreased dramatically northward. Along this section, we also tried to collect stories of the earthquake in every village along the fault trace to determine whether or not offsets we found in the field formed during the earthquake. The interview records and field photos are included in the Appendix 2 (Table S1 and Table S2). Our work was a complement to that of Tsutsumi and Sato

(2009), who conducted a similar survey farther south (from 17.2°N to 16.5°N). Our and their work allows us to make a more complete interpretation of slip during the Pegu earthquake of 1930.

Figure 1c shows measurements of small dextral offsets along the southern Sagaing fault, deduced from our combined field observations. The y-axis spans ~100 km of the Sagaing fault that experienced high seismic intensities during the Pegu earthquake. Measured offsets range from ~20 meters to less than 1 meter. The lack of large offsets south of ~ 17°N likely reflect the southward-decreasing age of the southward-prograding fluvial plain. Local minimum offset values form a bell-shaped distribution centered at ~17°N. This distribution is comparable in form to the pattern of the seismic intensity along the fault during the Pegu earthquake. Therefore, we suggest that these horizontal offsets are coincident with the Pegu earthquake, the most recent large earthquake in the region.

Offset ancient structure

The Payagyi ancient fortress

Fifteen-meter resolution ASTER visible and near infrared (VNIR) imagery and 1:25000 aerial photos show that the Sagaing fault cuts through a rectangular earthen embankment west of Payagyi, 16 km north of Bago (Fig. 2a). The age and offset of this man-made feature offers a great opportunity to constrain the fault slip rate along the Pegu section of the Sagaing Fault. Tsutsumi and Sato (2009) also documented this offset ancient structure, but they were unable to measure the amount of displacement directly in the field.

There is no direct historical evidence that clarifies the function and the age of this feature. However, circumstantial evidence suggests it is either a fortress/stockade, or the temporary palace for royal usage. If the rectangular embankment is a military fortress (the standard military device for attackers and defenders in the history of Myanmar), then its construction could have occurred during 15th to 17th century. This was time of great military activity in the region, and Pegu (Bago) was wealthy enough to build outlying defenses such as this one. It is also possible that the structure was built in mid-18th century, when Pegu was besieged, before being conquered by the Burmese King Alaungpaya in 1755-57 (Harvey, 1925). Both offensive and defensive sides built more than 40 stockades at that time, but mainly south of Pegu (Bago). Since there was also a second Alaungpaya army advancing from Taungoo in the north, this structure might have been built to defend Pegu from this northern troop.

Alternatively, the embankment might have served as a temporary palace to guard their religious treasures, built in 1574 or 1576, during the construction/renovation of the Payagyi Pagoda, 1.5 km to the east. The construction of a temporary palace is mentioned by U Kala, who wrote about Burmese history in the early 18th century. The English translation of his description is included in the Appendix 2 (Table S3).

Archeological materials found during our survey support, but do not prove, a 15th-16th-century date of construction. We found fragments of celadon pottery characteristic of 15th-16th-century Thai and Burmese ceramic production (Bob Hudson, field conversation, 2008) within the confines of the ancient structure. Although these fragments were found on the surface and were disturbed by the modern cultivation, they still suggest that there was human activity in this area in the 15th-16th centuries. It is reasonable to hypothesize that the construction of the embankment occurred then.

The trace of the fault is clearly demarcated geomorphologically from the northern wall through about the northern two thirds of the interior of the feature (Fig. 2b). The southern intersection of the fault trace and the fortress wall has been destroyed by construction of a modern E-W road.

The northern intersection is readily apparent in high-resolution satellite imagery and the 1:25000 aerial photos, but it is difficult to estimate the right-lateral offset. The fault trace inside the ancient fortress wall aligns well with other tectonic features north and south of the fortress (Fig. 2b). Its northern extension corresponds to the western edge of a tectonically warped terrace, which blocks an eastward flowing stream, resulting in the creation of a sag-pond north of the fortress. The fault scarp is unclear near the southern fortress wall, but probably runs under the E-W running dirt-road. Farther south, the Sagaing fault is also unclear on the young floodplain but probably corresponds to the western edge of a deformed terrace.

Estimation of offsets

In the summer of 2008 and spring of 2009, we used a total station to map the topography of the ancient fortress in order to estimate the offset of the northern fortress wall. Our survey allowed us to construct a 50-cm-resolution digital terrain model (DTM) within the fortress walls (Fig. 2c). This digital topography provides a crystal-clear image of not only the fault scarp south of the northern wall but also the geometry of the wall. The fault scarp height decreases from ~1.4 m at the northern wall to ~20 cm 270 meters to the south. The change of scarp height is an indication that the vertical component of slip varies along strike, a common observation along strike slip faults (Yeat et al., 1997). The northern fortress wall has been obliterated in the vicinity of the fault trace but is still clear on either side. The topographic saddle between the eastern and western section of the fortress wall may be the result of fluvial erosion after tectonic damage.

Estimation of offset on the northern fortress wall is complicated by the fact that the separation of the northern edge of the wall differs markedly from the separation of the southern edge. The width of the wall east of the fault is greater than that west of the fault. This width disparity may result from greater post-offset sedimentation on the downthrown western section of the wall. We tested this hypothesis by studying the stratigraphy in four pits dug through the wall (1-4 in Fig. 2c;

Fig. 3). In each excavation, we identify the contact between the wall and the underlying original sediment (Fig. 4). Each pit exposes a section of manmade fill, consisting of massive yellowish silt to sand with very small amounts of reddish brick and pottery fragments. This fill overlies layers of organic-rich clay to silt and less-organic brown silty sediments. Except for the organic-rich layer, it is not easy to correlate the natural sediments in these four pits. Such spatial variation in floodplain deposits is not uncommon. The organic-rich layer in these pits usually shows a sharp upper and a gradational lower boundary. These characteristics suggest an immature soil that was buried rapidly by construction of the earthen wall.

We found one charcoal fragment in Pit-1, in the floodplain sediment 15 cm below the base of the wall (Fig. 5). Radiocarbon analysis yielded an age of about 4514 B.P. However, another radiocarbon age, 32 cm below the base of the wall in Pit-1 ranges from 1210 C.E. to 1390 C.E., with 1210-1300 C.E being the most likely range (Table 1). Since this younger age should predate the date of fortress construction, the implied date of construction of the fortress wall is during or after the 14th century.

Note that the base of the fortress wall is about 30 cm below the ground surface west of the fault. This indicates a small amount of sediment has accumulated and slightly narrowed the width of the wall. The profile of the upthrown, eastern side does not show an accumulation of post-construction sediment (Fig. 3). Instead, we found evidence for about 1.5 m of erosion north of the wall. Sedimentation to the west of the fault and erosion to the east of the fault require a more careful reconstruction of the offset than a simple matching of the modern topography of the embankment.

To estimate the amount of offset, we first restore the geometry of the fort-wall on the downthrown (west) side of the fault by removing the post-construction deposit (Fig. 5). The two pit walls on the downthrown side show the elevation of the ground surface prior to wall construction. We then extend the fort-wall profiles to the pre-wall ground. We also restore the pre-wall topography of the northern side of the fort-wall on the upthrown (east) side by replacing the eroded post-constructional sediment. The estimated edge of the fort-wall highly relies on the slope we chose to represent the original wall shape. Here we choose a slope range from 7.5° to 20°, with the maximum slope close to the typical angle of repose for silt (19°; Cobb, 2009).

Figure 5 shows the final restored geometries of the fortress wall. The restored fortress wall geometries are similar to each other: Both east and west of the fault, the embankment crest is closer to the northern edge of the embankment than to the southern edge. Also, the height of fort-wall east of the fault is similar to its height west of the fault - about 3 meters. The widths are also similar: 37 m wide east of the fault and 30.5 to 35-m wide west of the fault. The widths of the fort-wall 1.5 m above the original ground surface are identical, about 22 m. These similarities support our restoration of the original topography of the embankment near the fault trace.

To estimate the amount of offset recorded by the northern embankment, we select its 3 clearest piercing points: Its northern base, the southern base, and the crest. Measured perpendicular to the embankment's trend, these three features are separated 4.6 to 6.9 m, 5.8 m and 8.8 to 11.7 m across the fault. To determine the equivalent three offsets, we must make a trigonometric correction, to measure the offset parallel to the fault trace. This correction is the cosine of the angle between the orientation of the fault (180˚) and the profiles (157˚). Both the separations and the derived offsets appear on Figure 5.

The estimates of separation are less precise for the base of the embankment, because of the uncertainty in extending the topographic profile of the wall downward to the original ground surface. The northern and southern walls display separations of 5 to 7.5 m and 9.5 to 13 m, respectively (Fig. 5). The matching of the crest gives a more precise estimate of 6.3 m. The separation of the southern base of the fort-wall is almost twice as large as the other two measurements. This is most likely the result of agricultural modification. A local farmer claimed that other farmers modified the southern base to create a paddy field about 20 years ago. They dug into the southern slope of the embankment on the upthrown side and used the sediment to create a small but elevated paddy field. As a result, the current southern edge of the embankment is 4 to 5 meters further south than its original position. In light of this history of modification, we discard the 9.3 to 13-m estimate of separation for the southern flank of the embankment.

Offset reconstruction

Figure 6 depicts the history of the embankment at its northern intersection with the fault. First, the perfectly linear embankment appears on undeformed fluvial plain across the Sagaing fault. Next, oblique slip of the Sagaing fault offsets it. During subsequent rainy seasons, eastward-flowing flood-waters deposit sediment onto the downdropped surface west of the fault. These flood-waters also eroded the faulted wall and surface east of the fault. Repetition of this process not only reduced the height of the fault scarp, but also reduced the apparent horizontal offset on the northern flank of the fort wall and enlarged the apparent horizontal offset on the southern flank of the fort wall.

With this working scenario, we further carry out a simple simulation to estimate the horizontal offset more precisely (Fig. 7). The idea of this simulation is to balance any vertical topographical change after the construction. This simulation also allows us to examine the fault separation derived from the previous section (Section 3.2). We first subtract 1.5 meters of elevation from the uplifted surface of the eastern section (Fig. 7b). This step removes the elevation difference due to faulting. We then add back about the same amount of sediments to the eastern section to make up for the sediment surplus and lost due to the post-constructional deposition and erosion (Fig. 7c). This step eliminates the influence of differential sedimentation. At the last step, we can offset the eastern profile back to visually match the western profile, and determine the horizontal offset (Fig. 7d and e).

The visual matching of the overall fort-wall profiles (Fig. 7d and 7e) suggests a separation of 4.8 to 5.8 m, which corresponds to a fault offset between 5.2 and 6.3 meters. This estimation is slightly smaller than the previous estimations made by matching the crest and the base of the fort-wall (5-7.5 m). The advantage of this simulation method is that it is not reliant on matching the southern flank, which has been modified by farmers. The only thing that matters is the fort-wall geometries on both sides of the fault. This result also confirms our interpretation that the fault-separation estimate from the southern base of the fort-wall is too large. Thus, the Sagaing fault offset that is recorded by the fortress wall is between 5 and 7.5 meters, most probably ~6 meters.

Paleoseismologic excavation in the ancient fortress.

A trench across the fault ~300 m south of the northern fort wall reveals a partial post-embankment earthquake history. The location of this hand-dug trench is shown in Fig. 2c. The fault scarp across the paddy fields there is 10 to 20 cm high. Contrasts in sediment color and grain size are faint in this trench. Most sediment is silt and clay, which we interpret as overbank deposits. These sediments are also strongly bioturbated, so few sedimentary contacts are apparent in either wall of the trench. These sediments are therefore far from optimal for providing a detailed paleoseismologic history.

Sedimentary units in the trench

Figure 8 is a map of the southern wall of the trench. This map shows 6 main sedimentary units: A topmost gray to orange mottled massive silt (a), a massive medium gray mottled clayey silt deposit (b), a dark organic-rich clay (h), a med-gray pedogenic clayey silt that is rich in dark, hard nodules (b1), a clayey silt layer that is rich in brick fragments (g) and a massive silty clay layer (e). All of these units exhibit extensive bioturbation, predominantly by crabs, which can penetrate from the ground surface to depths as great as 2 to 3 meters. Sediment fills some of the crab burrows;

other burrows are hollow but have 5- to 10-mm thick clay films lining their walls. We have mapped the burrows where they are clearly visible, but other burrows may have gone unrecognized.

Overlying all other units exposed in this trench is a massive cultivated silty layer. This deposit, labeled as layer (a), consists of a 20- to 40-cm thick, grey to orange mottled massive silt. The topmost part of layer (a) is a 2 cm thick light-grey loose silt, uniformly distributed on the paddy field and the paddy field boundary. This thin layer of silt is the most recent suspension deposit from flooding in the rainy season. Layer (a) is thicker on the northeastern side of the trench than it is on the southwestern side of the trench. It is because the northeastern side of the trench cuts across the paddy field berm, so the surface elevation of the northeastern side reflects the height of paddy field boundary, not the height of a fault scarp.

Unit (b) underlies the cultivated layer (a). This dry massive clayey silt layer is harder than overlying unit (a) and is distinctly darker. Unit (b) is about 40 to 60 cm thick and is composed of massive medium gray mottled clayey silt with very rare sub-mm to mm brick fragments. These fragments usually appear as dark-red to orange specks. The thickness of unit (b) increases gradually toward the northeast. Although the contact between units (a) and (b) is gradational over ~ 5 cm, it is clear that the contact is ~ 10 cm higher on the northeastern side of the trench than on the southwestern side. This contact may reflect the topography of the ground surface before it was modified to form the modern paddy field.

Unit (h) underlies unit (b) and is the most notable unit in the trench. This 8-cm-thick organic unit (h) is dark-grey organic clay. The unit has a sharp upper contact with overlying unit (b) and a gradational lower boundary marked by a color change. This morphology suggests it is a topsoil layer that was later buried by deposit (b) and (a). Its upper contact is coincident with the uppermost occurrence of hard, black Fe-Mn-rich soil nodules.

Under the thin paleosol is the med-gray mottled massive clayey silt. We mark this layer unit (b1), because its composition is similar to that of unit (b). Hard, black Fe-Mn soil nodules are common within this unit but do not exist in unit (b). These sub-angular to rounded hard nodules are usually smaller than 7 mm in diameter.

This unit also contains a very small percent of brick fragments that range in size from about 3 to 7 mm. These fragments increase upward in concentration, to about 20% at the top of the unit. This characteristic of the unit is distinct throughout the trench exposure, so we separate the brick-rich band as another mappable unit, (g). The size of these sub-angular brick fragments ranges from sub-cm to more than 5 cm. In none of these fragments is the original shape of the bricks preserved. Many fragments of charcoal co-exist with these fragments. The structure of the charcoal indicates it is the product of the burning of wood. These 5-mm to 1-cm-size pieces are commonly sub-rounded to rounded, which is an indication that they have been transported by water from their source, either a campfire or a burning timber.

Radiocarbon ages of charcoal from close to the upper and lower contacts of unit (g) (samples P814 and P801 in Table 1) are 990 C.E. to 1180 C.E. (Table 1).

The lowest unit exposed in the trench unit (e) is undifferentiated massive silty clay. This deposit consists of light gray to orange mottled silty clay, with thin lenses of light orange silty sand near the base of the trench. The hard, dark Fe-Mn nodules are also abundant in this deposit. Their concentration in this unit is similar to that in the overlying two layers. Rare small fragments of brick exist in the upper 25 cm of this deposit. We recovered several pieces of charcoal in this unit. They were angular to sub-angular rectangular forms, with woody cellular structures preserved. Radiocarbon analyses of charcoal from the upper part of unit (e) (samples P807, P805, P806 and P809 in Table 1) yield ages similar to those of samples in unit (g), 990 C.E. to 1230 C.E. A single radiocarbon date from several charcoal clasts (P811) at the base of the trench, yielded much older age (750 B.C.E. to 100 B.C.E).

The fact that the radiocarbon ages of seven samples of charcoal from different strata within the trench are similar (990 C.E. to 1230 C.E.) suggests two possible interpretations: Either all these units below paleosol (h) formed in two hundred years or less, by very rapid deposition of very fine grain material, or their charcoal originated from material with that range in ages. In the former case, the strata would be well dated by the charcoal ages. In the latter case, the dates of sedimentation are the same as or younger than the charcoal ages.

The fact that all seven samples yielded older ages than the age of organic material (PYG0101a in Table 1) under the fortress-wall is important in interpreting the date of construction of the embankment. If these dates represent the age of the strata, brick-rich layer (g) is at least 200 years older than the fortress, and we might expect to observe another cultural layer above unit (g), related to the fortress construction. However, no such cultural horizon exists above the brick layer (g). Thus, we suggest these fragments originated upstream as burned construction timbers. Traditional Burmese buildings were constructed of timber and brick. This style of construction still existed in the 16th century royal palace in Bago. If the embankment served as military defense structure within the same period, we would expect to find the remains of similar construction materials within the confines of the ancient walls. The mixture of brick and charcoal fragments in the trench strata lend support to this hypothesis. Therefore, it is reasonable to interpret these fragments of charcoal as the cooled embers of construction timbers that were burned during or after the destruction of the fortress and were later transported and buried at the trench site. Thus, we suggest that the radiocarbon ages of these fragments are greater than the depositional age of these sediments.

Fault traces on the southern trench wall.

We found two plausible faults in the southern wall of the trench, which extend above the brick-rich unit (g) (I and II in Figure 8). Because all of the faulted strata are extensively burrowed and have lost their fine structure, we cannot recover many details of the faulting, including any minor faults in the wall of the trench. Thus, our interpretation of faulting relies principally on changes in elevation of stratal contacts.

Fault I is the younger of the two. Units (g) and (h) have an abrupt 8 cm vertical discontinuity across Fault I. Bioturbation obscures the upward termination of the fault in unit (b). There is no direct evidence that Fault I breaks the upper contact of unit (b). However, that contact does have an elevation change of several cm across the upward projection the fault. Moreover, the thickness of unit (b) is not greater on the downthrown side, which suggests it did not form after faulting.

Fault II is the older of the two faults. It disrupts the brick layer (g) but does not appear to affect overlying paleosol (h). Its sense of vertical separation is toward the east, opposite the direction of the fault scarp visible in the topography. The youngest rupture of Fault II clearly post-dates deposition of brick-rich layer g. However, it must antedate the formation of paleosol h, since Fault II does not disrupt the paleosol.

Two other features may also indicate a rupture between the formation of units g and h. The funnel shape of the lower contact of layer (g) east of the fault could reflect filling of a ground fissure that formed before the formation of paleosol (h). The U-shape downward protrusion of unit b1 into unit e might also indicate a fissure that formed between deposition of units g and h. If these are, indeed, the result of faulting between deposition of units g and h, the simplest hypothesis is that they formed at the same time as the scarp of Fault II.

Fault I may have last moved during either the 1930 earthquake or during an earlier rupture, or both. It is conceivable that the small vertical separation at the base (and possibly the top) of unit b reflects minor slip near the northern terminus of the 1930 rupture. If the top of unit b is not disrupted, it is also possible that Fault I broke during a rupture earlier than 1930. There are no local farmers old enough to attest to effects associated with the 1930 earthquake and we found no datable materials in unit b to constrain the date of the rupture.

Fault II broke after the formation of brick layer (g) but before the formation of paleosol h. Assigning a date to this rupture depends upon one's interpretation of the age of these two units. We have hypothesized that radiocarbon dates from charcoal in that layer and layer b1 are older than the units themselves, having come from campfires or burnt timbers upstream. We also hypothesize that the brick-rich layer g is associated with the destruction of the fortress. If these hypotheses are correct, then Fault II ruptured either during or after destruction of the ancient fortress. In summary, these two fault ruptures suggest two or more faulting events, possibly including the 1930 earthquake, after the destruction of the fortress.

Discussion

The age of ancient fortress

The radiocarbon dates from charcoal within and beneath brick-rich unit (g) provide an oldest plausible range of dates for construction of the fortress – 990 to 1230 C.E. Celadon potteries that we found in nearby paddy fields were produced in the 15th or 16th century (Bob Hudson, field conversation, 2008). Although these fragments were sitting on the modern, cultivated surface, their presence implies human activity at the site during the 15th or 16th century. The occurrence of only a single cultural horizon within the trench strata implies that the fortress operated only for a short period.

The youngest plausible date of construction of the Payagyi ancient fortress is 1634 C.E., the year that Bago ceased being the capital of the country. Its loss of importance at that time deprived the kingdom of any reason to build such a well-designed defensive structure nearby. Although Bago once again became the capital of the Mon people from 1740 – 1757 C.E. (Ooi, 2004), we found no archeological evidence that the fortress had been used during this period.

The historical, radiometric and stratigraphic data thus imply that the ancient fortress was most likely built between 990 C.E. and 1634 C.E. Moreover, history tells us that only in the latter half of that period, between 1369 and 1634 C.E., was Bago the regional political center of this area (Ooi, 2004, and Lieberman, 1980). It was the capital of the Mon kingdom from 1369 to 1539 C.E. and was the official capital of Burma from 1539 to 1599 and 1613 to 1634 C.E.

If this rectangular earthen structure 16 km north of Bago was built to protect the city, the timing of its construction and operation would thus have to fall between the mid-14th century and early 17th century. Furthermore, the rectangular earthen structure shares the same architecture form with the wall of Pegu city (also rectangular), which was built when Pegu was the official capital of the country between 1539 and 1599 C.E. (Fedrici, 2004), so we believe the construction and use of this earthen structure would most likely also occur during this period, before the city of Pegu was ruined by the war.

This interpretation is not in conflict with the radiocarbon age of organic material under the fortress (PYG0101a), which constrains construction of the embankment to after a date in the range of 1220 C.E. to 1300C.E. Also, it is not in conflict with the history recounted in the introduction, in which we suggest that the structure could have been built in 1574 C.E. for temporary royal use.

Late Holocene slip rate along the Southern Sagaing fault

We can now use the constraints on the age of the embankment to constrain the slip rate of the Sagaing fault over the past few hundred years. The 5 to 7.5 meter offset of the northern fortress wall has accrued since a date in the range of 1369 and 1634 C.E. Dividing the range of offsets by the range in dates yields a range in slip rate of 8 to 20 mm/yr. If we assume a tighter range in construction dates, 1539 to 1599 C.E., when the city of Pegu was the official capital of the country, the range of fault slip rate narrows to 11 to 18 mm/yr. We favor a slip rate of 14 mm/yr, calculated by dividing the best estimate of offset, 6 m, by the age of the embankment, assuming it was built for temporary royal usage in 1574 C.E.

This fault slip rate is, of course, an aliased estimate, in that we have not considered where in its seismic cycle the fault was at the time of embankment construction or is now. Our slip rate is comparable to two slip-rate estimates 500 to 550 km further north along the fault (Bertrand et al., 1998 and Vigny et al., 2003). The similarity of our estimate to theirs implies that the slip rate does not vary appreciably from 23° N to lower Myanmar (17.5° N). If the slip rate along the Sagaing fault varies significantly at different latitudes, we should have observed other subsidiary structures to accommodate the differential slip rates along the Sagaing fault. The lack of such structures along the Sagaing fault is consistent with our interpretation of no significant rate difference between the central and southern Sagaing fault.

The similarity also implies that the averaged slip rate has been time-invariant for the past quarter million years (Fig. 9). Our slip-rate estimation is not only similar to the current rate from the short-term geodetic observation across the central Sagaing fault (Vigny et al., 2003), but is also similar to the long-term averaged slip rate estimated by Bertrand et al (1998) at the offset Singu basalt flow, in central Myanmar. Myint Thein et al. (1991) also suggest a similar averaged rate, 18.5 mm/yr, based upon a metamorphic belt offset across the central Sagaing fault. Although they did not have a solid constraint on the timing of fault initiation, the similarity of their result may imply little or no variability over an even longer interval - ten million years.

All four of these estimates are slower than those inferred from broader-scale models (Curray et al., 1982; Meade, 2007; Liu and Bird 2008). Meade's micro-plate model does not include an active convergent boundary (megathrust in Figure 1) between the Indian and Burma plate.

Therefore the difference between his rate prediction and these slip-rate estimations could result from the slip partitioning between the Sagaing fault and the megathrust or from deformation within the Burma plate. On the other hand, Liu and Bird's kinematic plate model does consider a separate Burma plate. However, their model also predicts a higher Sagaing fault slip rate than other geological and geodetic estimations. Again, this disparity suggests that either there is significant deformation within the Burma plate or that the initial fault-slip parameters in their model are inappropriate.

Another issue is the difference between the spreading rate in the Andaman Sea Basin (38 mm/yr) and the observed slip rate on the Sagaing Fault (Fig. 9). We can explain this difference again by internal deformation of the Burma plate, and/or by plate rotation. Gahalaut and Gahalaut (2007) demonstrate how plate rotation and plate geometry affects the fault slip rate in this area. Their model shows a nearly constant 16-17 mm/yr fault slip rate along the Sagaing fault, which agrees with the rates derived from fault-crossing studies. However, their parameters predict a much lower spreading rate (21mm/yr) in the central Andaman Sea spreading center than the rate that previous study suggests (38 mm/yr, Kamesh Raju et al., 2004). Despite this disparity, their result still points out that part of the slip rate disparity between the spreading center and the transform fault may result from the relative plate rotation between Burma and Sunda plate. These discrepancies in rates show that more attention needs to be paid to the possibilities of internal deformation and the relative motion of the Burma plate.

Seismic potential and behavior of the southern Sagaing fault.

In this last section of the paper, we will discuss the seismic potential of the southern Sagaing fault. We will also construct speculative fault slip scenarios along the southern Sagaing fault for the past 500 years. We use the meager evidence from the Payagyi fortress trench, measurements of fault displacement associated with the May 1930 earthquake, intensities from the December 1930 earthquake and the history of damaging earthquakes from nearby cities to construct our fault-slip scenarios. This exercise helps us evaluate the future seismic potential of the southern Sagaing fault.

The pattern of surface rupture associated with the Pegu earthquake in 1930 raises an interesting issue concerning the fault-slip behavior of the southern Sagaing fault. Since the slip distribution curve has a bell-shaped pattern and the active fault trace continues both to the north and south of the rupture (Fig. 1c), the 1930 rupture cannot be representative of all ruptures along that portion of the fault. Along at least a 50-km-long section of fault between 17.5°N and 18°N, shaking intensity was low during the last two significant earthquakes in the region, the Pegu (Ms 7.2) and Pyu (Ms 7.3) earthquakes in 1930. This section of the fault is either locked or creeping. In either case, it did not fail during the 1930 sequence. Not only does this section lack moderate seismicity in the global seismic catalog over the past three decades, but local villagers we interviewed also claimed that they had only experienced two to three earthquakes in their life time. These observations suggest that this section is, indeed, locked. The 50-km length of this section implies that it is capable of generating an earthquake of M 7+ (Well and Coppersmith, 1994). Judging from the fact that this section did not fail during the 1930 sequence, it is a reasonable candidate for the next seismic rupture of the southern Sagaing fault.

Although we lack paleoseismological and geodetic data along this fault section that would aid in forecasting its long-term seismic potential, we may still provide a reasonable speculation about its seismic behavior by constructing fault slip scenarios that match our observations along the southern Sagaing fault.

Here we favor a variant of the uniform fault-slip model to explain the slip history of the southern Sagaing fault over the past 500 years. Tsutsumi and Sato (2009) and this study show that the surface displacements near 17°N are close to 3 m, 6 m, 9 m and 13 m (Fig.1c). Although these field observations are sparse, mostly because small tectonic landforms have been easily destroyed over the centuries by flooding and agricultural activities on the active fluvial plain, they still seem to indicate that fault slip along the central portion of the 1930-rupture is close to 3 meters. This bell-shaped pattern of these smallest offsets supports a uniform slip model for fault-slip behavior along the southern Sagaing fault.

We propose two fault-slip scenarios for the southern Sagaing fault. These scenarios cover the straight section of the fault trace from 16.5˚N to 18˚N. For the purpose of constructing these speculative scenarios, we assume that the bend in the Sagaing fault at 18˚N, which has an unusually high degree of background seismicity, is a low-coupled patch that presents a natural northern limit to large seismic ruptures (Fig. 1b).

Next, we use field measurements of small tectonic offsets, our paleoseismological results at the fortress, historical earthquake accounts and seismic records from the cities of Bago and Yangon to constrain the earthquake rupture history of the past five centuries. The dates of historical earthquakes after 1564 C.E. come from several different sources (Milne, 1911; Chhibber, 1934; Thawbita, 1976; Saw Htwe Zaw, 2006 and Win Swe, 2006). To identify only those events that are likely to have produced large surface offsets, we use only the dates of earthquakes that appear in more than one account (Table 2). We attempt to discriminate further the smaller from the larger events by using other available information. For example, the 1917 earthquake appears in several local catalogs but not in any instrumental catalogs. Moreover, stories we collected from villagers also suggest shaking in 1917 was weaker than in 1930, both north and south of Bago (appendix S. Table.1). Therefore, we interpret the 1917 event to be moderate in size, and discount the possibility of large surficial fault slip on the Sagaing fault.

The age of the Payagyi ancient fortress and our paleoseismology evidence for the number of fault ruptures since its construction also help us constrain the earthquake history. The fortress was most likely built in 1574 C.E. and has been offset by at least 2 earthquakes (3 if one allows the possibility that a small amount of slip occurred there during the 1930 earthquake). Furthermore, our best estimate of total offset of the fortress wall is 6 m, which constrains the cumulative slip since 1574 C.E. there.

All of these constraints on earthquake rupture history have gone into the construction of Scenario-1 (Fig. 10a), which also assumes a classical uniform-slip behavior for the fault (Schwartz and Coppersmith, 1984). That is, the pattern of slip is similar from event to event. In this scenario the last event north of Bago occurred in 1888 C.E., with 2.5 meters of slip through the ancient fortress. The average earthquake recurrence interval for the section of the fault north of the 1930 surface rupture is 140-180 years, which we calculate by dividing the fault slip rate of 14-18 mm/yr into 2.5 meter of slip per event. Likewise, the average frequency of 1930-type events (M 7.3) is 250 – 320 years. Together, these two segments produce a cumulative recurrence of strong earthquakes in the region of Bago ranging between 90 and 115 years.

An alternative construction that also is faithful to the scant historical, paleoseismological and slip data is Scenario 2 (Fig. 10b), which uses the form of the uniform slip model proposed for another strike-slip fault, the Imperial Fault (Sieh, 1996). In contrast to Scenario 1, slip in repeated events along the 1930 section is characteristically less than along the section farther north. In this scenario, the last major event to break the ancient fortress wall occurred in 1768 C.E., and 6 meters of slip occurred farther north. The frequency of strong earthquakes in the Bago region ranges from 167 to 215 years. In this case, the magnitudes of earthquakes in the Bago region vary from M 7.3 to M 7.5. The largest earthquakes are less frequent. M 7.5 earthquakes occur every 333 to 430 years, with stronger shaking at Bago than that during the 1930 event.

Our two uniform-slip scenarios are intended merely to stimulate further discussion and work aimed at understanding the past history and future potential of this important section of the Sagaing fault.

Conclusion

We have measured ~6 meters of dextral offset of an ancient fortress wall across the southern Sagaing fault in Myanmar. Historical evidence and radiocarbon dating of relevant cultural and natural strata imply a most-likely age for the fortress wall of 1574 C.E. Excavations reveal that strata that are younger than construction of the fortress have been offset at least twice by the Sagaing fault. Isoseismals of the historical 1930 earthquake imply that the rupture that caused this M 7.2 earthquake was predominantly south of the fortress and that rupture at the site must have been less than about a meter. This leaves 5 to 6 meters for earlier events subsequent to the late 16th century.

We have constructed plausible uniform-slip models of the earthquake history of this section of the southern Sagaing fault, using the scant available paleoseismic and historical data. They suggest the existence of two distinct segments of the fault, which together produce return times for destructive earthquakes in the region ranging between about one and two centuries.

The 11-18 mm/yr slip rate that we calculate from the offset fortress wall is significantly slower than the 38 mm/yr rate determined from the spreading history of the Andaman Sea. This discrepancy must be explained either by clockwise rotation of the Burma plate or one or more currently unrecognized structures running northward from the spreading centers into Myanmar.

Acknowledgements

We benefited greatly from discussions with Win Swe, Bob Hudson, J. Bruce H. Shyu and their colleagues. The comments and suggestions of Christophe Vigny and another reviewer also helped us improve this manuscript. We also appreciate the generous support of the Immediate Past President of the Myanmar Engineering Society (MES), Mr. Than Myint, and help from the Myanmar Geosciences Society (MGS), the Department of Meteorology and Hydrology (DMH), the Department of Natural Museum, Library and Archaeology of the Ministry of Culture in Myanmar, and Thingazar Travels & Tours Company. This research was supported initially by the Caltech Tectonics Observatory and later by the Earth Observatory of Singapore (EOS), Nanyang Technological University, Singapore.

Reference

Bird, P. 2003. An updated digital model of plate boundaries, Geochem. Geophys. Geosyst., 4(3), 1027, doi:10.1029/2001GC000252.

Berglar, K., Gaedicke, C., Franke, D., Ladage, S., Klingelhoefer, F. & Djajadihardja, Y.S., 2010. Structural evolution and strike-slip tectonics off north-western Sumatra, Tectonophysics, Vol 480, 1-4, 119-132, doi:10.1016/j.tecto.2009.10.003.

Bertrand, G., Rangin, C., Maury, R. C., Htun, H. M., Bellon, H. & and Guillaud, J. P., 1998. The Singu basalts (Myanmar): new constraints for the amount of recent offset on the Sagaing Fault. C. R. Acad. Sci., Ser. IIA, Earth Planet. Sci., 327, 479-484.

Brown, C. J., & Leicester, P., 1933. The Pyu earthquake of 3rd and 4th December, 1930, and subsequent Burma earthquakes up to January, 1932, Mem. Geol. Surv. India, 62, 1–140.

Brown, C. J., Leicester, P. & Chhibber, H. L., 1931. A preliminary note on the Pegu earthquake of May 5th, 1930, Rec. Geol. Surv. India LXV, 221–284.

Chlieh, M., Avouac, J-P., Hjorleifsdottir, V., Song, T-R. A., Chen, J., Sieh, K., Sladen, A., Herbert, H., Prawirodirdjo, L., Bock, Y. & Galetzka, J., 2007. Coseismic Slip and Afterslip of the Great

(Mw 9.15) Sumatra-Andaman Earthquake of 2004. Bull. Seism. Soc. Am., 97, 1A, S152-S173, doi:10.1785/0120050631.

Cobb, F., 2009. Structural Engineer's Pocket Book, 2nd ed., Butterworth Heinemann, Oxford, ISBN-13: 978-0-7506-8686-0, 102.

Curray, J. R. 2005. Tectonics and history of the Andaman Sea region. J. Asian Earth Sci. 25(1), 187-232.

Curray, J.R., Moore, D.G., Lawver, L.A., Emmel, F.J., Raitt, R.W., Henry, M. & Kieckhefer R., 1979. Tectonics of the Andaman Sea and Burma, in Geological and Geophysical Investigations of Continental Margins, Vol. 29, pp. 189–198, eds Watkins, J.S., Montadert, L. and Dickenson P., Am. Assoc. Petrol. Geol. Mem.

Curray, J.R., Emmel, F.J., Morre, D.G. & Raitt, R.W., 1982. Structure, tectonics, and geological history of the northeastern Indian Ocean, in Ocean basins and margins, Volume 6: The Indian Ocean. pp. 399-450, eds, Nairn, A.E.M., and Stehli, F.G., New York, Plenum.

Chhibber, H.L., 1934. The Geology of Burma, McMillan and Co. Ltd, St. Martin’s Street, London, 47–70.

Fedrici, C. 2004. Account of Pegu, Original English edition 1588; reproduced in SOAS Bulletin of Burma Research, 2, 2, 130-159.

Fitch, T.J. 1972. Plate convergence transcurrent faults and internal deformation adjacent to South-East Asia and western Pacific. J. Geophys. Res, 77, 4432-4460.

Gahalaut, V. K. & Gahalaut, K. 2007. Burma plate motion, J. Geophys. Res., 112, B10402, doi:10.1029/2007JB004928.

Genrich, J.F., Bock, Y., McCaffrey, R., Prawirodirdjo, L., Stevens, C.W., Puntodewo, S.S.O., Subarya, C. & Wdowinski, S. 2000. Distribution of slip at the northern Sumatra fault System, J. Geophys. Res, 105, 28, 327-341.

Harvey, G.E. 1925. History of Burma from the Earliest Times to 10 March 1824, The Beginning of the English Conquest. 415 p, Longmans, Green and Co., London.

Kamesh Raju, K.A., Ramprasad, T., Rao, P.S., Ramalingeswara Rao, B. & Varghese, J. 2004. New insights into the tectonic evolution of the Andaman basin, northeast Indian Ocean. Earth planet. Sci. Lett. 221(1-4), 145-162.

Lacassin, R, Replumaz, A. & Hervé Leloup, P. 1998. Hairpin river loops and slip-sense inversion on southeast Asian strike-slip faults, Geology, 26, 703-706.

Lacassin, R., Maluski, H., Leloup, P. Tapponnier, H., P., Hinthong, C., Siribhakdi, K., Chuaviroj, S. & Charoenravat, A., 1997. Tertiary diachronic extrusion and deformation of western Indochina: Structural and 40Ar/39Ar evidence from NW Thailand, J. Geophys. Res., 102(B5), 10,013–10,037.

Le Dain, A. Y., Tapponnier, P. & Molnar, P., 1984. Active faulting and tectonics of Burma and surrounding regions, J. Geophys. Res., 89(B1), 453–472.

Lieberman, V. 1980. The Transfer of the Burmese Capital from Pegu to Ava. J. Roy. Asiat. Soc. 64-83.

Liu, Z. & Bird, P. 2008. Kinematic modeling of neotectonics in the Persia-Tibet-Burma orogen, Geophys. J. Int., 172(2), 779-797. doi:10.1111/j.1365-246X.2007.03640.x.

McCaffrey, R. 1991. Slip vectors and stretching of the Sumatran fore arc, Geology 19, 881-884.

Meade, B. J. 2007. Present-day kinematics at the India-Asia collision zone, Geology 35(1): 81-84.

Milne, J. 1911. A catalogue of destructive earthquakes A. D. 7 to A. D. 1899, BAAS, London.

Morley C.K. 2002. A tectonic model for the Tertiary evolution of strike-slip faults and rift basins in SE Asia, Tectonophysics, 347 (4), 189-215.

Myint Thein, Tint, K. & Aung, A.K. 1991. On the lateral displacement of the Sagaing fault, Georeport, 1(1) 23-34.

Ooi, K.G. 2004. Southeast Asia: A historical encyclopedia from Angkor Wat to East Timor. 1500 p. ABC-CLIO. Santa Barbara, California.

Pacheco, J.F. & Sykes, L.R. 1992. Seismic moment catalog of large shallow earthquakes, 1900 to 1989, Bull. Seismol. Soc. Am., 82, 1306-1349.

Replumaz, A. 1999. Reconstruction de la zone de collision Inde-Asie - Etude centrée sur l'Indochine. Ph. D. Thèse, Université Paris 7-IPG, Paris.

Saw Htwe Zaw, 2006. Hazard Assessment in Multi-hazard Design, The symposium on “Tectonics, Seismotectonics, and Earthquake Hazard Mitigation and Management of Myanmar”, abstract.

Schwartz, D. & Coppersmith, K. 1984. Fault Behavior and Characteristic Earthquakes: Examples From the Wasatch and San Andreas Fault Zones, J. Geophys. Res. 89(B7), 5681-5698.

Sieh, K. 1996. The repetition of large-earthquake ruptures: Proceedings of the National Academy of Sciences 93 (9), 3764-3771.

Sieh, K. & Natawidjaja D. 2000. Neotectonics of the Sumatran fault, Indonesia: J. Geophys. Res 105, 28,295-28,326.

Socquet, A., Vigny, C., Chamot-Rooke, N., Simons, W., Rangin, C. & Ambrosius, B. 2006. India and Sunda plates motion and deformation along their boundary in Myanmar determined by GPS, J. Geophys. Res., 111, B05406, doi:10.1029/2005JB003877.

Sokolov, V. & Wald D.J. 2002. Instrumental Intensity Distribution for the Hector Mine, California, and the Chi-Chi, Taiwan, Earthquakes: Comparison of Two Methods, Bull. Seismol. Soc. Am, 92, 2145-2162.

Tapponnier, P., Peltzer, G., Le Dain, A.Y., Armijo, R. & Cobbold, P., 1982. Propagating extrusion tectonics in Asia: New insights from simple experiments with plasticine, Geology, 10, 611-616.

Thawbita. 1976. Chronology - Earthquakes of Burma, J. Burm. Res. Soc., 59.1-2, 97-99.

Tsutsumi, H. & Sato, T. 2009. Tectonic Geomorphology of the Southernmost Sagaing Fault and Surface Rupture Associated with the May 1930 Pegu (Bago) Earthquake, Myanmar, Bull. Seismol. Soc. Am., 99: 2155-2168.

U Kala. Maha-ya-zawin-gyi, 1961-ed,. Vol. 3, Hsaya U Kin So, Rangoon. in Burmese.

Vigny, C., Socquet, A., Rangin, C., Chamot-Rooke, N., Pubellier, M., Bouin, M.N., Bertrand, G. & Becker, M. 2003. Present-day crustal deformation around Sagaing fault, Myanmar, J. Geophys. Res., 108(B11), 2533, doi:10.1029/2002JB001999.

Wells, D.L. & Coppersmith, K.J. 1994. New empirical relationships among magnitude, rupture length, rupture width, rupture area, and surface displacement. Bull. Seismol. Soc. Am. 84, 974–1002.

Win Swe, 1970. Rift-features at the Sagaing-Tagaung ridge. 5th Burma Research Congress.

Win Swe, 2006. Earthquake hazard potentials in Myanmar: a science to public welfare outlook, The symposium on “Tectonics, Seismotectonics, and Earthquake Hazard Mitigation and Management of Myanmar”, abstract.

Wood, H.O. & Neumann F. 1931. Modified Mercalli intensity scale of 1931, Bull. Seismol. Soc. Am., 21, 277-283.

Yeats R.S. Sieh, K.E. & Allen, C.R. 1997. The Geology of Earthquakes, 568 pp. Oxford Press, New York.

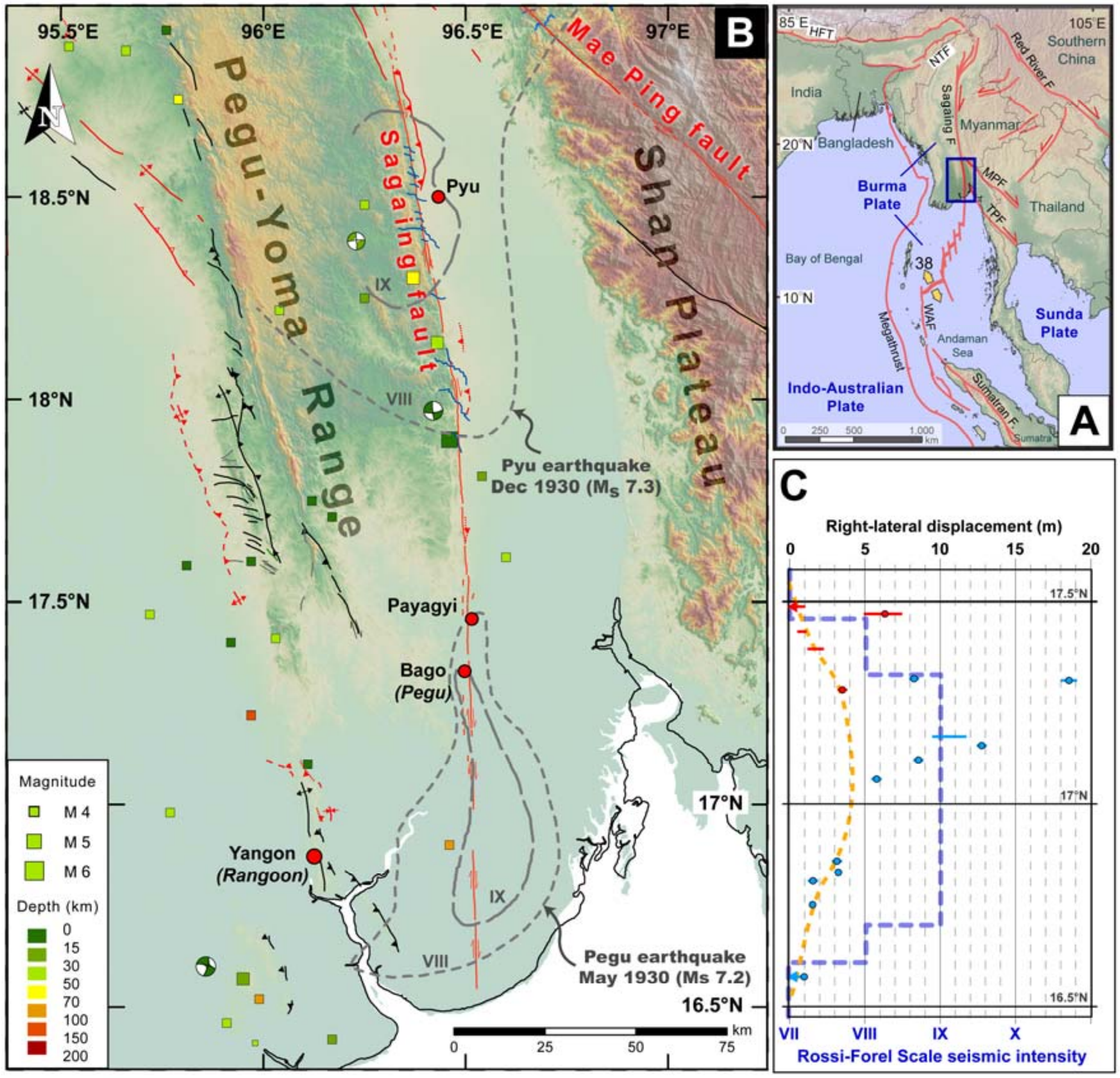

Figure 1. Active tectonic framework and recent earthquake history of south-central Myanmar (Burma).

(a) Myanmar is currently experiencing strain partitioning between the Indian and Sunda plates. In the west the Indian plate is colliding obliquely with the Burma plate along the northern extension of the Sunda megathrust (Socquet et. al., 2006). In the east, relative motion between the Burma and Sunda plates occurs along the 1200-km-long Sagaing fault. Farther south, this relative motion rifts the Andaman Sea Basin and bisects Sumatra along the 1900-km-long Sumatran fault (Sieh and Natawidjaja, 2000) and West Andaman fault (Berglar et al., 2010). Red lines represent major tectonic faults (after Tapponnier et al., 1982, Lacassin et al., 1997 and Lacassin et. al., 1998). Arrows indicate their sense of slip. Orange arrows show the rifting direction of the Andaman Sea spreading center; Spreading rate (mm/yr) is from Kamesh Raju et al. (2004). HFT = Himalayan Frontal Thrust; NTF = Naga thrust fault; MPF = Mae Ping fault; TPF = Three Pagodas fault. WAF = West Andaman fault. Blue box shows the map area of Fig.1(b).

(b) Active structures of south-central Myanmar. Active structures are red. Blue lines indicate large offset stream channels. Colored squares are background seismicity from the USGS/NEIC global earthquake catalog since 1973. Focal mechanisms are from the Global CMT Catalog since

1976. Grey dashed lines delimit high seismic intensities during the May 1930 Pegu earthquake and Dec 1930 Pyu earthquake (Brown et al., 1931; Brown and Leicester, 1933).

(c) Right-lateral displacements along the part of the southern Sagaing fault that bisects the high-intensity region of the May 1930 Pegu earthquake. Blue dots are measurements from Tsutsumi & Sato (2009). Red dots are our measurements. Horizontal bars show estimated uncertainty of each measurement. Yellow dashed line represents the inferred slip distribution during the May 1930 Pegu earthquake as judged from the smallest right-lateral displacements measured in the field. Blue dashed line, which indicates the distribution of seismic intensity of the Pegu earthquake (Brown et al., 1931), shows good correlation with the inferred coseismic slip distribution.

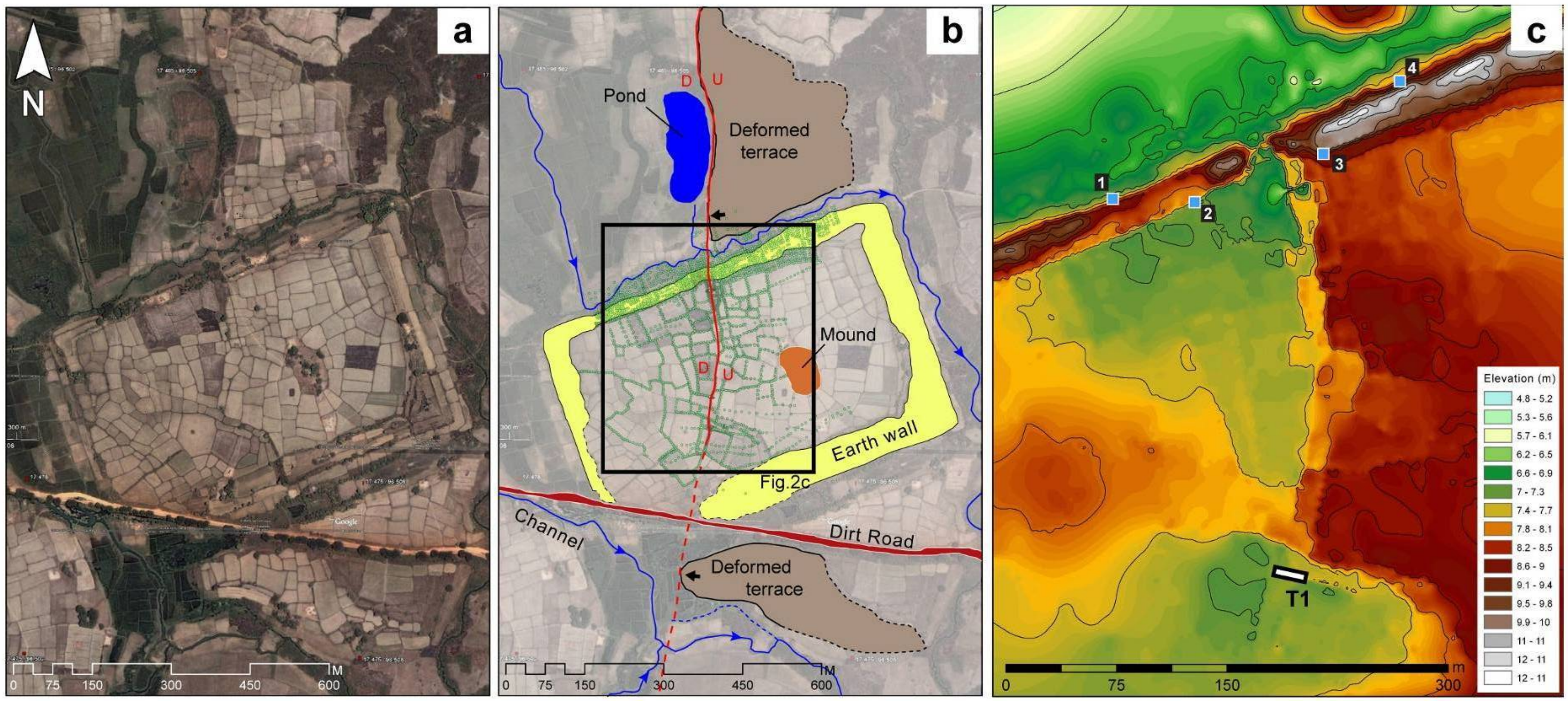

Figure 2. Landforms of the Payagyi ancient fortress, 16 km north of Bago. (a) Birds-eye view of the Payagyi ancient fortress from a Google Earth® image. The ancient fortress is at 17.480°N, 96.505°E and appears as a 650 m by 400 m rectangle amid rice paddies. (b) Geomorphologic interpretation from aerial photography and satellite imagery. Yellow depicts the fortress wall visible on the images. The vertical red line shows the trace of the Sagaing fault on the fluvial plain as revealed by field mapping and remote sensing. Black arrows indicate tectonic tilting of high terraces. Green dots are points surveyed by total station in spring 2009. The digital topography generated from the survey is in panel c. (c) Digital terrain model (DTM) of part of the Payagyi ancient fortress. Grid cell size is 50 cm. The trace of the Sagaing fault is clear as a west-facing topographic scarp cutting across the middle of the map. Blue squares show the locations of pits dug through the base of the earthen fortress wall. T1 is the trench we dug across the fault.

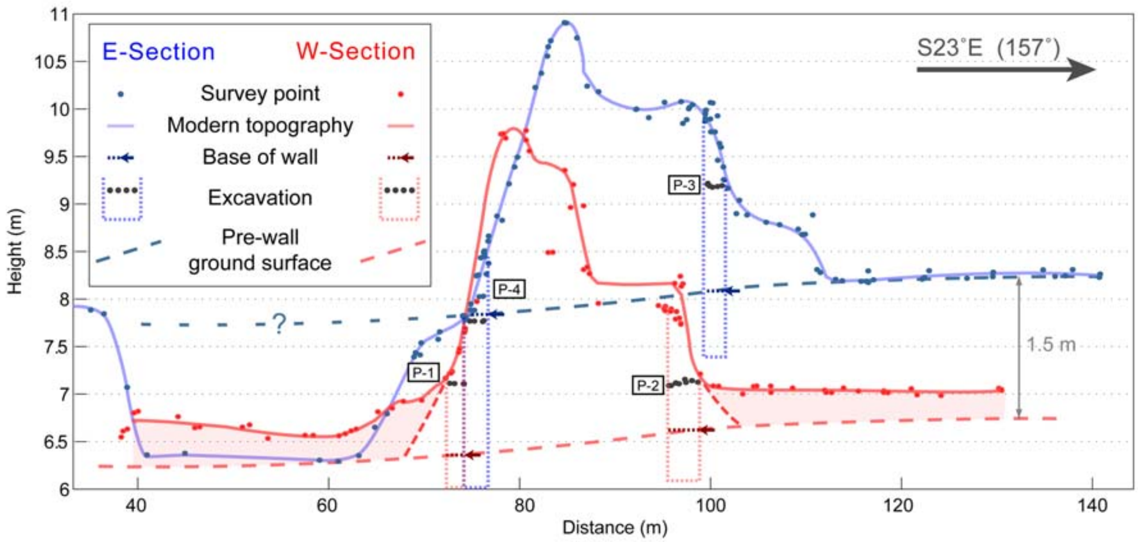

Figure 3. Survey profiles across the northern fortress wall. Blue points are east of the fault and red points are west of the fault (that is, the red points are on the viewers side of the fault and the blue points are on the opposite side). All survey points are projected onto a line oriented 157°, perpendicular to the wall. Blue and red lines indicate the modern shape of the fortress wall. P-1 through P-4 indicate the four pits in Figs. 2c and 4. Dotted polygons show the cross-section of each pit, perpendicular to the wall. Short dashed lines and arrows show the base of the fort wall revealed in the pits. Blue and red dashed lines illustrate the original topography on each side of the fault, prior to the construction of the fortress. The red shadows indicate the thickness of post-fortress sediment on the downthrown (west) of the fault.

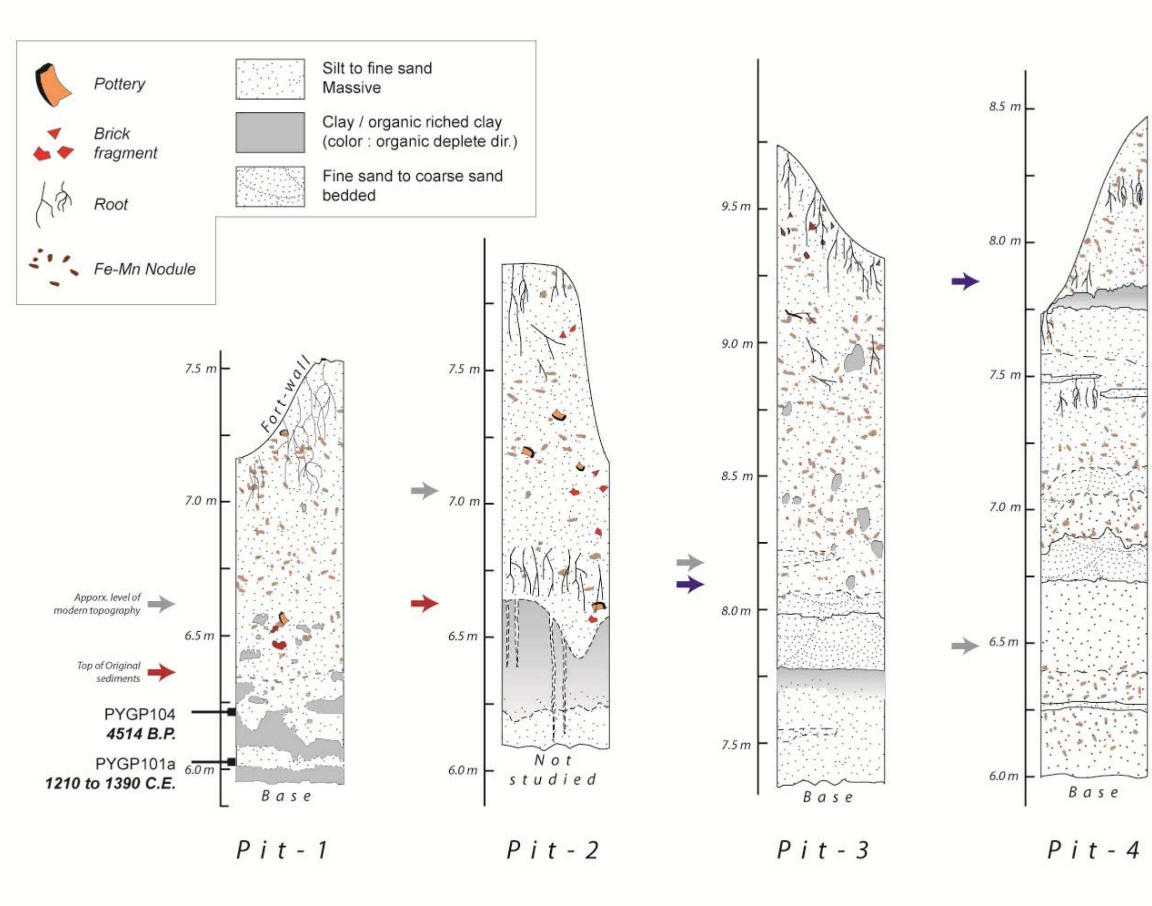

Figure 4. Stratigraphic columns of the four pits dug through the base of the fortress wall (Fig 3c). Blue and red arrows indicate the base of the fortress wall and ground surface prior to construction. Light-grey arrows show the projected elevation of modern topography from inside and outside of the fortress.

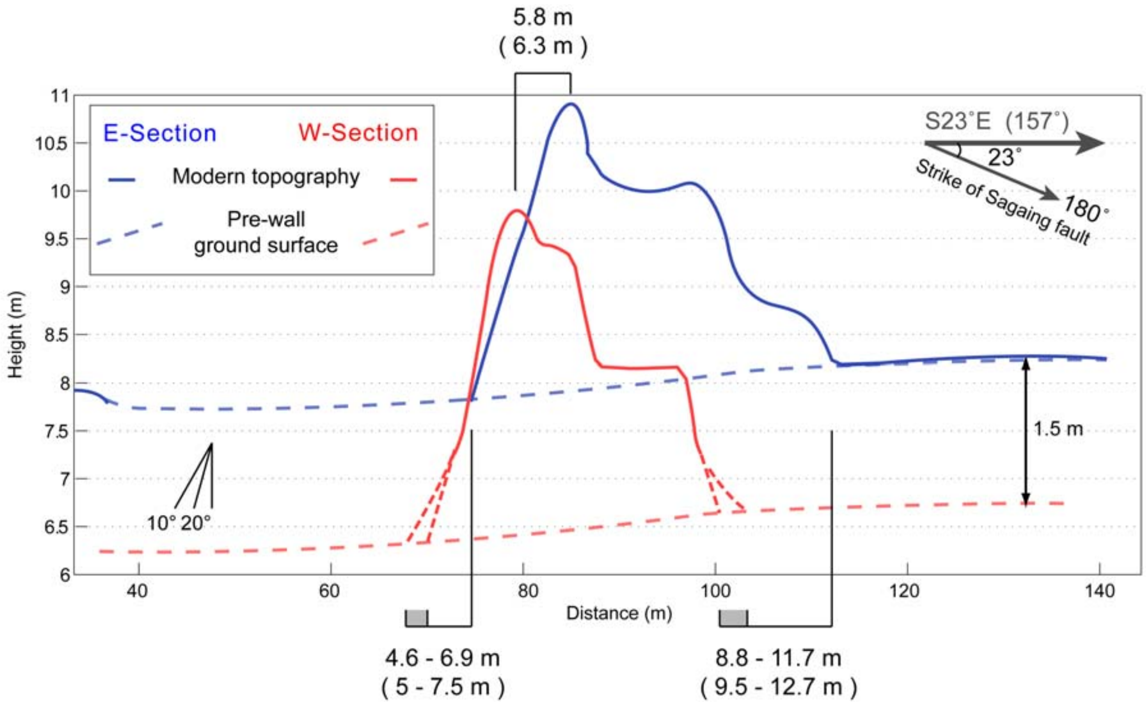

Figure 5. Fort-wall geometry after restoration by removal of post-fortress sedimentation and erosion. The red dashed line shows the inferred geometry of fortress wall west of the fault. The numbers not in parentheses are the horizontal separations perpendicular to the wall at the edges and the crest of the fortress wall. The numbers in parentheses are the fault offset, using a simple cosine correction that takes into account the difference in angle between the orientation of the profile (157°) and the strike of the fault (180°).

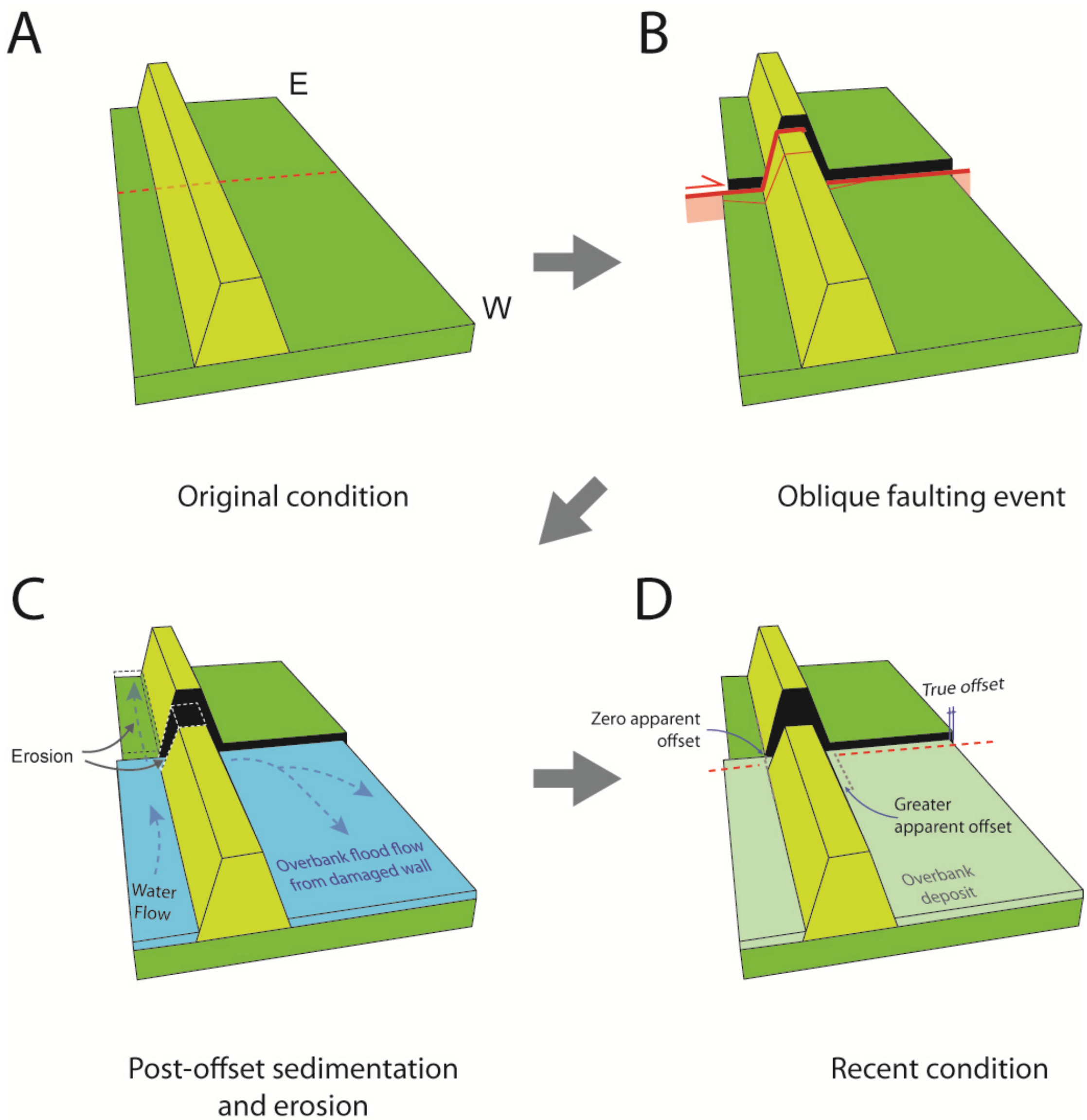

Figure 6. This schematic model shows the relationship of the Sagaing fault rupture to the sedimentation on the downthrown side near the northern fortress wall. See detail in Section 3.3.

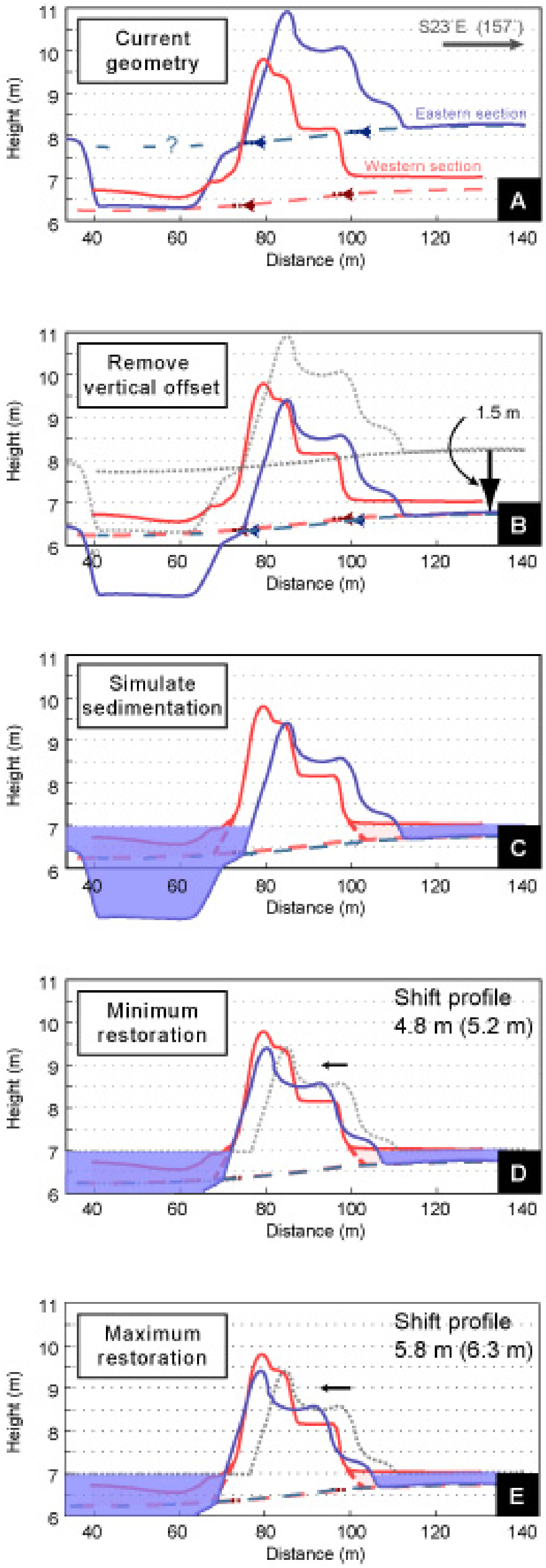

Figure 7. A sequential restoration of the fortress wall offset.

(A) The current relationship of the eastern (blue) and western (red) sections of the fortress walls, as viewed along the axis of the wall.

(B) Relationship after removal of the vertical offset from the eastern (distant) profile, as judged by the difference in elevation between the original, pre-fortress land surfaces. For reference, the grey-dashed line shows the original location of the eastern profile.

(C) Addition of sediment on top of the eastern section, to equal the amount of sediment that accumulated on the downthrown, western profile.

(D) Relationship after restoring the minimum right-lateral offset, 5.2 m.

(E) Relationship after restoring the maximum right-lateral offset, 6.3 m.

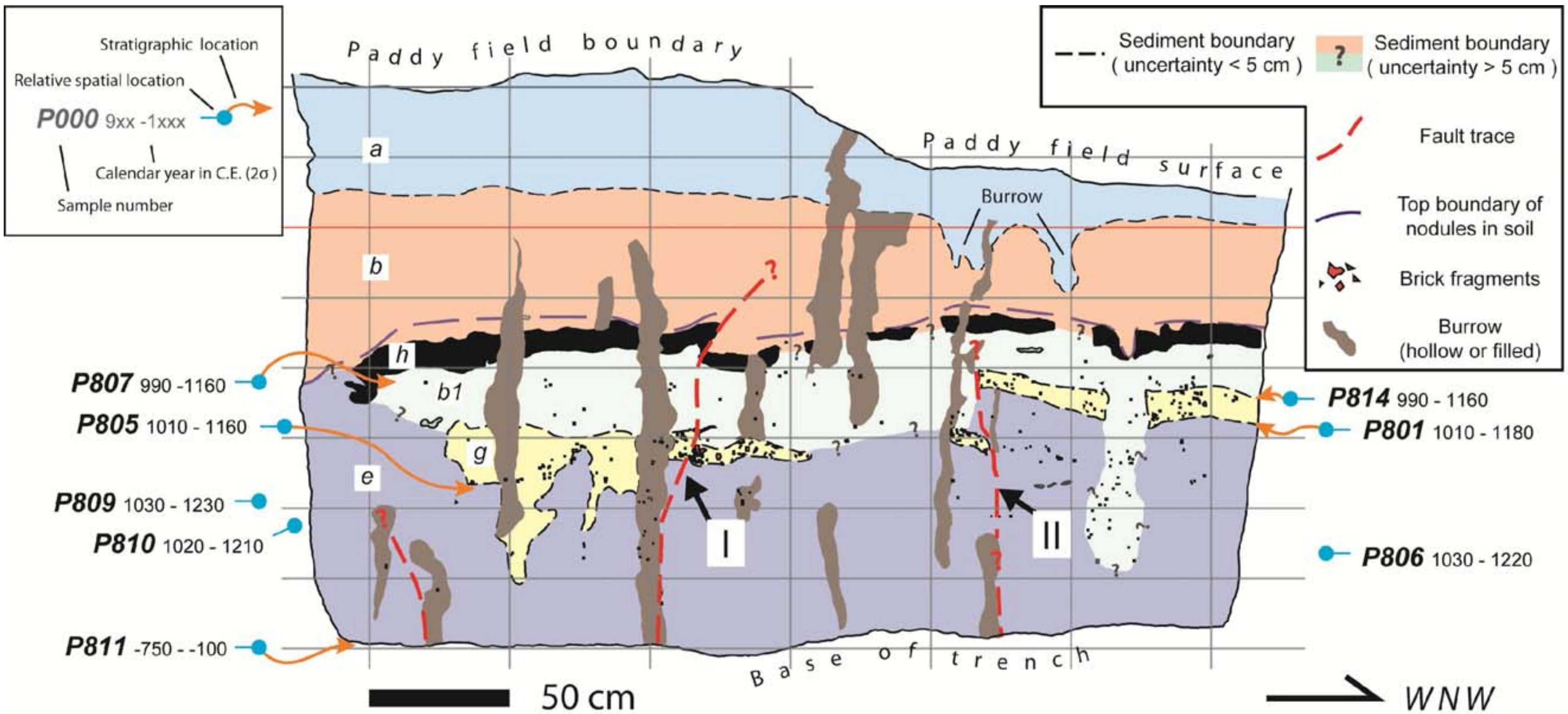

Figure 8. Map of the southern wall of Trench 1. Grid is 50 cm by 25 cm. I and II mark two possible fault traces, which appear to extend upward to two discrete horizons. Thus, they may reflect the occurrence of two distinct events, between the time of the abandonment of the ancient fortress and the 1930 Pegu earthquake. Blue dots show the stratigraphic location of radiocarbon samples. The 2-sigma range of the ages is in calendar years (CE).

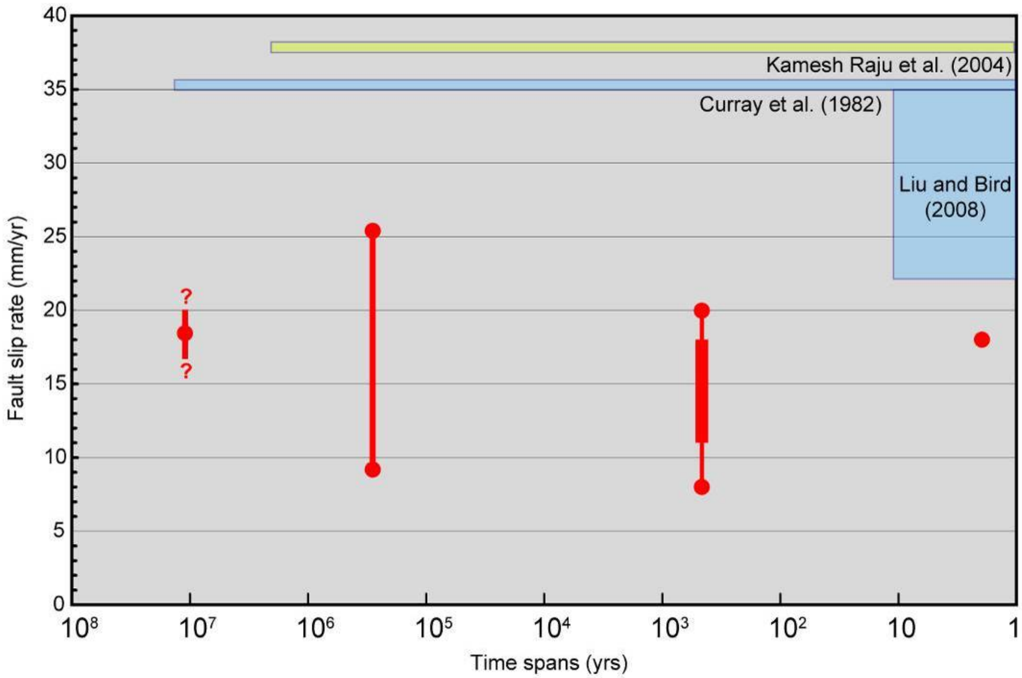

Figure 9. Slip-rate estimations along the Sagaing fault averaged over different time spans. Rates based upon models (green and blue) are greater than those based upon field observations (red). Red dots are the maxima and minima of different estimated slip rates, based on features offset by the central and southern Sagaing fault or on geodetic measurements made in 1998 and 2000. From left to right, the data sources are Myint Thein et al. (1991), Bertrand et al. (1998), this study and Vigny et al. (2003). For the fault slip rate from this study, the thick red line indicates the range of fault slip rate based upon construction of the ancient fortress between 1539 to 1599 C.E. Blue colored boxes show the slip rate predictions from a block-motion model and a general transform-fault model. Green box is the spreading rate at the Central Andaman sea spreading center (38mm/yr, Kamesh Paju et al., 2004). Slip rates based upon the block model are much greater than the slip rate of the Sagaing fault.

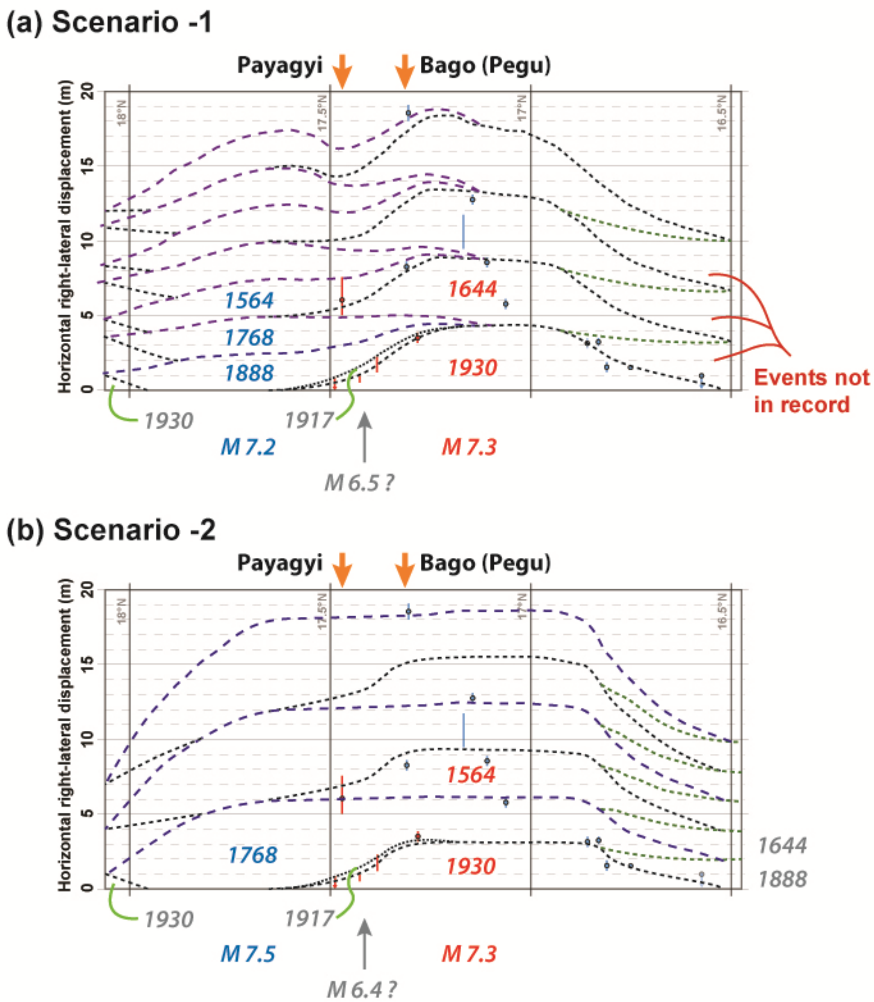

Figure 10. Two fault-slip scenarios for the southern Sagaing fault.
(A) A classic uniform-slip model. (B) Imperial-fault slip model. Field measurements (blue and red dots and vertical bars) are the same as in Fig.1c. Colored dashed lines denote different types of the fault rupture. Red and blue numbers suggest dates for each rupture, based upon the dates of earthquakes known from historical records.

Table 1. Analytical results of all of the samples dated in this research.

Radiocarbon age in the Payagyi ancient fortress

Location	Sample No.	Lab No.	Stratigraphic Unit	$\delta^{13}C$ (‰)	^{14}C age (BP)	+/- (BP)	Calendar year (2-Sigma)			Sample Type
							From (C.E.)	To (C.E.)	Probability	
Trench (T-1)	PYGP801	AA86448	g-e	-26	940	38	1010	1180	95.4%	Charcoal
	PYGP805	AA87349	e (top)	-28.4	965	36	1010	1160	95.4%	Charcoal
	PYGP806	AA86450	e	-27.3	898	38	1030	1220	95.4%	Charcoal
	PYGP807a	Beta-268175	h-b1	-27.8	980	40	990	1160	95.4%	Charcoal
	PYGP809	AA87347	e	-27.3	882	38	1030	1230	95.4%	Charcoal
	PYGP810	AA87346	e	-28	922	36	1020	1210	95.4%	Charcoal
	PYGP811	AA87348	e (bottom)	-25	2295	80	-750	-100	95.4%	Charcoal
	PYGP814	AA18449	b1-g	-26.2	969	38	990	1160	95.4%	Charcoal
Pit-1	PYGP104	AA86447	Sediment (-15cm)	-23.5	4514	76	-3500 -3400	-3450 -2900	2.5% 92.9%	Charcoal
	PYGP101a	Beta-268173	Sediment (-32cm)	-13.9	740	40	1210 1360	1300 1390	92.4% 3.0%	Organic sediment

The calendar year is converted by Oxcal 3.1, with Intcal'04 Calibration curve

Table 2. Earthquake and damage record from different source near Bago from 875 C.E. to May-1930 C.E.

Chhibber (1934) (Yangon & Bago)	Thawbita (1976) (Yangon & Bago)	Win Swe (2006) (Bago)	Milne (1911) (Yangon)	Saw Htwe Zaw (2006) (Yangon)
		1564		1564
		1570		
		1582	No record at India before 1618 C.E.	
	1588			
	1590			
				1608
No record before 1762 C.E.				1620
		1644		1644
				1649
				1652
				1661
				1664
				1679
	Jun-4-1757			
	Jun-12-1768 (Yangon)	1768		1768
		1830		
1864 (Yangon)				
1884 (Yangon)				
		Oct-8-1888	Oct-9-1888	1888
			Dec-13-1894	
		Mar-6-1913		
1917	Jul-5-1917	Jul-5-1917		
			Catalog ends in 1900 C.E.	1919
1927 (Yangon)	1927 (Yangon)			
1930	May-5-1930	May-5-1930		1930

Chapter 4

Permanent upper-plate deformation in western Myanmar during the great 1762 earthquake: Implications for neotectonic behavior of the northern Sunda megathrust

Originally published in Wang, Y., et al. (2013), Permanent upper plate deformation in western Myanmar during the great 1762 earthquake: Implications for neotectonic behavior of the northern Sunda megathrust, J. Geophys. Res. Solid Earth, 118, 1277–1303, doi:10.1002/jgrb.50121.

Abstract

The 1762 Arakan earthquake resulted from rupture of the northern Sunda megathrust, and is one of those rare pre-instrumental earthquakes for which early historical accounts document ground deformations. In order to obtain more comprehensive and detailed measurements of coseismic uplift, we conducted comprehensive field investigations and geochronological analyses of marine terraces on the two largest islands in western Myanmar. We confirm 3 to 4 m of coseismic coastal emergence along southwestern Cheduba Island, diminishing northeastward to less than 1 m. Farther northeast, uplift associated with the earthquake ranges from slightly more than 1 m to 5-6 m along the western coast of Ramree Island, but is insignificant along the island's eastern coast. This double-hump pattern of uplift coincides with the long-term anticlinal growth of these two islands. Thus, we propose the 1762 earthquake resulted from slip on splay faults under the islands, in addition to rupture of the megathrust. Elastic modeling implies fault slip during the 1762 earthquake ranges from about 9 to 16 m beneath the islands and corresponds to a magnitude of Mw 8.5 if the rupture length of the megathrust is ~500 km. The island's uplift histories suggest recurrence intervals of such events of about 500 to 700 years. Additional detailed

paleoseismological studies would add significant additional detail to the history of large earthquakes in this region.

Introduction

Co-seismic deformation above subduction megathrusts is a key to understanding great earthquake ruptures along convergent plate margins. Usually deformation patterns imply rupture solely on the underlying megathrust, as in the 2005 Nias and 2007 Solomon Islands earthquakes (e.g., Briggs et al., 2006; Konca et al., 2007; Taylor et al., 2008). Less commonly, upper-plate structures are also involved, as in the cases of the great 1964 Alaskan and 1946 Nankaido earthquakes (e.g., Plafker, 1965; Fukao, 1979; Kato, 1983; Park et al., 2000). Although they are smaller than their associated megathrusts, upper-plate structures may play significant roles in the generation of seismic shaking or tsunami, as appears to have been the case with the great 2004 Sumatran earthquake and tsunami (DeDontney and Rice, 2012). Structures in the forearc region may also be related to major asperities of large megathrust earthquakes (e.g., Sugiyama, 1994; Wells et al., 2003). 19th-century reports of coastal uplift during the great 1762 Arakan earthquake in western Myanmar are intriguing in this regard, because they imply that upper-plate structures played a role in the earthquake.

At about the same time that Darwin (1845) was documenting and publishing his famous observations of deformation associated with the great 1835 Chilean earthquake, British naval officers documented coastal emergence that may have occurred during the 1762 Arakan earthquake. Their observations suggested up to 7 meters of co-seismic uplift on Cheduba (Man-Aung) and neighboring Ramree Islands (Halsted, 1841; Mallet, 1878)(Fig. 1). They also described associated flights of marine terraces. These observations led them to speculate that these coastlines were being permanently uplifted during similar successive earthquakes (Halsted, 1841). The permanence of uplift implied by the flights of terraces does indeed suggest repeated inelastic deformation within the accretionary prism.

Though intriguing, the 19th-century observations are too sparse to enable one to conclude much about the nature of the faulting that caused the deformations or about the magnitude of the earthquake. One limitation is that most of the observations were made decades after the earthquake, so assignment of the observed deformations solely to the 1762 event is dubious. Another limitation of the historical observations is their small geographic spread. Most of the reliable observations are along the western side of Cheduba (Man-Aung) Island (Fig. 1b), with just a few other accounts from the west coast of Myanmar and Bangladesh.

This irregular and sparse distribution of observations and the uncertainty of the timing of uplift are inadequate for construction of a useful deformation pattern for the 1762 earthquake. Thus, we decided to reevaluate the 19th-century observations and to improve the quantity and quality of observations via a field investigation that included new geomorphic measurements and precise geochronological analyses of uplifted coastal features.

In the pages that follow, we describe our observations of the vertical deformation along the coasts of Ramree and Cheduba Islands associated with the 1762 event via measuring several different sea-level markers. U-Th dating techniques (Shen et al., 2003, 2012) on a multi-collector inductively coupled plasma mass spectrometer (MC-ICP-MS), Thermo Fisher Neptune, at the High-Precision Mass Spectrometry and Environment Change Laboratory (HISPEC), National Taiwan University, were used to determine the time of uplift of these features. Ages of several carbonate samples were also determined by radiocarbon dating technique. Moreover, we describe our mapping of regional geomorphic features, which provides the neotectonic context for understanding the dated uplifted features. We then discuss the possible sources and seismic parameters of the 1762 Arakan earthquake, including its earthquake magnitude and the recurrence interval.

Active tectonic context

The northern Sunda megathrust is the nominal boundary between the Indian and the Burma plates. In reality the boundary is not so simple, because thick sediments of the Bengal Fan sit atop the down-going Indian Ocean lithosphere, and much of this sedimentary section is being folded rather than subducted (Curray, 1991; Curray et al., 2003). These sediments sit at the boundary of two plates that are converging obliquely at about 23 mm/yr (Socquet et al., 2006) (Fig. 1b). Most of this dextral-oblique convergence appears to be taken up by the megathrust and structures above it in the accretionary prism.

In the vicinity of Cheduba and Ramree Islands, the Bengal Fan sediments are 8-12 km thick and exhibit a wide zone of folding and shortening above the down-going Indian Ocean lithosphere. Two active trench-parallel antiforms are readily apparent in the bathymetry and topography. Cheduba Island, 40 to 60 km northeast of the deformation front, is the subaerial expression of the western of these two; and Ramree Island, 70 to 100 km away from the trench, is the manifestation of the other (Fig. 1b). Both antiforms are doubly plunging and are asymmetric, as evidenced by their southwestern flanks being clearly steeper than their northeastern flanks. In each case, cumulative uplift appears to have been greater near their southwestern flanks, since their highest topography is closer to their southwestern flanks. Several studies have discussed the nature of these upper-plate structures. For example, Nielsen et al. (2004) documented the active folds and faults within the accretionary prism near the deformation front. Maurin and Rangin (2009) suggested that a northeast-dipping blind thrust fault 20 km west of Cheduba Island initiated after the late-Pliocene. Although there are no constraints on the rates of deformation, the existence of the antiforms strongly implies that a significant amount of Indian-Burma plate convergence is occurring within the accretionary wedge. Thus, the upper-plate structures are potential seismic sources in this area.

In this context, it is not surprising that abundant evidence for geologically recent uplift exists on and in the vicinity of Cheduba and Ramree Islands. Flights of marine terraces have long been known along western Myanmar coast. Brunnschweiler (1966) reported post-Pliocene marine terraces about 45-60 m above sea level along western Cheduba Island and 30 m high terraces along western Ramree Island. Than Tin Aung et al. (2008) described a series of marine terraces north of Ramree Island, the oldest of which is about ~3000 years old and 6-16 m above current mean sea level (MSL).

Several earlier observers suggested that the uplift occurred during seismic events: Halsted (1841) observed that the elevation difference between each marine terrace on western Cheduba Island is identical to the amount of the latest uplift there. Mallet's (1878) observations suggested to him that no changes occurred between Captain Halsted's observations and his own visit in the late 19th century. More recently, Shishikura et al. (2009) supported this view; they suggested that the elevation of the lowest terrace on western Cheduba Island is similar to the elevation recorded by Captain Halsted. This implies that no appreciable net vertical movement has occurred since the mid-19th century. Taken together, these observations imply that the majority of uplift occurs during or right after earthquakes and that recovery during the interseismic period is minimal. This deformation behavior thus provides us an excellent opportunity for studying the plausible co-seismic coastal uplift that occurred 250 years ago.

Sea-level indicators

To constrain land-level changes along the coasts of the islands precisely, one must measure the elevations of uplifted sea-level indicators relative to their modern equivalents. These indicators may be either marine organisms preserved in their living position or erosional and depositional features. Sea-level indicators form at a range of locations between high-water spring and low-water spring tides; therefore on a mesotidal coast as in western Myanmar, where mean tidal range is >2 m, these indicators form over a vertical range of about 3 m, as shown in Fig. 2.

The major types of sea-level indicators that we used comprise coastal erosional features (shoreline angles, sea notches and wave-cut platforms) and the living position of marine organisms (coral microatolls and oysters). Each of these has been extensively used elsewhere around the world to measure sea-level histories in a range of tidal environments (e.g., Chappell et al., 1983; Hull, 1987; ten Brink et al., 2006; Meltzner et al., 2010).

To estimate the relationship between the sea-level indicators and their associated water-levels, we first measure the modern indicators' elevations with respect to the water-level at the time of survey. We then relate this measured elevation to present MSL, using tidal predictions from the software package NLOADF (SPOTL v.3.2.4) (Agnew, 1997) and the regional harmonic tidal solutions for the Bay of Bengal from the Oregon State University (OSU) (http://volkov.oce.orst.edu/tides/BBay.html). This method is reliable for estimation of water-level in western Sumatra (e.g., Briggs et al., 2006; Meltzner et al., 2006, 2010).

Our survey results and other studies imply that most of the indicators we used reliably constrain paleo-water levels with precisions ranging from about ± 0.25 m to about ± 1 m (e.g., Chappell et al., 1983; ten Brink et al., 2006; Lewis et al., 2008). This is a considerable improvement in precision from just correlating the average terrace elevation to current MSL, which may have more than 2 m of uncertainty in this mesotidal environment.

Below, we describe the five major sea-level indicators that we use and their relationship to the tidal datum.

Biological indicators

Oysters

Emerged oysters have been widely used to constrain land-level changes (e.g., Davis et al., 2000; Awata et al., 2008; Lewis et al., 2008; Hsieh et al., 2009). Their upper growth limit is usually restricted below high-water level (e.g., Kelletat, 1988; Beaman et al., 1994; Lewis et al., 2008; Hsieh et al., 2009). On Ramree and Cheduba Islands, our surveys demonstrate that the upper growth limit of living oysters (e.g., Saccostrea spp.) occurs between mean higher high water (MHHW, ~1 m above MSL) and mean high water spring (MHWS, ~1.3 m above MSL). This upper growth limit is slightly higher than documented elsewhere (e.g., Kelletat, 1988; Beaman et al., 1994; Lewis et al., 2008).

In our area, living oysters commonly adhere to sandstone cliffs and isolated sandstone columns on wave-cut platforms. The vertical range of oyster growth overlaps with the zone of barnacle growth, but the highest barnacles are generally higher than the highest oysters, extending above MHWS. Because modern oysters in the littoral zone are easily collected by local fishermen, they rarely form prominent oyster encrustations, in stark contrast to older, fossil populations. Instead, they usually grow as individuals on rock surfaces. In locales not frequented by fishermen, we observed living oysters forming very dense belts beneath MHWS.

Coral microatolls and coral heads

In general, coral microatolls provide us with the most precise water-level indicators. Their upper growth limit develops between mean lower low water (MLLW) and mean low water spring (MLWS) in the mesotidal environment (Fig. 2). This is consistent with their being able to survive short periods of exposure above the sea during the lowest monthly tides. This relationship of the highest level of survival (HLS) of coral microatolls to low-tide levels has been used recently to document sea-level history (e.g., Chappell et al., 1983; Zachariasen et al., 1999; Natawidjaja et al., 2007; Kench et al., 2009; Meltzner et al., 2010).

Recent studies show that the relationship of HLS to low tides varies with tidal environments and coral species. In microtidal environments such as western Sumatra (maximum tidal range 0.8 to 1 m), HLS for massive species of the genus Porites is about 20 cm above extreme low water

(ELW) (Meltzner et al., 2010). For Goniastrea retiformis, HLS is about 10 cm higher there. In mesotidal environments (with 2-6 m tidal ranges) such as the Great Barrier Reef, the uppermost level of living corals approximates MLWS (e.g., Chappell et al., 1983; Hopley, 1986), which is approximately 70 cm higher than ELW.

Along coasts with tidal ranges similar to that of the western Myanmar coast (tidal range ~2 m) the HLS of microatolls is between MLLW and MLWS (Kayanne et al., 2007; Kench et al., 2009). This elevation is similar to HLS on the Great Barrier Reef. In addition, we observed that the HLS of living coral in a semi-confined tidal pool is not higher than MLLW on northern Ramree Island, whereas the HLS of microatolls in open water environments must be lower than MLLW. Thus, it is reasonable to suggest that the HLS of the microatolls of western Myanmar is at an elevation that is similar to the microatoll HLS in other mesotidal environments, and is not higher than the level of MLLW.

Although the uplifted microatolls are a precise water-level indicator, well-preserved microatolls are rarely found in our field area. In places where we did not find microatolls, we compare the elevation of the highest coral colony to the current MLLW. This yields a minimum water-level change since the growth of corals.

Erosional coastal features

Shoreline angles

The term “shoreline angle” refers to the locus of points that form the join between a wave-cut platform and a sea cliff. Uplifted shoreline angles are one of the most common coastal features in our field area and have been widely used in coastal geomorphic studies to reconstruct histories of sea-level change (e.g., Hull, 1987; ten Brink et al., 2006; Saillard et al., 2009). In macro- and mesotidal environments, field observations suggest they usually develop between MHWS and mean high water neap (MHWN) (Hull, 1987). In places where the tidal range is similar to our study area, modern shoreline angles develop in a more restricted position within this range, near the elevation of MHHW (ten Brink et al., 2006). Our field surveys confirm that shoreline angles usually form in our area near MHWS, about 20 cm above MHHW. In rare cases, though, we found that the shoreline angle has developed a bit higher, above MHWS, perhaps due to erosion by waves during storm surges.

Alluvial or talus deposits at the base of a sea cliff often obscure the shoreline angle. In such cases, the elevation of a shoreline angle would be overestimated unless it is dug out or exposed by erosion. Due to the very limited surveying time in the field, we did not try to dig the shoreline angle out while surveying the profiles. Instead, we extrapolated the terrace profile and the sea cliff slope to estimate the elevation of the shoreline angle to avoid the influence of later deposition.

The uncertainties in our measurements of shoreline angle elevations are likely greater than our measurements of biological sea-level indicators, due to both the obscuration by sediments on the wave-cut platform and the variability of the strength of storm surges. To account for these uncertainties and variability, we assumed our shoreline angle measurements represent MHWS + 1 m in our study area.

Sea notches

We found two types of wave-cut notches: tidal notches and surf notches. Each of these is distinguished by its particular shape. Tidal notches are U- or V-shaped indentations that develop on cliffs or steep slopes in hard rock. They result from wave action as the tides bring the sea surface through the intertidal range. The deepest part of the indentation occurs at the level of mean sea level (MSL) (Pirazzoli, 1986). In our area, tidal notches are most commonly cut into sandstone cliffs. They commonly have a gentle U shape, with the opening 1 to 2 m wide from the base of the U. Oysters and other marine organisms commonly grow within the notches.

Surf notches exhibit far less erosional height than tidal notches in our study area. We commonly found modern surf notches at active shoreline angles and on sandstone platforms near MHWS, well above the tidal notches. These notches often form above the high tide where the cliff is regularly washed by waves (Pirazzoli, 1986). Thus, unlike the tidal notches, their heights are related to the energy of the surf, rather than to the tidal range.

The accuracy with which marine notches reflect sea level varies, depending on the tidal range, the geomorphology of the site, and the slope of the bedrock (Pirazzoli, 1986). For example, along one short stretch of coast we found that the elevation of a modern tidal notch on a sandstone ridge facing the open ocean is nearly 1 m lower than that on another part of the same ridge, but at the top of a sandy beach. This elevation difference is very likely the result of differing wave run-ups in these two different settings during tidal surges. Therefore, we suggest the elevation of marine notches are uncertain by ± 1 m in our study area.

Wave-cut platforms

Although modern and uplifted wave-cut platforms are the most common features along the coasts of Cheduba and Ramree Islands, they are not a precise sea-level indicator in our study area. Wave-cut platforms generally develop within the intertidal zone and commonly extend below it, where bedrock can be eroded by wave action (Trenhaile and Layzell, 1981). Along mesotidal coasts, the elevation of the platform may ramp 3-4 m from below low tide to high tide. Thus a direct comparison of the elevation difference between a point on an uplifted platform and a point on the modern platform is not very useful in constraining uplift or subsidence. Since wave-cut platforms commonly develop between MHWS and MLWS, we suggest their elevations generally indicates MSL ± half of the tidal range. This great uncertainty makes wave-cut platforms the worst sea-level indicators in our study area. However, in places where no other indicator is available, and we were able to confirm the sediments are thin on the uplifted platform (i.e., <1 m), we estimated a minimal land-level change by measuring the elevation difference between the modern shoreline angle and an uplifted wave-cut platform.

Coastal emergence

Ramree Island

Ramree Island lies ~70 km east of the deformation front and is elongate parallel to the strike of the megathrust. This 80-km long, 20-km wide island is connected to the mainland of Myanmar by a marsh that is slightly higher than the intertidal zone (Fig. 1b).

Our field observations on the island were limited by the availability of access roads. A semi-paved road along the northern half of the island's western coast provides good access to its northwestern coastline, but the marshy northeastern part of the island is difficult to reach by car. Farther south, overland access is even more limited by the lack of roads. Therefore, we relied on chartered boats to sail to some larger towns on southeastern Ramree. Access to smaller villages along the southwestern coast was by foot. In places where chartered boats were unable to get close to shore, our observations were limited to views from offshore. These logistical difficulties significantly limited our ability to perform detailed, high-precision surveys along the southern coasts of Ramree Island.

Northern Ramree Island (Kyauk-Pyu area)

Ancient sea-level indicators reveal that changes in land level differ greatly between northwestern and northeastern Ramree Island. Evidence for progressive uplift is abundantly clear in the former and absent in the latter. About 3 km west of Kyauk-Pyu (Fig. 3), the largest city of the island, we found a series of uplifted tidal notches and bands of uplifted oysters on a sandstone ridge below the surface of the lowest marine terrace, T1 (KPU-15 in Fig. 3 and 4). These stacked ancient coastal features indicate successive uplift events during the Holocene period.

The lowest uplifted tidal notch is ~1.5 m above the modern notch. A layer of dead oysters encrusts the sandstone cliff slightly above the uplifted tidal notch, and is ~1 m above the top of the band of modern oysters (Fig. 4). A radiocarbon date from the dead oysters (assuming the global average marine reservoir correction) suggests this oyster reef grew between 1417 and 1618 C.E. (Fig. 4 and Table 1). This date is suspect because the local marine reservoir correction (Delta-R) is unknown. Nonetheless, this date is similar to other radiocarbon ages of uplifted corals and oysters north of Ramree Island (Than Tin Aung et al., 2008). Therefore, we believe the uplifted oyster layer (KPU-15), together with the lowest uplifted tidal notch, were elevated during a regional tectonic event. The fact that the radiocarbon age is a century or two earlier than the great 1762 Arakan earthquake encourages the speculation that it was during this earthquake that this lowest notch and its associated oysters rose out of the intertidal zone.

To the east, the magnitude of late-Holocene emergence is much smaller. Fossil mid-Holocene coral microatolls south of Kyauk-Pyu rest upon the T1 surface, which is only slightly above the current MHWS (Fig. 3). These microatolls are present from the terrace surface to the modern tidal flat, and the elevations of their upper surfaces are 1 to 1.5 m above MSL, or 2 to 2.5 m above the current MLLW. U-Th analyses show the ages of these corals range from 5000 to 7100 years B.P. (Table 2, KPU-102 to KPU-110). Both the ages and the elevations of these corals are consistent with the timing and water-level of the mid-Holocene high stand of the eastern Indian Ocean (Woodroffe and Horton, 2005; Briggs et al., 2008). Thus, these corals suggest negligible net uplift of northeastern Ramree Island since the middle of the Holocene epoch.

The broad morphology of Ramree Island reflects a northeastward tilt that is wholly consistent with the contrast in uplift between these two sites. A single, large, low terrace (T1) and a plexus of estuaries and tidal channels dominate the surface of the northeastern part of the island (Fig. 3). In great contrast to this, flights of marine terraces dominate the geomorphology of the southwestern coast of the island. This contrast implies northeastward tilt of the island, with significant net uplift of the southwestern coast tapering northeastward to zero.

Central Ramree Island

Uplifted corals and other sea-level indicators demonstrate that the central western coast of Ramree Island rose several meters during the last emergence event, much more than that on the northwestern tip of the island. In situ fossil coral heads (ZC-16, ZC-118, and ZC-119) rest on a T1 surface that is ~3.5 m above MSL (Fig. 5 and 6a). The fact that the highest upper surface of these corals is about 5 m above the current MLLW implies that they are now about 5 m above the modern highest level of coral growth. Farther inland are fossil oysters in growth position on bedrock of T1 that are about 5 m above their modern growth position (~MHHW; Fig. 6a). These two sea-level indicators demonstrate the land-level change since just before the last event is about 5 m along the central western coast.

Samples from within the coral heads yielded very precise U-Th ages. All three heads were living in the middle decades of the 18th century (Table 2). Among these U-Th dates, the age of ZC-16 provides us the best timing constraint of the uplift event. There are 4 annual bands between the dated annual band and the outermost band, which represents the date of death of the coral. Thus the coral appears to have died in 1762 ± 11 C.E., a perfect match for the 1762 earthquake. Although the growth bands are not as clear as the ZC-16 sample, the U-Th ages from the other two samples (ZC-118 and ZC-119) collected from the band further inside the colonies also yield a date of death very close to 1762 C.E. (Table 2). This also implies that the T1 wave-cut platform on the central western coast formed long before 1762, then supported coral growth through the decades before the uplift in 1762.

This extraordinary amount of land-level change along central western section of Ramree

Island attracted attention as early as the mid-19th century. This is where Mallet (1878) observed a "raised beach about 20 feet above the sea" during his survey in 1877. Following the description and the map in his report, we were able to survey the same section of the coast between the villages of Kyauk-Ka-Le (Kyauk-Gale) and Kon-Baung-Gyi (Kon-Baung; Fig. 5). We found the surface of T-1 there is 5.5 m above the current shoreline angle, with a very thin sedimentary cover (Fig. 6b). Although this is our highest measurement along this section of the coast, it is slightly lower than Mallet's observation in 1877. The 17th-century age of a coral fragment (ZC-04) within the thin sediments is consistent with the terrace being an active wave-cut platform a century or so before the uplift in 1762 (Fig. 6b; Table 2).

Geomorphological evidence of a progressive northeastward tilt is even clearer for central Ramree Island than it is for the northern sector of the island. Along most of this section of coast, 2 to 3 major terrace treads along the southwestern coast contrast with only one major terrace in the northeast (Fig. 5). Moreover, the highest terraces of the southwestern foothills show clear northeastward tilting of their surface in stereoscopic aerial photos. This eastward tilt is also consistent with the predominance of northeastward-flowing drainage networks over much smaller creeks flowing to the southwestern coast, similar to what have been observed on Makira (San Cristobal) Island, the Solomon Islands (Chen et al., 2011). The northeastward tilt of both the northern and central sectors of Ramree Island and the increase in uplift from the northern to the central western coast indicate the tilting results from the growth of the doubly plunging anticline that has raised the island (Fig. 1).

Southern Ramree Island

Geomorphic evidence for young land-level changes at the southern tip of the southwestern Ramree coast is also very clear, although the timing of the last uplift event is not as well constrained. A flight of marine terraces between the current shoreline and the western foothills indicates progressive uplift near the small village of Tet-Kaw (Fig. 7). The amount of the last emergence is well constrained by the elevation of T1's shoreline angle, which is about 1.4 to 2 m above its modern analogue at MHWS. The elevation of a group of small surf notches on a sandstone ridge is similar to that of the shoreline angle (Fig. 8b and 8c). These features suggest a smaller uplift, only 1.4 to 2 m from the current MHWS.

A lack of datable in situ materials associated with the T1 surface precluded determination of a date for the most recent uplift in this area. Agricultural activities appear to have removed most of the fossil corals and oysters from the terrace. Nonetheless, several loose coral blocks within the thin sediment cap of T1 provide some constraint. These coral blocks are 10 to 30 cm in diameter, significantly bigger than regular beach gravels (<5 cm) within the modern storm deposits. Thus it is unlikely that they were transported by normal storms or cyclones up onto the T1 surface after its emergence. Moreover, because we did not find any evidence of tsunami deposits along the coast, we believe these corals blocks are not tsunami deposits, but were deposited when the T1 surface was still the active wave-cut platform. Thus, the youngest age of these coral blocks may represent the maximum age of the formation of T1.

The U-Th ages of these coral blocks range from early mid-Holocene to the 16th century (Table 2, TK-130 to TK-132). The youngest U-Th age (1495-1564 C.E.) provides a maximum limiting age for wave action on T1. Providing we are correct in deducing that this block is not a tsunami block, this age implies emergence of the T1 surface after the 16th century. We propose that the 1.4 to 2.0 m obtained from the sea-level indicators of T1 represents net uplift during and subsequent to 1762 here.

The geomorphological contrast between the east- and west-facing coasts of the southern Ramree Island is like the contrast of the northern and central coasts. A flat, low T1 terrace dominates the southeastern part of the island, but its eastward tilt is not as prominent as it is across the northwestern and central sectors of the island (Fig. 7). The shoreline angle of T1 near the village of Kyauk-Ni-Maw suggests its corresponding MHWS is ~4 m higher than current MHWS. We found no in situ biological sea-level indicators on the T1 surface, but we did find a group of small coral heads within the T1 terrace deposits that provide a plausible age for T1 (e.g., KYM-125 in Fig. 7). Most of these heads are ~60 cm in diameter. The three U-Th ages obtained from two of the corals are consistent and suggest that the terrace formed sometime after 7300 to 7000 years B.P. (Table 2, KYM-125a/b and KYM-127). Although these corals are slightly older than the mid-Holocene ones on northeastern Ramree Island, their ages are still close to the timing of the mid-Holocene high stand in this region (Woodroffe and Horton, 2005). Thus, the only plausible interpretation is that T1 near Kyauk-Ni-Maw formed during the mid-Holocene high stand. The lack of other uplifted features between the mid-Holocene terrace (T1) and the modern coast suggests the land-level change must be very small since the mid-Holocene, less than ~4 m over the past 7,000 years if we assumed the sea level has been stable through the mid-Holocene to present.

Eastern Ramree Island

In the lowlands of eastern Ramree Island, we found no good evidence for any young uplift event. Sea-level indicators, where present, are barely higher than the current high-tide level. Both remote and field investigations revealed only one coastal plain surface between the modern shoreline and the foothills of eastern Ramree Island. Sandstone platforms and surf notches emerge above the water during low tides, but their elevations are not significantly higher than high-tide levels.

We found one site with sea notches and associated shoreline angles higher than the modern high-tide level (Fig. 1 and 9). This site is at the end of a sandstone ridge and exhibits one sea notch and one shoreline angle, at elevations ~4 m and ~2 m above the current MSL respectively. Since this site is very difficult to access, we were not able to determine the elevation of the notches accurately, nor did we find any datable materials at this site to constrain their ages. However, because the ~4 m elevation of the higher sea notch above MSL is almost identical to the elevation of T1's shoreline angle near Kyauk-Ni-Maw, we speculate this higher notch also formed during the mid-Holocene high stand and that the net uplift since the mid-Holocene is very similar in these two places.

A lower surf notch and the associated shoreline angle ~0.7 m above MHWS may represent slight uplift, but these could also be active, modern features, given our uncertainty in high water spring level here. When we visited this site during low tide, we noticed that the recent high water mark was slightly higher than this lower shoreline angle, which suggests the water can reach the lower shoreline angle at least during the very high-water period. Moreover, we did not find any other shoreline angle lower than this that may represent the modern shoreline angle. Judging from both lack of promising active shoreline angles matching to the elevation of MHWS, and the uncertainty of the shoreline angle's elevation (MHWS to MHWS + 1m), we therefore suggest the amount of land-level change here from the last event is smaller than the uncertainty of the sea level indicator, i.e., less than 1 m.

Summary of Ramree Island

In summary, all of the features that indicate young uplift of Ramree Island are along the western coast. There is clear evidence that the last big uplift occurred during the 1762 earthquake and that the greatest amount of uplift was at least ~5.5 m along the central-western Ramree coast. The amount of uplift diminished northwestward and southeastward to only 1 to 2 m. We found no significant uplift associated with the 1762 earthquake along the northeastern coast of Ramree Island. Moreover, even mid-Holocene features are no more than ~4 m above their modern analogues. Because sea level in the mid-Holocene was likely a few meters higher than modern sea level, this likely indicates that uplift of the northeastern coastlines has been no more than a meter or so in the past 7 millennia. The elevation of these mid-Holocene features also implies that the swampy northeastern coast has not been subsiding over the past several thousand years.

Cheduba Island

Between Ramree Island and the deformation front is Cheduba (Man-Aung) Island (Fig. 1b). Its greater proximity to the deformation front (35 to 60 km) implies that it would experience greater uplift during a conventional megathrust earthquake. The longest dimension of Cheduba Island is ~30 km, but this is merely the exposed part of a ~140-km long doubly plunging submarine ridge that strikes parallel to the deformation front. The topography of the island and the submarine ridge is highly asymmetrical, with the southwestern flank being significantly higher, steeper, and more rugged than the northeastern flank (Fig. 1b).

Unlike Ramree Island, a semi-paved road encircles the entire Cheduba Island, providing good access to its coasts. We surveyed five representative coastal sections around the island during our short visit.

In general, our surveys confirmed Captain Halsted's early 19th-century observations that large uplifts occurred along the western coast of Cheduba in 1762 (Halsted, 1841). We also surveyed land-level changes along the island's eastern coast, where fewer previous terrace observations exist (e.g., Brunnschweiler, 1966). Broadly speaking, our observations show that all of Cheduba Island rose during the last major uplift event, up to ~4 m along its western coast and ~1 m along its eastern coast.

Northwestern Cheduba Island (Ka-Ma village)

Figure 10 shows the distribution of marine terraces near the village of Ka-Ma, along the northern southwestern coast of Cheduba Island. Here, we were able to map more than five terrace treads between the foothills and the current coastline, as reported previously by Brunnschweiler

(1966) and Shishikura et al. (2009). These terraces are mainly uplifted wave-cut platforms, cut into mélange or highly deformed sandstone and shale. A ~1-m thick bed of reef fragments, including clastic debris and in situ corals mantles the bedrock platform of the lowest terrace (T1). Microatolls and corals with flat erosional surface on top (pseudo-microatolls) are present along the seaward edge of the T1 surface. Some of these emerged coral fossils have fallen to the current wave-cut platform during the erosional retreat of the modern sea cliff. Most of these fallen blocks appear along the current high-tide mark below the sea cliff.

The elevation of T1 is about 3 to 4 m above MSL, but southwest of Ka-Ma, we can separate it into two sub-terraces (T1 and T1a) based on non-stereoscopic satellite images. Field measurements show that the lower terrace, T1a, is ~0.6 m lower than T1 (Fig. 10b).

The coral morphology and their U-Th ages reveal a complicated coral emplacement history of the lowest terraces (T1 and T1a). Coral colonies exist all over T1 from its seaward side to near its shoreline angle. Close to the terrace riser between T1 and T2, field measurements show the elevation of a group of rounded corals is significantly higher than the elevation of microatolls along T1's seaward side (Fig. 10). Although some of these rounded heads seem to retain their normal position, others are highly eroded. This situation is very similar to that at the current coastline where we found the fallen coral heads from the T1a terrace to the present wave-cut platform. Therefore, we suggest these high and rounded heads were dropped onto T1 while T1 was the active shore platform.

Sample KM-143, from a massive coral block, yielded a very old age for one of these high coral heads, around 449-477 C.E. (Table 2). This age for one of the fallen blocks gives an age that predates the cutting of T1.

Another coral sample from a microatoll on the lower T1a surface constrains the maximum age of the last-uplift event near the Ka-Ma village. Along the modern sea cliff, we found another group of microatolls on the surface of T1a, separated from T1 by a ~0.6 m high terrace riser (Fig. 10b). These microatolls are slightly eroded and tilted and are close to the shoreline angle of T1a. Due to our very limited time in the field, we did not dig these microatolls out to confirm if they are in situ or displaced. But we speculate that they were dropped from the original T1 surface to the lower T1a during the landward erosional advance of T1a's shoreline angle. This interpretation is consistent with their slightly eroded nature, their tilt, and their location on T1a, very near the uplifted T1 terrace riser.

The other hypothesis is that those microatolls grew on the higher part of the platform while the platform was submerged by interseismic subsidence. However, if this were the case, the shoreline angle itself would have also been modified due to the easily eroded nature of the soft mélange bedrock materials. Such evidence does not appear along this small terrace riser between T1 and T1a. Thus, these microatolls predate the emergence of T1a.

The U-Th age of sample KM-144 from one of these microatolls suggests the emergence of T1a occurred no earlier than 1409-1445 C.E. (Table 2). This age allows the speculation that T1a emerged during the 1762 earthquake.

The amount of land-level change from 1762 to now, however, is not well constrained at this location. The top of the microatolls (e.g., KM-144) that is very close to the T1a shoreline angle suggests at least 4.2 m emergence from the mid-15th century to now. On the other hand, the shoreline angle of T1a itself is only ~2.2 m above the current MHWS at the same location. These led us to suggest the emergence from 1762 to now must be between 4.2 to 2.2 m at this location, where the mid-19th century account from Captain Halsted suggests about 4.5 m (16 feet) uplift (Halsted, 1841).

Southwestern Cheduba Island (Ka-I area)

The coral microatolls near the village of Ka-I provide the best constraints on land-level change during the 1762 earthquake along the southwestern coast of Cheduba Island. In this area, we were able to identify ~4 major terrace treads from non-stereoscopic satellite imagery (Fig. 11). The lowest terrace, T1, is about 2 to 4 m above MSL. Uplifted coral colonies, especially coral microatolls, are abundant on the lower portion of the T1 surface. The tops of these microatolls are ~3.4 m above current MLLW. This difference represents the minimum uplift during and subsequent to the most recent large event. This number is very close to the ~3.6-m value reported from the southern end of Cheduba Island by Halsted (1841).

Among these uplifted coral microatolls, we collected one sample (KI-152) from a giant (~4 m in diameter) microatoll for U-Th dating. The sampled annual band is few centimeters from the microatoll's non-eroded perimeter. Its U-Th age indicates that the coral died sometime between 1724 and 1832 C.E., a period that includes the date of the 1762 earthquake (Table 2).

Around the giant microatoll (KI-152), we found several smaller coral microatolls whose upper surfaces display evidence for slowly rising sea level during their growth. This "up-grown morphology" of Hopley (1986) or the "cup-microatoll" morphology of Zachariasen et al. (2000) is common above the Sunda megathrust in Sumatra, where the forearc islands slowly submerge during the interseismic period and then rapidly uplift during giant earthquakes (e.g., Natawidjaja et al., 2007).

In order to constrain long-term uplift rates in this area, we also collected several U-Th samples from corals at higher elevations (Fig. 11). The highest coral sample (KI-156) is from a coral on the surface of T3, 11.4 m above current MLLW. U-Th analysis yielded an age of about 2100 years B.P. (Table 2). A sample (KI-155) from a coral microatoll on T2 (8.5 m above MLLW) yielded an age of about 2600 years B.P. Another coral microatoll near T1's shoreline angle (4.5 m above MLLW) yielded a U-Th age of 913-955 C.E. Although one of these dates is out of sequence, taken together they suggest a late-Holocene average uplift rate of about 3-5 mm/yr.

Eastern Cheduba Island (Kan-Daing-Ok area)

The magnitude of the most recent large uplift event decreases significantly from the southwestern to the northeastern side of Cheduba Island. This is evident in terrace elevations. Along the southeastern coast, the seaward edge of T5 coincides with the 15-m contour extracted from SRTM data (Fig. 12). However, along the southwestern coast, the seaward edge of T4, rather than T5, follows the 15 m contour line (Fig. 10 and 11).

Along the southeastern coast, we surveyed two separate profiles to constrain recent land-level changes (Fig. 12). Near the northern profile, modern erosion of the coastline exposes the stratigraphy beneath both T1 and T2. In each case, sediment mantling the wave-cut platform is less than 30 cm. Therefore, the topographic profile here approximates the shape and elevation of these wave-cut platforms. Here, the topographic profile shows the shoreline angle of T1 is ~1.1 m above the current MHWS (Fig. 13a). Oyster and barnacle encrustations are abundant on in situ sandstone blocks near the elevation of the shoreline angle of T2 (~8.5 m above MSL). These encrustations and T2's shoreline angle emerged during an event prior to the uplift of T1. Radiocarbon analyses of these fossils suggest an age for T2 that ranges from the mid-15th to the late-17th century (Table 1, KK-145 to KK-148). Since the emergence of the T2 surface must be earlier than the formation of T1, the emergence of T1 occurred after the 15th century. Thus, we believe T1 at this location rose out of the water during the 1762 earthquake and is contemporaneous with the youngest terraces on the southwestern coast of the island.

Three kilometers farther south along the coast, we constructed another topographic profile just south of the village of Kan-Daing-Ok (Fig. 13b). Our analysis of non-stereoscopic satellite imagery suggests that all of T1 has been eroded away there. Along the modern shoreline, we found a group of highly eroded, massive and displaced coral heads, the upper surfaces of which are at elevations near current MHHW, similar to the situation south of the Ka-Ma village. We believe these corals grew near the seaward edge of a raised terrace (T2 or T1), and tumbled into the modern intertidal zone during the erosion of the modern sea cliff into the higher terrace. Even though the elevations of these corals can no longer be used to constrain the amount of uplift since they died, their ages may still help us constrain the timing of the most recent large uplift event.

We collected a sample from one of these corals (SC-150) and another from the highest coral head that rests on the T2 surface (SC-151) for U-Th analysis. The fallen coral on the modern platform grew around 1355-1368 C.E., but the coral on the T2 surface was growing in the period between 651 and 680 C.E. (Table 2). Both of these samples antedate the 1762 earthquake, so any uplift associated with the 1762 earthquake must be smaller than the elevation of SC-151, i.e., less than 5 m.

In fact, if the lower coral were displaced from the eroded surface of T2, the amount of emergence would be much less than 5 m. We analyzed the relationship between elevations of T2's shoreline angle and the coral heads. The higher coral's elevation (~4 m above modern MSL) is very close to the altitude of T2's shoreline angle (~4.5 m above MSL according to Shishikura et al. (2009)). This elevation difference is much smaller than the modern tidal range (~2.3 m), and suggests the fossil coral and the shoreline angle are contemporaneous. Thus, either the higher coral lived prior to the formation of T2's shoreline angle and was displaced to its current position, or the coral grew after the development of the shoreline angle during the interseismic subsidence. Here we prefer the former interpretation because if the coral grew after the formation of the shoreline angle, we would expect the shoreline angle to be modified by later erosion of the soft mélange bedrock. On the other hand, if we extend the surface trend of T2 to the place above SC-150, the elevation of this extended T2 surface would be 2-2.5 m lower than T2's shoreline angle, which matches the modern tidal range (~2.3 m, Fig. 13c). Therefore, it is reasonable to suggest the U-Th age of SC-150 represents the age of T2. As a result, the amount of emergence from 1762 C.E. to the present at this location has to be smaller than 3.3 m, which is the elevation from T2's shoreline angle to the current MHWS.

Northeastern Cheduba Island (Man-Aung Town area)

Terrace elevations at the northeastern tip of Cheduba Island are significantly lower than those along the western coast. For example, the surface of T3 in this area coincides with the 5 m contour line extracted from SRTM data (Fig. 14a), whereas T3 along the southwestern coast is about 10 m above MSL. This implies that long-term net uplift diminishes from southwest to northeast across the island. Evidence along the modern coast also suggests relatively small net uplift in the northeast during the late Holocene epoch.

North of Man-Aung Town, the main settlement of Cheduba Island, is a low sandstone ridge. Beneath the encrustations of modern oysters, but within the modern intertidal zone, are fossil coral heads. The elevation of these fossil corals, ~20 cm above MLLW, indicates that they have risen slightly above their modern maximum growth limit. U-Th analyses of three samples show that all grew in the 7th and 8th centuries (Table 2, MA-135, 136, and 138). Unfortunately, these coral colonies are not microatolls, so they could have grown substantially below MLLW. Nonetheless, their elevations above MLLW suggest very little emergence in the past 1400 years.

Elevation differences between the modern beach berm and an ancient one provide a better estimation of uplift in 1762 here. Near the coral fossils the modern beach berm (on the seaward edge of T1) is 0.8 ± 0.2 m below another beach berm (on the seaward edge of T2). These two berms sit in nearly identical environments with respect to the ocean, so it is reasonable to argue that their elevation difference reflects net uplift between the time of formation of the older berm and the present. We did not find datable materials to constrain the age of the uplifted beach berm, but we propose that it was raised during the 1762 earthquake.

Northwestern Cheduba Island (Taung-Yin area)

At the northern tip of Cheduba Island an unusually wide and high T1 surface lies between the modern coastline and the foothills (Fig. 15). On high-resolution satellite imagery are two obscure terrace risers that cut obliquely across this wide terrace, separating it into three sub-terraces (T1a, T1b, and T1c). These two terrace risers are not apparent in the topographic profile that we surveyed in the field (Fig. 15b), perhaps because of our choice of location for the survey or because of agricultural modifications. Slight undulations in curvature along the surveyed profile of T1 suggest, however, that the higher and lower portions of T1 may not have formed at the same time.

Near the highest portion of T1, at about 7.3 m above MHHW, are fossil oysters that encrust an isolated sandstone block. A radiocarbon analysis of one of these oysters yields a mid-15th century to early-17th century age range (Table 1, TY-140). Thus we conclude that net uplift during and since the 1762 earthquake is no more than about 7 to 7.5 m. However, since these oysters grew on the T1b surface, the actual amount of uplift during the 1762 event in this area may be much smaller, and may correspond to the elevation of T1a's shoreline angle, which we did not measure in the field.

Summary of Cheduba Island

Our results indicate that, like Ramree Island, Cheduba Island tilted northeastward during the 1762 earthquake. The greatest uplift (3.5 to 4.5 m) occurred along the southwestern coast. Uplift decreased northeastward to less than 1 m at the northeastern corner of the island.

As on Ramree Island, the patterns of uplift on Cheduba Island are consistent with the broad topography of the island and offshore bathymetry. This similarity implies that the 1762 pattern reflects much longer term neotectonic patterns of deformation.

Discussion

Because our coastal survey was conducted ~250 years after the 1762 earthquake, the coastal emergence we documented reflects the co-seismic uplift plus later deformation and changes in sea level. Therefore, in the following section we first deconvolve the 1762 co-seismic uplift from vertical motions reasonably ascribed to recent global sea-level change and interseismic deformations. We later discuss the 1762 net-uplift pattern and compare it to the other well-documented subduction zone earthquakes. We then consider a variety of structural configurations to arrive at the most plausible fault-rupture model of the 1762 earthquake. Finally, we discuss the implications of our findings upon estimation of the earthquake magnitude, and nominal recurrence intervals for events like the great Arakan earthquake.

Recovering co-seismic uplift from the emergence measurements

Displacement of sea-level indicators above or below their modern analogues may result from several different processes, not all of which are tectonic. In addition to tectonic causes such as co-seismic and post-seismic uplift, interseismic strain accumulation, or deformation associated with later, minor earthquakes, changes in sea level itself may also contribute. Figure 16 illustrates these plausible components to emergence measurements. Below, we attempt to untangle these contributions to our uplift measurements, so that we can understand their influences and the source parameters of the 1762 earthquake.

Non-tectonic water-level change

The land-level change (Uz) that we observed along the western Myanmar coast is affected by both tectonic deformation (Ut) and non-tectonic water-level change through time (S*T). The following equations describe simply their relationships to the observed land-level change:

$$Uz = Ut + S*T \quad (1)$$

$$Ut = \Delta Z + I*T \quad (2)$$

In the latter equation, ΔZ represents the combination of co-seismic and post-seismic deformations. We do not separate them here, because they are difficult to separate using just our post-earthquake field measurements. Interseismic deformation (I) and sea-level change (S) both accumulate with time (T).

Since sea-level rise varies with location (e.g., Llovel et al., 2009), ideally we would use the appropriate curve for the west coast of Myanmar. Unfortunately such a local curve is unavailable, so we must use the estimated global average to eliminate the contribution of sea-level rise to our measurements. Recent studies show that average global sea level has risen about 25 cm since the mid-19th century (Jevrejeva et al., 2008; Church and White, 2011). If this globally averaged rise in sea level is representative of sea-level change along the coast of Myanmar, then our comparisons of elevated 18th-century sea-level indicators with their modern counterparts would underestimate uplift by at least 25 cm. This might explain, for example, the difference between our measurement of 3.4 m at the southwestern corner of Cheduba Island and Captain Halsted's measurement of ~3.6 m (Halsted, 1841). It might also partially explain why we measured 5 to 5.5 m of uplift on the central southwestern coast of Ramree Island, whereas Mallet reported ~6.1 m uplift in mid-19th century (Mallet, 1878).

Figure 17 shows net-uplift values after removal of the effect of globally averaged sea-level rise. This correction reduces the differences between our measurements (the blue dots) and the observations that were made in the 19th century (the green squares). The fact that our 21st-century measurements are so similar to the 19th-century measurements implies that interseismic subsidence related to locking of the underlying megathrust between the mid-19th century and now is within the error of the measurements. Let us now take a closer look at this likely component to the difference between our measured sea-level markers and their modern analogues.

Interseismic deformation

Measurements along the central to southern southwestern coast of Cheduba Island demonstrate the inability of our measurements to resolve interseismic vertical deformations. Along this part of the coast, Halsted (1841) measured uplifts of ~3.6 to 3.9 m based on the elevation of the terraces. However, he did not mention the reference level of his measurement in the original report. We assume that he referred his measurements to MSL, but have to assign an uncertainty equal to the tidal range of ± 1.4 m in this area. The microatolls we surveyed near the village of Ka-I suggest a net uplift of 3.7 ± 0.2 m, after the sea-level rise correction. As a result, the land-level change produced by interseismic deformation through the past 170 years is 0.05 ± 1.6 m. This yields a range of interseismic deformation rates (I) that is not very informative – somewhere between subsidence at 9 mm/yr and emergence at 10 mm/yr.

Modern observations suggest that the coastline has subsided between earthquakes. Shishikura et al. (2009) noted that a comparison of old topographic maps with current topography implies subsidence of Cheduba Island. The concave upward morphology of the upper surfaces of coral microatolls at the southern tip of Cheduba Island indicates that the coast there was subsiding in the decades prior to uplift of the microatolls in 1762. Thus, we can constrain the interseismic rate (I) to between -9 to 0 mm/yr along the southern coast of Cheduba Island.

In fact, our interpretation of interseismic subsidence roughly coincides with the prediction from a simple back-slip elastic deformation model. By assuming a fully locked 16°-dipping megathrust above 30 km in depth, the 23 mm/yr plate motion between the Indian and the Burma plates reveals a 5 to 3 mm/yr subsidence rate from the southwestern Cheduba to the southwestern Ramree coasts. Unfortunately, because the interseismic deformations vary not only as a function of the distance from the trench, but also as a function of the fault coupling ratio, these estimations can only be treated as the maximum subsidence rate above the megathrust. Nevertheless, this maximum constraint shows the deficit between the true co-seismic uplifts and our net-uplift observation is likely smaller than 1 m, assuming a maximum 4 mm/yr average subsidence rate in this region.

Possible later uplift events

We now consider the possibility that deformation related to other earthquakes contributes to our measurements. Historical records affirm that the 1762 earthquake was the largest earthquake along the northern Sunda megathrust in the past few hundred years. Nonetheless, several other strong earthquakes did occur in the 19th century (Oldham, 1883). The most plausible candidates for having produced additional deformation in the region are earthquakes in 1848 and 1858. Northern Ramree Island experienced strong shaking during these events. Historical records, however, contain no hint that Cheduba and Ramree Islands rose during these events. For example, Mallet made no mention of any recent coastal uplift seen during his visit to the central southwestern Ramree coast in 1877 other than the 1762 event. Instead, he reported that the coastline of Round Island in Captain Halsted's map was very similar to the coastline geometry at the time of his visit. Our surveys of central southwestern Ramree Island and southwestern Cheduba also show the last emergence occurred in the 18th century. Since we lack evidence of post-1762 uplift along these coasts, and since strong shaking reports are limited to northern Ramree Island, we believe that significant coastal uplift of the entire coast did not occur during the earthquakes of the mid-19th century. Nonetheless, lesser local uplift may have occurred but gone unreported along, for example, the northern Ramree Island.

The uplift pattern of the 1762 earthquake

Despite these minor ambiguities, our survey results still improve significantly our knowledge of deformations associated with the 1762 earthquake. The density of observations on Cheduba and Ramree Islands, for example, is now much greater (Figure 17; Table 3). Our U-Th results also provide age constraints that demonstrate uplift in 1762 C.E. along both the western coast of Ramree Island and the entire coast of Cheduba. Our observations, together with the historical accounts, provide a general net-deformation pattern for the 1762 earthquake.

In general, as previous studies have suggested, the largest uplifts of 1762 were 3 to 4 m along the western coast of Cheduba Island. Elsewhere along the coast of Cheduba, 1762 uplift ranges from ~2 to ~1 m. Uplift is smallest (<1 m) at the northeastern corner of the island.

Along the western coast of Ramree Island, the net-deformation pattern is more complicated. The vertical deformations decrease not only northeastward, moving away from the trench, but also parallel to the trench, from a high of about 6 m along the central-western Ramree coast. It is noteworthy that even the lesser amounts of uplift along the western coast of Ramree island (~1 to 2 m) are higher than uplift closer to the trench, on the northeastern tips of Cheduba Island. Taken together, the deformation of Ramree and Cheduba Islands is double peaked, with highs along the trenchward coasts of both islands (Fig. 18).

The significance of the upper plate structures

The double-hump uplift pattern of 1762 coincides with the regional antiformal shape of Cheduba and Ramree Islands and the associated bathymetry. These two trench-parallel active antiforms are apparent in the topography and bathymetry on Fig. 17. The two red-dashed lines there represent the crests of the antiforms inferred from the shallow water bathymetry (Fig. 1). The fact that the southwestern flanks of the anticlines are topographically steeper than the northeastern flanks implies an asymmetric fold geometry.

Although the locations of the greatest 1762 uplift are not exactly coincident with the anticlinal crests, the similarity between the pattern of uplift in 1762 and the form of the anticlines lead us to hypothesize that the upper-plate secondary structures associated with the antiforms ruptured during the 1762 event. Such failure of multiple splay faults during a single earthquake is not unknown; multiple failures occurred during other large thrust-fault earthquakes, such as the 1964 Alaskan earthquake (Plafker, 1965) and the 2008 Wenchuan earthquake (Xu et al., 2009).

The evidence of splay faulting is quite clear across the central profile. The magnitude and gradient across central southwestern Ramree coast is unlike any documented pure megathrust rupture (right side of Fig. 19). Magnitudes and gradients this steep did, however, occur during the 1960 Chilean and the 1964 Alaskan earthquakes (left side of Fig. 19). Previous studies imply that both of these earthquakes involved failure of large splay faults (e.g., Plafker, 1972). In the case of the Alaskan earthquake, two splay faults clearly ruptured the surface on each side of an offshore island. The similarity between the 1762 uplift pattern and the 1964 Alaskan earthquake pattern strongly suggests that splay faulting was involved during the 1762 Arakan earthquake, and both faults beneath Ramree and Cheduba Islands moved during this event.

However, rupture on the splay faults may not explain all the deformation of 1762 event. The magnitude and gradient of vertical deformation across the southern profile is not as sharp as they are across the central profile. The broad uplift pattern across the southern profile is similar to that expected of a pure megathrust rupture. Thus, the rapid southward diminishment of slip on one of the splay faults may imply slip on the megathrust alone beneath the southern profile. Moreover, the two antiforms manifested by the two islands are ~100 km long, only a fraction of the 500-km length of reported coastal deformation during the 1762 earthquake (e.g., Oldham, 1883; Cummins, 2007). Therefore, we believe the Arakan earthquake of 1762 resulted from rupture of both the megathrust and major splay faults.

The source of the 1762 earthquake

We hypothesize that slip on the faults that produced the 1762 earthquake should also be able to produce the long-term deformation of Ramree and Cheduba Islands. The subsurface structures beneath the islands are poorly known, so the best approach to inferring their geometry is to test a variety of geometries to explore which are the most plausible for generating both the 1762 uplift pattern and the islands' topography.

We propose three structural geometries: A simple megathrust model, a megathrust model with a ramp, and a megathrust model with two splay faults (Fig. 20). We fixed the dip angle of the northern Sunda megathrust to be 16° in the simple megathrust model and in the splay-fault model. In the ramp model, we added a 30° fault ramp along a 10° dipping megathrust. In the splay-fault model, we added two splay faults beneath Cheduba and Ramree Islands, with the splay faults cropping out several km southwest of the southwestern coasts of the islands. We assume the dip of each of the splay faults is 45°, so that these upper-plate faults would be able to connect to the megathrust beneath the eastern limb of these antiforms. We also assume that co-seismic fault slip on the splay faults is partitioned from the megathrust; hence, the more slip on the splay faults, the less slip would propagate updip along the megathrust.

All three models are capable of producing a double-hump uplift pattern similar to that measured along our southern profile (Fig. 20). The greatest depth of slip on the fault plane is no deeper than 30 to 35 km in these models, as is typical for the seismic megathrust ruptures. However, the long-term uplift patterns vary significantly in these models due to the differential uplift rates above the fault produced by different fault geometries (e.g., Hubert-Ferrari et al., 2007). We found that only the splay-fault model is able to produce the long-term deformation pattern of the two antiforms. On the contrary, the simple megathrust model produces a uniform vertical deformation pattern relative to the footwall block, while the megathrust with ramp model generates a broad fault-bend fold above the ramp area. This result further supports our idea that the splay-fault model is the most appropriate source geometry for the 1762-type earthquake along the northern Sunda megathrust belt.

In order to fit the 1762 net-uplift patterns using the splay-fault model, the required total slip on the megathrust and the splay faults ranges from 9 to 16 m (Fig. 21). Along the southern profile, our solution shows the 45° blind splay fault beneath Ramree Island absorbs ~1.5 m slip from the megathrust, and the total slip on the megathrust is ~9 m above a depth of 32 km. Farther west, more than 65% of slip (>5 m) partitioned from the megathrust to the other splay fault beneath Cheduba Island, creating nearly 4 m of uplift along its southwestern coast. The deformation pattern across northern Ramree Island may also be explained by a similar slip pattern.

Maximum fault slip occurred beneath the central profile, from northern Cheduba Island to central Ramree Island. Our solution suggests slip of ~16 m beneath this profile. Nearly 55% of slip (~8 m) partitioned to the splay fault beneath Ramree Island, if the fault dips 50° beneath the island. Under Cheduba Island, the frontal splay fault may have taken all the rest of slip from the megathrust (~8 m), in order to fit the 4 m uplift of the northern southwestern Cheduba coast.

From the modeled fault slip on the megathrust during the 1762 event, we are able to calculate the magnitude of the earthquake. Since the rupture area on the splay faults is much smaller than that on the megathrust itself, we chose to calculate the moment magnitude using only the rupture area on the megathrust. Our model suggests that the megathrust slips 7.5 m or more between the depth of 14 km and 32 km, which is more than 50% of the fault's seismogenic width. Above the depth of 14 km, the slip on the megathrust is minimal in our model. Therefore, the rupture width is ~60 km along the megathrust, with an average slip of 7.5 m. We assumed the fault length to be 500 km based on the historical land-level change records from Foul Island to Chittagong, comparable to the length used by Cummins (2007). Together, these parameters suggest the magnitude of 1762 earthquake is Mw 8.5.

The estimated Mw 8.5 of 1762 earthquake is about 2.8 times smaller than the Mw 8.8 estimated by Cummins (2007). The principle reason is that in our model, the slip is partitioned between the megathrust and the splay faults. As a result, our modeled fault width and the co-seismic slip are smaller. However, it is unlikely that such a splay fault geometry would remain the same along the entire 500 km length of the megathrust. Furthermore, we did not include the rupture of the splay faults or the slip on the shallow part of the megathrust in our calculation. Thus our estimate provides a plausible lower bound for the magnitude of the 1762 earthquake.

Earthquake recurrence intervals

Both paleoseismological and historical evidence for repeating great earthquakes along the northern Sunda megathrust is scant. Earthquake stories told by local villagers and geomorphic observations from previous studies suggest that events similar to the 1762 earthquake recur every several centuries to every millennium or so (e.g., Halsted, 1841; Shishikura et al., 2009). To estimate a plausible range for an average recurrence interval, we used the following equation to calculate the seismic interval (ΔT) from the long-term uplift rate (R), the interseismic deformation rate (I), and the amount of co-seismic uplift (ΔZ) based on the characteristic slip model:

$$\Delta Z/\Delta T + I = R \qquad (3)$$

In equation (3), we assumed that the long-term deformation is the sum of the interseismic deformation and the co-seismic plus post-seismic deformations. Therefore, if the uplift event occurs regularly, the relationship can be written in the form of equation (3), in which the ΔT represents the recurrence interval. Since the actual co-seismic deformation (ΔZ) is poorly constrained from geomorphic studies after the earthquake, we use the observed net uplift (Ut) in equation (2) to replace ΔZ by combining equations (2) and (3):

$$(Ut - I*T)/\Delta T + I = R \qquad (4)$$

Hence, the recurrence interval (ΔT) changes as the function of the interseismic deformation rate (I) as we re-arrange equation (4) to equation (5):

$$\Delta T = (Ut - I*T)/(R- I) \qquad (5)$$

At the southwestern corner of Cheduba Island, the long-term uplift rate (R) that we estimated from coral fossils found in higher elevations is between ~3.5 and ~5.2 mm/yr. The observed net uplift (Ut) from the 1762 earthquake to the present is 3.7 m and the estimated interseismic uplift rate (I) ranges from -9 to 0 mm/yr, more likely between -5 and -3 mm/yr as predicted in the back-slip elastic model. As a result, the ΔT ranges from 400 to 700 years if the long-term uplift rate (R) is about 5 mm/yr. If the long-term uplift rate (R) is slower, such as 3.5 mm/yr, the corresponding recurrence interval (ΔT) would change to between about 450 and about 1000 years (Fig. 22). If we apply the -5 to -3 mm/yr interseismic uplift rate predicted from the back-slip model to this diagram, we can further narrow down the 1762-type recurrence interval to ~500 to ~700 years under the same conditions.

Such range of recurrence interval is very close to the estimations from our elastic deformation model, in which we suggest the maximum fault slip is about 16 m beneath Ramree Island. By dividing 16 m to the 23 mm/yr plate motion between the Indian and the Burma plates, we estimated the recurrence interval to be ~700 years. The similarity between these two independent estimations again supports our splay-fault model, in which the major deformation results from the activity of upper-plate structures, rather than the megathrust itself.

This 500 to 700 years interval is similar, but shorter than the recurrence intervals (~900 years) estimated by previous studies (e.g., Than Tin Aung et al., 2008; Shishikura et al., 2009). The earlier estimations heavily rely on the ages of uplifted terraces; thus any events that did not produce the emergence of marine terraces may be ignored in their studies. Our preliminary U-Th analyses of uplifted corals in southwestern Cheduba coast show such undocumented events may exist in the past 1000 years. These undocumented events may result from minor slips on the upper-plate secondary structures, or pure failure of the megathrust that does not produce any long-term deformation. The occurrence of such events may result in shorter earthquake recurrence intervals than what we estimated from the characteristic slip model. Thus, more detailed field investigations are necessary along the western coast of Myanmar to understand the detailed deformation history in the past several thousand years.

Summary and conclusions

From field observations and age analysis of uplifted coral and oyster fossils, we have obtained a detailed dataset of coastal uplift amount of Ramree and Cheduba Islands during the 1762 Arakan earthquake. Up to 6 m of uplift occurred at the central-western Ramree coast during the earthquake, as recorded by observations in the 19th century. Our remote sensing study and field investigations also suggest that the entire Ramree Island has been affected by an eastward tilting during the Holocene epoch. This regional tilting coincides with the net-uplift pattern of the 1762 earthquake, during which only western Ramree Island uplifted significantly.

Results of our field surveys enabled us to determine the net-uplift pattern of the 1762 Arakan earthquake along the southern part of the northern Sunda megathrust. A net-uplift profile perpendicular to the trench from the western Cheduba coast to eastern Ramree Island shows the net-uplift amount decreases from ~4 m in the west to nearly 0 m in the east. A secondary net-uplift high is present at central-western Ramree Island. This double hump uplift pattern coincides with the long-term uplift patterns of Ramree and Cheduba Islands, and is difficult to explain by pure elastic deformations of the megathrust. Thus we propose that upper-plate splay faults play important roles in the 1762 earthquake.

By fitting the coastal net-uplift data with the simple megathrust-splay faults model, we estimate the total slip on the megathrust-splay fault system to have been about 9 to 16 m beneath Cheduba and Ramree Island. This modeling result also indicates the 1762 earthquake had a moment magnitude of about 8.5. This estimation is likely a minimum, because we ignored the contributions from slip along the shallow megathrust and from slip on the splay faults.

Our first-order estimation shows the recurrence interval of events similar to the 1762 earthquake ranges from ~400 years to less than 1000 years, and is most likely between 500 to 700 years, along the northern Sunda megathrust. Since the last large earthquake occurred nearly 250 years ago, detailed paleoseismological studies are urgently needed in order to understand the earthquake history and future earthquake hazards along the northern Sunda megathrust.

Acknowledgments

We have benefited greatly from discussions with Win Swe, J.-P. Avouac, and M. Shishikura. We also appreciate the generous support of the Immediate Past President of the Myanmar Engineering Society (MES), U Than Myint, and the assistance from members of the Myanmar Geosciences Society (MGS), the Department of Meteorology and Hydrology (DMH) of Myanmar, and Thingazar Travels & Tours Company. The comments and suggestions of R. Bilham and an anonymous reviewer significantly improved this manuscript. This research was supported by the Earth Observatory of Singapore (EOS) and by the National Science Council (NSC) of Taiwan (NSC 99-2116-M-002-009, 100-2116-M-002-005, and 101-2116-M-002-013 to J.B.H.S.). U-Th dating at the HISPEC was supported by NSC grant 100-2116-M-002-009 to C.-C.S.

References

Agnew, D. C. (1997), NLOADF: A program for computing ocean-tide loading, J. Geophys. Res., 102, 5109-5110.

Amante, C., and B. W. Eakins (2009), ETOPO1 1 Arc-Minute Global Relief Model: Procedures, Data Sources and Analysis, NOAA Technical Memorandum NESDIS NGDC-24, 19 pp.

Awata, Y., S. Toda, H. Kaneda, T. Azuma, H. Horikawa, M. Shishikura, and T. Echigo (2008), Coastal deformation associated with the 2007 Noto Hanto earthquake, central Japan, estimated from uplifted and subsided intertidal organisms, Earth Planets Space, 60, 1059-1062.

Beaman R, P. Larcombe, and R. M. Carter (1994), New evidence for the Holocene sea-level high from the inner shelf, central Great Barrier Reef, Australia, J. Sediment. Res. A, 64, 881–885.

Briggs, R. W., et al. (2006), Deformation and slip along the Sunda megathrust in the great 2005 Nias-Simeulue earthquake, Science, 311, 1897-1901.

Briggs, R. W., et al. (2008), Persistent elastic behavior above a megathrust rupture patch: Nias island, West Sumatra, J. Geophys. Res., 113, B12406, doi:10.1029/2008JB005684.

Brunnschweiler, R. O. (1966), On the geology of the Indo-Burma ranges, J. Geol. Soc. Aust., 13, 127-194.

Chappell, J., A. Chivas, E. Wallensky, H. A. Polach, and P. Aharon (1983), Holocene palaeo-environmental changes, central to north Barrier Reef inner zone, J. Aust. Geol. Geophys., 8, 223-235.

Chen, M.-C., C. Frohlich, F. W. Taylor, G. Burr, and A. Q. van Ufford (2011), Arc segmentation and seismicity in the Solomon Islands arc, SW Pacific, Tectonophysics, 507, 47-69.

Cheng, H., R. L. Edwards, J. Hoff, C. D. Gallup, D. A. Richards, and Y. Asmerom (2000), The half-life of uranium-234 and thorium-230, Chem. Geol., 169, 17-33.

Chlieh, M., et al. (2007), Coseismic slip and afterslip of the great (Mw 9.15) Sumatra-Andaman earthquake of 2004, Bull. Seism. Soc. Am., 97, S152-S173.

Church, J., and N. White (2011), Sea-level rise from the late 19th to the early 21st century, Surv. Geophys., 32, 1-18.

Cummins, P. R. (2007), The potential for giant tsunamigenic earthquakes in the northern Bay of Bengal, Nature, 449, 75-78.

Curray, J. R. (1991), Possible greenschist metamorphism at the base of a ~22-km sedimentary section, Bay of Bengal, Geology, 19, 1097-1100.

Curray, J. R., F. J. Emmel, D. G. Moore (2003), The Bengal fan: morphology, geometry, stratigraphy, history and processes, Mar. Pet. Geol., 19, 1191-1223.

Darwin, C. (1845), Journal of Researches into the Natural History and Geology of the Countries Visited during the Voyage of H.M.S. 'Beagle' Round the World: Under the Command of Capt. Fitzroy, 2nd ed, Corrected with Additions, John Murray, London.

Davis, A. M., J. C. Aitchison, P. G. Flood, B. S. Morton, R. G. V. Baker, and R. J. Haworth (2000), Late Holocene higher sea-level indicators from the South China coast, Mar. Geol., 171, 1-5.

DeDontney, N., and J. R. Rice (2012), Tsunami wave analysis and possibility of splay fault rupture during the 2004 Indian Ocean earthquake, Pure Appl. Geophys., 169, 1707-1735.

Farías, M., G. Vargas, A. Tassara, S. Carretier, S. Baize, D. Melnick, and K. Bataille (2010), Land-level changes produced by the Mw 8.8 2010 Chilean earthquake, Science, 329, 916.

Fukao, Y. (1979), Tsunami earthquakes and subduction processes near deep-sea trenches, J. Geophys. Res., 84, 2303-2314.

Halsted, E. P. (1841), Report on the Island of Chedooba, J. As. Soc. Bengal, 114, New Series No. 27, 419-436.

Hopley, D. (1986), Corals and reefs as indicators of paleo-sea levels with special reference to the Great Barrier Reef, in Sea-Level Research: A Manual for the Collection and Evaluation of Data, edited by van de Plassche, O. V., Geo Books, Norwich.

Hsieh, M. L., and R. J. Rau (2009), Late Holocene coseismic uplift on the Hua-tung coast, eastern Taiwan: Evidence from mass mortality of intertidal organisms, Tectonophysics, 474, 595-609.

Hubert-Ferrari, A., J. Suppe, R. Gonzalez-Mieres, and X. Wang (2007), Mechanisms of active folding of the landscape (southern Tian Shan, China), J. Geophys. Res., 112, B03S09, doi:10.1029/2006JB004362.

Hull, A. G. (1987), A late Holocene marine terrace on the Kidnappers coast, North Island, New Zealand, Quat. Res., 28, 183-195.

Jaffey, A. H., K. F. Flynn, L. E. Glendenin, W. C. Bentley, and A. M. Essling (1971), Precision measurement of half-lives and specific activities of U-235 and U-238, Phys. Rev., 4, 1889-1906.

Jarvis, A., H. I. Reuter, A. Nelson, and E. Guevara (2008), Hole-filled SRTM for the globe Version 4, available from the CGIAR-CSI SRTM 90m Database (http://srtm.csi.cgiar.org).

Jevrejeva, S., J. C. Moore, A. Grinsted, and P. L. Woodworth (2008), Recent global sea level acceleration started over 200 years ago?, Geophys. Res. Lett., 35, L08715, doi:10.1029/2008GL033611.

Kato, T. (1983), High-angle reverse faulting associated with the 1946 Nankaido earthquake, Tectonophysics, 96, 31-44.

Kayanne, H., et al. (2007), Coseismic and postseismic creep in the Andaman Islands associated with the 2004 Sumatra-Andaman earthquake, Geophys. Res. Lett., 34, L01310, doi:10.1029/2006GL028200.

Kelletat, D., (1988), Zonality of modern coastal processes and sea-level indicators, Paleogeogr. Paleoclimatol. Paleoecol., 68, 219-230.

Kench, P. S., S. G. Smithers, R. F. McLean, and S. L. Nichol (2009), Holocene reef growth in the Maldives: evidence of a mid-Holocene sea level highstand in the central Indian Ocean, Geology, 37, 455-458.

Konca, A. O., V. Hjorleifsdottir, T.-R. A. Song, J.-P. Avouac, D. V. Helmberger, C. Ji, K. Sieh, R. Briggs, and A. Meltzner (2007), Rupture kinematics of the 2005, Mw 8.6, Nias-Simeulue earthquake from the joint inversion of seismic and geodetic data, Bull. Seism. Soc. Am., 97, S307-S322.

Le Dain, A. Y., P. Tapponnier, and P. Molnar (1984), Active faulting and tectonics of Burma and surrounding regions, J. Geophys. Res., 89, 453-472.

Lewis, S. E., R. A. J. Wust, J. M. Webster, and G. A. Shields (2008), Mid-late Holocene sea-level variability in eastern Australia, Terra Nova, 20, 74-81.

Llovel, W., A. Cazenave, P. Rogel, and M. Berge-Nguyen (2009), 2-D reconstruction of past sea level (1950-2003) using tide gauge records and spatial patterns from a general ocean circulation model, Clim. Past Discuss., 5, 1109-1132.

Mallet, F. R. (1878), The Mud volcanoes of Ramri and Cheduba, Geol. Surv. India Records, 11, part 2, 188-207.

Maurin, T., and C. Rangin (2009), Structure and kinematics of the Indo-Burmese Wedge: Recent and fast growth of the outer wedge, Tectonics, 28, TC2010, doi:10.1029/2008TC002276.

Meltzner, A. J., K. Sieh, M. Abrams, D. C. Agnew, K. W. Hudnut, J.-P. Avouac, and D. H. Natawidjaja (2006), Uplift and subsidence associated with the great Aceh-Andaman earthquake of 2004, J. Geophys. Res., 111, B02407, doi:10.1029/2005JB003891.

Meltzner, A. J., K. Sieh, H.-W. Chiang, C.-C. Shen, B. W. Suwargadi, D. H. Natawidjaja, B. E. Philibosian, R. W. Briggs, and J. Galetzka (2010), Coral evidence for earthquake recurrence and an A.D. 1390-1455 cluster at the south end of the 2004 Aceh-Andaman rupture, J. Geophys. Res., 115, B10402, doi:10.1029/2010JB007499.

Natawidjaja, D. H., K. Sieh, J. Galetzka, B. W. Suwargadi, H. Cheng, R. L. Edwards, and M. Chlieh (2007), Interseismic deformation above the Sunda Megathrust recorded in coral microatolls of the Mentawai islands, West Sumatra, J. Geophys. Res., 112, B02404, doi:10.1029/2006JB004450.

Nielsen, C., N. Chamot-Rooke, C. Rangin, and The ANDAMAN Cruise Team (2004), From partial to full strain-partitioning along the Indo-Burmese hyper-oblique subduction, Mar. Geol., 209, 303-327.

Oldham, T. (1883), Catalogue of Indian Earthquakes, Memoirs of the Geological Survey of India, 19(3), 170 pp.

Park, J. O., T. Tsuru, S. Kodaira, A. Nakanishi, S. Miura, Y. Kaneda, and Y. Kono (2000), Out-of-sequence thrust faults developed in the coseismic slip zone of the 1946 Nankai earthquake (Mw = 8.2) off Shikoku, southwest Japan, Geophys. Res. Lett., 27, 1033-1036.

Pirazzoli, P. A. (1986), Marine notches, in Sea-Level Research: A Manual for the Collection and Evaluation of Data, edited by van de Plassche, O. V., Geo Books, Norwich.

Plafker, G. (1965), Tectonic deformation associated with the 1964 Alaska earthquake. Science, 148, p. 1675-1687.

Plafker, G. (1972), Alaskan earthquake of 1964 and Chilean earthquake of 1960: Implications for arc tectonics, J. Geophys. Res., 77, 901-925.

Reimer, P. J., et al. (2009), IntCal09 and Marine09 radiocarbon age calibration curves, 0-50,000 years cal BP, Radiocarbon, 51, 1111-1150.

Saillard, M., S. R. Hall, L. Audin, D. L. Farber, G. Hérail, J. Martinod, V. Regard, R. C. Finkel, and F. Bondoux (2009), Non-steady long-term uplift rates and Pleistocene marine terrace development along the Andean margin of Chile (31°S) inferred from 10Be dating, Earth Planet. Sci. Lett., 277, 50-63.

Shen, C.-C., H. Cheng, R. L. Edwards, S. B. Moran, H. N. Edmonds, J. A. Hoff, and R. B. Thomas (2003), Measurement of attogram quantities of 231Pa in dissolved and particulate fractions of seawater by isotope dilution thermal ionization mass spectroscopy, Anal. Chem., 75, 1075-1079.

Shen, C.-C., et al. (2012), High-precision and high-resolution carbonate 230Th dating by

MC-ICP-MS with SEM protocols, Geochim. Cosmochim. Acta, 99, 71-86.

Shishikura, M., et al. (2009), Geomorphological evidence of great Holocene earthquakes of western Myanmar, Proceedings of the International Workshop on Tsunami and Storm Surge Hazard Assessment and Management for Bangladesh, CDMP, 35-40.

Socquet, A., C. Vigny, N. Chamot-Rooke, W. Simons, C. Rangin, and B. Ambrosius (2006), India and Sunda plates motion and deformation along their boundary in Myanmar determined by GPS, J. Geophys. Res., 111, B05406, doi:10.1029/2005JB003877.

Sugiyama, Y. (1994), Neotectonics of Southwest Japan due to the right-oblique subduction of the Philippine Sea Plate, Geofisica Int., 33, 53-76.

Taylor, F. W., R. W. Briggs, C. Frohlich, A. Brown, M. Hornbach, A. K. Papabatu, A. J. Meltzner, and D. Billy (2008), Rupture across arc segment and plate boundaries in the 1 April 2007 Solomons earthquake, Nat. Geosci., 1, 253-257.

ten Brink, U. S., J. Song, and R. C. Bucknam (2006), Rupture models for the A.D. 900-930 Seattle fault earthquake from uplifted shorelines, Geology, 34, 585-588.

Than Tin Aung, K. Satake, Y. Okamura, M. Shishikura, Win Swe, Hla Saw, Tint Lwin Swe, Soe Thura Tun, and Thura Aung (2008), Geologic evidence for three great earthquakes in the past 3400 years off Myanmar, J. Earthquake Tsunami, 2, 259-265.

Trenhaile A. S., and M. G. J. Layzell (1981), Shore platform morphology and the tidal duration factor, Trans. Inst. Brit. Geogr., New Series, 6, 82-102.

U.S. Army Map Service (GDVLB) (1955a), Kyaukpyu, Burma, Edition 1-AMS, 1:250,000, Series U542, U.S. Army, Washington D.C.

U.S. Army Map Service (GDVLB) (1955b), Sandoway, Burma, Edition 1-AMS, 1:250,000, Series U542, U.S. Army, Washington D.C.

Wells, R. E., R. J. Blakely, Y. Sugiyama, D. W. Scholl, and P. A. Dinterman (2003), Basin-centered asperities in great subduction zone earthquakes: A link between slip, subsidence, and subduction erosion?, J. Geophys. Res., 108(B10), 2507, doi:10.1029/2002JB002072.

Woodroffe, S. A., and B. P. Horton (2005), Holocene sea level changes in the Indo-Pacific, J. Asian Earth Sci., 25, 29-43.

Xu, X., X. Wen, G. Yu, G. Chen, Y. Klinger, J. Hubbard, and J. Shaw (2009), Coseismic reverse- and oblique-slip surface faulting generated by the 2008 Mw7.9 Wenchuan earthquake, China, Geology, 37, 515-518.

Zachariasen, J., K. Sieh, F. W. Taylor, R. L. Edwards, and W. S. Hantoro (1999), Submergence and uplift associated with the giant 1833 Sumatran subduction earthquake: Evidence from coral microatolls, J. Geophys. Res., 104, 895-919.

Zachariasen, J., K. Sieh, F. W. Taylor, and W. S. Hantoro (2000), Modern vertical deformation above the Sumatran subduction zone: Paleogeodetic insights from coral microatolls, Bull. Seismol. Soc. Am., 90, 897-913.

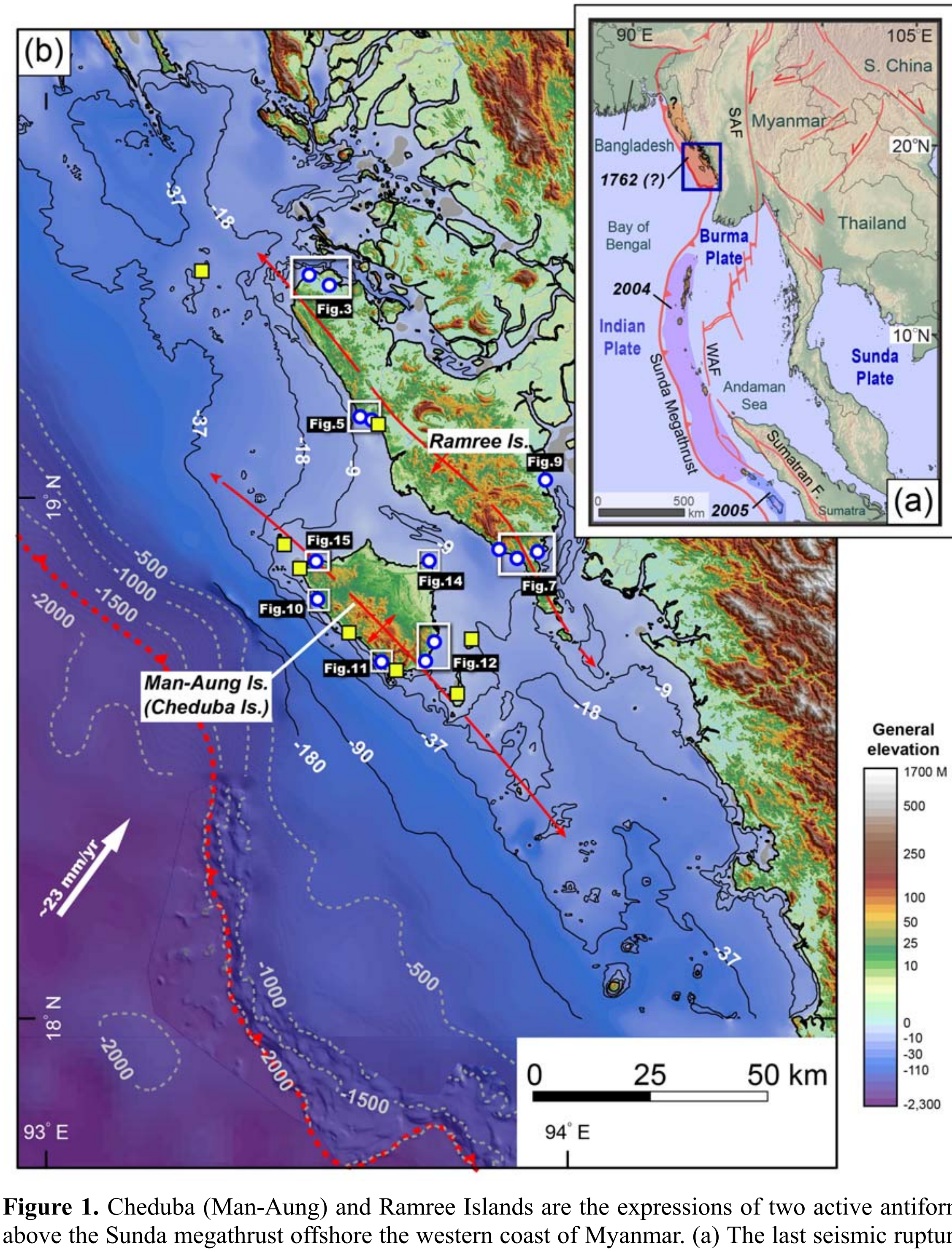

Figure 1. Cheduba (Man-Aung) and Ramree Islands are the expressions of two active antiforms above the Sunda megathrust offshore the western coast of Myanmar. (a) The last seismic ruptures of the northern Sunda megathrust, between the Indian and the Burma plates. Orange color depicts the inferred 1762 Arakan rupture from historical reports. This ~500 km long seismic patch is the only megathrust-related rupture north of the 2004 patch (shown in purple, after Chlieh et al. (2007)) from the 18th century to the present. Red lines are major active faults in Southeast Asia (after Le Dain et al. (1984)), where most of the major faults are strike-slip faults on the Burma and the Sunda

plates. Blue box shows the area of Figure 1b. SAF: Sagaing fault system; WAF: West Andaman fault. (b) The accretion-related topography above the Sunda megathrust and our survey locations in Cheduba and Ramree Islands. This section of the megathrust receives ~23 mm/yr of oblique plate convergence from the northeastward motion of the Indian plate (Socquet et al., 2006). This plate-convergence creates a series of megathrust-parallel underwater ridges within the accretionary prism. Cheduba and Ramree Islands are the two highest portions of these tectonic ridges. Black solid contours are modified from the U.S. Army topography maps (U.S. Army Map Service, 1955a, 1955b). Grey dashed contours are from ETOPO-1 (Amante et al., 2009). The high-resolution bathymetry along the trench front is digitized from Nelson et al. (2004). Yellow squares indicate the observation points in the 19th century (Halsted, 1841; Mallet, 1878). White dots represent the survey locations of this study, between 2010 and 2011.

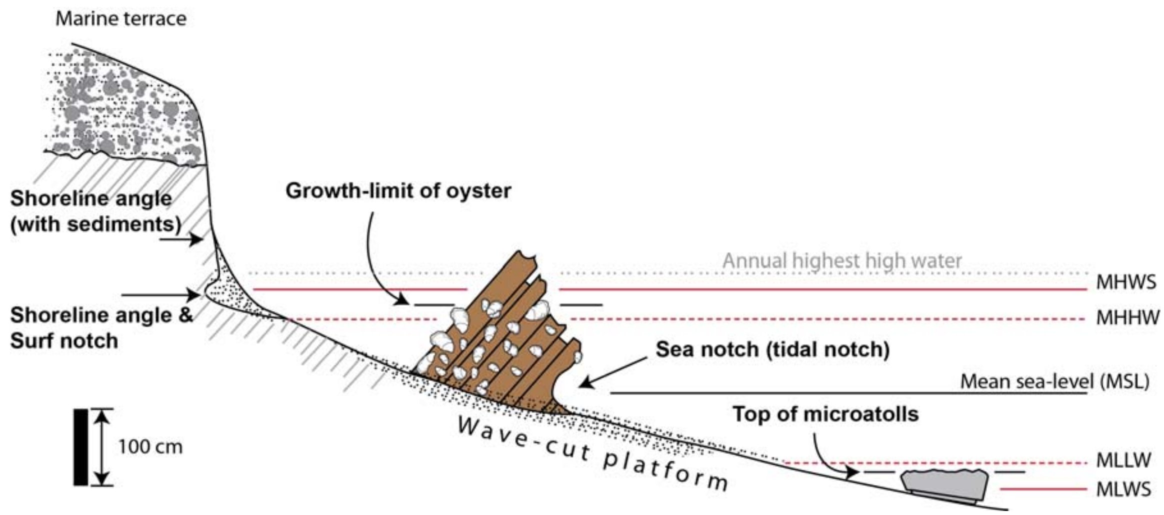

Figure 2. Natural sea-level indicators and their relationships with the tidal levels in the area of Cheduba and Ramree Islands. This schematic diagram shows the modern positions of various sea-level indicators in mesotidal environments (with tidal range of 2-4 m). The upper growth-limit of oysters and the coastal erosional features (shoreline angles and wave-cut notches) are mostly related to the water level from mean sea level (MSL) to high tide. The top of coral microatolls, however, represents the water level that is ~1-2 m lower than the other features. The elevation of microatolls is inferred from Kayanne et al. (2007), and the other indicator's elevations are from this study. MHWS: mean high water springs; MHHW: mean higher high water; MLLW: mean lower low water; MLWS: mean low water springs.

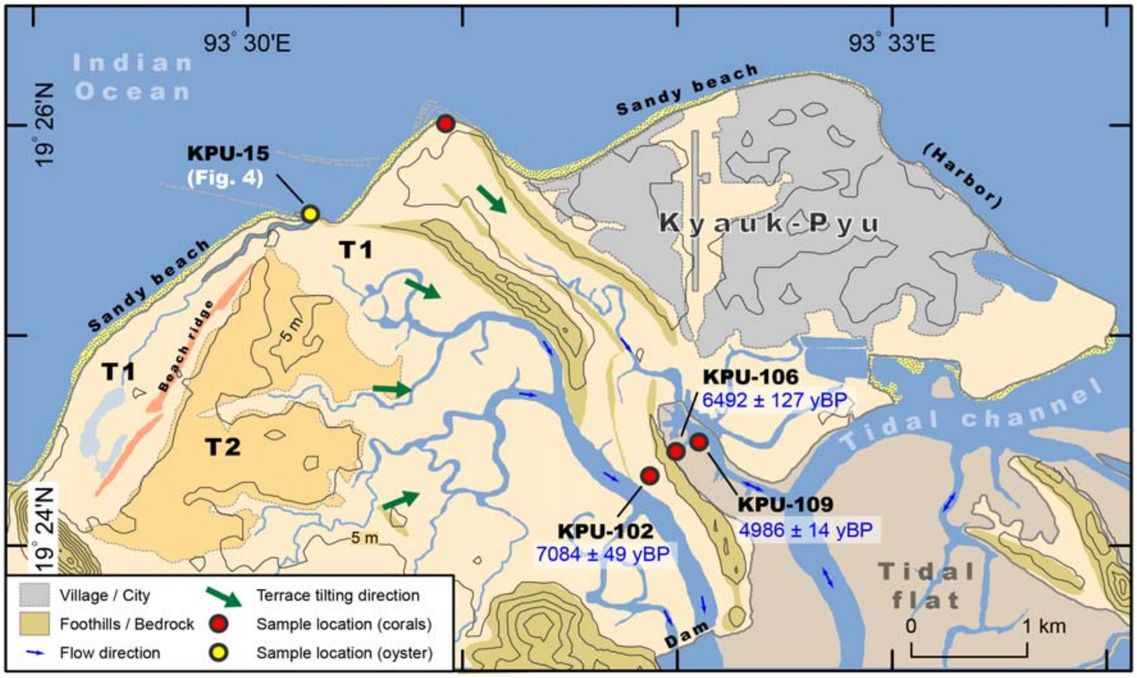

Figure 3. The patterns of marine terraces, current drainages and tidal flats show the eastward tectonic tilting in northern Ramree Island over the past several thousand years. The geomorphic characteristics in the northwestern part of the island are very different from those in the northeastern part of the island. In the east, mid-Holocene fossil coral microatolls (KPU-102, KPU-106, and KPU-109) are present slightly above the modern high tide, reflecting a very small long-term uplift. To the west, however, a flight of wave-cut notches shows clear signs of long-term successive uplift, and the last uplift event occurred after the 16th century (KPU-15, Figure 4). Blue numbers show the U-Th age of the coral microatolls in years B.P. (yBP).

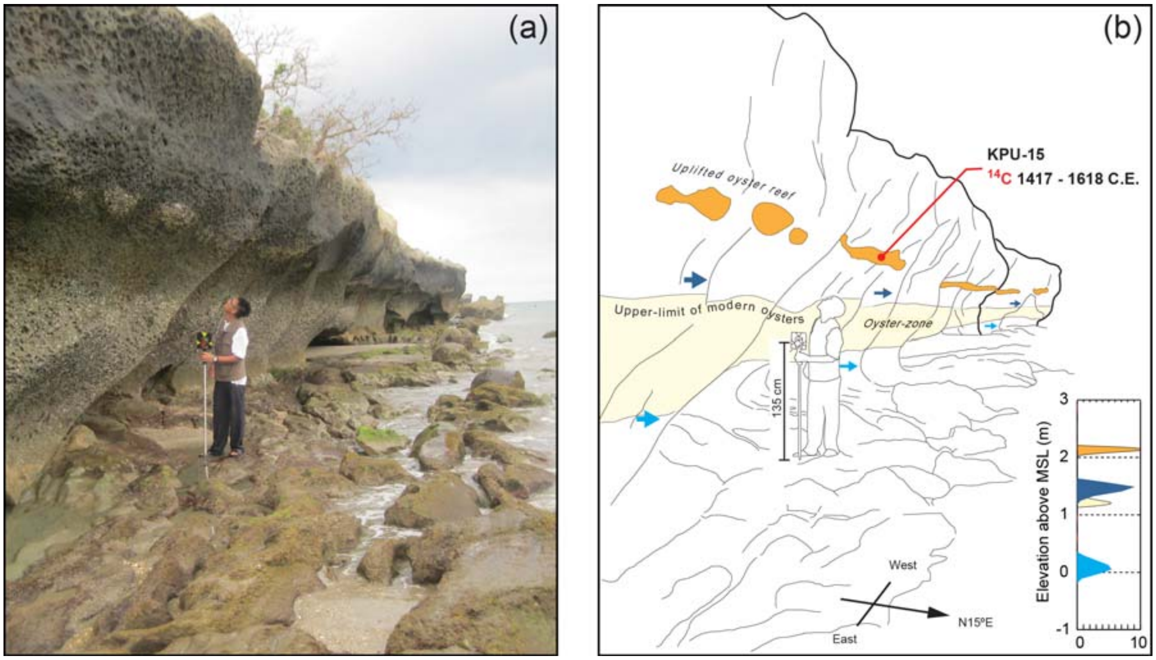

Figure 4. (a) Photograph and (b) line sketch of site KPU-15. Here, a belt of uplifted oyster fossils and a wave-cut notch beneath T1 suggest about 1-1.5 m of land-level change since the 16th century. Several levels of higher wave-cut notches on a sandstone ridge at the same site suggest successive uplift events in the past several thousand years. The radiocarbon age of uplifted oyster fossils (KPU-15) above the lowest uplifted sea notch suggests the last land-level change event occurred after the 16th century. The uplifted oyster fossils (shown in orange) are ~1 m above the modern oyster growth zone (shown in yellow). This elevation difference is similar to that between the modern sea notch (light blue arrows) and the uplifted sea notch (dark blue arrows). The elevation distributions of the oyster fossils and the wave-cut notch are shown in the inset of (b). The color code is the same as that in the line sketch.

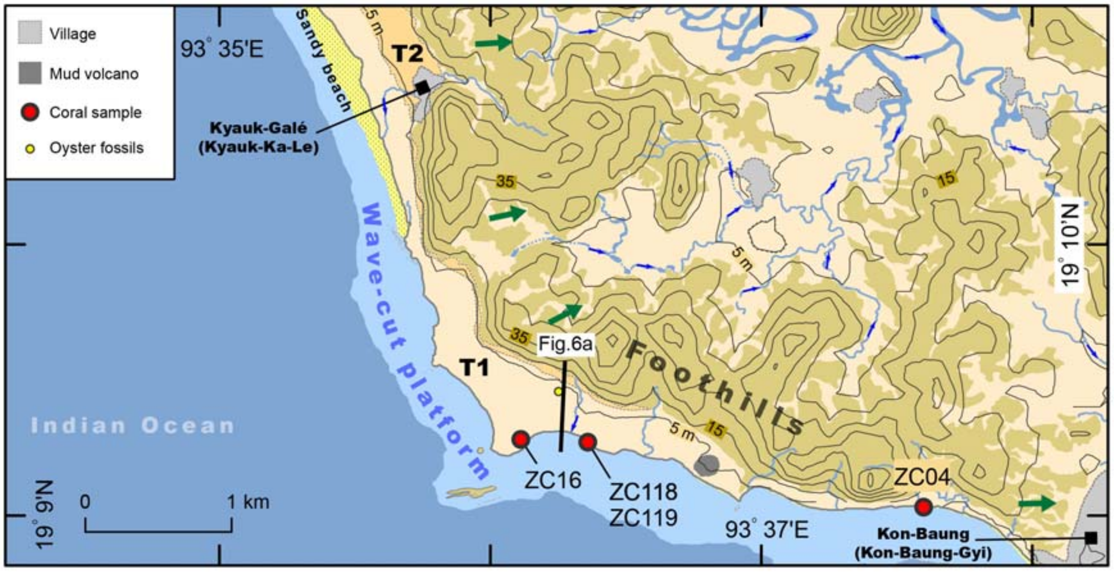

Figure 5. The patterns of modern drainages and marine terraces of the central-western coast of Ramree Island also show an eastward tilt. The fluvial plain and terraces northeast of the foothills show clear eastward tilting in the analysis of aerial photos and drainage patterns. West of the foothills, the elevation of the lowest terrace between the villages of Kyauk-Ka-Le (Kyauk-Galé) and Kon-Baung-Gyi (Kon-Baung) was described by Mallet (1878) to be ~6 m above the water level at the time of his visit.

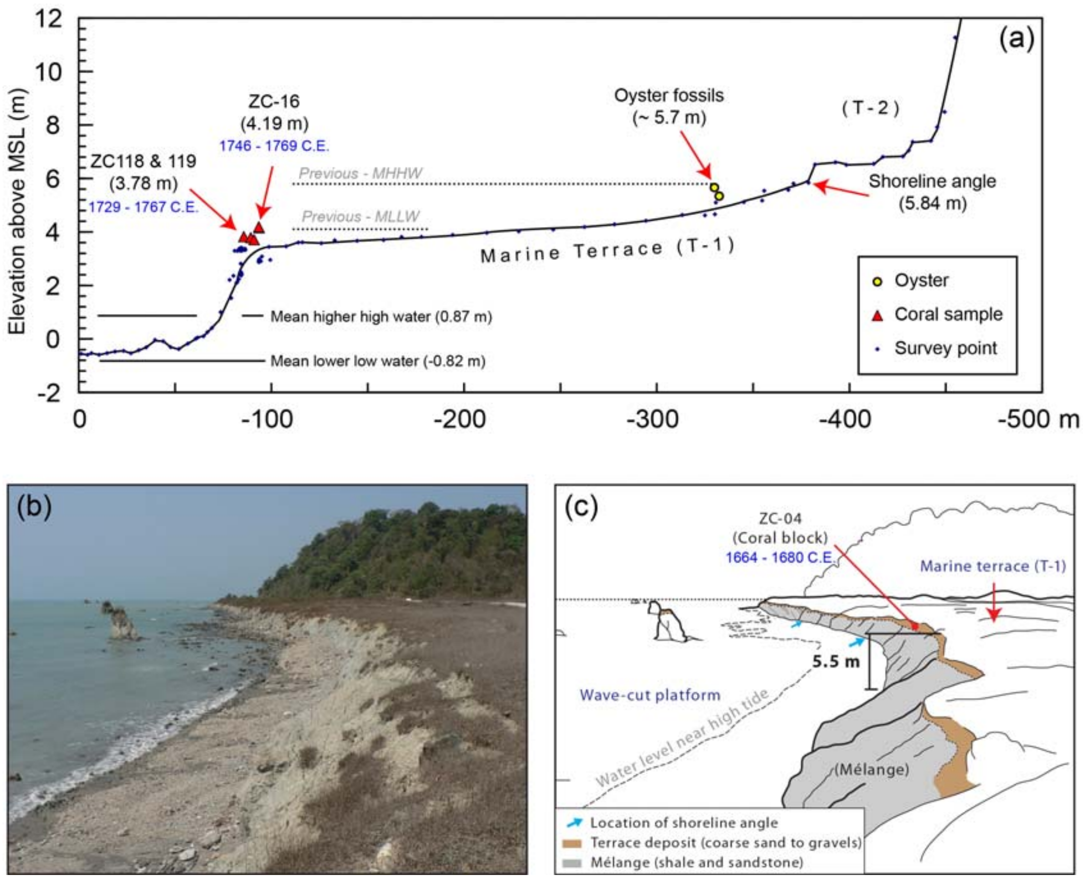

Figure 6. Our field survey sites at the central-western Ramree coast. (a) The U-Th ages of uplifted coral microatolls on the lowest terrace (T1) show that ~5 m of land-level change occurred in the 18th century, most likely during the 1762 earthquake. The profile location is indicated in Figure 5. All sea-level indicators on T1 show identical amount of land-level change relative to their equivalent tide-water level. (b) Photograph and (c) line sketch of site ZC-04. Here, a dated coral block within the terrace deposits of T1 also indicates an uplift event occurred after the 17th century. The terrace surface elevation at ZC-04 is higher than that at the previous site (ZC-16), at 5.5 m above the modern shoreline angle. This yields the minimal amount of land-level change at ZC-04. However, both the amounts at ZC-16 and ZC-04 are lower than the 19th-century account of Mallet (1878).

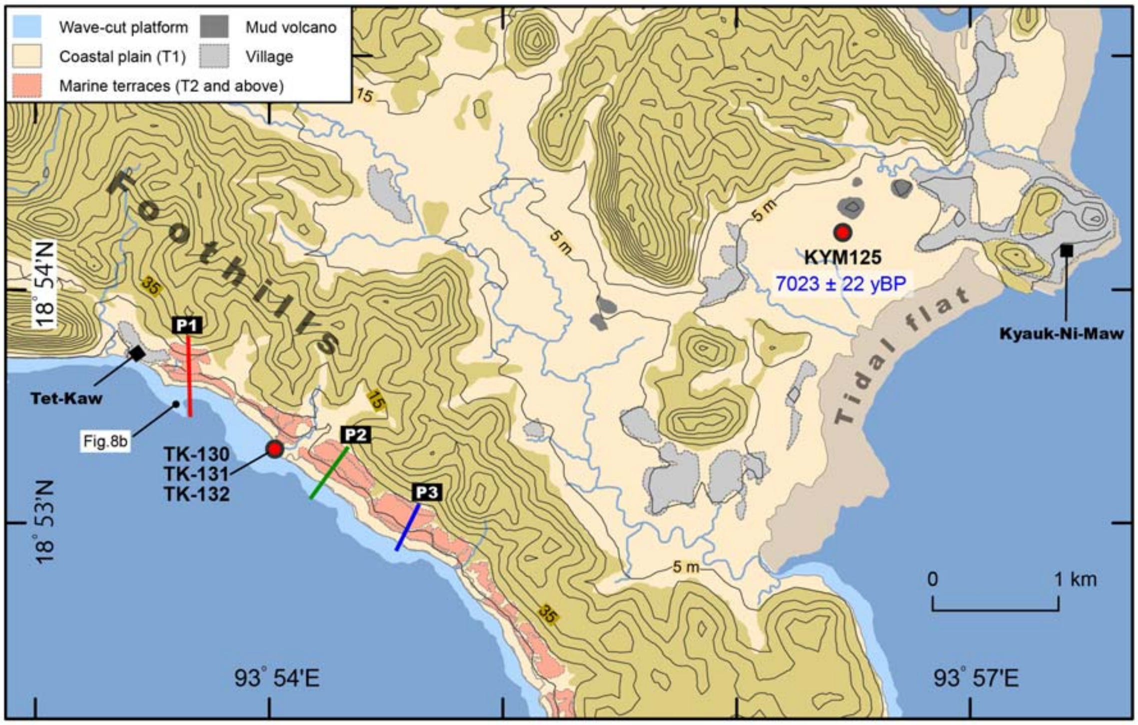

Figure 7. The different geomorphic characteristics of the southwestern and southeastern Ramree coast indicate the long-term uplift and eastward tilt of southern Ramree Island. Similar to the northeastern Ramree coast, the U-Th age of fossil corals on T1 (KYM-125) suggests the lowest terrace formed during the mid-Holocene period. However, the geomorphic characteristics west of the foothills are very different. A flight of marine terraces along the western coast suggests successive uplift during the past thousands of years. Colored lines are topographic profiles across these marine terraces shown in Figure 8a. Red dots show the locations of dated corals.

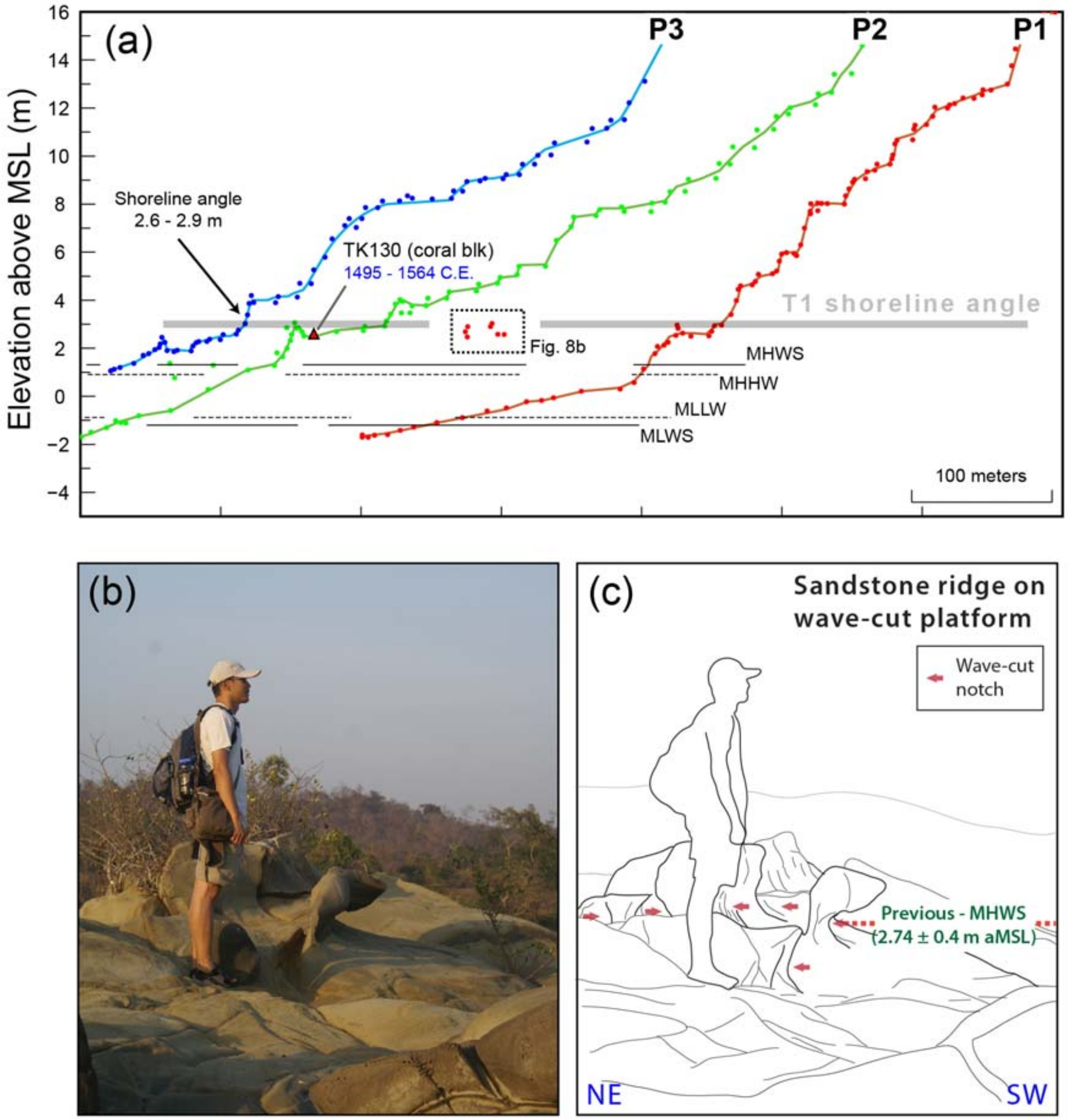

Figure 8. (a) Three topographic profiles at southwestern Ramree Island show ~1.5 m of land-level change of T1 after mid-16th century. The shoreline angle of T1 is about 1.5 m above its equivalent position in the modern tidal range. U-Th ages of coral blocks in the terrace deposits of T1 (e.g., TK-130) suggest the uplift event occurred after mid-16th century. (b) Photograph and (c) line sketch of a series of small uplifted surf notches on an offshore sandstone ridge near profile P1. The location of this photograph is shown in Figure 7. These notches show the same amount of uplift as the shoreline angle of T1. The elevations of these small surf notches are ~1.5 m above the modern MHWS, where the modern shoreline angles and surge-notches develop (see Figure 2).

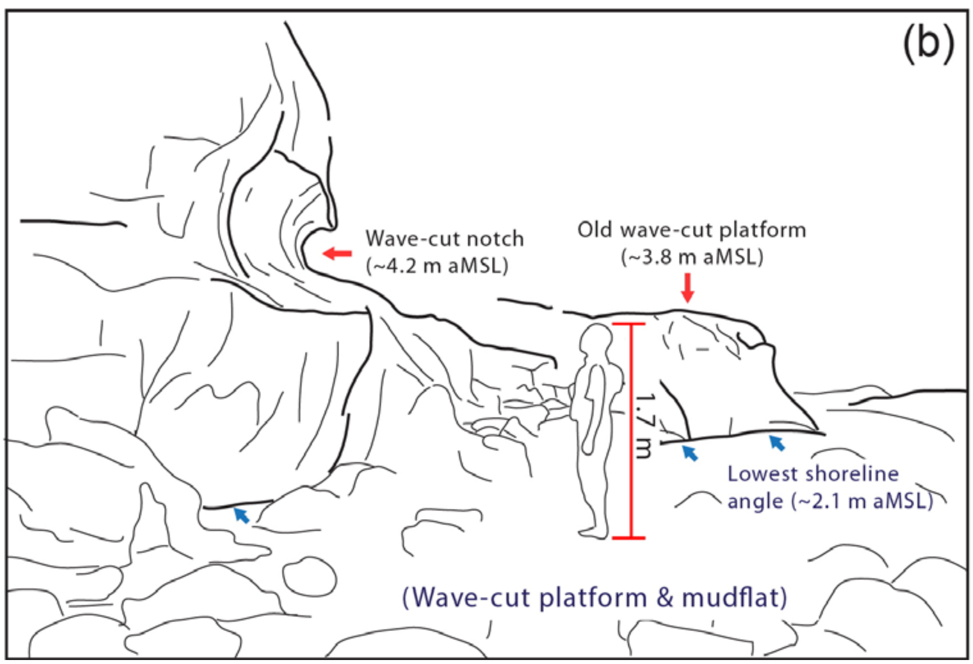

Figure 9. (a) Photograph and (b) line sketch of an inferred mid-Holocene wave-cut notch and wave-cut platform on the southeastern coast of Ramree Island. The location of this photograph is shown in Figure 1b. The wave-cut notch is ~4 m above the current MSL. Its elevation is similar to the elevations of mid-Holocene corals in northeastern and southeastern Ramree Island. Below the inferred mid-Holocene notch, the lowest preserved shoreline angle in the area is ~2.1 m above MSL. This implies <1 m of land-level change. See text for discussion.

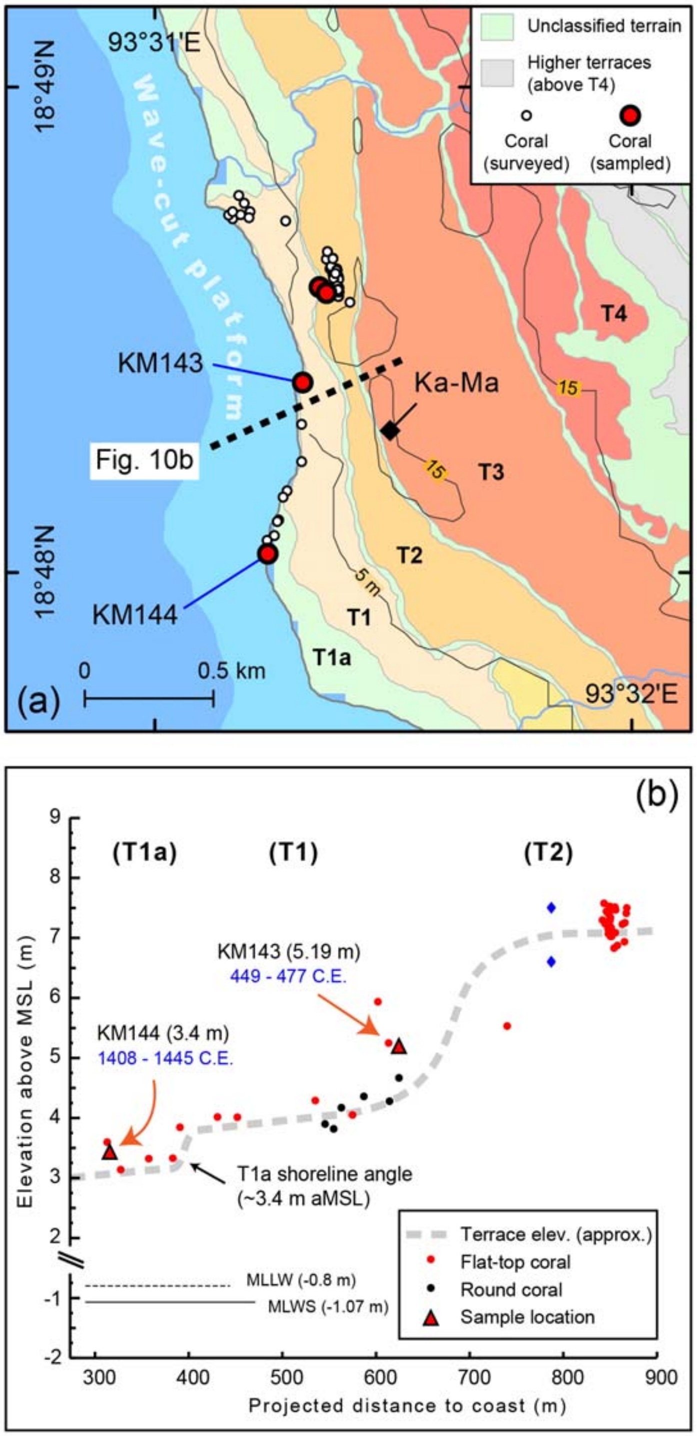

Figure 10. (a) The flight of marine terraces along the western coast of Cheduba Island near the village of Ka-Ma shows successive uplift. The geomorphic interpretations on this and following figures are based on analysis of non-stereoscopic high-resolution satellite imagery. See text for detailed discussion. Black dashed line indicates the approximate location of the topographic profile in Figure 10b. (b) The U-Th age of an eroded coral microatoll (KM-144) on the lowest terrace (T1a) suggests ~4.2 m of land-level change after mid-15th century. The elevation difference between T1a and T1 is ~0.6 m. The U-Th age of KM-143 is discussed in the text. The elevations of the terraces are inferred from the surveyed coral elevations.

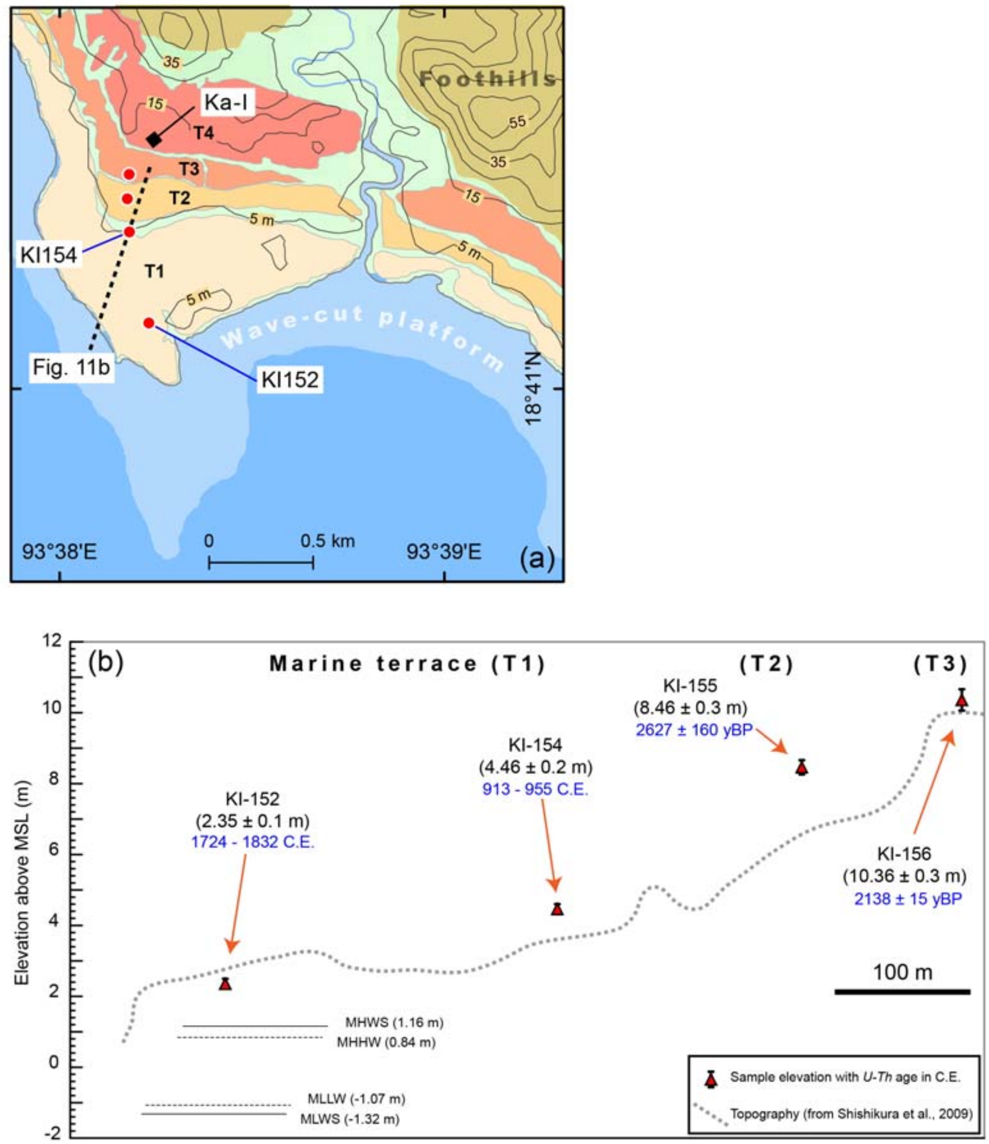

Figure 11. (a) Map and (b) a topographic profile of marine terraces near the village of Ka-I at the southern tip of Cheduba Island. Here, the flight of terraces shows progressive late Holocene uplift of the coast. The U-Th age of a coral microatoll (KI-152) on T1 shows ~3.4 m of land-level change after 1724-1832 C.E., most likely during the 1762 earthquake. See text for detailed discussion.

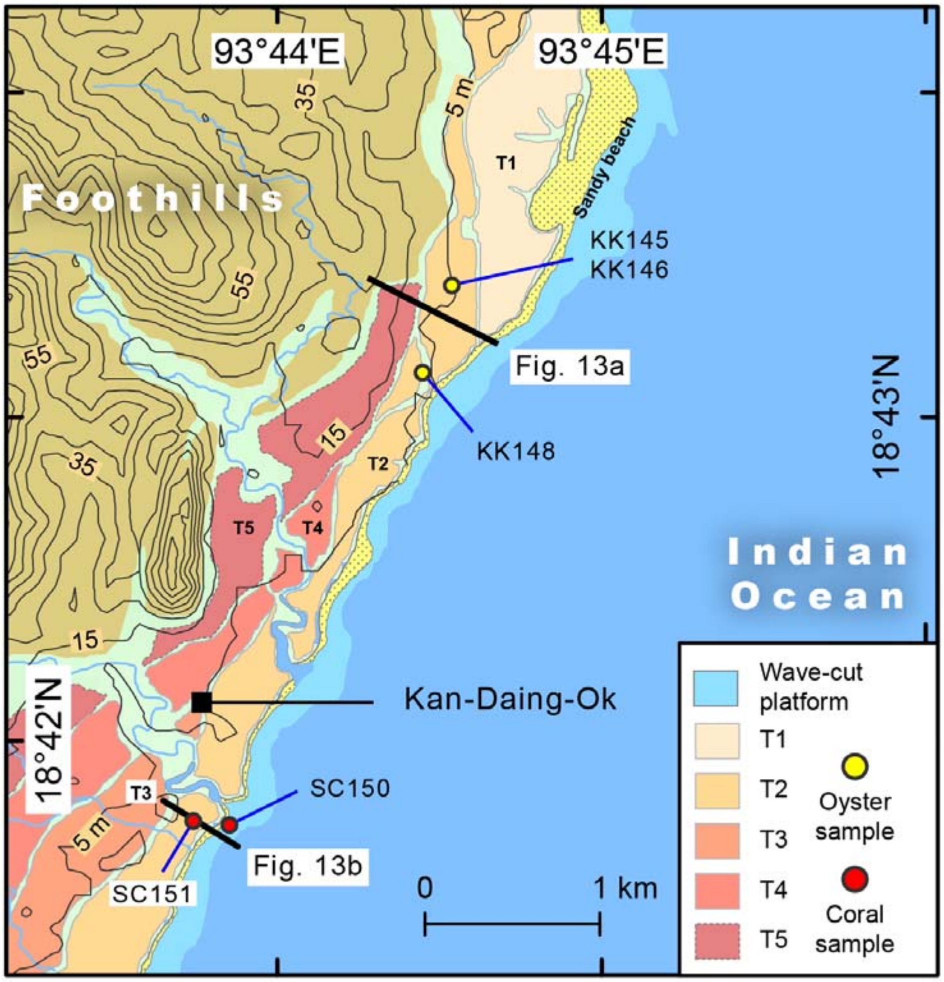

Figure 12. Map of the topographic profiles and sample locations on the marine terraces along the eastern coast of Cheduba Island.

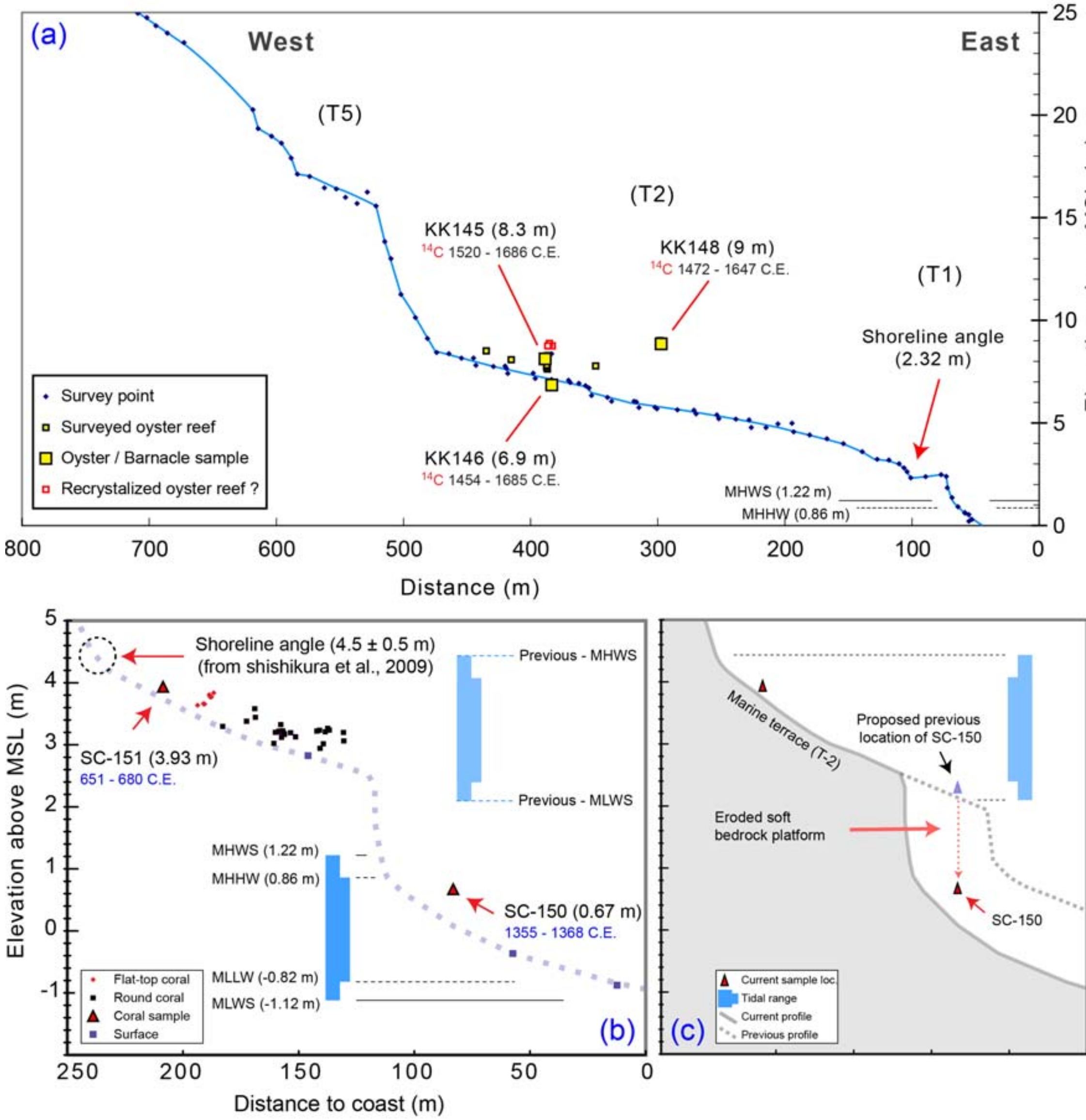

Figure 13. (a) A topographic profile north of the village of Kan-Daing-Ok (the location of the profile is shown in Figure 12). Here, uplifted shoreline angle and oyster reefs show ~1.1 m of land-level change after the 17th century. 15th to 16th century radiocarbon ages of the oysters on T2 suggest the lowest terrace (T1) formed after the 17th century, likely during the 1762 earthquake. (b) The shoreline angle of T2 and the U-Th age of an eroded coral (SC-150) near the modern high-tide suggest 1.5-~3 m of land-level change after the 14th century south of Kan-Daing-Ok. The topography profile and the elevation of the shoreline angle are modified after Shishikura et al. (2009). The location of this profile is shown in Figure 12. (c) A proposed differential erosion model to interpret the elevation of sample SC-150. See text for discussion.

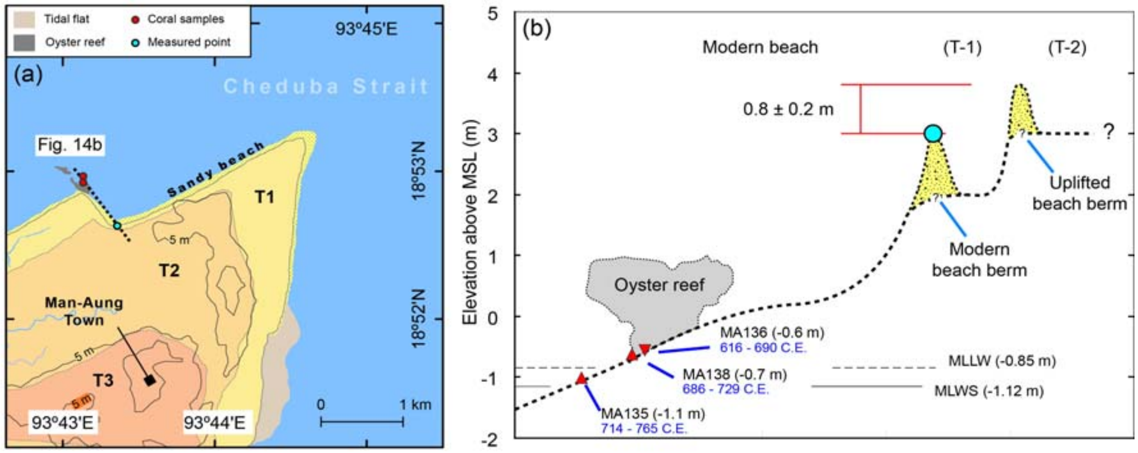

Figure 14. (a) Marine terraces at the northeastern tip of Cheduba Island are lower than their equivalents along the western Cheduba coast. The elevation of T2 near Man-Aung Town is less than 5 m from the contour of SRTM dataset (Jarvis et al., 2008), whereas T2 is higher than the 5 m contour along the western coast of Cheduba Island (see Figures 10 and 11). (b) The elevation difference between the modern and uplifted beach berm implies <1 m of land-level change from the latest tectonic event to the present. The U-Th ages of uplifted corals beneath the modern oyster reef suggest the event occurred after the 8th century. Black dashed line shows the approximate topography from our field observations. Blue dot is the top of the modern beach berm on T1.

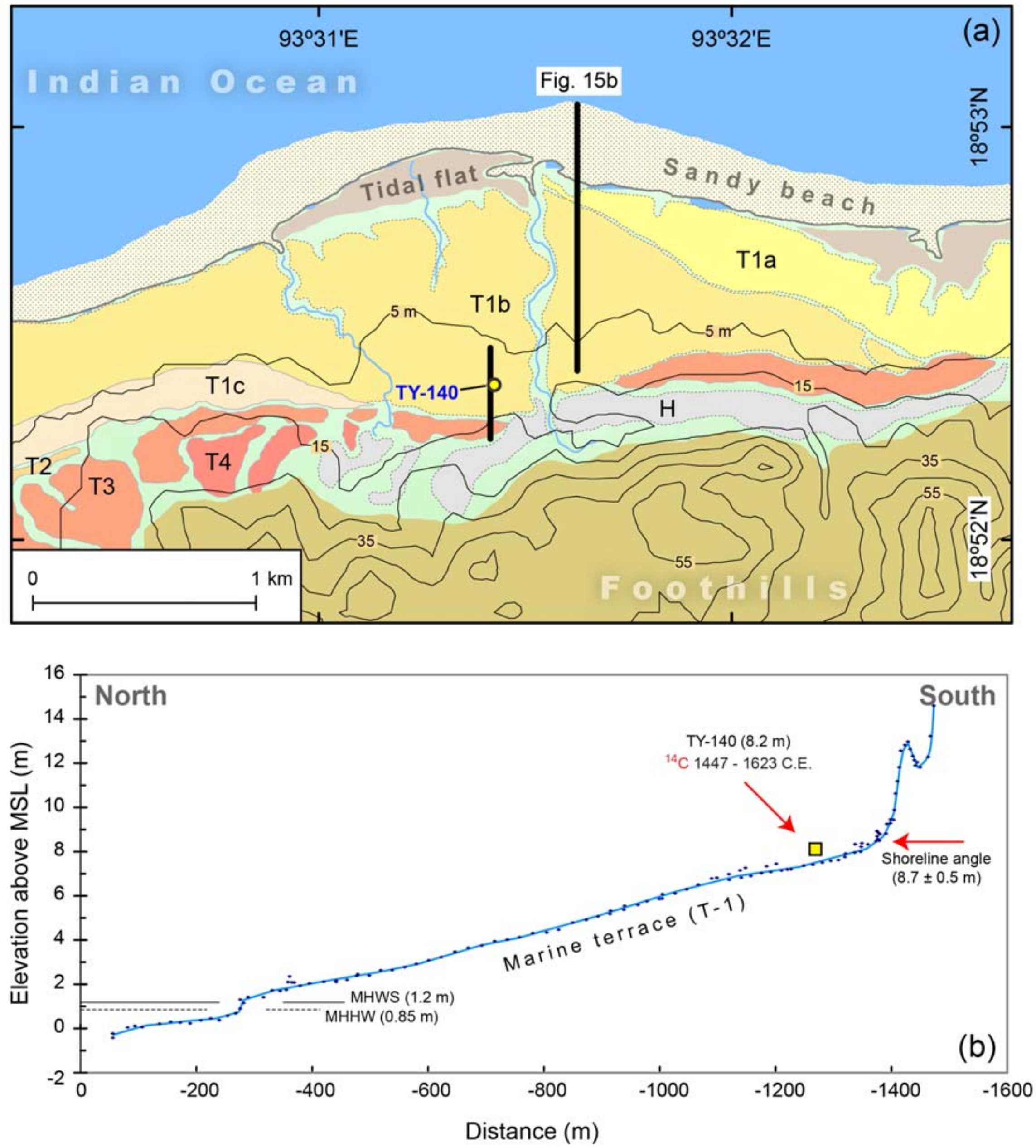

Figure 15. The age of the marine terrace in the northern part of Cheduba Island appears to suggest large uplift during the 1762 earthquake. (a) Based on the analysis of high-resolution satellite images, we separated the lowest marine terrace T1 into three sub-terraces (T1a, T1b, and T1c). However, the terrace risers are not clearly identifiable in the field, perhaps due to the recent agricultural disturbance. (b) A topographic profile of the area. The age of uplifted oyster fossils and preserved uplifted shoreline angle of T1 suggests ~7-7.5 m of land-level change after the 15th-17th century.

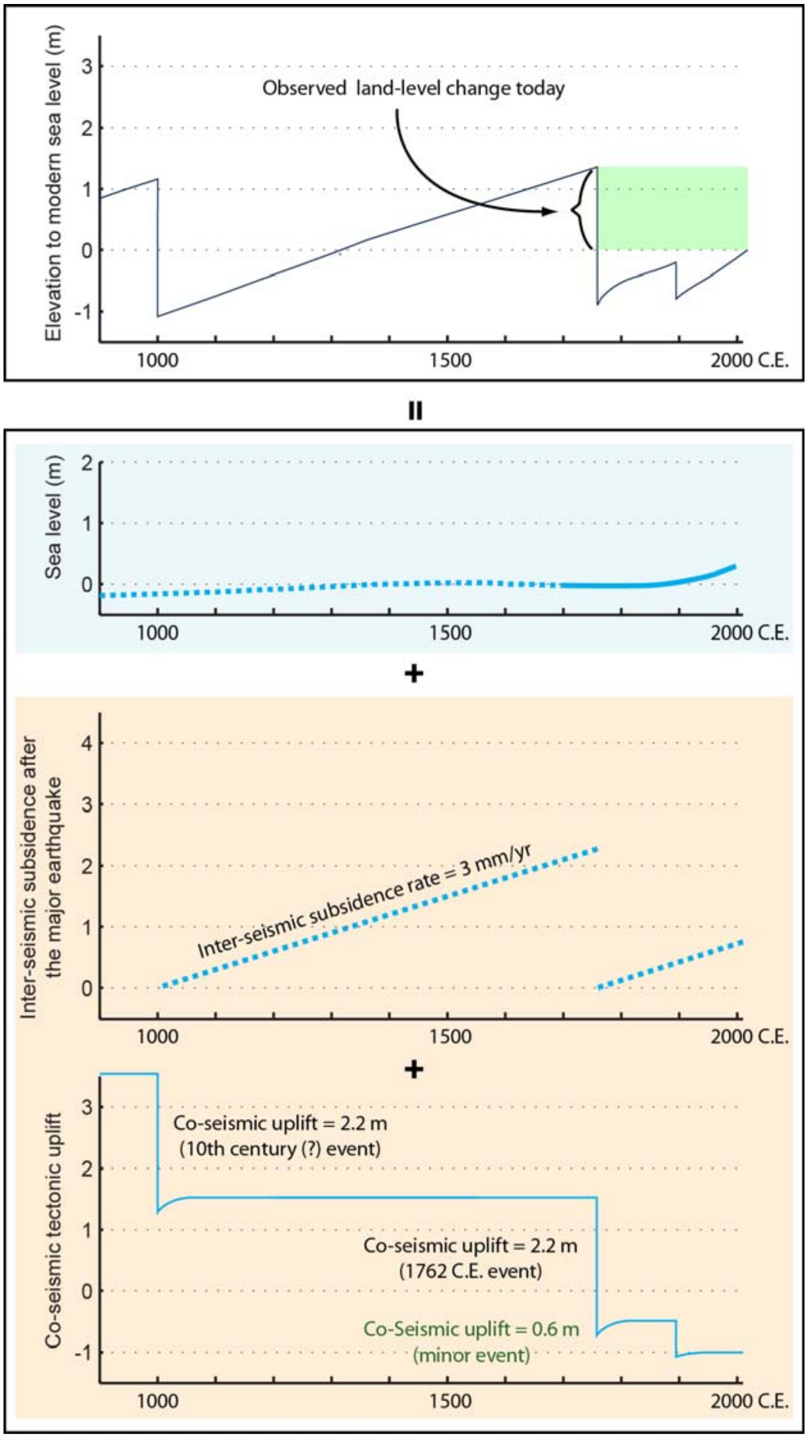

Figure 16. A cartoon that shows the contributions of various processes to sea-level history of the past several hundred years. The green shaded area indicates why the net land-level change that we surveyed may well be different than the uplift of 1762.

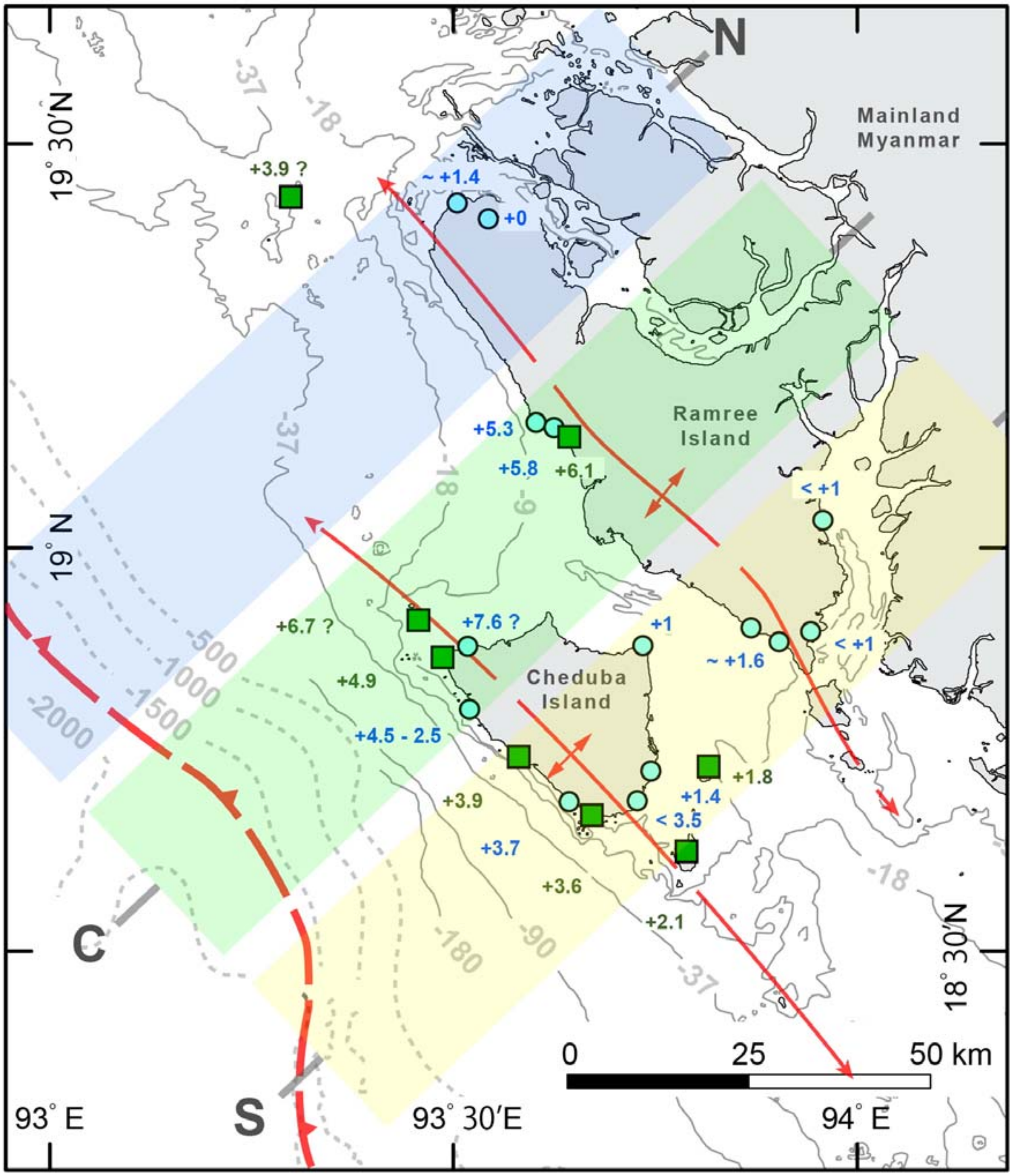

Figure 17. A compilation of measurements of 1762 uplift values, from our surveys (circles) and 19th-century documents (squares). The pattern of 1762 uplift suggests that Cheduba and Ramree Islands uplifted as separate anticlinal welts. This coseismic pattern mimics the anticlinal forms visible in the onshore and offshore topography. Hence, we suggest that the 1762 earthquake was associated with incremental uplift of two doubly-plunging anticlines above the megathrust. Colored bars indicate the bands from which data were taken to create the three uplift profiles of Figure 18.

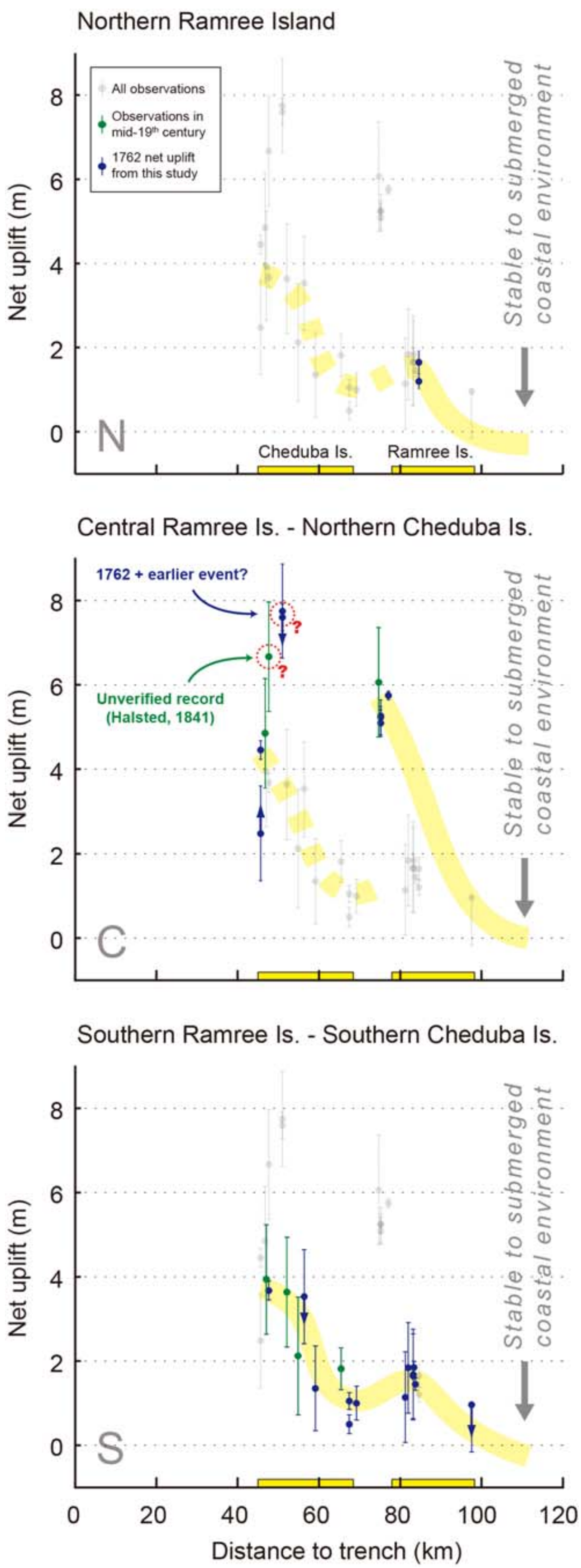

Figure 18. Three profiles of net post-1762 uplift drawn perpendicular to the megathrust. All the data from the islands appear in each profile as gray line with their uncertainties. Measurements unique to each profile appear as dark blue (modern) and green (historical) dots. Thick yellow lines show inferred uplift pattern across each profile. The highest uplifts appear along the central profile (C). This suggests either highest fault slip on the megathrust or a change in fault geometry along this profile. Red dashed circles with question marks are measurements that we suspect to be overestimated.

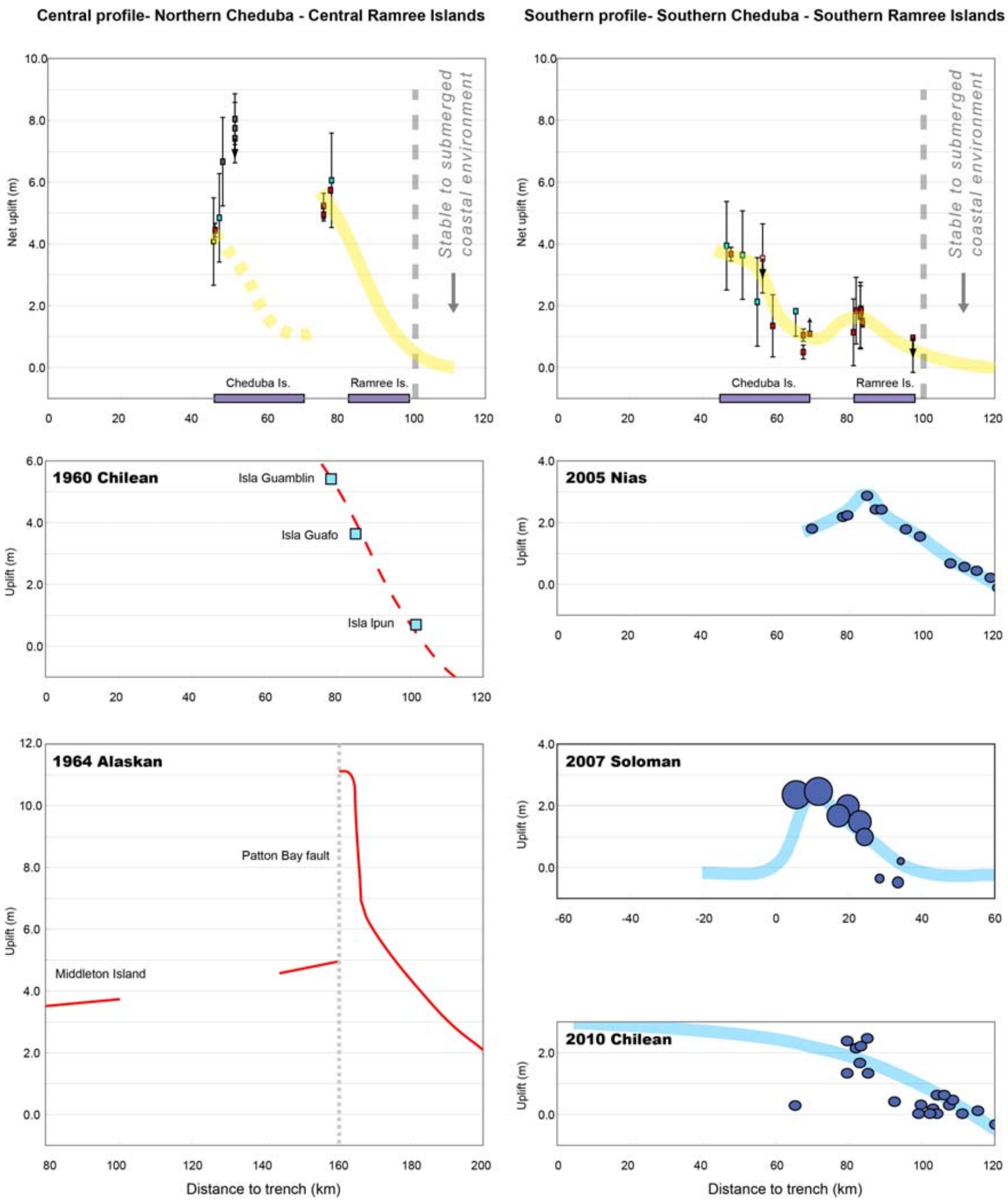

Figure 19. A comparison of trench-perpendicular uplift patterns of several well-documented megathrust earthquakes and the 1762 event supports the hypothesis that the 1762 pattern resulted in part from slip on splay faults beneath the islands. The steep gradients along the central profile are similar to those for earthquakes in which splay faults ruptured. The three deformation profiles in the lower right panels have low gradients and are believed to have resulted from simple slip on the megathrust. The two deformation profiles in the lower left panels exhibit large uplifts and steep gradients caused by slip on underlying splay faults. The 1960 Chilean and 1964 Alaskan uplift patterns are from Plafker (1972); uplift pattern of the Nias earthquake of 2005 is from Briggs et al. (2006); uplift pattern of the Solomon earthquake of 2007 is from Taylor et al. (2008), and the 2010 Chilean earthquake's land-level change distribution is from Farías et al. (2010).

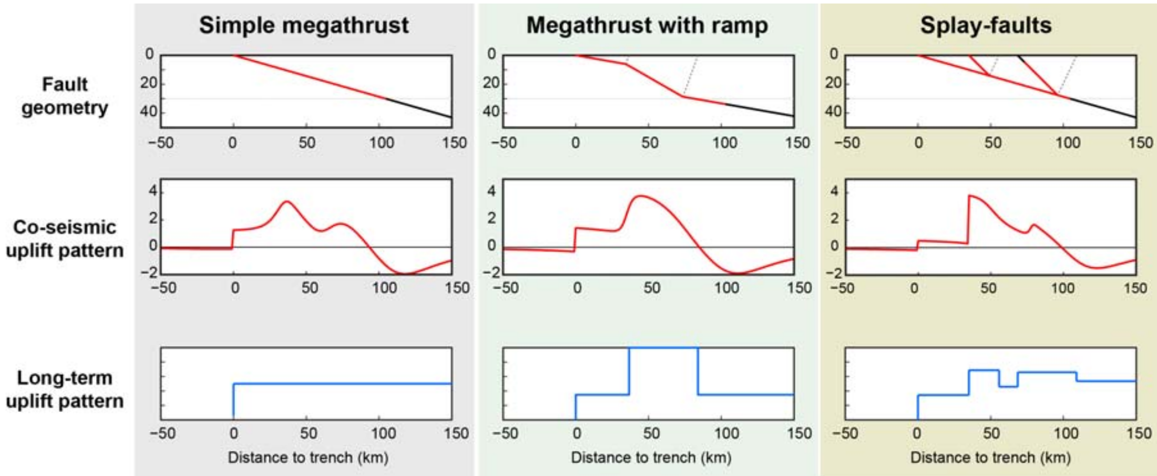

Figure 20. A cartoon diagram shows the co-seismic uplift pattern and long-term deformation pattern produced by three different scenario fault ruptures. Red lines in the upper panels show the part of the fault or faults that slip during an earthquake. We apply the uniform slip constraint on each section of the fault in the ramped megathrust and the splay-fault model, and the non-uniform slip to the simple megathrust model. The co-seismic uplift patterns of such an earthquake appear in the central row. All of the three geometries appear to be able to produce similar co-seismic deformation patterns. However, the long-term uplift patterns related to these geometries, shown as the light blue lines in the lower panels, are different. Only the megathrust model with splay faults is capable of producing the double hump topography of Cheduba and Ramree Islands.

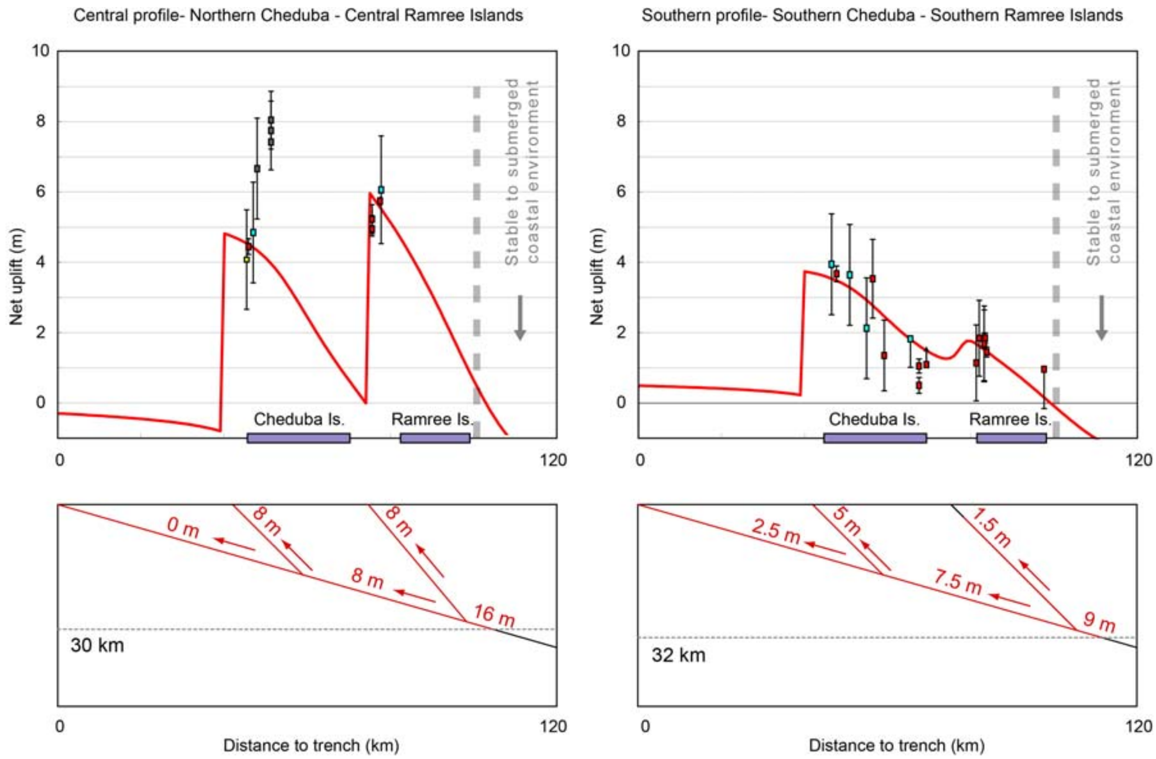

Figure 21. Plausible 1762 fault-slip patterns beneath the central and southern profiles across Cheduba and Ramree Islands. The red lines in the upper panels show the uplift patterns. The lower panels show the fault geometries and amount of slip on the megathrust and splay faults for each model. The grey-dashed lines indicate the maximum depth of fault slip.

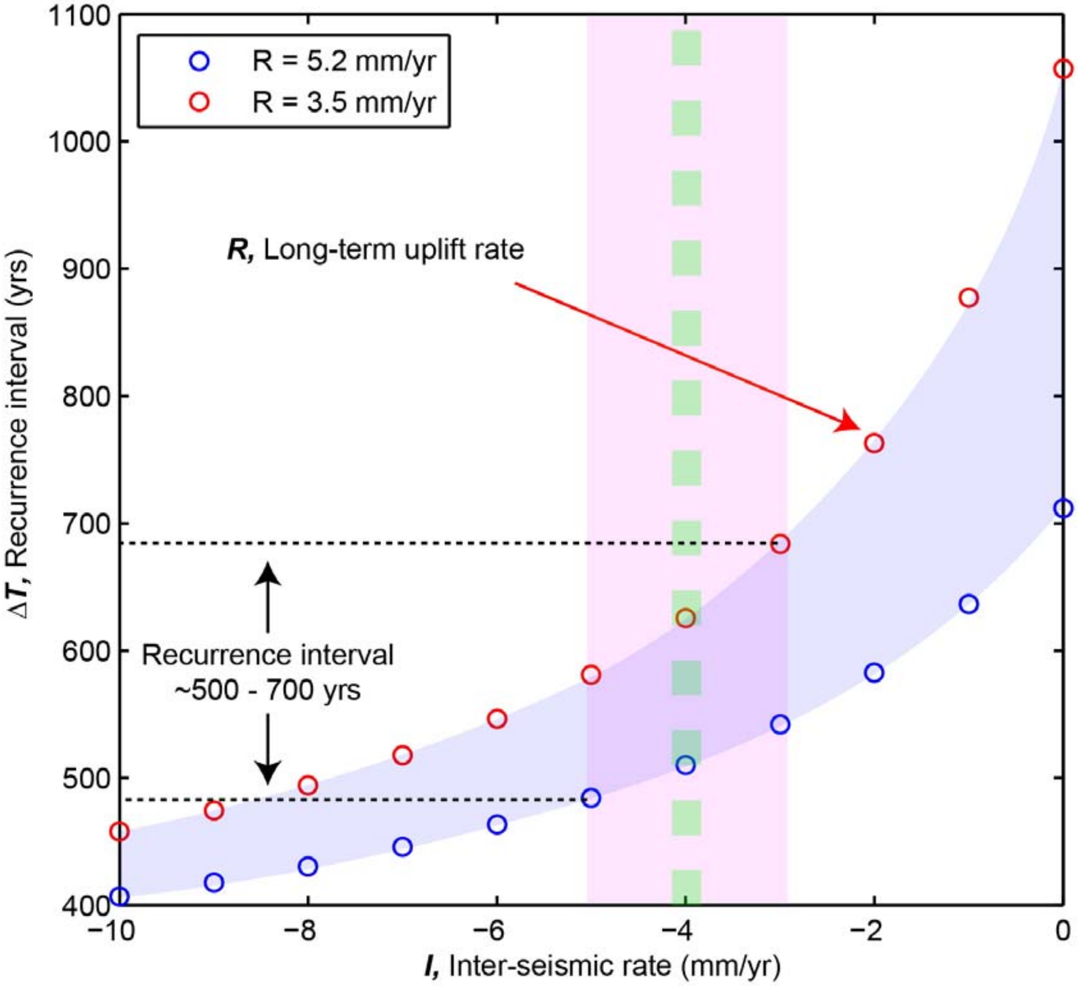

Figure 22. Range of nominal recurrence intervals for 1762-like earthquakes, based on the relationships between the long-term uplift rate and the interseismic subsidence rate at the southwestern corner of Cheduba Island (Ka-I area). We suggest the nominal recurrence interval ranges from ~400 to ~1000 years. Blue shadowed area shows the range of the long-term uplift rate from uplifted corals in Ka-I area, and green dashed line depicts the average interseismic subsidence rate from the elastic deformation model. The pink-colored bar shows the range of the subsidence rates from the model. If the modeled interseismic subsidence rate represents the actual subsidence rate between two seismic events, the recurrence interval of 1762-like events would be ~500 to ~700 years.

Table 1. Radiocarbon ages obtained in this study.

Lab-ID	Sample	Sample type	Measured Age (B.P.)	δ13C (‰)	Conventional Age (B.P.)	Calendar year* (2σ) From		To
Northern Ramree Island								
Beta-285817	KPU-15	Oyster	420 ± 50	-0.10	830 ± 50	1417	to	1618
Eastern Cheduba Island								
Beta-301002	KK-145	Oyster	280 ± 40	-0.30	690 ± 40	1520	to	1686
Beta-301003	KK-146	Oyster	330 ± 70	-0.10	740 ± 70	1454	to	1685
Beta-301004	KK-148	Oyster	350 ± 40	-0.50	760 ± 40	1472	to	1647
Northwestern Cheduba Island								
Beta-301005	TY-140	Oyster	380 ± 40	0.70	800 ± 40	1447	to	1623

* Samples are calibrated using the modeled ocean average Marine09 calibration curve (Reimer et al., 2009).

** We assume $\Delta R = 0$ due to the lack of proper information along the eastern side of Bay of Bengal.

Table 2. U-Th Compositions and ^{230}Th Ages for Fossil Coral Samples of Myanmar by MC-ICP-MS

		^{238}U		^{232}Th		$\delta^{234}U_{initial}$		[^{230}Th/^{238}U]		[^{230}Th/^{232}Th]		Age		Age		Age		Calendar Year		
Sample ID	Type	ppb		ppt		corrected[a,b]		activity[c]		ppm[d]		Uncorrected		Corrected[c,e]		Years (B.P.)[f]		(C.E.)		
Northern Ramree Island																				
KPU-102a	*Coral remains*	2498	±2	2830	±12	148.9	±1.5	0.0731	±0.0002	1065	±5	7187	±24	7145	±49	7084	±49	−5183	to	−5085
KPU-103	*Coral remains*	2516	±2	2764	±9	149.9	±1.7	0.0736	±0.0002	1106	±5	7229	±26	7188	±48	7127	±48	−5226	to	−5129
KPU-104b	*Coral (Round)*	2490	±2	93	±7	148.9	±1.7	0.0669	±0.0001	29568	±2107	6561	±15	6559	±15	6498	±15	−4563	to	−4534
KPU-106	*Coral microatoll*	2505	±2	7273	±38	150.1	±1.6	0.0680	±0.0006	387	±4	6662	±65	6553	±127	6492	±127	−4669	to	−4415
KPU-107	*Coral microatoll*	2672	±2	5090	±13	149.7	±1.7	0.0667	±0.0003	578	±3	6532	±29	6460	±77	6399	±77	−4526	to	−4373
KPU-108	*Coral, overturned*	2673	±2	22559	±74	148.4	±1.7	0.0784	±0.0006	153	±1	7731	±63	7415	±323	7354	±323	−5727	to	−5081
KPU-109a	*Coral microatoll*	2730	±2	446	±7	147.9	±1.8	0.0519	±0.0001	5241	±84	5053	±13	5047	±14	4986	±14	−3050	to	−3022
KPU-110a	*Coral microatoll*	2625	±1	767	±7	150.8	±1.1	0.0634	±0.0001	3585	±33	6199	±15	6189	±18	6128	±18	−4196	to	−4159
Central Western Ramree Island																				
ZC-16a	*Coral*	3023	±3	899	±4	146.9	±1.6	0.0276	±0.00003	154	±2	264	±3	252	±11	192	±11	1746	to	1769
ZC-118a	*Coral microatoll?*	2929	±3	566	±7	149.0	±1.7	0.0287	±0.00004	245	±5	273	±4	266	±8	205	±8	1737	to	1753
ZC-119a	*Coral microatoll?*	2740	±4	1354	±8	151.4	±2.2	0.0296	±0.00005	99	±2	281	±5	263	±19	202	±19	1729	to	1767
ZC-119-1	*Coral microatoll?*	3332	±4	2316	±7	151.9	±2.0	0.0295	±0.00003	70	±1	280	±3	264	±9	203	±9	1738	to	1756
ZC-04	*Coral block*	3045	±3	604	±5.4	149.9	±1.5	0.0363	±0.00003	303	±4	346	±3	338	±8	278	±8	1664	to	1680
Southern Ramree Island																				
KYM-125a	*Coral*	2628	±3	716	±7	150.1	±1.8	0.0722	±0.0002	4378	±43	7094	±20	7084	±22	7023	±22	−5095	to	−5050
KYM-125b	*Coral*	2708	±3	1167	±7	150.0	±2.2	0.0748	±0.0002	2866	±19	7352	±23	7336	±28	7275	±28	−5353	to	−5297
KYM-127	*Coral*	2715	±3	710	±7	150.2	±2.0	0.0720	±0.0002	4546	±47	7068	±22	7058	±24	6997	±24	−5071	to	−5024
TK-130	*Coral block*	2957	±5	2707	±8	153.1	±2.5	0.0543	±0.00006	98	±1	515	±6	481	±35	420	±35	1495	to	1564
TK-131	*Coral block*	2933	±4	1042	±8	153.1	±2.2	0.0587	±0.00005	273	±3	557	±5	544	±14	483	±14	1453	to	1481
TK-132	*Coral block*	2861	±4	642	±7	154.6	±2.4	0.0747	±0.0002	5497	±61	7319	±25	7310	±26	7249	±26	−5326	to	−5273
Ka-Ma, Cheduba Island																				
KM-143a	*Coral remains*	2926	±4	905	±7	147.2	±2.2	0.0163	±0.00007	868	±8	1559	±8	1548	±14	1487	±14	449	to	477
KM-144a	*Coral microatoll*	2733	±4	1289	±7	146.9	±2.3	0.0063	±0.00005	221	±2	603	±5	585	±18	524	±18	1408	to	1445
Ka-I, Cheduba Island																				
KI-152a	*Coral microatoll*	2167	±3	3106	±10	149.2	±2.3	0.0030	±0.00006	35	±1	287	±6	233	±54	172	±54	1724	to	1832
KI-154a	*Coral microatoll*	2390	±4	1272	±7	146.9	±2.4	0.0115	±0.00007	356	±3	1097	±7	1077	±21	1016	±21	913	to	955
KI-155a	*Coral microatoll*	2140	±3	9038	±24	150.4	±2.7	0.0296	±0.0002	116	±1	2846	±23	2688	±160	2627	±160	−837	to	−517
KI-156a	*Coral*	1896	±3	534	±7	149.6	±2.5	0.0230	±0.00009	1350	±18	2210	±10	2199	±15	2138	±15	−203	to	−173
KI-157a	*Coral microatoll*	2339	±4	206	±6	148.3	±2.5	0.0078	±0.00005	1460	±44	745	±5	742	±6	681	±6	1263	to	1276
Sachet, Cheduba Island																				
SC-150a	*Coral remains*	2543	±4	206	±7	148.2	±2.2	0.0068	±0.00005	1395	±46	652	±5	649	±6	588	±6	1355	to	1368
SC-151a	*Coral*	3056	±5	1083	±7	149.6	±2.2	0.0142	±0.00006	662	±5	1359	±6	1346	±15	1285	±15	651	to	680
Man-Aung, Cheduba Island																				
MA-135	*Coral*	3142	±4	2056	±9	147.6	±2.1	0.0135	±0.00008	341	±2	1296	±8	1271	±26	1210	±26	714	to	765
MA-136a	*Coral, overturned*	2688	±3	2554	±9	145.2	±1.9	0.0145	±0.00009	252	±2	1394	±9	1358	±37	1297	±37	616	to	690
MA-136b	*Coral, overturned*	2633	±3	354	±7	148.9	±1.9	0.0145	±0.00006	1782	±34	1389	±6	1384	±8	1323	±8	619	to	635
MA-138b	*Coral*	2393	±5	1284	±7	147.6	±2.9	0.0138	±0.00007	425	±3	1323	±8	1303	±22	1242	±22	686	to	729

Analytical errors are 2σ of the mean.

[a] $\delta^{234}U = ([^{234}U/^{238}U]_{activity} - 1) \times 1000$.

[b] $\delta^{234}U_{initial}$ corrected was calculated based on ^{230}Th age (T), i.e., $\delta^{234}U_{initial} = \delta^{234}U_{measured} \times e^{\lambda_{234} * T}$, and T is corrected age.

[c] $[^{230}Th/^{238}U]_{activity} = 1 - e^{-\lambda_{230}T} + (\delta^{234}U_{measured}/1000)[\lambda_{230}/(\lambda_{230} - \lambda_{234})](1 - e^{-(\lambda_{230} - \lambda_{234})T})$, where T is the age. Decay constants are 9.1577×10^{-6} year^{-1} for ^{230}Th, 2.8263×10^{-6} year^{-1} for ^{234}U [*Cheng et al.*, 2000], and 1.55125×10^{-10} year^{-1} for ^{238}U [*Jaffey et al.*, 1971].

[d] The degree of detrital ^{230}Th contamination is indicated by the [^{230}Th/^{232}Th] atomic ratio instead of the activity ratio.

[e] Age corrections were calculated using an estimated atomic ^{230}Th/^{232}Th ratio of 6.5 ± 6.5 ppm [Zachariasen et al., 1999].

[f] Years before present (B.P.) is referenced to 1950 C.E.

Table 3. Net uplift in Ramree and Cheduba Islands Inferred From Sea Level Indicators

Name	Location		Uplift Feature	Elevation (m)		Reference Level	Elevation (m)		Land-Level Change (m)		Calibrated Net Uplift (m)[a]		Survey Method[b]	Remark
	Latitude	Longitude												
Northern Ramree Island														
E-KPU	19.41	93.53	Coral, microatolls	1.3	±0.2	MLLW	−0.8	±0.2	2.2	±0.3	2.4	±0.3	T.S.	Mid-Holocene
KPU15_O	19.43	93.51	Uplift Oyster	2.2	±0.1	Living oysters	1.2	±0.1	1.0	±0.2	1.2	±0.2	T.S.	
KPU15_N	19.43	93.51	Tidal notch	1.5	±0.1	Active tidal-notch	0.1	±0.2	1.4	±0.3	1.7	±0.3	T.S.	
Central Ramree Island														
Mallet (1878)	19.15	93.6	Raised beach	6.1	–	MSL?	–	±1.3	–	–	6.1	±1.3	–	*Mallet*, 1878
ZC16_C	19.16	93.60	Coral, microatolls	4.2	±0.1	MLLW	−0.8	±0.2	5.0	±0.2	5.3	±0.2	T.S.	Confirmed by U-Th date
ZC16_O	19.16	93.60	Oyster fossils	5.7	±0.1	MHHW	0.9	±0.3	4.8	±0.3	5.1	±0.3	T.S.	
ZC16-SA	19.16	93.60	Shoreline angle	5.8	±0.1	Shoreline angle	0.9	±0.4	5.0	±0.4	5.2	±0.4	T.S.	
ZC04	19.15	93.63	Uplifted platform	5.5	±0.1	Shoreline angle	–	–	5.5	±0.1	5.8	±0.1	L.R.	Min. Constrain
Southern Ramree Island														
KYM	18.90	93.96	Shoreline angle	4.0	±1.0	Shoreline angle	–	–	4.0	±0.1	4.3	±0.1	E.L.	Mid-Holocene
TKN_N	18.89	93.89	Shoreline angle	2.7	±0.1	MHWS	1.3	+ 1.0	1.4	- 1.0	1.6	- 1.0	T.S.	
TKN_N	18.89	93.89	Surge notches	2.7	±0.4	MHWS	1.3	+ 1.0	1.4	- 1.1	1.7	- 1.1	T.S.	
TKC	18.89	93.90	Shoreline angle	2.9	±0.1	Shoreline angle	1.3	±0.1	1.6	±0.1	1.9	±0.1	T.S.	
TKS	18.88	93.91	Shoreline angle	2.6	±0.1	Shoreline angle	1.4	±0.1	1.2	±0.1	1.5	±0.1	T.S.	
WTK	18.90	93.87	Shoreline angle	2.2	±0.4	MHWS	1.3	+ 1.0	0.9	- 1.1	1.1	- 1.1	L.R.	
WTK	18.90	93.88	Shoreline angle	2.9	±0.4	MHWS	1.3	+ 1.0	1.6	- 1.1	1.8	- 1.1	L.R.	
Eastern Ramree Island														
ERM	19.03	93.96	Tidal notch	4.2	±0.5	MSL	0.0	±1.0	4.2	±1.1	4.5	±1.1	R.M.	Mid-Holocene?
ERM	19.03	93.96	Shoreline angle	2.1	±0.5	MHWS	1.4	+ 1.0	0.7	- 1.1	1.0	- 1.1	R.M.	
Man-Aung, Cheduba Island														
MA_C	18.88	93.72	Coral fossils	−0.6	±0.1	MLLW	−0.9	±0.2	0.3	±0.2	0.5	±0.2	L.R.	Min. net uplift since 600 C.E.
MA_B	18.88	93.72	Uplift beach berm			Beach berm			0.8	±0.2	1.1	±0.2	L.R.	
MA_T	18.88	93.74	Uplift platform	2.1	±0.4	MHWS	1.3	–	0.8	±0.4	1.1	±0.4	L.R.	Min. Constrain
Ka-Ma, Cheduba Island														
NW_Che	18.87	93.5	Elevated terrace	4.8	–	MSL?	–	±1.3	–	–	4.8	±1.3	–	*Halsted*, 1841
KM	18.81	93.52	Coral, microatolls	3.4	±0.1	MLLW	−0.8	±0.2	4.2	±0.2	4.5	±0.2	T.S.	Max. Constrain
KM	18.81	93.52	Shoreline angle	3.4	±0.5	MHWS	1.2	+ 1.0	2.2	- 1.1	2.5	- 1.1	T.S.	Min. Constrain
Ka-I, Cheduba Island														
C_Che	18.75	93.6	Elevated terrace?	3.9	–	MSL?	–	±1.3	–	–	3.9	±1.3	–	*Halsted*, 1841
S_Che	18.67	93.7	Elevated terrace	3.6	–	MSL?	–	±1.3	–	–	3.6	±1.3	–	*Halsted*, 1841
KI	18.68	93.64	Coral, microatoll	2.4	±0.1	MLLW	−1.1	±0.2	3.4	±0.2	3.7	±0.2	T.S.	Confirmed by U-Th date
Eastern Cheduba Island														
KK	18.72	93.74	Shoreline angle	2.3	±0.1	MHWS	1.2	+ 1.0	1.1	- 1.0	1.4	- 1.0	T.S.	Min. Constrain
SC	18.70	93.73	Shoreline angle	4.5	±0.5	MHWS	1.2	+ 1.0	3.3	- 1.1	3.5	- 1.1	REF.	Max. Constrain
Northwestern Cheduba Island														
NW Reef	18.93	93.45	Elevated rocks?	6.7	–	MSL?	–	±1.3	–	–	6.7	±1.3	–	*Halsted*, 1841 (unconfirmed)
DY	18.88	93.53	Oysters	8.2	±0.1	MHHW	0.85	±0.3	7.4	±0.3	7.6	±0.3	T.S.	Max. Constrain
	18.88	93.53	Shoreline angle	8.7	±0.5	MHWS	1.2	+ 1.0	7.5	- 1.1	7.8	- 1.1	T.S.	Max. Constrain
Other Islands														
FLAT	18.62	93.77	Elevated terrace	2.1	–	Sea level	0	±1.4	–	–	2.1	±1.4	–	*Halsted*, 1841
Round	18.73	93.81	Shell taxa	1.8		High tide	–	±0.5	–	–	1.8	±0.5	–	*Mallet*, 1878

[a]Calibrated net uplift (m) = Land-level change − Sea level change from the 19th to 21st century. The amount of sea level change is from Jevrejeva et al. [2008].
[b]T.S. = Surveyed by total station; L.R. = surveyed by laser range finder; R.M. = remote measurement; E.L. = surveyed by eye-leveling; REF. = data from published references.

Chapter 5

Surface Ruptures of the M_w 6.8 March 2011 Tarlay Earthquake, Eastern Myanmar

Soe Thura Tun[1], Yu Wang[2, 3], Saw Ngwe Khaing[4], Myo Thant[5], Nyunt Htay[6], Yin Myo Min Htwe[7], Than Myint[1] and Kerry Sieh[3]

1. Myanmar Earthquake Committee, Myanmar Engineering Society, Hlaing University's campus, Yangon, Myanmar
2. Division of Geological and Planetary science, California Institute of Technology, Pasadena, CA 91125, USA
3. Earth Observatory of Singapore, Nanyang Technological University?N2-01A-10B, 50 Nanyang Avenue, Singapore 639798
4. Department of Geology, Hinthada University, Hinthada, Ayeyarwady, Myanmar
5. Department of Geology, University of Yangon, Yangon, Myanmar
6. Myanmar Geosciences Society, Hlaing Universities' campus, Yangon, Myanmar
7. Department of Meteorology and Hydrology, Office building No-5, Ministry of Transport, Naypyidaw, Myanmar

Abstract

Field observations indicate that the M_w 6.8 Tarlay (Myanmar) earthquake on 24 March 2011 resulted from the rupture of a short section of the left-lateral Nam Ma Fault. The Nam Ma Fault is one of many left-lateral faults that comprise the Shan fault system, which has accommodated more than 100 km left-lateral displacement in a triangular area between the Red River Fault and the Sagaing Fault around the eastern Himalayan syntaxis. We document coseismic left-lateral offsets ranging from approximately 10 cm to more than 1.25 m over a 19-km section of the fault from the field investigation and the interpretation of high-resolution satellite imagery. The comparison of the field survey results and the interpretation from the satellite imagery suggests that most of the

offset paddy-related features faded out within one to two years except for those in a few areas at the western part of the fault. Our field measurements also indicate that the magnitude of sinistral offset decreases gradually eastward before terminating inside the Tarlay Basin, along the southern edge of a 2-km-wide releasing stepover.

Our survey confirms that a structurally limited segment of the westernmost part of the Nam Ma Fault was responsible for the Tarlay earthquake. If the rest of the Nam Ma fault moves entirely in a single event, it is capable of generating an M_w 7.7 earthquake between Myanmar and Laos.

Introduction

Myanmar spans a very complex and broad tectonic belt that accommodates the northward translation of the Indian Plate past the Sunda Plate (e.g., Socquet et al., 2006). This motion is primarily expressed by right-lateral slip on the Sagaing Fault, which bisects Myanmar from south to north (Fig.1) (Win Swe, 1970; Curray et al., 1979; Le Dain et al., 1984), and right-lateral oblique convergence across the northern Sunda megathrust beneath the western coast and adjacent Indoburman Ranges (Nielsen et al., 2004; Socquet et al., 2006).

To the east, Myanmar also experiences the tectonic effects of the southward extrusion of southern China around the eastern end of the Himalayan collision zone (e.g., Le Dain et al., 1984; Holt et al., 1991; Lacassin et al., 1998; Wang et al., 1998). This manifests itself as a set of arcuate, predominately left-lateral, southwest-striking faults called the Shan fault system that span the border of China with Vietnam, Laos, Thailand and Myanmar (Fig. 1). The Shan fault system, including the Nanting Fault, the Jing Hong fault, Mengxing Fault, the Nam Ma Fault, the Mae Chan Fault and other parallel left-lateral faults have accommodated more than 100 km of left-lateral displacement at the northern Sunda plate between the Burma and the Southern China plate (Wang et al., in preparation). Together with their conjugate right-lateral faults, this fault system plays an important role in accommodating the deformation around the eastern Himalayan syntaxis, predominantly from China toward Myanmar (e.g., Holt et al., 1991; Wang et al., 1998; Socquet and Pubellier, 2005).

In the past century, the Shan fault system has experienced many significant and destructive earthquakes, including the 1976 Longling earthquake (M_w 6.7), the 1988 Lancang earthquake (M_w 7.0) and the 1995 Menglian earthquake (M_w 6.8) (Fig.1). Although their focal mechanisms and locations are consistent with the geometries of the conjugate right-lateral and left-lateral faults within the Shan fault system, very few surface ruptures associated these events have been documented. Thus, the source of earthquakes and the rupture behaviors of these strike-slip faults remain largely unclear.

The Nam Ma fault is one of these left-lateral faults for which knowledge was very limited. The 215-km-long Nam Ma fault runs approximately N70° E from the Yunnan to Myanmar, appearing as a narrow fault zone from both the LANDSAT imagery and the SRTM topography (Fig. 2). Our geomorphic mapping suggests that both the northeastern and the southwestern end of the Nam Ma fault terminate in transtensional basins, where the fault splays into several left-lateral and normal horsetail faults.

In its central part, the Nam Ma fault offsets the Mekong River channel 12 ± 2 km left-laterally (Lacassin et al., 1998). The Mekong River forms a hairpin river loop immediately south of the Nam Ma fault trace, suggesting that the Nam Ma fault was once a right-lateral fault and may have accommodated about 30 km right-lateral motion before it reactivated as a left-lateral fault between 20 Myr and 5 Myr ago (Lacassin et al., 1998). Based on the regional tectonic history and the offset of the Mekong River, Lacassin et al. (1998) suggests the average slip rate of the Nam Ma fault is about 2.4 to 0.6 mm/yr. This long-term slip rate is about half of the Mengxing fault slip rate (4.8 to

1.2 mm/yr) estimated by the same study, but much faster than the average slip rate of the Mae Chan fault (0.3 to 0.075 mm/yr) in the Thailand area (Fig. 2).

The March 24, 2011 Tarlay earthquake (M_w 6.8) is the first destructive earthquake that struck the Thailand-Myanmar border since the beginning of the 20th century (Engdahl and Villasenor, 2002). The Tarlay earthquake occurred about four years after the M_w 6.3 earthquake in Laos (Fig. 2). The M_w 6.8 event caused at least 74 deaths, 125 injuries and over 3,000 displaced at the Myanmar region (OCHA, 2012). A preliminary assessment in the earthquake-affected area suggests that 12% of buildings were destroyed by the earthquake, while the other 32% became uninhabitable (OCHA, 2011). The earthquake was felt from Kunming to Bangkok and Yangon, over 1000 km from the epicenter (USGS, Significant earthquake archive, 2011).

The size and shallow depth (< 15 km) of the mainshock indicated that the causative fault may have ruptured the surface, and the proximity of mainshock and aftershocks' epicenters to the left-lateral Nam Ma Fault suggested the rupture of a known fault (Fig. 2). Thus, a survey team from the Myanmar Earthquake Committee (MEC) and the Department of Meteorology and Hydrology of Myanmar (DMH) conducted a brief reconnaissance survey at the western part of the Nam Ma fault about two weeks after the earthquake. The main purpose of this reconnaissance survey was to confirm the source of the event, and to document the surface failure soon after the earthquake since most of the offset features may disappear or be altered after the earthquake.

In the pages that follow, we describe our field observations of the coseismic deformation along the westernmost part of the Nam Ma fault associated with the 2011 Tarlay earthquake. This is the first-of-its-kind field study in Myanmar. We also describe our finding from the post-quake high resolution satellite (HRS) imagery. We then discuss the preservation of coseismic deformation features via comparing the field observation and the interpretation of the satellite imagery, and the earthquake potential of the Nam Ma fault.

Field Observations

Logistics, scope of reconnaissance and methods

The part of the Shan Plateau we studied consists of small, cultivated valleys nestled among heavily forested, hilly terrain. The general inaccessibility of the hilly tracts, due to recent rain after the earthquake, led us to focus our 5-day (April 6 to April 10) reconnaissance along roads and in accessible valleys. Thus, our documentation focuses on flat, cultivated terrain within the hilly area (Fig. 3).

In addition to mapping and measuring the fault rupture, we also documented damage to manmade structures and non-tectonic ground failure, such as liquefaction and landslides (Fig. 3). Readers interested in these aspects of the earthquake may visit the electronic supplement to this article, which contains the surveyed waypoint locations and the associated field photographs.

Due to the lack of precise survey instruments (e.g., total stations) immediately after the earthquake, we used a tape measure and compass to measure the strike-slip offsets parallel to the observed average local strike of the fault rupture. We did not attempt to make formal estimates of measurement uncertainties during our short reconnaissance investigation. Rather, we selected offset reference lines (e.g., edges of paddy fields, channels) with the least irregularity and locations where the fault rupture appeared to be the simplest. In general, we believe the measurement errors are less than 10% of the measured value at the place where the fault rupture is clean. However, if tectonic warping near the fault rupture is significant, we are likely underestimating the amount of fault offset by several tens of centimeters. We used a hand-held GPS receiver to determine the location of each measurement and usually recorded the location after the GPS displayed a minimum error.

Field measurements

In this section, we describe the offsets from 47 sites that exhibited tectonic ground rupture. Additional information for these sites is available in the electronic supplement to this article. We begin with the site that exhibited the clearest evidence of tectonic offsets: the paddy fields west-southwest of Kya Ku Ni (Fig. 3).

Kya Ku Ni

The westernmost measurements are from paddy fields approximately 16 km southeast of the USGS epicenter. The trace of the rupture trends northeastward and is particularly clear along a 2-km section of the valley floor west of the Kya Ku Ni (Fig. 4). The rupture exhibits classical left-lateral slip features (Yeats et al., 1997): right-stepping en echelon Reidel shears, clear sinistral offsets of manmade features such as paddy berms and tire tracks, and several centimeters of vertical displacement (Fig. 5). The displacements are large enough to have produced a moletrack (Fig. 5).

Figure 4 shows a map view of the survey locations and 34 measurements along this stretch of paddy fields. Along the central part of the surveyed section, the left-lateral offsets vary by one order of magnitude, from 12 to 125 cm (Table 1). Over 90% of the measured displacements exceed 45 cm, and the average value is 81 cm. We did not find any systematic change in the sinistral offset along this 1-km-long section. We measured offsets of ~1.2 m at three different localities along the rupture; between these localities, sinistral offsets were smaller. Our field observations show some of these small offsets are associated with tectonic warping within several meters of the moletrack (e.g., Fig. 5d). Such off-fault warping may partly explain the large variation in offsets along this short section of the fault, as previous studies have suggested for other recent strike-slip ruptures (e.g., Rockwell et al., 2002; Rockwell and Klinger, 2011). Nevertheless, the multiple observations of large offsets indicate that the maximum sinistral offset for this section is approximately 1.25 m.

We found no clear measurable offset features in the paddy fields west of the westernmost recorded observations (Waypoint 364; Fig. 4). The moletrack was clear up to 400 m west-southwest of the westernmost measured offset at the Kya Ku Ni site (Fig. 4). Some of the paddy berms were clearly disrupted by the moletrack (Fig. 5e). Unfortunately, these field boundaries were highly oblique to the moletrack and were clearly warped across the wide rupture zone; we were unable to directly measure these offsets. We did not attempt to follow the rupture farther west into uncultivated hills. However, the analysis of the optical HRS imagery suggests the rupture extends at least 3 km westward beyond our last surveyed point (Fig. 3).

Pu Ho Mein

The cultivated valley near Pu Ho Mein village was easily accessible and we were able to observe how the fault rupture extended from the Kya Ku Ni area. Figure 6 shows locations of ground failure.

We found a small number of sites with tectonic fractures in this vicinity. Many localities clearly experienced ground failure, but none was convincingly tectonic. Most of these locations were on the southern slope of the valley, south of the fault trace mapped from the SRTM dataset and other optical satellite images (Fig. 6). Because of the dense vegetation on the hill slope, we were unable to make continuous observations following the surface rupture over this approximately 2-km-long section. Instead, we connect our surveyed tectonic fracture locations to map the extent of the fault rupture.

Compared to the Kya Ku Ni areas, the surface fault slip was much smaller at the Pu Oh Mein site. Approximately 2.4 km southwest of the village, we observed right-stepping en-echelon cracks trending 70° across a field (Waypoint 533; Fig. 7a, b). Although these en-echelon cracks disrupted the paddy berms in the field, no measurable offsets were found at these field boundaries (Fig. 7a). The lack of a clear moletrack and the small amounts of crack opening suggest that the sinistral offset at this location was no more than 10 or 20 cm near the surface. Approximately 1 km southwest of the town (Waypoint 522, 523), a series of right-stepping en echelon cracks suggest a few cm of sinistral slip across the fault (Fig. 7c, d). These observations suggest that the fault slips are relatively minor along the shallow part of the fault, where the surface deformation may be dominated by rotation and warping near the rupture.

Not all of the ground fissures that we mapped in Pu Ho Mein area can be linked by a single line of rupture. For example, we observed several ground fissures develop within about three hundred meters from the projection of the fault rupture at the Pu Ho Mein village. The orientation of these fissures is similar to the strike of the fault; thus we cannot exclude the hypothesis that these fissures are resulting from secondary faulting within the fault damage zone.

Tarlay

Northeast of Pu Ho Mein, we find the fault rupture near the Tarlay Township (Fig. 8). Comparing with the evidence at Kya Ku Ni area, the evidence for tectonic rupture was more subdued, and the magnitude of left-lateral slip was substantially less than at Kyi Ku Ni. Among these other sites, the ruptures near the Tarlay Township were the largest. Most of the observed ground failure was related to slumping and liquefaction along riverbanks. Away from the river, standing water in rice paddies and the height of the rice crop made tracing the rupture more difficult than in the drier paddy fields west of Kya Ku Ni. In Tarlay, the amount of slip was much smaller, so there were no moletracks or vertical displacements to help guide our search.

In general, most of the observed ground-failure locations are aligned with the fault rupture that we mapped from the western foothills (Fig. 3). However, the fault ruptures east of Tarlay do not match the pre-existing geomorphic features that we mapped from the LANDAT imagery. Instead, the fault rupture lies ~200 meters south of our pre-mapped fault trace, where the surface is covered by young and loose fluvial deposits along the Nam Lam River (Fig. 8).

Four locations within 2 km along the projected fault trace, based upon our mapping of the fault using SRTM topography and LANDSAT imagery, exhibit left-lateral displacements of 15 to 53 cm. The westernmost site (Waypoint 293) yielded the largest offset, but its offset is complex and was in the earthen abutment of the Tarlay Bridge. The stone bridge across the Nam Lam River experienced minor damage (Fig. 9a). At the southern end of the bridge, the eastern side of the abutment displayed a simple, 53-cm sinistral offset. The sinistral offset on the western side of the abutment was much smaller, but the slip sense is consistent with the left-lateral slip observed at the eastern side of the bridge. This offset cannot be explained by failure of the embankment fill and likely reflects tectonic offset.

Approximately 600 m northeast of the bridge, there were clear 40-cm sinistral offsets of a narrow irrigation channel and its two shoulders (Waypoint 547; Fig. 9b). Our observation also suggests that near the rupture trace was significant surface warping that we can’t measure in the field. Approximately 1.2 km farther northeast were two fractures that offset a paddy embankment by a total of 37 cm (Waypoint 577; Fig. 9c), showing the distributed deformation along the fault trace. Two fractures 500 m to the northeast strike substantially more northerly (30° to 70°) than the overall strike of the fault zone, with sinistral offsets of 36 and 15 cm. Another 300 m to the northeast, the offset in the paddy edge suggests 15 cm of sinistral offset along the projected surface rupture (Waypoint 609; Fig. 9d). We also found two enigmatic, but sharp, normal-dextral offsets in a paddy berm just south of the offset at Waypoint 609. These two offsets were oriented differently (30°) than the general strike of the fault (70°) and correspond to a right-lateral offset of the field boundary of 10 and 13 cm, respectively. We suspect these normal-dextral offsets are part of the en-echelon fractures south of the main fault rupture. However, we cannot trace their extent in the rice paddies.

The field survey team also visited two sites (Waypoints 276, 290) at the northern edge of the Tarlay basin, where the main trace of the Nam Ma Fault was apparent in the geomorphology (Fig.

3; Fig. 8). Observations at both sites suggest that this part of the main surface trace of the Nam Ma Fault experienced only very minor, if any, fault slip during the 2011 earthquake.

One of these sites is east of the town of Tarlay, where several discontinuous fissures developed along a road that is nearly parallel to the Nam Ma Fault (Waypoint 276; Fig. 8). One of these fissures cut across a bamboo fence in a field; however, no offset or bend in the fence was observed across the fissure (Fig. 10a). The second site is at the mountain front northwest of Tarlay (Waypoint 290; Fig. 8), where two nearly parallel ground fractures developed during the earthquake according to the villager. These fractures trend about N30E. The northern fracture showed no sign of offset where it crossed the boundary of a paved road (Fig. 10b). The other fissure, on the bottom of a fishpond south of the road, displayed no disruptions along the pond's bank.

The lack of offset features along the main trace of the Nam Ma Fault suggests that the fault at the northern edge of the basin did not play an important role in the March 2011 earthquake. Most of the observable ground failures were within the flat basin area, where they developed along the eastern projection of the fault trace southwest of the town of Tarlay.

Eastern end of the rupture

Two areas to the northeast of Tarlay display sinistral offsets that are approximately along the projection of the fault trace from the southwest. Because we found only two disturbed locations that are far apart, we are not sure whether the easternmost survey locations reflect tectonic rupture. Figure 11 shows these two locations along the northeastern extension of the surface rupture observed at Tarlay. At Waypoint 327, we measured a 20-cm sinistral horizontal offset and a 20-cm vertical offset down to the south at the edge of a paddy (Fig. 12a). Nearby, at Waypoint 325, the measured sinistral offset is 30 cm and the vertical offset is several centimeters (Fig. 12b).

The ruptures at these two locations strike roughly parallel to the general strike of the surface rupture and are aligned with other surface ruptures extending from the Tarlay area. These fractures may represent the northeastern-most extent of tectonic rupture in 2011.

Farther northeast, we observed a group of ground failures associated with considerable liquefaction (Waypoint 302 to 311; Fig. 11). Most of the fractures had a clear dip-slip component, but none exhibited clear sinistral offset. We measured vertical offsets of 15 cm at Waypoint 302 (Fig. 12c) and 40 cm at Waypoint 311, with a clear northward tilting near the fracture (Fig. 12e). These may be tectonic in origin, but they are so small that we cannot be certain. Also, the strikes of these features (approximately 20°) differed from the general orientation of the rupture (70°), which makes their origin uncertain. In fact, the widely distributed liquefaction suggests intense reworking of near-surface sediments along these surveyed cracks, thus we can not exclude the possibility that these surface cracks are resulting from the sand ejection and ground compaction during the earthquake.

Remote sensing observations

Kya Ku Ni and further west

To complement our field survey, we also use the post-quake high resolution satellite (HRS) images to study and quantify the fault rupture along the westernmost segment of the Nam Ma fault. The spatial resolution of the HRS images (WorldView-2) is about 0.5 m, and they were collected between Feb 2012 and Feb 2013. We especially focus on the area near the Kya Ku Ni and further southwest, as our survey shows the left-lateral offset at this location is large enough (> 0.5 m) to be measured from the images. We also search the area near Pu Ho Mein and the area northeast of Tarlay, to see if there are any preserved fault traces that we did not map during our reconnaissance survey in April 2011.

At the Kya Ku Ni site, our mapping shows that about 8 paddy field boundaries still preserve a measurable left-lateral deflection in the Sep 2012 image. The left-lateral displacements measured from the Sep 2012 image range from 1.1 to 1.6 m at Kya Ku Ni section (Fig. 3). These remote measurements are systematically higher than the field survey results from Apr 2011, but within the uncertainty of our HRS imagery (±0.5 m; e.g., Klinger et al., 2005).

West of the Kya Ku Ni area, our mapping from HRS image suggests that the fault rupture extends at least 3 km further southwest from our last surveyed point (Fig. 3). The comparison of the pre-quake HRS image from the Google Earth and the 2013 WorldView-2 image shows that the rupture clearly transects through the paddy fields west of the Kya Ku Ni surveyed sites, showing a nearly one-km-long moletrack in the field (Fig. 13a). The paddy field boundaries and roads across the rupture show clearly left-lateral deflections in both the 2012 and 2013 HRS images. Our measurements from the HRS images suggest that most of the left-lateral offsets are about 1 to 1.5 m, whereas the maximum left-lateral offset is 2.5 ± 0.5 m at one location. The average 1 to 1.5 m left-lateral offset is similar to the estimation from the pixel-tracking analysis of the L-Band radar image (Wang et al., 2013), and similar to the measurements at Kya Ku Ni site. We also notice that two small sag ponds appear at the north side of the moletrack, suggesting the block north of the fault was dropped down approximately 10-20 cm during or after the earthquake. Further west, the rupture trace becomes unclear in the HRS images. Only few paddy field boundaries still show left-lateral deflection two years after the earthquake.

Figure 13b shows the western-most location where we are able to confirm the fault rupture from the 2013 HRS image, about 3 km from the last surveyed point at the Kya Ku Ni site. The rupture transects through a narrow river valley and forms a sag pond northwest of the fault trace. We estimate the left-lateral offset to be about 1 m from the left-lateral deflection of one paddy field berm. The fault rupture soon propagates into the mountains west of this point and can hardly be traced from the satellite image. Approximately 3 km further west, about 6 km southwest of our last field observation point, another E-W running scarp appears in the 2013 HRS image that we suspect to be the 2011 fault rupture. However, we are not able to identify any offset feature along the scarp as the field boundaries are nearly parallel to the suspect scarp (Fig. 13c).

Discussion

Compilation of results

The left-lateral and vertical-slip distributions of the 24 March 2011 earthquake rupture are presented in Figure 3, which shows the 46 left-lateral offsets that were recorded in the field, and 26 left-lateral offsets that were mapped from 2012 and 2013 HRS images. We interpret all but the easternmost two field measurement (Waypoints 302 and 311) to be tectonic in origin. Table 1 lists data relevant to these field measurements.

Difficult logistics prevented a comprehensive post-earthquake survey of the entire rupture during the 5 days in the field. Nevertheless, the data we collected suggest that the amount of left-lateral offset decreased gradually northeastward from more than a meter near Kya Ku Ni to several tens of centimeters east of Tarlay.

Among our field observations, we find most of the surface ruptures within the Tarlay basin accompanied by significant surface warping near the fault, especially in the water-saturated rice paddy fields. Field observations suggest that the surface warping sometimes occurred over ten meters from the fault rupture (e.g., Fig. 9b), which makes it difficult to measure the tectonic warping without knowing its original geometry before the earthquake. Thus our measurements within the Tarlay basin likely underestimate the tectonic offset across the fault trace. Alternatively, we suggest the horizontal offsets near the fault are smaller than one meter in the Tarlay basin, as we can not observe any paddy field berms’ left-lateral deflection from the HRS imagery. If the tectonic displacements in the Tarlay basin are greater than one meter, such as in the fault offsets west of the

Kya Ku Ni village, we should be able to observe left-lateral deflections on the features that cross the fault unless the displacement is highly distributed.

Our observations also showed that the block south of the fault dropped along most of the surveyed sections, with few exceptions west of Kya Ku Ni. This observation agrees with the moment tensor solution for the Tarlay earthquake from the Global CMT project, which indicates that the fault-slip plane dips steeply to the south and has a very minor normal-slip component.

The rupture length of the 2011 Tarlay earthquake

Our field survey results and remote sensing interpretation imply that the total rupture length is at least 19 km during the 2011 earthquake (Fig. 3). The ruptures primarily follow a previously mapped fault segment along the westernmost part of the Nam Ma Fault (Fig. 2; Fig. 3). The western end of this fault segment is approximately 9 km west of our westernmost survey point, and its eastern end is within a basin that reflects a 5-km-wide dilatational stepover of the Nam Ma Fault. The 2011 rupture was confined within this westernmost section of the Nam Ma Fault, which encourages us to consider the length of the fault segment as the maximum rupture length of the Tarlay earthquake.

Based on the geomorphological evidence from the 90-m SRTM, 15-m Landsat imagery and 0.5-m HRS images, the fault trace does not extend more than 9 km southwest from our southwesternmost measurement. We did not observe any other faults in the remote sensing dataset near the southwestern tip of the ground rupture. Therefore, the southwestward extension of the surface rupture could not exceed the tip of the fault. To the northeast, the surface rupture most likely terminates between Waypoints 327 and 304 in the center of the basin. If the fault terminated very close to Waypoint 304, the rupture would not extend more than 5 km northeast of our easternmost measurement point (Waypoint 327). As a result, the maximum plausible surface rupture length of the Tarlay earthquake is 30 km from the western hills to the basin.

Our estimate of the fault rupture length is very similar to that based on the earthquake magnitude and the empirical relationship from Wells and Coppersmith (1994). On average, a shallow M_w 6.8 strike-slip earthquake produces an approximately 30-km-long surface rupture and about 1 m of maximum surface displacement (Wells and Coppersmith, 1994). The similarity between our interpretation and the global data suggests that the entire westernmost segment of the Nam Ma fault ruptured during the 2011 M_w 6.8 Tarlay earthquake.

Preservation of offset features

Our analysis of post-earthquake HRS images suggests that most of the offset features, if not all, become invisible in the paddy fields east of the Kya Ku Ni area about 1 year after the earthquake. At the Kya Ku Ni site, we found that about half of the offset features that experienced more than 80 cm offset disappeared within 1.5 years after the earthquake. This observation suggests most of the offset features that experienced less than 1 m horizontal displacement in a similar agricultural environment may soon disappear after the earthquake. For features that show about 1 to 1.5 m horizontal displacement, our observation from the HRS images suggests they are commonly modified by the famers, but still retain the general left-lateral deflection across the fault even 2 years after the earthquake. Thus, we are still able to measure their horizontal displacement 1.5 to 2 years later, with a similar outcome to the field survey results obtained right after the earthquake (Fig. 3).

At some locations, we find that not only the offset paddy field boundaries and roads were preserved, but also the fault rupture trace remained visible in the cultivated fields from the satellite imagery. One example is the site just west of Kya Ku Ni, where the left-lateral displacements are similar to those at the Kya Ku Ni area (Fig. 3). Although both of these sites share similar left-lateral displacements, the fault rupture traces at Kya Ku Ni had completely disappeared in the Sep 2012 image, while the adjacent section is still visible in the paddy fields (Fig. 13a).

We attribute this different degree of preservation to vertical displacement of the fault. At the Kya Ku Ni site, our field observations suggest that the vertical displacement was very minor across the fault; therefore we believe that the farmers could easily fix the fault rupture before the coming growing season. To the west, our mapping from 2012 and 2013 HRS images suggests that the block north of the fault dropped several tens centimeters along the preserved fault trace. It is likely that the farmers tend to convert these rupture traces to the field boundaries and thus the fault traces were preserved in the field.

Seismic potential of the rest of the Nam Ma Fault

Only the westernmost 20 to 30 km of the Nam Ma Fault ruptured during the 2011 Tarlay earthquake. The rest of the 215-km-long Nam Ma Fault has not been associated with any major earthquakes for at least the past century. The historical earthquake record in Thailand suggests that the last major event that struck the nearby Chiang Rai city was in A.D. 1715 (Bott et al., 1997). This more-than-a-century-long quiescence of the fault suggests significant stress accumulation in the blocks bounding the majority of the Nam Ma Fault.

For the westernmost 30-km-long segment of the Nam Ma fault, we can estimate the frequency of Tarlay-like earthquakes by calculating the seismic moment accumulation rate on the given fault plane. We consider that the fault plane that generates the Tarlay earthquake is 30 km long, and the downdip limit of the rupture patch is similar to the locking depth of the central Sagaing fault, at 15 km in depth (Vigny et al, 2003). We also adapt the 2.4 to 0.6 mm/yr averaged Nam Ma fault slip rate from Lacassin et al. (1998) and a reference crustal shear modulus of 32 GPa to calculate the seismic moment accumulation rate on the given fault plane. Our result suggests that the westernmost segment of the Nam Ma fault can produce an M_w 6.8 earthquake about every 600 to 2300 years, depending on the slip accumulation rate on the fault plane. This 600 to 2300 year interval is very close to the estimated interval (520 to 2100 years) from the field observed maximum surface offset (1.25 m), but as twice long as the recurrence interval (260 to 1050 years) estimated from the predicted average displacement (0.63 m) of an M_w 6.8 earthquake from Wells and Coppersmith (1994).

The rest of the Nam Ma fault may capable of generating a M_w 7.7 to 7.8 earthquake if the rest of ~195 km long fault ruptured at once (Wells and Coppersmith, 1994; Blaser et al., 2010). By assuming the same fault rupture width (15 km) and the slip rate (2.4 to 0.6 mm/yr) throughout the entire Nam Ma fault, we expect that a magnitude 7.7 earthquake would occur approximately every 1800 to 7200 years on the 215-km-long Nam Ma fault. Whether this type of earthquake occurred on the Nam Ma fault or not is currently unclear, as the information of historical earthquakes is spotty and only covers a short period of time (Bott et al., 1997). Future paleoseismological study will significantly improve our knowledge of the Nam Ma fault slip behavior.

Conclusions

Our field observations confirm that the westernmost segment of the Nam Ma Fault caused the Tarlay earthquake of 24 March 2011. This is the first time that any coseismic fault surface ruptures have been mapped in the Myanmar area after an earthquake. The N70E trending surface ruptures are consistent with the Global CMT parameters for the earthquake. Field observations confirm that fault slip was almost purely sinistral, with minor dip-slip displacement along the fault rupture. The observed maximum offset of 1.25 m occurred approximately 9 km west of the western end of the topographically defined fault trace. The amount of sinistral offset decreased gradually eastward before terminating within the Tarlay Basin, along the southern edge of a 2-km-wide releasing stepover of the Nam Ma fault.

Our observations suggest that the surface rupture extends more than 19 km along a 30-km-long, previously mapped fault segment that is structurally distinct from the main trace of the

Nam Ma Fault. If this entire fault segment slipped during the mainshock, the maximum rupture length is likely to be about 30 km from the foothills west of the town of Tarlay to the dilatational basin. This is very similar to the average length of surface ruptures for an M_w 6.8 earthquake. Judging from the lack of observed rupture along other sections of the fault and the similarity of the rupture length to the global dataset, we believe the westernmost segment of the Nam Ma fault is solely responsible for the Tarlay earthquake. Such an earthquake may recur on the same section of the fault every 600 to 2300 years, based on the long-term slip rate of the Nam Ma Fault. The rest of the Nam Ma fault is capable of generating an M_w 7.7 to 7.8 earthquake if the fault ruptured all at once. Future paleoseismological study is important to improve our understanding of seismic hazard in this area.

Data and Resources

Earthquake epicenters used in this study were collected from the NEIC PDE catalog: http://earthquake.usgs.gov/earthquakes/eqarchives/epic/ (last accessed Nov 2011). The CMT solutions were obtained from the Global Centroid Moment Tensor Project database using www.globalcmt.org/CMTsearch.html (last accessed Nov 2011).

The digital elevation data were obtained from the SRTM 90m database: http://srtm.csi.cgiar.org/ (last accessed: June 2012). The Landsat imagery is collected from the USGS Earth Resources Observation and Science Center (EROS) searched using http://glovis.usgs.gov/ (last access June 2012).

Acknowledgments

We deeply appreciate the assistance of the Venerable U Wazibate, who supplied our field party with a four-wheel-drive vehicle. We greatly appreciate the Public Works Department

(Ministry of Construction), the Department of Meteorology and Hydrology (Ministry of Transport) and Ahkhar ethnic leaders in Tachileik City for their assistance in field planning. We also thank Paul Tapponnier and Yves Descatoire for their help in guiding our fieldwork in the days after the earthquake. Discussion with Win Swe helped improve the quality of the manuscript. Financial support for the field reconnaissance came from the Myanmar Geosciences Society, the Myanmar Engineering Society, the Myanmar Earthquake Committee, Resource & Environment Myanmar Co. Ltd. and Thingazar Tours.

References

Blaser, L., F. Kruger, M. Ohrnberger & F. Scherbaum (2010), Scaling relations of earthquake source parameter estimates with special focus on subduction environment, Bull. seism. Soc. Am., 100(6), 2914–2926.

Bott, J., I. Wong, S. Prachuab, B. Wechbunthung, C. Hinthong and S. Surapirome (1997), Contemporary seismicity in northern Thailand and its tectonic implications, In: Dheeradilok, P., (Ed.), Proceedings of the International Conference on Stratigraphy and Tectonic Evolution of Southeast Asia and the South Pacific, Department of Mineral Resources, Bangkok, 453 – 464.

Curray, J., D. Moore, L. Lawver, F. Emmel, R. Raitt, M. Henry, and R. Kieckhefer (1979). Tectonics of the Andaman Sea and Burma, Am. Assoc. Pet. Geol. Mem., 29 189-198.

DeMets, C., R.G. Gordon, and D.F. Argus (2010), Geologically current plate motions, Geophys. J. Int., 181(1), 1-80, doi: 10.1111/j.1365-246X.2009.04491.x.

Engdahl, E.R. & A. Villasenor (2002), Global Seismicity: 1900–1999, International Handbook of Earthquake and Engineering Seismology, v. 81A, Elsevier Science Ltd., Amsterdam, The Netherlands, 665–690.

Holt, W. E., J. F. Ni, T. C. Wallace, and A. J. Haines (1991), The active tectonics of the eastern Himalayan syntaxis and surrounding regions, J. Geophys. Res., 96(B9), 14595–14632, doi:10.1029/91JB01021.

Klinger, Y., X. Xu, P. Tapponnier, J. V. der Woerd, C. Lasserre and Geoffrey King (2005), High-Resolution Satellite Imagery Mapping of the Surface Rupture and Slip Distribution of the Mw ~7.8, 14 November 2001 Kokoxili Earthquake, Kunlun Fault, Northern Tibet, China, Bull. Seism. Soc. Am. 95(5) 1970-1987.

Kreemer, C., W.E. Holt, and A.J. Haines (2003), An integrated global model of present-day plate motions and plate boundary deformation. Geophys. J. Int., 154: 8–34. doi: 10.1046/j.1365-246X.2003.01917.x.

Lacassin, R., A. Replumaz, and P. Herve Leloup (1998). Hairpin river loops and slip-sense inversion on southeast Asian strike-slip faults, Geology, 26(8) 703-706.

Le Dain, A., P. Tapponnier, and P. Molnar (1984). Active faulting and tectonics of Burma and surrounding regions, J. Geophys. Res., 89(B1) 453-472.

Nielsen, C., N. Chamot-rooke and C. Rangin (2004). From partial to full strain partitioning along the Indo-Burmese hyper-oblique subduction: Mar. Geol. 209 303-327.

OCHA (2011) Myanmar: Earthquake in Shan State Situation Report No. 6, UN Office for the Coordination of Humanitarian Affairs.

OCHA (2012) Myanmar: Natural Disasters 2002-2012, Map, UN Office for the Coordination of Humanitarian Affairs.

Prawirodirdjo, L. and Y. Bock, (2004), Instantaneous global plate motion model from 12 years of continuous GPS observations, J. Geophys. Res., 109, B08405, doi:10.1029/2003JB002944.

Rockwell, T. K., S. Lindvall, T. Dawson, R. Langridge, W. Lettis, and Y. Klinger (2002). lateral offsets on surveyed cultural features resulting from the 1999 Izmit and Duzce Earthquakes, Turkey, Bull. Seism. Soc. Am. 92(1) 79-94.

Rockwell, T.K. and Y. Klinger (2011). The variability of along-strike co-seismic slip: A new example from the Imperial fault of southern California. 2nd INQUA-IGCP-567 International Workshop on Active Tectonics, Earthquake Geology, Archaeology and Engineering, Corinth, Greece (2011), 200-203.

Sella, G. F., T. H. Dixon, and A. Mao (2002), REVEL: A model for recent plate velocities from space geodesy, J. Geophys. Res., 107(B4), 2081, doi:10.1029/2000JB000033.

Socquet, A., and M. Pubellier (2005), Cenozoic deformation in western Yunnan (China-Myanmar border), J. Asian Earth Sci., 24, 495–515.

Socquet, A., C. Vigny, N. Chamot-Rooke, W. Simons, C. Rangin, and B. Ambrosius (2006). India and Sunda plates motion and deformation along their boundary in Myanmar determined by GPS, J. Geophys. Res., 111 B05406.

Vigny, C., A. Socquet, C. Rangin, N. Chamot-Rooke, M. Pubellier, M.-N. Bouin, G. Bertrand, and M. Becker, (2003). Present-day crustal deformation around Sagaing fault, Myanmar, J. Geophys. Res., 108(B11), 2533, doi:10.1029/2002JB001999.

Wang, E., B. C. Burchfiel, L. H. Royden, L. Chen, J. Chen, W. Li, (1998), Late Cenozoic Xianshuihe-Xiaojiang and Red River fault systems of southwestern Sichuan and central Yunnan, China, Spec. Pap. Geol. Soc. Am., 327, 108.

Wang, Y.Z., E.N. Wang, Z.K. Shen, M. Wang, W.J. Gan, X.J. Qiao, G.J. Meng, T.M. Li, W. Tao, Y.L. Yang, J. Cheng and P. Li, (2008) GPS-constrained inversion of present-day slip rates along major faults of the Sichuan-Yunnan region, China. Science in China Series D: Earth Sciences, 51(9), 1267-1283.

Wang, Y., Y.-N. Lin, M. Simons, Soe Thura Tun, (2013), Shallow rupture of the 2011 Tarlay earthquake (Mw 6.8), Eastern Myanmar, Bull. Seism. Soc. Am. In review.

Win Swe (1970). Rift-features at the Sagaing-Tagaung ridge: In Proc. 5th Burma Research Congress, Rangoon.

Wells, D. L., and K. J. Coppersmith (1994). New Empirical Relationships Among Magnitude, Rupture Length, Rupture Width, Rupture Area, and Surface Displacement, Bull. Seism. Soc. Am. 84(4) 974-1002.

Yeats, R. S., K. Sieh, and C. R. Allen, (1997). The geology of earthquakes, New York, Oxford Univ. Press.

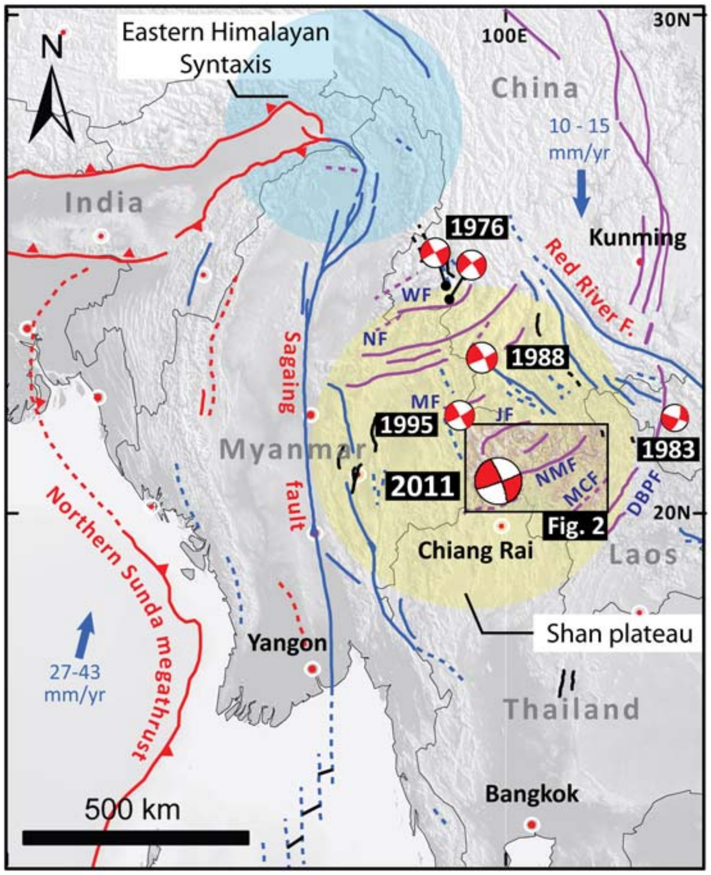

Figure 1. The neotectonic context of Myanmar and adjacent regions. The Shan fault system in eastern Myanmar lies between the Sagaing fault and the Red River fault, and is one of the three major fault systems that dominate the active tectonics of the Myanmar region. Its predominantly southwest-striking left-lateral faults span a 700-km wide section of the Chinese border with Vietnam, Laos, Thailand and Myanmar. The western part of the Nam Ma fault in the southern part of the Shan fault system produced the 2011 Tarlay earthquake. The active faults are based upon analysis of bathymetry and SRTM topography. Red line = reserves fault, Blue line = right-lateral fault, and purple line = left-lateral fault. The focal mechanisms of recent large (M_w >6.5, since 1976) earthquakes are from the Global CMT project. The plate motion rate relative to the Sunda plate is calculated from various plate-rotation models (Sella et al., 2002; Prawirodirdjo and Bock, 2004; Kreemer et al., 2003; Socquet et al., 2006; Wang et al., 2008; DeMets et al., 2010). WF: Wanding fault; NF: Nanting fault; MF: Menglian fault; JF: Jing Hong fault; NMF: Nam Ma fault; DBPF: Dien Bien Phu fault; CMF: Mae Chan Fault.

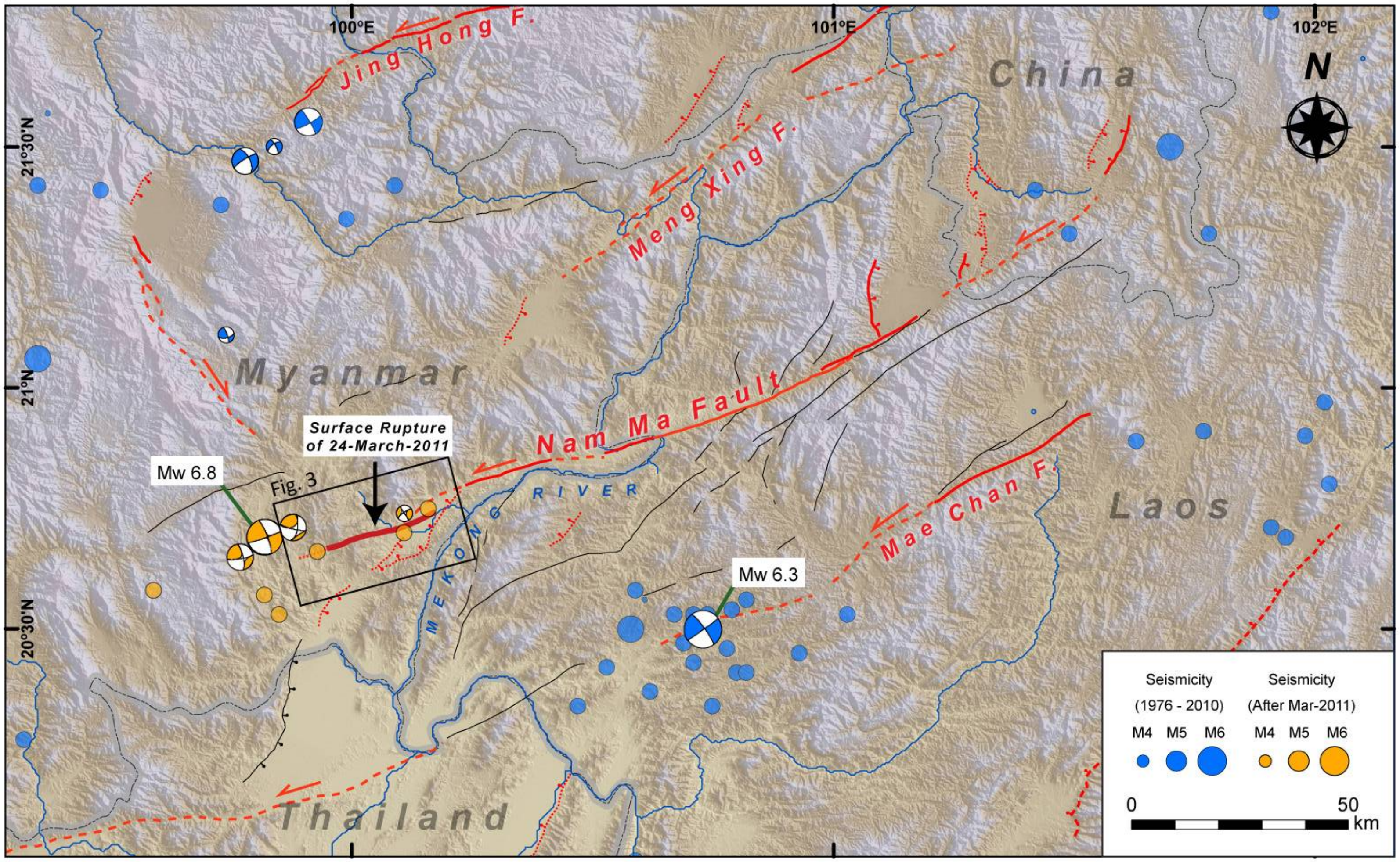

Figure 2. Map of the active faults around the Nam Ma Fault, based on geomorphological analysis of optical imagery and SRTM topography. The surface rupture in 2011 occurred along the thick bold line. The basemap is shaded 90-m SRTM topography.

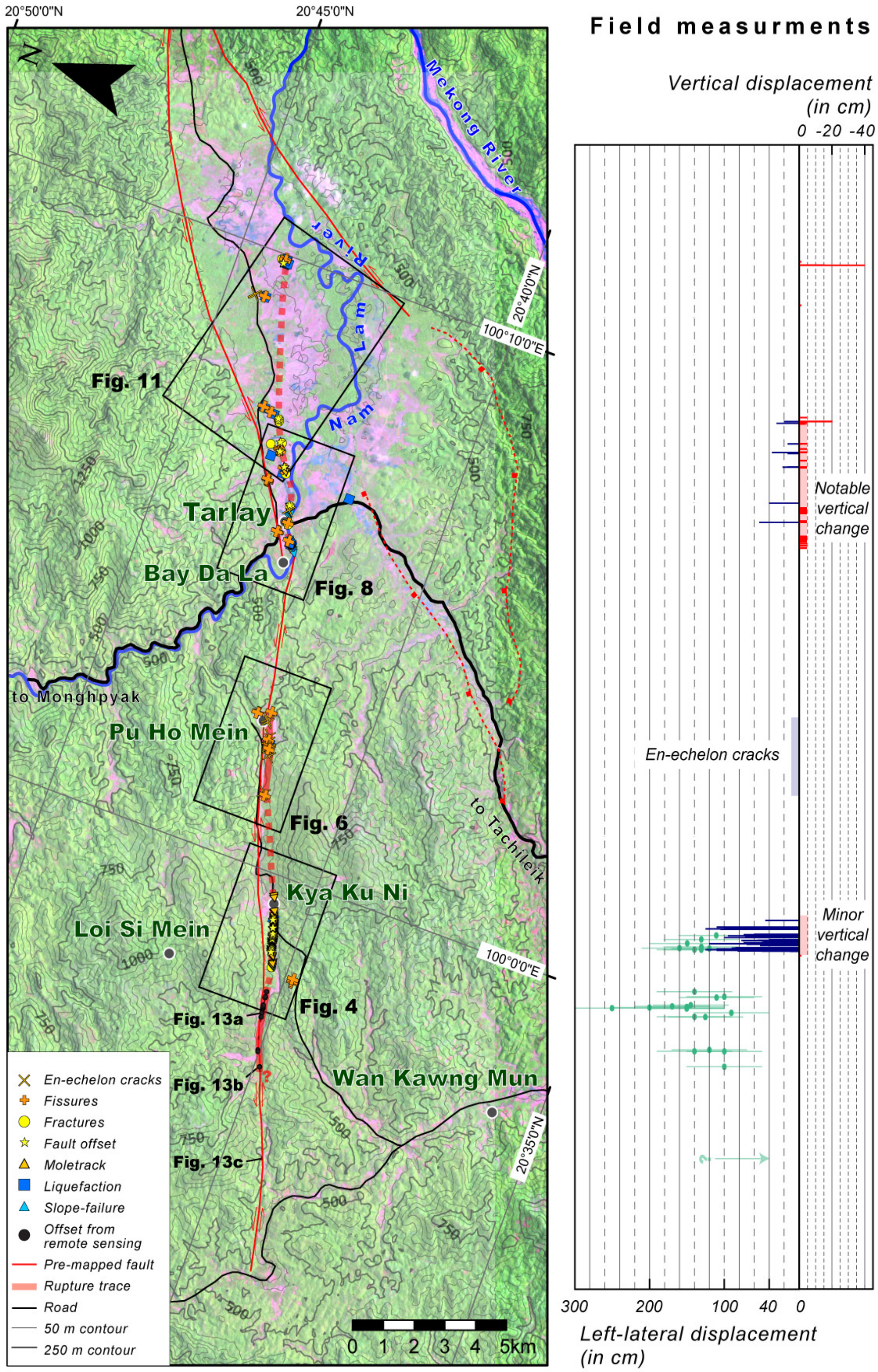

Figure 3. The surface rupture and surveyed locations for the 24 March 2011 Tarlay earthquake along the westernmost section of the Nam Ma Fault. The green dot shows the surface displacement measured from 0.5-m WorldView-2 images after earthquake. Blue

column is the field measurement result. Blue shaded area shows the area where we observe only en-echelon cracks along the fault. Red line is the vertical displacement measured in the field.

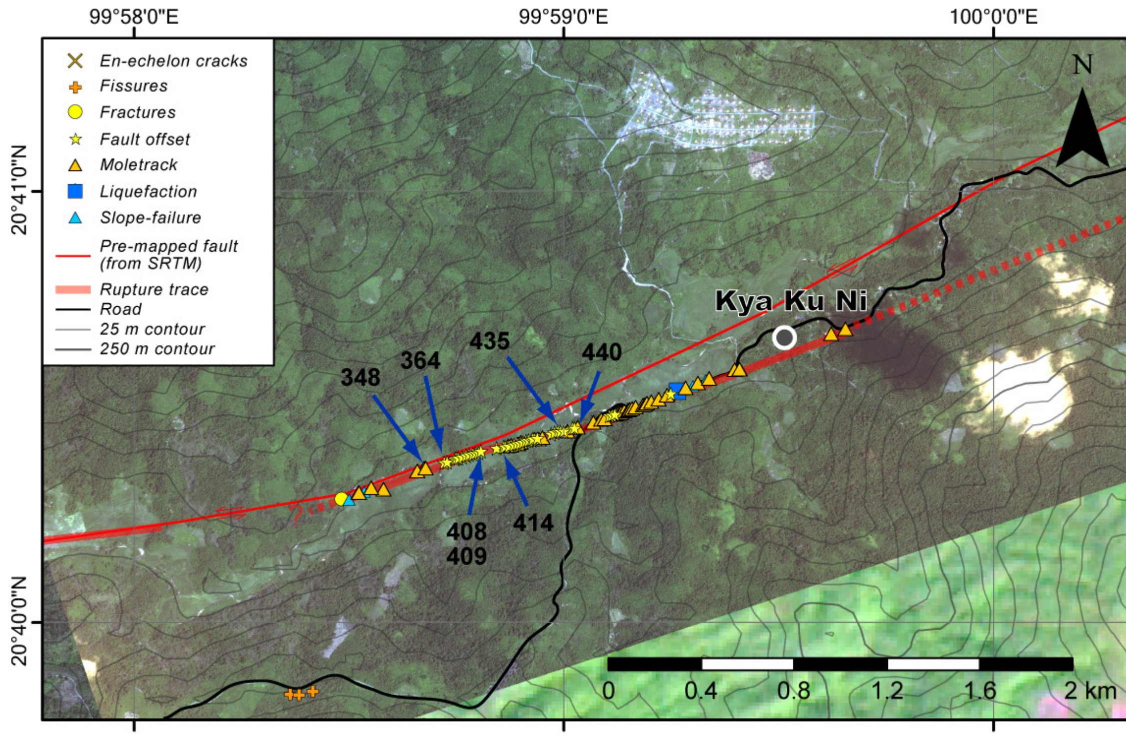

Figure 4. Map of the westernmost mapped fault rupture crossing paddy fields west of Kya Ku Ni village. The basemap is 0.5-m WorldView-2 imagery collected on Sep 29, 2012. The 25 m contour is generated from the 90-m SRTM dataset.

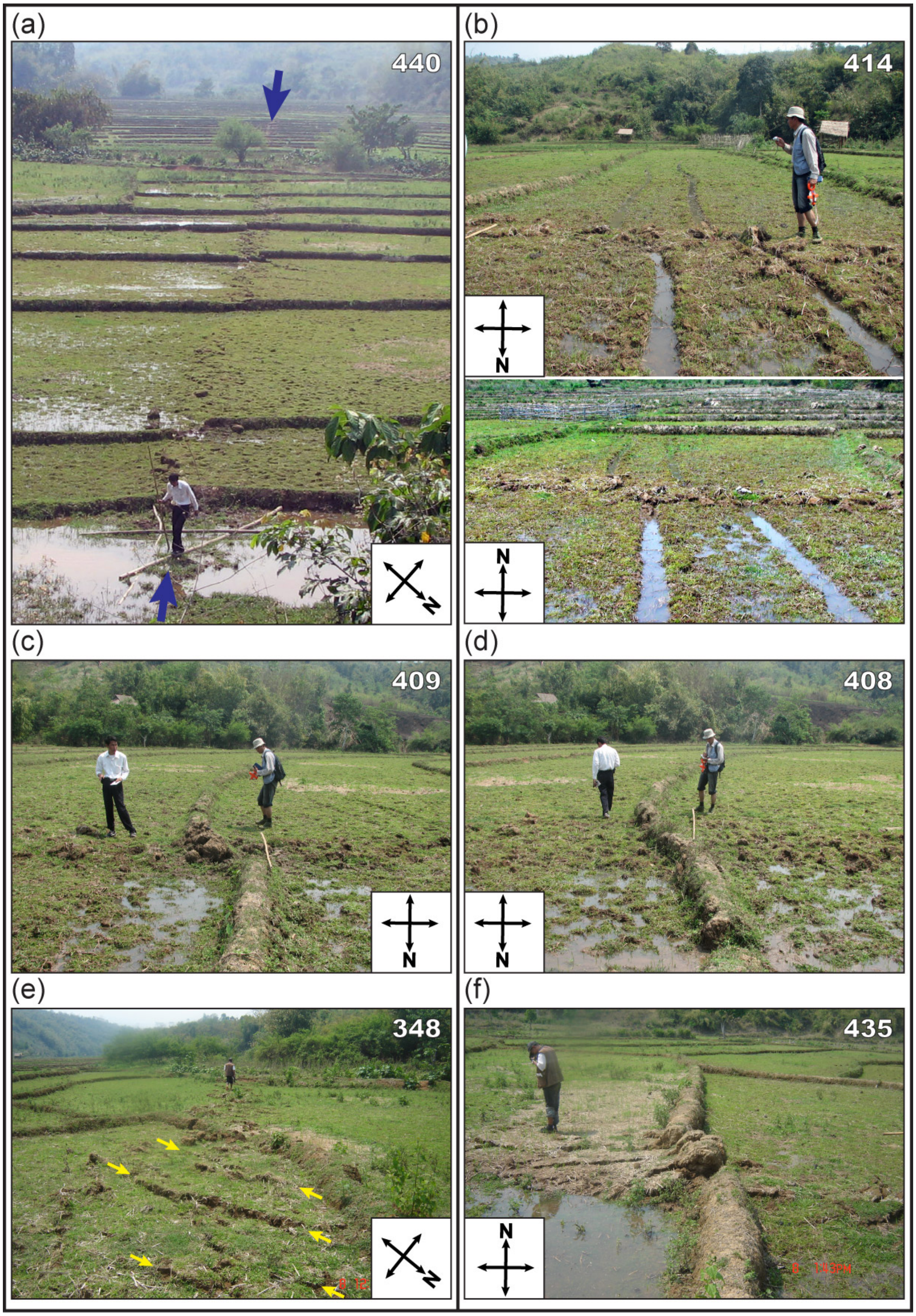

Figure 5. Photographs of the fault rupture in the paddy fields southwest of Kya Ku Ni.

(a) Overview of the rupture, looking southwestward from near Waypoint 440. Note the right-stepping Riedel shears, the moletrack and the small vertical component of slip implied by the water on the south (left) side of the fault rupture.
(b) 52-cm sinistral offset of two vehicle tracks at Waypoint 414, viewed from the south and the north. Note the likely tectonic warping of tracks on the far side of the fault in the upper photo.
(c) 85-cm sinistral offset and surface warping of the paddy boundary at Waypoint 409.
(d) 90-cm sinistral surface warping across the fault zone at Waypoint 408, just west of Waypoint 409. The paddy boundary is clearly warped across the rupture zone.
(e) 3-m-wide right-stepping Riedel shears zone at Waypoint 348.
(f) 72-cm left-lateral offset of a paddy divider near Waypoint 435. Note the subsidence of the south side, the moletrack and the right-stepping Riedel shears.

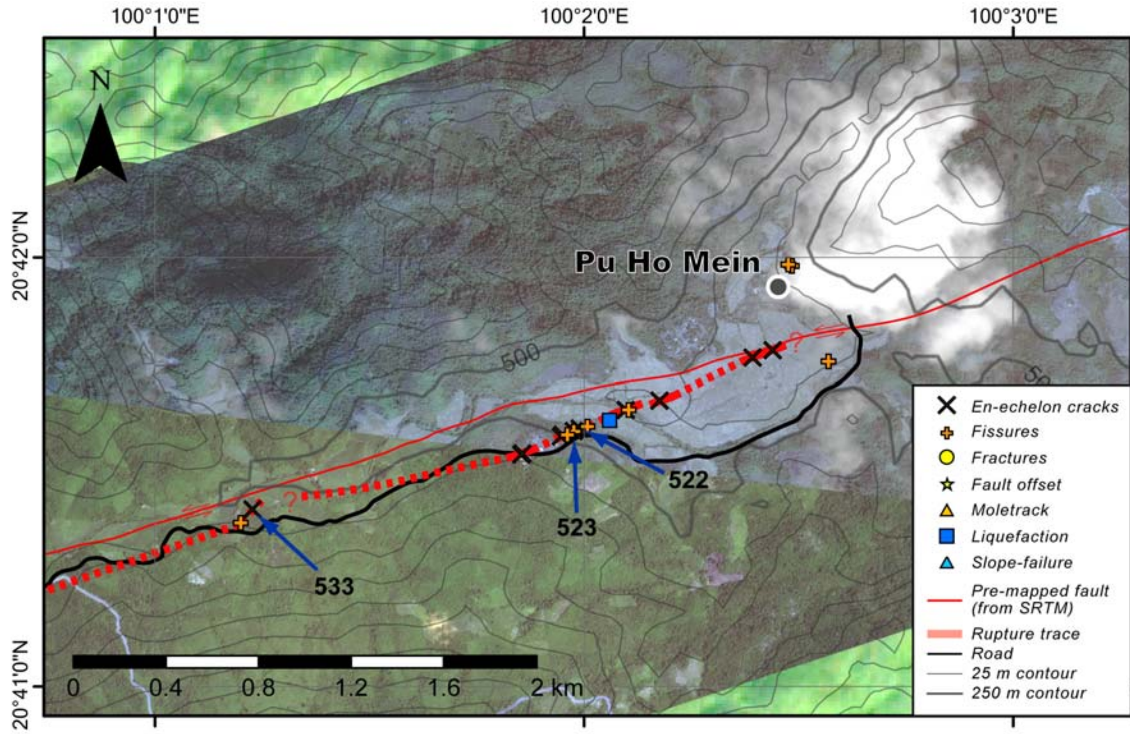

Figure 6. Map view of the area surrounding Pu Ho Mein village, showing locations of where we documented ground failure. Right-stepping en echelon cracks and other fractures suggest sinistral tectonic rupture. The basemap is from 0.5-m WorldView-2 imagery collected on Feb 12, 2012 and Sep 29, 2012. The 25 m contour is generated from the 90-m SRTM dataset.

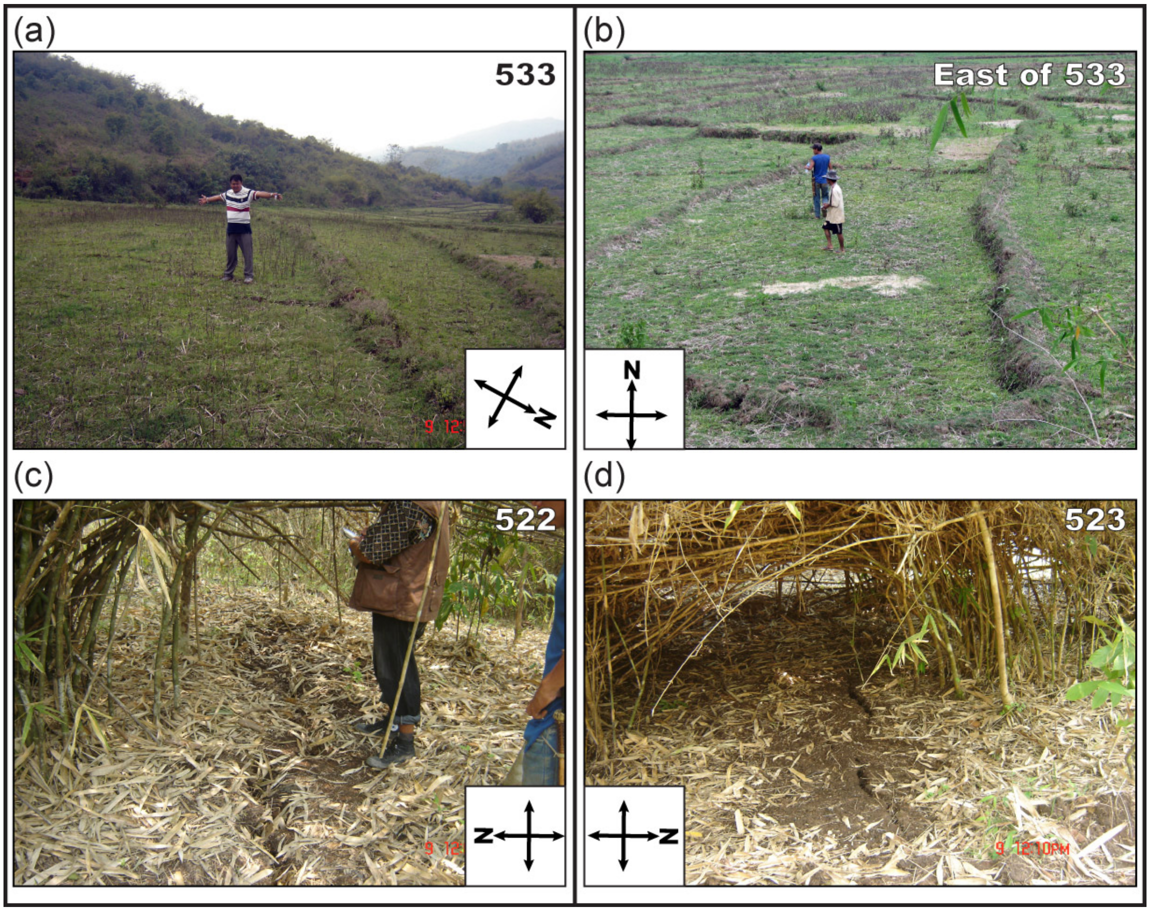

Figure 7. Photographs from three locations in the valley near Pu Ho Mein that may have experienced sinistral tectonic rupture.
(a) Right-stepping en echelon fractures across a dry paddy field at Waypoint 533.
(b) A long fracture and sand blows in paddy fields east of Waypoint 533.
(c) Right-stepping en echelon fractures at Waypoint 522 suggest a few cm of sinistral slip.
(d) Right-stepping en echelon cracks at Waypoint 523 suggest a few cm of sinistral slip.

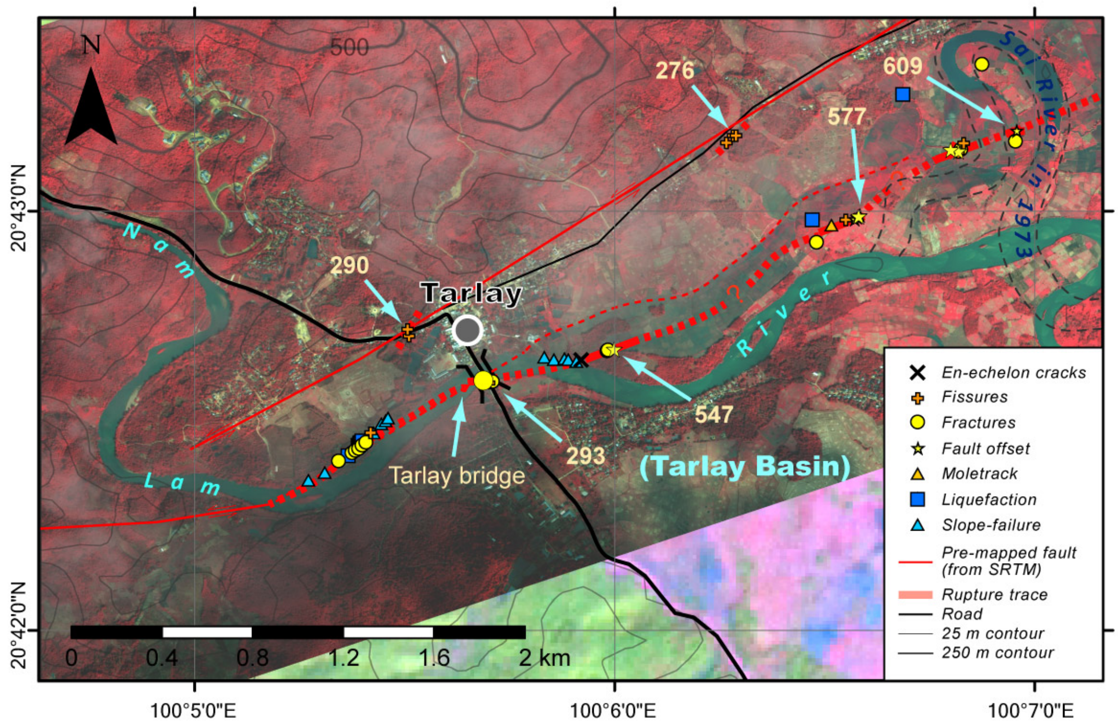

Figure 8. Map of sites inspected in the vicinity of the Tarlay Township, showing several locations of left-lateral offset, which coincide with other ground-failure locations along the Nam Lam River. The thin dashed line shows the inferred fault location south of Tarlay from the 15-m LANDSAT and other high-resolution satellite imagery. The basemap is the 0.5-m false-color WorldView-2 image collected on Feb 12, 2012.

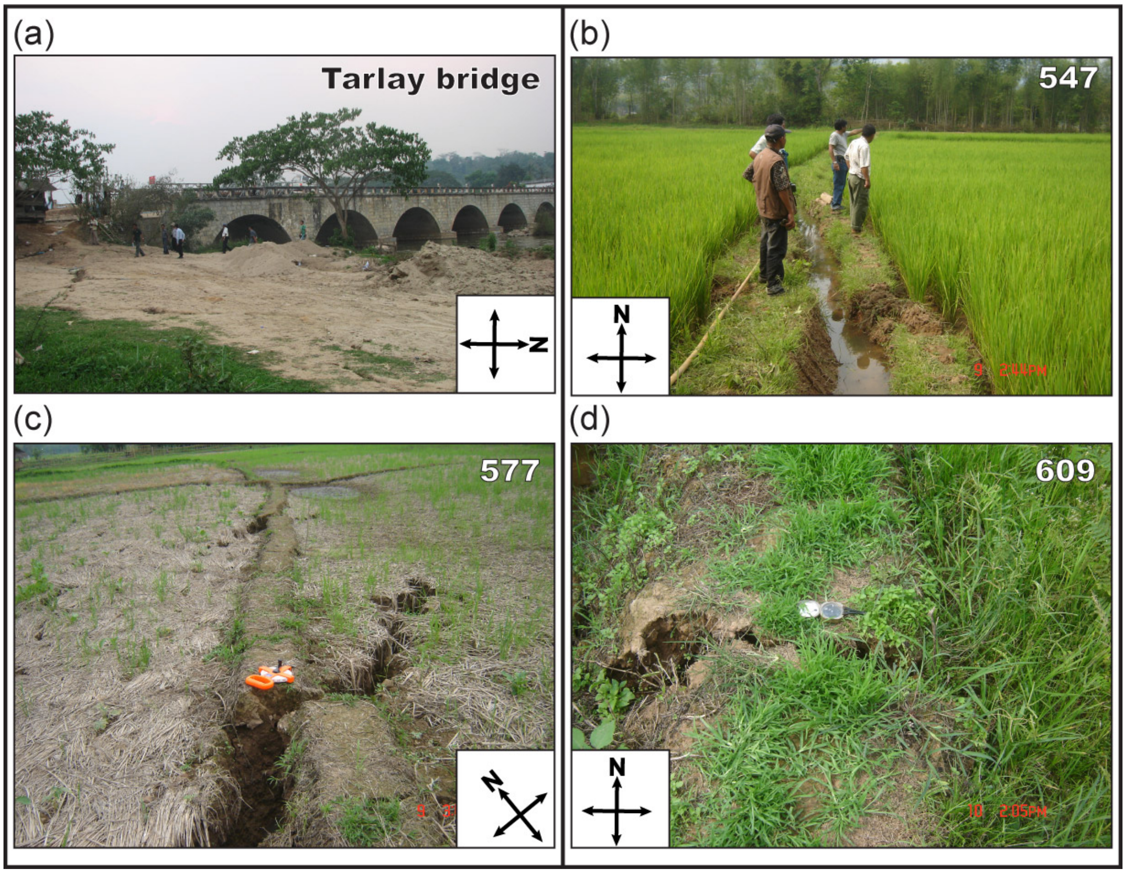

Figure 9. Photographs of left-lateral displacements near Tarlay that appear to be tectonic.
(a) Westward view of a faulted bridge embankment and the mostly undisturbed stone bridge across a river.
(b) 40-cm left-lateral offset on a narrow rupture crossing an irrigation channel and two paddy berms at Waypoint 547.
(c) Dual traces of the fault rupture offset a paddy field by 22 cm (in the foreground) and 15 cm (in the background) at Waypoint 577. The vertical displacement is a few cm at this location.
(d) 15-cm left-lateral offset of the paddy field boundary near Waypoint 609. The south side moved slightly down.

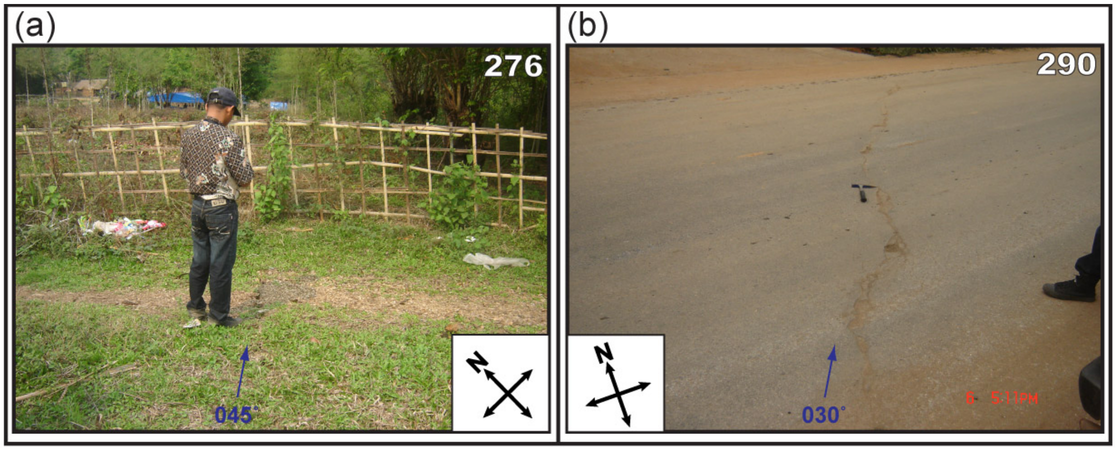

Figure 10. Photographs of ground cracks and fissures north of Tarlay.

(a) Ground fissure near the mountain front east of Tarlay, near Waypoint 276. The bamboo fence next to the fissure shows no horizontal displacement.

(b) Surface cracks across the paved road northwest of Tarlay, near Waypoint 290. The edge of the pavement does not clearly show horizontal displacement along the crack.

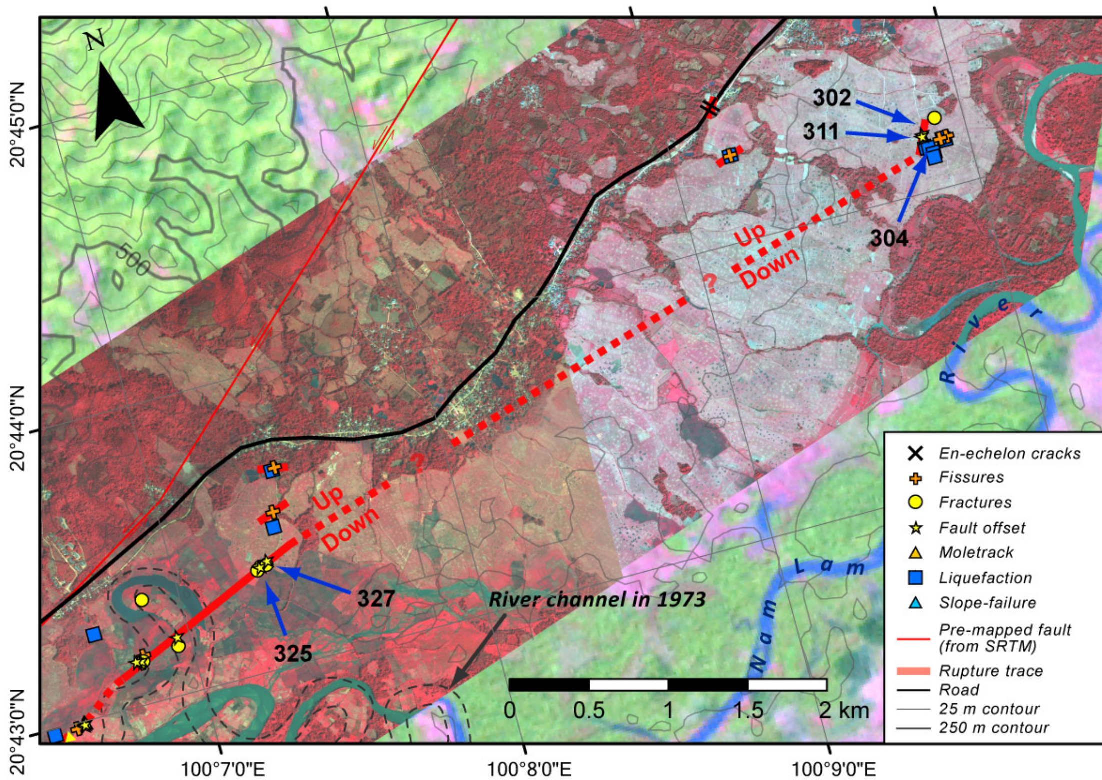

Figure 11. Map of the sites with horizontal offsets east of Tarlay.

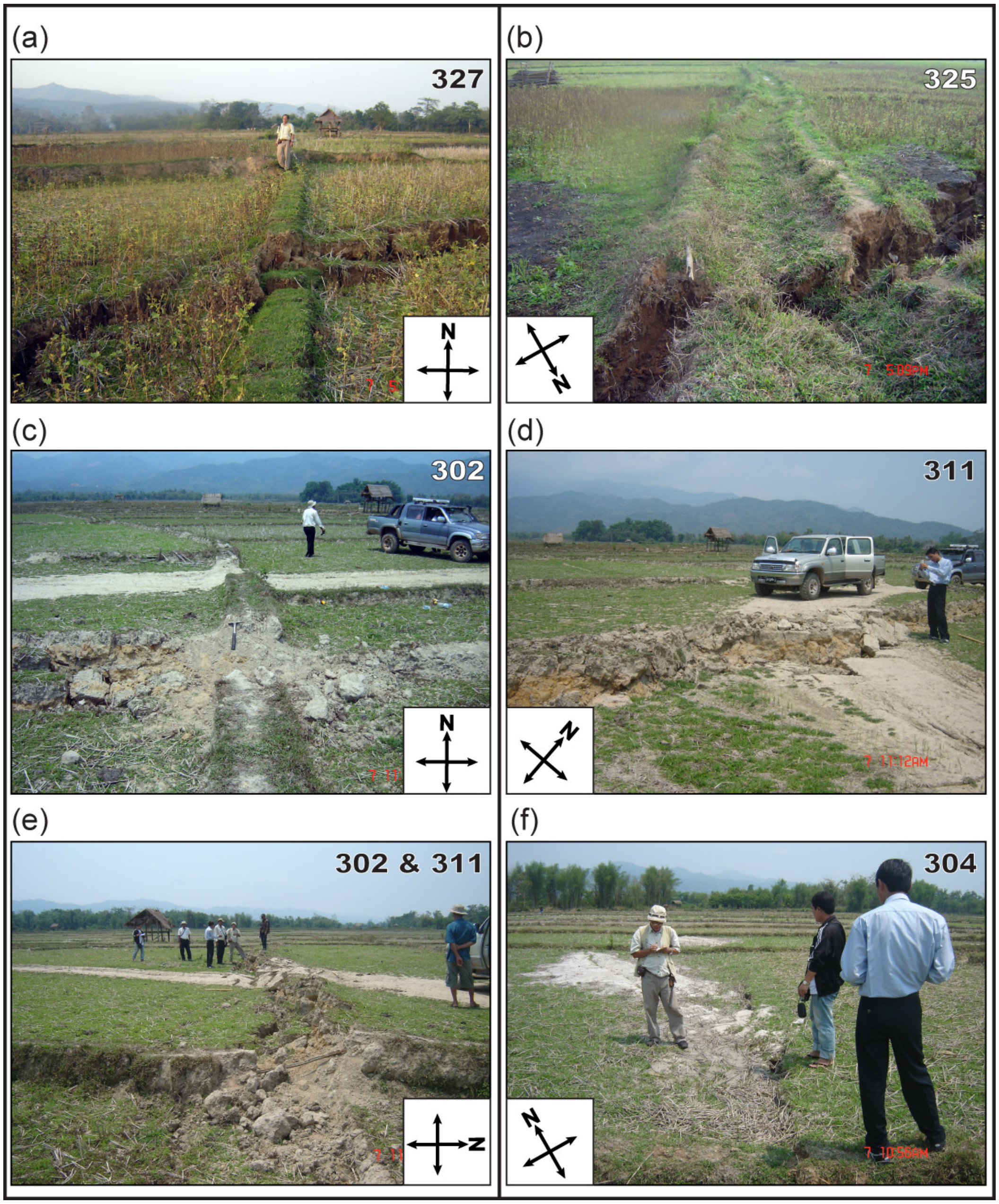

Figure 12. Photos of plausible tectonic offsets east of Tarlay.

(a) Left-lateral offset of 20 cm at Waypoint 327. The vertical displacement is 20 cm.
(b) Left-lateral offset is 30 cm at Waypoint 325. No vertical displacement.
(c) Right-lateral offset of 6 cm at Waypoint 302. The vertical displacement is approximately 15 cm.
(d) Purely dip-slip offset of 40 cm at Waypoint 311, close to Waypoint 302.
(e) A southwestward view of the surface rupture at Waypoints 302 and 311.
(f) A long fissure and accompanying sand blows at Waypoint 304, south of the fault rupture.

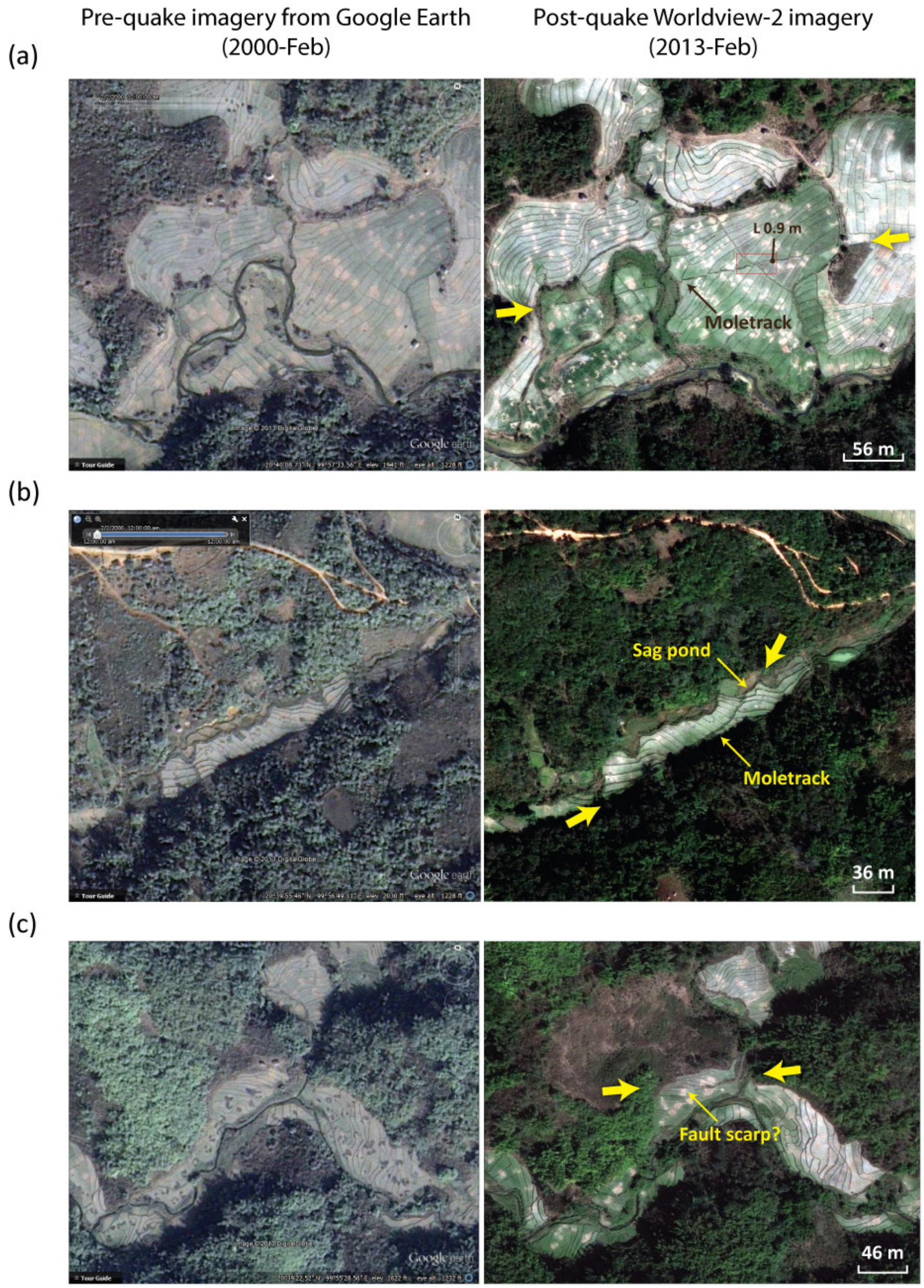

Figure 13. The pre-earthquake and post-earthquake HRS image west of the Kya Ku Ni site. (a) The preserved fault trace in the paddy fields about 1-km west of our last surveyed surface ruptures location, showing more than 0.9 m left-lateral displacement along the rupture. (b) The preserved fault trace and sag pond in the riverbed. See text for detail discussion. (c) The suspect preserved fault rupture in the river valley, about 6-km west of our last field surveyed location.

Table 1. Field measurements of the surface rupture of the 24 March 2011 Tarlay earthquake.

Waypoint	Date	Location (WGS 84)		Strike of feature	Offset (in cm)		Description
		LAT	LON		L-lateral offset	Vertical offset	
293	6-Apr-11	20.70992	100.09478	E-W	53	S	Offset of Tarlay bridge (eastern side)
302	7-Apr-11	20.73650	100.16414	20º	-6.36	15.24	Offset paddy field berm
311	7-Apr-11	20.73639	100.16408	25º		40	Offset dirt road and field
325	7-Apr-11	20.72244	100.12150	70º	30	S	Offset paddy field berm and dirt road
327	7-Apr-11	20.72272	100.12197	70º	20	20	offset field berm and fractures at fields
364	8-Apr-11	20.67292	99.97911	70º	12	S	Offset paddy field berm
368	8-Apr-11	20.67294	99.97917	70º	50		Offset paddy field berm
371	8-Apr-11	20.67294	99.97925	70º	82		Offset paddy field berm
373	8-Apr-11	20.67300	99.97939	70º	110		Offset paddy field berm and water channel
374	8-Apr-11	20.67306	99.97956	70º	125		Offset paddy field berm
403	8-Apr-11	20.67308	99.97967	70º	100		Offset paddy field berm
405	8-Apr-11	20.67311	99.97981	70º	110		Offset paddy field berm
407	8-Apr-11	20.67314	99.97992	70º	80		Offset paddy field berm
408	8-Apr-11	20.67317	99.98003	70º	90		Offset paddy field berm
409	8-Apr-11	20.67322	99.98011	70º	85		Offset paddy field berm
414	8-Apr-11	20.67333	99.98072	70º	52		Offset paddy field berm
416	8-Apr-11	20.67339	99.98100	70º	70		Offset paddy field berm and water channel
418	8-Apr-11	20.67342	99.98119	70º	120		Offset paddy field berm
420	8-Apr-11	20.67347	99.98139	70º	74		Offset paddy field berm
421	8-Apr-11	20.67350	99.98153	70º	47		Offset paddy field berm
425	8-Apr-11	20.67361	99.98186	70º	50		Offset paddy field berm
426	8-Apr-11	20.67364	99.98197	70º	75		Offset paddy field berm
427	8-Apr-11	20.67367	99.98208	70º	77		Offset paddy field berm, and moletrack
428	8-Apr-11	20.67369	99.98214	70º	55		Offset paddy field berm
429	8-Apr-11	20.67372	99.98231	70º	40		Offset paddy field berm
432	8-Apr-11	20.67389	99.98283	70º	100		Offset paddy field berm
434	8-Apr-11	20.67397	99.98311	70º	55		Offset paddy field berm
435	8-Apr-11	20.67397	99.98319	70º	72		Offset paddy field berm
436	8-Apr-11	20.67400	99.98333	70º	95		Offset paddy field berm

Table 1. Field measurements of the surface rupture of the 24 March 2011 Tarlay earthquake. (Continued)

Waypoint	Date	Location (WGS 84)		Strike of feature	Offset (in cm)		Description
		LAT	LON		L-lateral offset	Vertical offset	
438	8-Apr-11	20.67411	99.98367	70º	74		Offset paddy field berm
439	8-Apr-11	20.67411	99.98375	70º	60		Offset paddy field berm
444	8-Apr-11	20.67458	99.98511	70º	105		Offset paddy field berm
445	8-Apr-11	20.67458	99.98511	70º	105		Offset paddy field berm
446	8-Apr-11	20.67461	99.98519	70º	125		Offset paddy field berm
447	8-Apr-11	20.67464	99.98531	70º	100		Offset paddy field berm
449	8-Apr-11	20.67469	99.98542	70º	80		Offset paddy field berm
452	8-Apr-11	20.67481	99.98567	70º	110		Offset paddy field berm, and moletrack
453	8-Apr-11	20.67481	99.98569	70º	110		Offset paddy field berm, and moletrack
465	8-Apr-11	20.67544	99.98747	70º	45		Offset oblique paddy field berm
547	9-Apr-11	20.71117	100.09997	70º	40		Offset paddy field berm and water channel
564	9-Apr-11	20.71117	100.09997	70º	15		Offset paddy field berm
577	9-Apr-11	20.71644	100.10967	70º	22	S	Offset paddy field berm
578	9-Apr-11	20.71647	100.10972	70º	15		Offset paddy field berm
608	10-Apr-11	20.71983	100.11594	88º	15	SE	Offset paddy field berm
609	10-Apr-11	20.71983	100.11594	88º	15	SE	Offset paddy field berm
610	10-Apr-11	20.71944	100.11589	30º	-10	SE	Right-lateral offset of paddy field berm
613	10-Apr-11	20.71911	100.11372	30º	-13	SE	Right-lateral offset of paddy field berm
615	10-Apr-11	20.71903	100.11364	70º	36	S	Offset paddy field berm
617	10-Apr-11	20.71908	100.11333	30º	15		Disturbed field boundary

Chapter 6

Shallow rupture of the 2011 Tarlay earthquake (M_w 6.8), Eastern Myanmar.

Yu Wang[1, 2], Yu-Nung Nina Lin[1], Mark Simons[3], Soe Thura Tun[4]

1. Division of Geological and Planetary Sciences, California Institute of Technology, Pasadena, USA
2. Earth Observatory of Singapore, Nanyang Technological University, Singapore
3. Seismological Laboratory, Division of Geological and Planetary Sciences, California Institute of Technology, Pasadena, USA
4. Myanmar Earthquake Committee, Myanmar Engineering Society, Myanmar

Submitted to *Bulletin of the Seismological Society of America*

Abstract

We use L-band ALOS PALSAR data to infer the distribution of subsurface fault slip during the Tarlay earthquake (M_w = 6.8) in eastern Myanmar. We find that the total length of surface rupture is approximately 30 km, with nearly 2 m maximum surface offset along the westernmost section of the Nam Ma fault (the Tarlay segment). Finite fault inversions constrained by InSAR and pixel-tracking data suggest that fault slip is concentrated within the upper 10 km of the crust. Maximum slip exceeds 4 m at a depth between 3 and 5 km. Comparison between field measurements and near-fault deformation obtained from InSAR range-offset result suggests about 10-80% of displacement occurred within a 1-km-wide zone off the main surface fault trace. This off-fault deformation may explain the shallow slip deficit that we observed during this earthquake. We estimate a recurrence interval for Tarlay-like events to be 1600 to 6500 years at this section of the Nam Ma fault. Detailed paleoseismological study is essential to clarify the slip behavior and the earthquake recurrence interval of the Nam Ma fault.

Introduction

While major tectonic faults in the Indochinese peninsula have been mapped (e.g. Le Dain et al., 1984; Lacassin et al., 1998), we have little understanding of their rupture characteristics including their average rupture recurrence intervals, the depth of the seismogenic zone and the spatial and temporal variation in seismic and aseismic slip behavior. Several M ~ 7 earthquakes occurred in the central part of Indochina during the late 20th century (e.g., the M_w 7.0 Lancang-Gengma earthquakes in 1988 and the M_w 6.8 Myanmar-China earthquake in 1995), but the distribution of fault slip in these events was not well constrained by data. Thus, the March 24, 2011 M_w 6.8 Tarlay earthquake (also known as the Mong Hpayak earthquake) provides a unique opportunity to infer faulting behavior in the golden triangle area between Myanmar and Laos.

The Tarlay earthquake occurred at the westernmost section of the Nam Ma fault (Fig. 1) with a coseismic surface rupture extending more than 17-km along the previously mapped Nam Ma fault trace (Soe Thura Tun et al., in preparation). Associated surface rupture was partially mapped in the field by the Myanmar Earthquake Committee about two weeks after the mainshock. However, because of limited road access in the field and diffuse surface deformation in several regions, the extent of fault offset was only measured at limited locations. Thus, satellite-based interferometric synthetic aperture radar (InSAR) imagery provides key observations revealing the pattern of coseismic ground deformation and surface displacements across the ruptured section of the Nam Ma fault. We exploit the InSAR data to constrain a finite fault source model, which in turn helps further our understanding of faulting behavior in the golden triangle region.

We use both InSAR and pixel-tracking techniques to estimate different components of ground deformations associated with the Tarlay earthquake. We compare these ground deformations to the fault offset measurements from a post-earthquake survey. We then invert for the distribution of fault slip on a model of the Nam Ma fault plane, and use this model to explore the behavior of shallow fault slip during the Tarlay earthquake. We conclude by estimating possible earthquake recurrence scenarios of the Nam Ma fault system, assuming the earthquake represents the characteristic event along the Nam Ma fault.

The Nam Ma Fault and the 2011 Tarlay Earthquake

The Nam Ma fault forms part of a major left-lateral fault system in the northern Sunda Block between Myanmar and Laos (Fig. 1). Although its fault trace lies in the golden triangle area where field investigation has been nearly impossible due to logistical concerns, this 215-km-long structure has been mapped from the interpretation of satellite imagery and 90-m SRTM digital elevation model (DEM) (e.g., Lacassin et al., 1998). In the central portion of the Nam Ma fault, the Mekong River forms a hairpin loop where the river flows across the fault trace (Fig. 1) (Lacassin et al., 1998). This geomorphic feature suggests the Nam Ma fault was once a right-lateral fault before slip-reversal of the Red River fault, and was subsequently reactivated as a left-lateral fault with an estimated average slip rate of 0.6-2.4 mm/yr (Lacassin et al., 1998).

Along the western end of the Nam Ma fault in remote eastern Myanmar, the fault trace exhibits classical horsetail geometry, suggesting that this fault system transitions from a single fault zone into a diffuse zone with several sub-parallel fault segments. The Tarlay segment is one of these fault segments at the western end of the Nam Ma fault. This segment runs N70°E east of the Tarlay Township, transecting the hilly area west of the Mekong River (Fig.1 & 2). To the west, our interpretation from the 90-m SRTM DEM suggests that the Tarlay segment terminates at a small tectonic basin within the mountains (marked by Q in Fig. 2). To the east, a triangle-shaped transtensional basin appears where the trace of the Tarlay segment propagates straightly into the basin (Fig. 2). Active tectonic features gradually disappear along the Tarlay segment within this transtensional basin, while a series of triangular facets and offset alluvial fans reappear along the main Nam Ma fault trace that bounds the northern margin of the basin. These observations imply the presence of a left step-over between the Tarlay segment and the main trace of the Nam Ma fault, where transfer of slip northwards creates a releasing bend along the northern part of the basin.

The inferred epicenter of the March 24, 2011 Tarlay earthquake (M_w 6.8) from NEIC catalog falls very close to the western end of the Tarlay segment (Fig. 1). Most fault plane solutions suggest this earthquake occurred on a nearly vertical fault with purely left-lateral slip (see Data and Resources Section). These solutions match our general concept of the slip sense and orientation of the Nam Ma fault. Epicenters of aftershocks from NEIC catalog from March to April 2011 also encircle the Tarlay segment (Fig. 1). Post-earthquake field investigation revealed coseismic left-lateral offsets in the central part of the segment. In the transtensional basin at the eastern end, the rupture pattern becomes more complicated, suggesting near-surface distributed deformation (Soe Thura Tun et al., in preparation). We use ALOS L-band PALSAR satellite imagery to derive a more complete view of surface rupture and to estimate the distribution of fault slip at depth.

InSAR data

From 2007 until 2011, the Japanese ALOS PALSAR L-band sensor acquired radar imagery permitting measurement of co-seismic ground deformation in regions where dense vegetation usually causes decorrelation in shorter wavelength InSAR imagery (e.g., C- and X-band). For the Tarlay earthquake, ALOS acquired pre- and post-earthquake SAR images along ascending track 126 and descending track 486 that cover the westernmost section of the Nam Ma fault (Tarlay segment; Fig. 1). The pre- and post-quake data are about 2 months apart (Table 1). This relatively small interval of time helps to minimize the effects of temporal decorrelation.

We use the repeat orbit interferometry processing package ROI_PAC (Rosen et al., 2004). Both ascending and descending images suffer from decorrelation near the trace of the Nam Ma fault; nevertheless, they still show clear ground deformation around the Tarlay segment (Fig. 3a and 3b). Both interferograms show simple concentric fringes around the fault without any complicated bifurcations. The pattern suggests a relatively simple geometry for faulting at the surface. The termination pattern around the western and eastern end of the fault looks somewhat different. To the west, fringes merge into the tip of the fault trace, implying that the fault earthquake rupture extends to the western end of the Tarlay segment, about 9 km west of the westernmost field surveyed point (Fig. 2; Fig. 3a and 3b). To the east, fringes bend into the fault trace at an angle, suggesting that co-seismic slip gradually decreases toward the eastern fault termination. A large area of decorrelation in the descending track coincides with the location of the transtensional basin. We believe this area of decorrelation suggests a plausible distributed deformation zone, or that strong secondary ground deformation (e.g., liquefaction and slope failure along the river bank) took place inside the basin (Fig. 3a).

We also applied pixel-tracking analysis on the SAR amplitude data for descending track 126 to further constrain near-field deformation and to provide an additional component of deformation. Pixel-tracking technique produces deformation images with higher level of noise, and therefore multi-looking (spatial averaging) is usually necessary to improve the signal-to-noise ratio. We caution that some deformation features, in particular the sharp discontinuity across the fault trace, may be lost during this process.

Figure 3c shows the azimuth component (AZO) of the pixel-offsets estimates. Although data from pixel-tracking is noisier than InSAR where fringes are visible, they allow deformation estimates in the near-field where the interferograms completely decorrelate. From the western to the central part of the segment, the near-field data shows a sharp deformation pattern across the fault. To the east, the boundary between opposite-moving displacements neither follows our pre-mapped Tarlay segment (Fig. 3c), nor does it match the field observation result. This mismatch again suggests either secondary ground deformation effects (e.g., liquefaction) took place inside the basin or the fault slip during the earthquake did not form a localized rupture trace near the surface. We also note that we did not find any evidence of surface rupture along the northern boundary of this transtensional basin, suggesting that surface rupture did not extend beyond the Tarlay segment.

We carried out the same pixel-tracking analysis on scenes from ascending track 486. Since its line-of-sight direction (LOS) is almost parallel to the direction of the surface rupture, and given that this event is almost purely strike-slip, the signal in the azimuth direction is small compared to the noise level. Therefore we do not to include this set of AZO observations in our model, but instead used the range offset result (RAO) for validation. Range offsets and interferometric measurements measure the same line-of-sight component of the deformation field, so the information they provide is redundant (Fig. 3b & 4). However, range offsets are less influenced by decorrelation, they can sometimes better resolve displacements near the fault, and they do not need to be phase unwrapped. Using these data we estimate near-fault deformation within a ±500-m window across the fault (Fig. 4). We compare these near-fault observations with both the predictions of shallow fault slip in our inferred model and the fault offset data from the field survey.

The slip distribution of Tarlay earthquake

Using both the ascending and descending InSAR data, plus the AZO observations from the descending track, we estimate the distribution of subsurface fault-slip on the Tarlay segment. In order to improve model efficiency, we adopt a spatially variable data resampling/averaging approach based on the estimation of the inherent data resolution for a given source model (Lohman and Simons, 2005). This approach reduces the total number of data points to less than 1000, while preserving the essential information contained in the original data (Fig. 5).

Our fault model has a general strike of N70°E, similar to the strike of the observed surface rupture and the pre-mapped Tarlay segment from SRTM data (Fig. 2). Since no well-located aftershock data is available in this area, we adopt the dip angle of 86° SE from the Global Centroid Moment Tensor (GCMT) solution, which agrees with the field observation of the southern side of the Tarlay segment as the down-thrown side (Soe Thura Tun et al., in preparation). We discretized the fault plane into 1 km x 0.6 km rectangles from the surface to 12 km depth. We use elastic Greens functions based on a homogeneous elastic half space model with a Poisson's ratio of 0.25.

We regularize the solution using a Laplacian damping term, and further control the solutions by minimizing total potency of the inferred model. The degree of smoothing and potency constraint is chosen through an L-curve (Fig. 6). We computed an ensemble of models with different combinations of regularization weighting parameters (λ_1 for smoothing and λ_2 for potency constraint), and plot the values of reduced chi-square (χ^2_{re}) as a function of λ_1 and λ_2. We use two criteria to choose our best model: (1) the intersection between the knees of the χ^2_{re} plane along the λ_1 and the λ_2 directions, and (2) the proximity of reduced chi-square to unity, where model errors equal to observation errors. We also tested the necessity of the total potency constraint, and found that if we remove the total potency constraint, slip tapers toward the lower left corner of the fault plane (Fig. 6e). If we allow the fault to extend deeper, this tapering pattern goes all the way down to whatever maximum depth of the given fault model. This tapering pattern is thus the result of overfitting long wavelength noise in our dataset, and therefore we consider the slip potency constraint as a necessary regularization term to minimize this artifact.

Our selected model (Fig. 6b) fits the data well in general, although some systematic pattern appears in the residuals (Fig. 5). We then carried out a grid search to obtain the optimized dip angle, in order to figure out if the systematic pattern results from this specific issue. However, the improvement of goodness of fit is marginal between our current dip angle (86°SE) and the best solution (87°SE), with only 0.2% decrease in the RMS residual. The systematic pattern does not vanish in all the 21 planar fault models that we tested (from 80°SE to 90° at 0.5° increment). It is hence likely that the fault plane is curved instead of purely planar, or that some secondary fault in the flower structure of the Tarlay segment has been active during this event, although there is no sign on the surface of such a structure.

Our preferred coseismic model (Fig. 7) is almost purely left-lateral with a minimal dip slip component. This result matches field observations, in which most surface ruptures also appear to be purely left-lateral (Soe Thura Tun et. al., in preparation). The inferred slip occurs within the upper 10 km of the crust, where the major slip patch concentrates between depths of 2.5 and 6 km, with a maximum slip of nearly 4.5 m at the central part of this depth range. The region of high slip is centered close to the western part of the fault plane, with its slip decreasing faster to the west than to the east.

Toward the eastern and western end of the rupture, our preferred model shows different slip behavior near the termination of the fault. To the east, the slip patch extends smoothly upward, forming a narrower and shallower rupture patch beneath the basin, and gradually diminishes at shallow depths (< 3 km in depth). In contrast, at the western end of the fault, the depth distribution of fault slip retains a similar width toward its western termination. The model also suggests that fault slip decreases rapidly at the western end of the Tarlay segment, from 3 m to less than 1 m beneath the western termination of the pre-mapped surface fault trace (Fig. 7).

Both our preferred model and the measurement from range-offset data suggest the rupture broke the surface along the entire Tarlay segment. The amount of slip near the surface is small compared to the maximum fault slip at 2.5 to 6 km in depth. Thus, our model suggests a significant reduction in slip within the topmost 2 km of crust, where co-seismic slip decreases from 4 m at 3 km deep to about 1 m near the surface (Fig. 7).

Near the central part of the fault, offsets measured in the field and modeled shallow slip are roughly consistent with each other. Further east, the agreement between the shallow slip and the field measurements is not as close (Fig. 7b). This section is also where pixel offset data are too noisy for us to obtain measurable near-fault deformation. The modeled shallow slip shows larger amplitude of surface slip than measured in the field. We attribute this difference to the finite size of our topmost fault patches and mapping of any diffuse deformation (off-fault deformation) onto the single fault plane.

Using the reference value of the shear modulus of the Earth's crust (30-33 GPa), we infer a geodetic moment on the order of 1.6 - 1.8 x 1019 Nm, corresponding to M_w 6.8, in agreement with the NEIC moment magnitude estimated from the global seismic network. Effects of postseismic deformation may be included in our model, but we expect the influence to be small due to the short time interval (less than 10 days) between the earthquake and the post-earthquake SAR images.

Discussion

Characteristics of the surface rupture

Pixel-tracking and InSAR observations indicate that the entire length of the Tarlay segment ruptured during the March 2011 earthquake, as also hypothesized from field investigations (Soe Thura Tun et al., in preparation). Both slip on the uppermost row of slip patches in our preferred model and the near-fault deformation measured from range offsets suggest a broad bell-shaped pattern of surface rupture with a peak value of 1.5 to 2 m (Fig. 7). We find that near-fault deformation does not always occur within a narrow zone of the surface rupture (Fig. 4). In some places, there is a clear sigmoidal pattern as one traverse the fault, the width of which varies along strike. We select three profiles to compare on-fault and off-fault deformation. We assume that field measurements represent actual on-fault displacement and the pixel offsets capture the total near fault deformation.

Profile 23 demonstrates an end member where most of the deformation concentrates along the fault surface rupture (Fig. 4c). The sharp sigmoidal pattern over a short distance in the profile suggests that most of the ground deformation occurred on the fault. Nevertheless, we still find about 10-30 cm more displacement from the pixel offsets than from the field measurements, suggesting a plausible 10 to 20% of deformation occurred over distances of ~800 m across the rupture. Since this 10-30 cm difference is very close to the measurement precision of the pixel tracking analysis, the real off-fault deformation could be even less. In fact, the field survey found a narrow rupture zone only along this section (Soe Thura Tun et al., in preparation).

Toward the east, profile 33 shows a different type of deformation near the main fault trace (Fig. 4d). This profile reveals a more gentle sigmoidal deformation pattern compared to profile 23, but the overall near-fault deformation remains large (approximately 1.1 m). Such gentle deformation curve suggests that either rupture failed to reach the surface, or that slip is distributed over a wide damage zone composed of multiple small fault planes. Field observation reports a series of aligned en echelon cracks on the ground along this section of the fault, suggesting that deformation on the main fault trace is no more than 10-20 cm near the surface (Soe Thura Tun et al., in preparation). Field investigation also found several plausible fissures within a range of several hundreds of meters away from the fault near this profile. The lateral extensions of these plausible fissures were difficult to trace. Based on these geologic observations, we argue distributed slip can explain the gentle deformation pattern. However, it is difficult to tell whether these deformations mainly occurred along different secondary faults in the damage zone, or formed as dragging and warping in the country rocks around the main fault.

Further east, profile 48 is located within the transtensional basin (Fig. 4e). This profile again shows a gentle sigmoidal deformation pattern across the fault similar to profile 33. Field observations report offset rice paddy field boundaries within the disrupted fields, where the maximum offset is 20 to 30 cm, compared to the 40-65 cm of near-fault deformation. Thus, we suggest that tectonic deformation off the main fault along profile 48 is up to 30 cm within the 1-km zone across the fault, accounting for ~50% of the total displacement.

Field measurements within the basin area are consistently lower than near-fault deformation from the pixel-tracking result (Fig. 7b), indicating possibly extensive off-fault deformation in the basin. Off-fault deformation may be attributed to the lower brittle strength of the saturated fluvial sediments that fill the basin. By comparison, off-fault deformation is less significant near the central part of the fault in general, where the fault trace transects a granitic batholith with only a thin alluvial layer mantled on top. This difference suggests that lithology, or the condition of the country rocks, may be a key factor controlling the fraction of off-fault deformation during an earthquake.

Shallow slip deficit

The apparent deficit of shallow slip in our preferred slip model is similar to that seen in many other magnitude ~7 strike slip fault events (e.g., Simons et al., 2002; Fialko et al., 2005; Fialko et al., 2010; Sudhaus et al., 2011). Figure 7c illustrates the comparison of normalized slip potency as a function of depth between the Tarlay event and other studied earthquakes (e.g., Simons et al., 2002; Fialko et al., 2005; Kaneko and Fialko, 2011). We find the shallow slip deficit of the Tarlay earthquake resembles that of the 1992 Landers earthquake and the 2010 El Mayor-Cucapah earthquake. Among these three events, the shallow slip deficit is up to 50-60%, and the potency gradients in the top 2 to 3 km layer are identical.

Although the cause of such shallow slip deficit has not been conclusively identified, simulations reveal several possible sources for this phenomenon. Kaneko and Fialko (2011) suggest part of this deficit results from inelastic deformation near the earth surface, especially when the country rock's cohesion is low. Such inelastic slip can further enhance the inference of a slip deficit when we try to fit the inelastic ground deformation via the purely elastic model (e.g., Simons et al., 2002; Barbot et al., 2008; Kaneko and Fialko, 2011).

In the case of the Tarlay earthquake, we see plausible off-fault sympathetic deformation ranging from 10% to up to 80% of the total near-fault deformation at different locations (Fig. 4c to 4e). It seems reasonable to attribute the cause of the shallow slip deficit to inelastic off-fault deformations along the fault. However, while we are seeing a large degree of variation in the deformation off the main fault, we do not find an obvious relationship with the inferred shallow slip deficit at any given location. This discordance may result from errors both in the observations and in the models, or that the variation in off-fault deformations is only superficial, or that off-fault deformation and the shallow slip deficit achieve the balance only in the context of multiple earthquake cycles rather than a single event. Despite this ambiguity, we emphasize the importance of recognizing along-strike variations of both aforementioned behaviors and the comparison with geological observations, which in turn may allow us to unravel the enigma of shallow slip deficit in the future.

Inferred recurrence interval on the Tarlay segment

The difference between the maximum fault slip at depth and the maximum fault offset on the surface makes a significant difference when we estimate the average recurrence interval of earthquake from the coseismic fault offset data. If the fault slip during the Tarlay earthquake represents the characteristic slip pattern of the Tarlay segment, we can roughly estimate its recurrence interval by dividing its maximum fault slip with its average long-term slip rate. Lacassin (1998) suggested the slip-rate of the Nam Ma fault be 0.6-2.4 mm/yr, based on the channel offset of the Mekong River and the regional tectonic history. Therefore, if the 4 m fault slip at depth represents the characteristic slip on the Tarlay segment, the average recurrence interval of a Tarlay-earthquake-like event is about 1600 to 6500 yr along this segment. Such frequency is three times lower than the estimation from the maximum surface offset (1.25 m), where the interval falls to the range of 600 – 2300 yrs (Soe Thura Tun et al., in preparation). The large variation in these first-order estimates of recurrence interval underscores the need for paleoseismological studies. As many strike slip faults produce sequential and clustered events within a short period of time (e.g., North Anatolian Fault; Stein et al., 1997; Sagaing fault; Yeats et al., 1997), we cannot at present conclusively estimate seismic hazard along the Nam Ma fault,

Conclusions

We have successfully conducted the InSAR and pixel-tracking analyses from ALOS L-band PLSAR dataset. The deformation pattern suggests a simple linear fault plane, with the eastern end submerged into the transtentional basin. Our slip inversion model suggests the entire 30-km long Tarlay segment ruptured during the 2011 earthquake. The rupture has a narrow and concentrated region of slip in the shallow part of the crust (< 10 km), with the peak slip at 2.5 to 6 km. Fault slip in the topmost 600-m layer reveals a broad bell-shape slip pattern and generally agrees with field observations and near-fault deformation measured from the pixel-tracking data.

By comparing the field survey result and the near-fault deformation, we find 10% to 80% of the ground deformation occurred outside the main surface rupture. Such off-fault deformation is likely to be inelastic, and may be the cause of shallow-slip deficit that we observed in our slip model.

Given the average slip rate of 0.6-2.4 mm/yr on Nam Ma fault, we estimate the recurrence interval at the Tarlay segment to be 1600 to 6500 yr. This estimate is three folds greater than the estimate from the maximum surface offset. Detailed paleoseismological study at the Nam Ma fault is essential to clarify the regional seismic hazard potential in the golden triangle area.

Data and Resources

Epicenters of the mainshock and aftershocks were collected from the USGS/NEIC PDF catalog (last accessed on Dec-2011). GCMT solutions of aftershocks were collected from Global Centroid Moment Tensor (GCMT) Project database: www.globalcmt.org/CMTsearch.html (last accessed on Dec-2011). The CMT solution of mainshock was obtained from the USGS Significant Earthquake Archive: http://earthquake.usgs.gov/earthquakes/eqinthenews/2011/usc0002aes/#scitech (last accessed on Mar-2012). ALOS data is copyright Japanese Aerospace Exploration Agency and METI and provided through the US Government Research Consortium Data Pool at the Alaska Satellite Facility.

Acknowledgement

We have benefited greatly from discussions with Kerry Sieh and Paul Tapponnier. The comments from reviewers Roland Bürgmann and the other anonymous reviewer greatly helped us to improve the quality of the manuscript. This research is supported by the NASA grant NNX12AO30G and by the Earth Observatory of Singapore (EOS).

References

Bender, F., 1983. Geology of Burma, Gebrüder Borntraeger, 293 pp.

Barbot S., Y. Fialko, D. Sandwell, (2008). Effect of a compliant fault zone on the inferred earthquake slip distribution, J. Geophys. Res., 113, B06404, 2008, doi:10.1029/2007JB005256.

Fialko, Y., D. Sandwell, M. Simons, and P. Rosen (2005). Three-dimensional deformation caused by the Bam, Iran, earthquake and the origin of shallow slip deficit, Nature 435 295-299. doi:10.1038/nature03425.

Fialko, Y., A. Gonzalez, J. Gonzalez, S. Barbot, S. Leprince, D. Sandwell and D. Agnew (2010). Static rupture model of the 2010 M7.2 El Mayor-Cucapah earthquake from ALOS, ENVISAT, SPOT and GPS data, EOS, Trans. Am. geophys. Un. 91(52) T53B–2125.

Kaneko, Y., and Y. Fialko (2011). Shallow slip deficit due to large strike slip earthquakes in dynamic rupture simulations with elasto-plastic off fault response, Geophys. J. Int. 186 1389-1403.

Lacassin, R., A. Replumaz, and P. H. Leloup (1998). Hairpin river loop and slip sense inversion on SE-Asian strike-slip faults, Geology 26 703-706.

Le Dain, A. Y., P. Tapponnier, and P. Molnar (1984). Active faulting and tectonics of Burma and surrounding regions, J. Geophys. Res. 89(B1) 453–472, doi:10.1029/JB089iB01p00453.

Lohman, R. B., and M. Simons (2005). Some thoughts on the use of InSAR data to constrain models of surface deformation: Noise structure and data downsampling, Geochem. Geophys. Geosyst. 6 Q01007, doi:10.1029/2004GC000841.

Rosen, P. A., S. Hensley, G. Peltzer, and M. Simons (2004), Updated repeat orbit interferometry package released, Eos Trans. AGU 85(5) 47 doi:10.1029/2004EO050004.

Simons M., Y. Fialko, and L. Rivera (2002). Coseismic Deformation from the 1999 M_w 7.1 Hector Mine, California, Earthquake as Inferred from InSAR and GPS Observations, Bull. Seismol. Soc. Am. 92 1390-1402.

Soe Thura Tun, Saw Ngwe Khaing, Y. Wang, Myo Thant, Nyunt Htay, Yin Myo Min Htwe, Than Myint and K. Sieh (2013). Surface Ruptures of the 2011 Tarlay Earthquake and Their Relationship to the Active Tectonics of Eastern Myanmar, in preparation.

Stein, R. S., A. A. Barka, and J. H. Dieterich (1997). Progressive failure on the northern Anatolian fault since 1939 by earthquake stress triggering, Geophys. J. Int. 128 694-604.

Sudhaus, H. amd S. Jónsson (2011). Source model for the 1997 Zirkuh earthquake (M_w = 7.2) in Iran derived from JERS and ERS InSAR observations, Geophys. J. Int. 185 676-692, doi:10.1111/j.1365-246X.2011.04973.x.

Yeats, R. S., K. Sieh, and C. R. Allen, (1997). The geology of earthquakes, New York, Oxford Univ. Press. 576 pp.

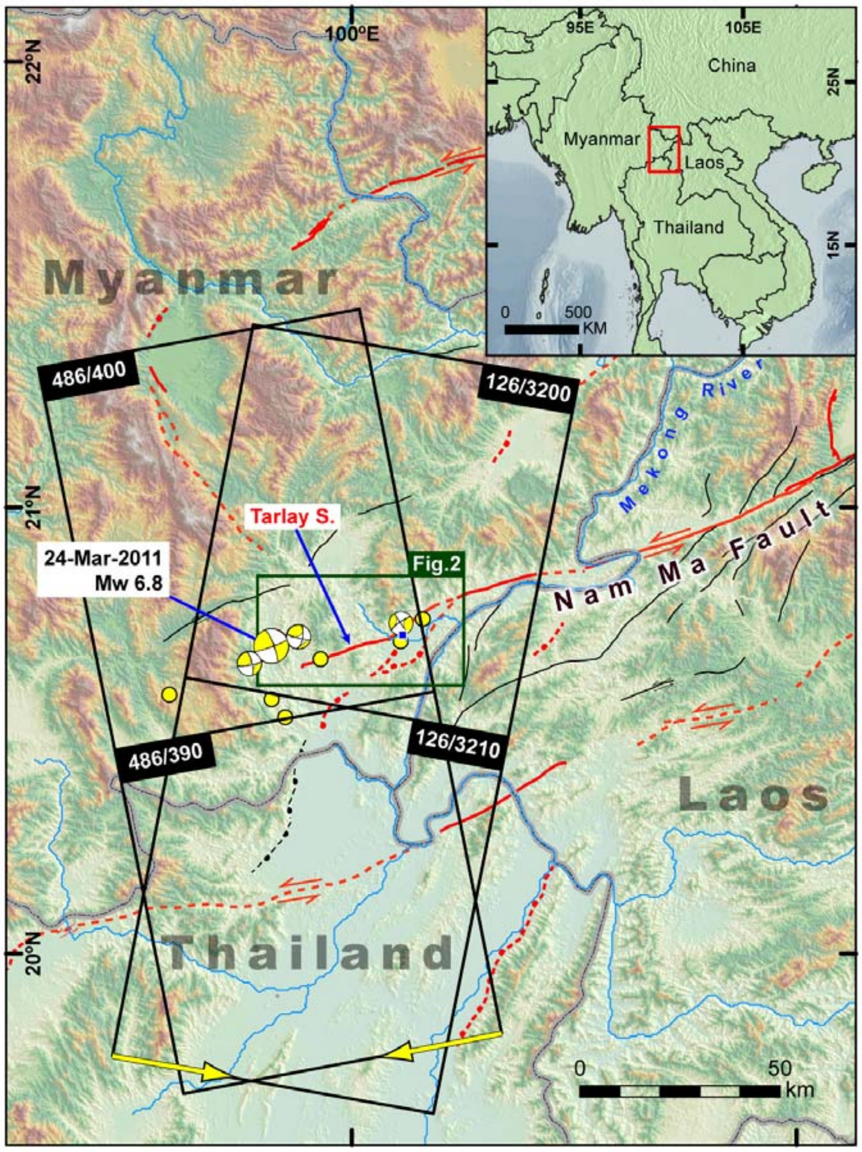

Figure 1. The March 24, 2011 Tarlay earthquake (Mw 6.8) occurred along the western edge of the Nam Ma fault system, located near the Myanmar-Laos boarder. CMT solutions are for the mainshock and major aftershocks. Other aftershocks of smaller magnitudes are indicated by yellow circles. Black boxes outline the footprint of the ALOS L-band SAR data used in this study, with the line-of-site (LOS) vectors in yellow arrows. Red lines are the active (solid) and suspect active (dashed) strike-slip faults mapped from the 90-meter SRTM shaded relief imagery with the assistance from the published geological map (e.g. Bender, 1983). Black lines are the bedrock faults that do not show associated active geomorphic features from the digital elevation model. The small blue rectangle at the center of this map shows the location of Tarlay Township, which is the major city along the western Nam Ma fault. Country borders are shown in gray lines.

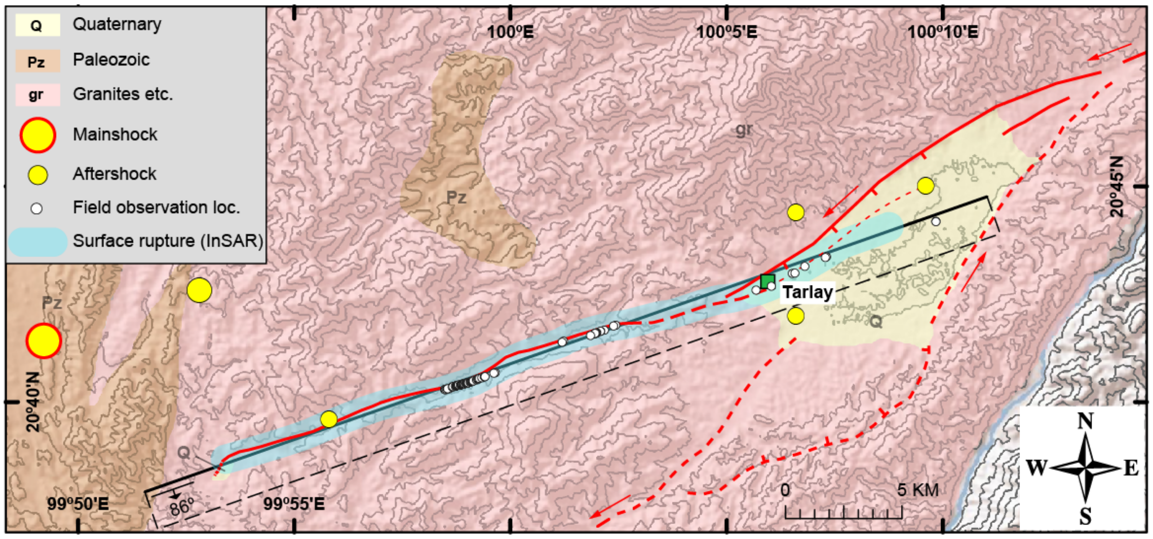

Figure 2. Detailed mapping of the Tarlay segment at the western most section of the Nam Ma fault, based on the 90-meter SRTM and 15-meter Landsat imagery. Most of the fault trace transects through the granitic formation (gr), with its western termination close to the Paleozoic sedimentary rocks (Pz; Bender, 1983). The white dots are the locations of surface rupture that Myanmar geologists found in the field (Soe Thura Tun, in preparation). In general, the surface rupture locations match the fault trace that we mapped from remote sensing datasets. The black rectangle indicates the southward dipping fault plane that we used in the dislocation model. Its surface trace is referenced to the field investigation results and our mappings.

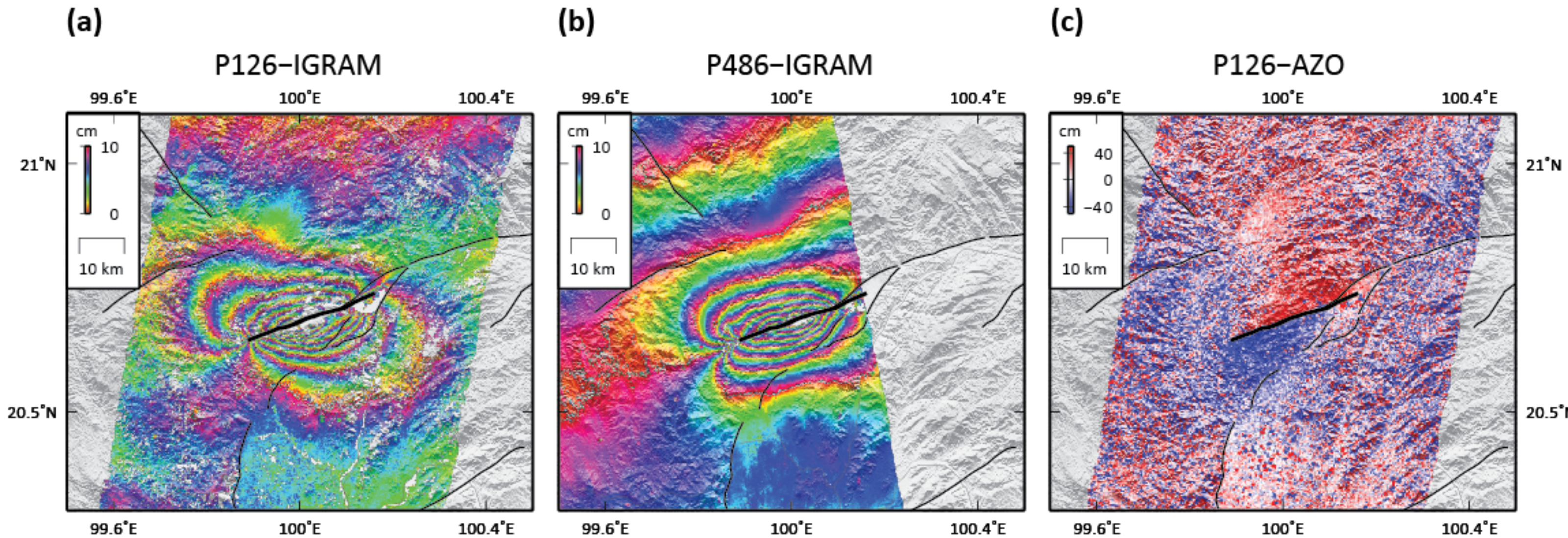

Figure 3. ALOS L-band InSAR (a and b) and pixel-tracking analysis results (c). The offset map of P126-AZO shows the ground deformations along the azimuth direction (AZO), while the other two InSAR results are the deformation along their line-of-sight directions (LOS, Fig. 1). The bold black-line shows the trace of Tarlay segment mapped from SRTM and LANDSAT imagery. Other thin black lines are the regional faults that did not rupture during this earthquake.

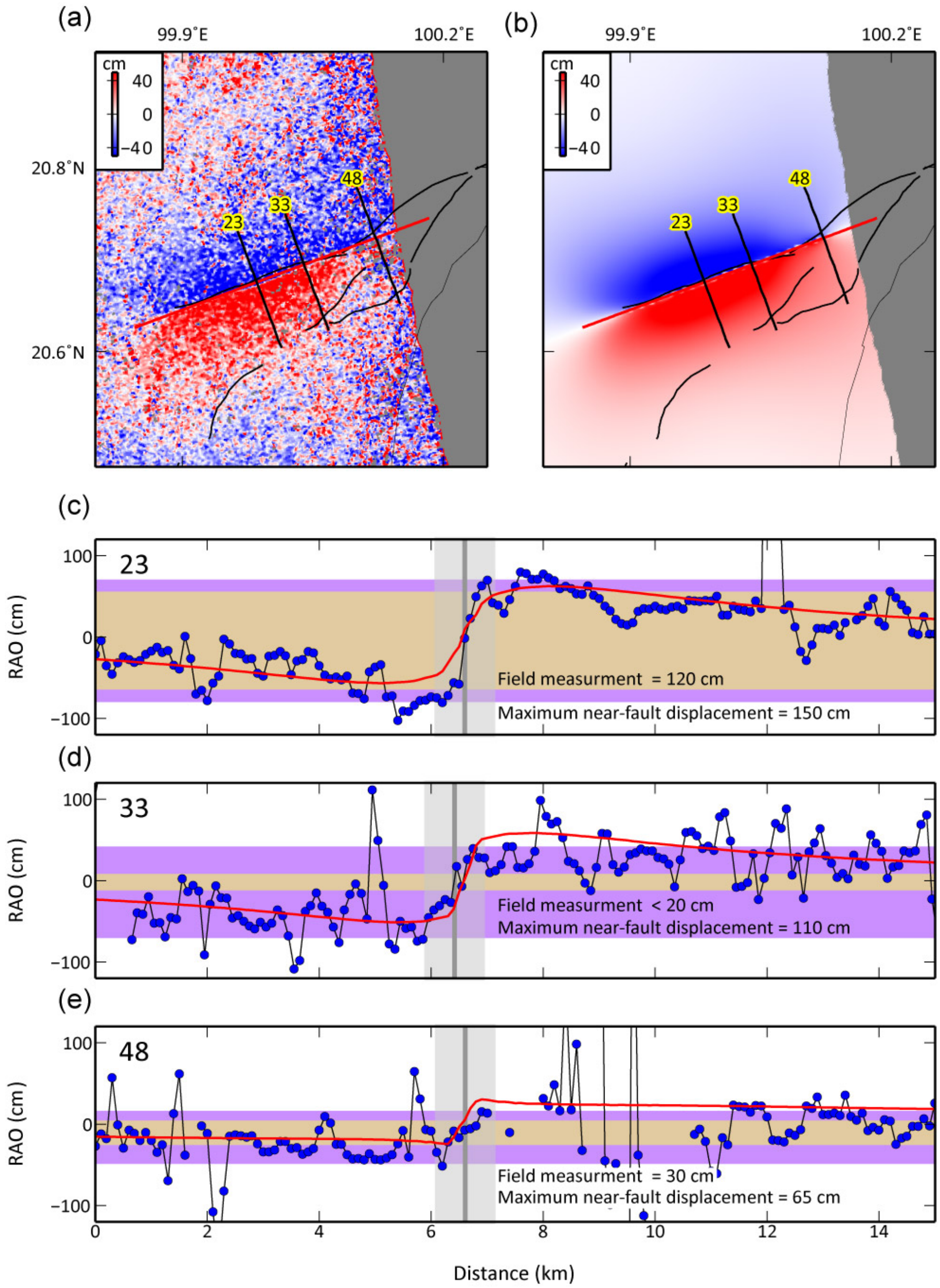

Figure 4. The range offset (RAO) for descending track 486 (a) and the prediction from our preferred finite fault model (b). The RAO data have been processed with multi-looking (spatial averaging) to improve the signal-to-noise ratio. The resolution for both the RAO data and the modeled results are 90 m. The deformation component of the RAO data is almost parallel to the strike of the fault, so here the RAO results are directly compared with the field measurements. (c) Ground deformation along profile 23 (blue dots) and the modeled deformation (red line). The width of the brown area indicates the amount of offset during field measurements at the same location, whereas the width of the purple region indicates the maximum near-fault displacement reading from the RAO data. (d) Ground deformation along profile 33, showing more distributed deformation across the fault. (e) Ground deformation along profile 48.

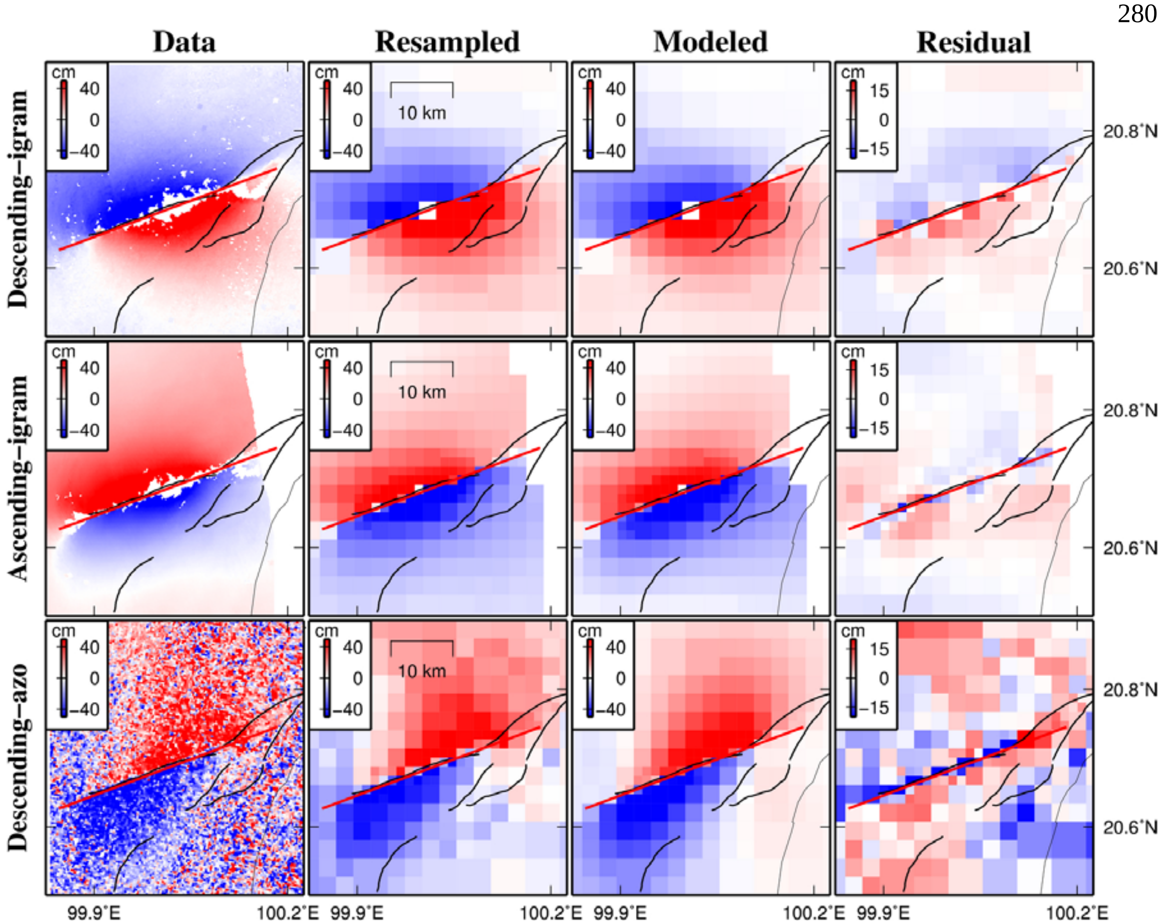

Figure 5. We resample all three ground deformation fields before invert for the fault slip distribution. Generally, the modeled deformation fields match the InSAR and pixel-tracking data with a single planar fault. The residuals show some systematic pattern, which do not vanish even with the optimized dip angle (87° SE). This pattern suggests that the fault plane may be curved rather than purely planar, or that some secondary structure in the flower structure of the Tarlay segment has been active during the earthquake, although there is no sign of such a structure on the surface.

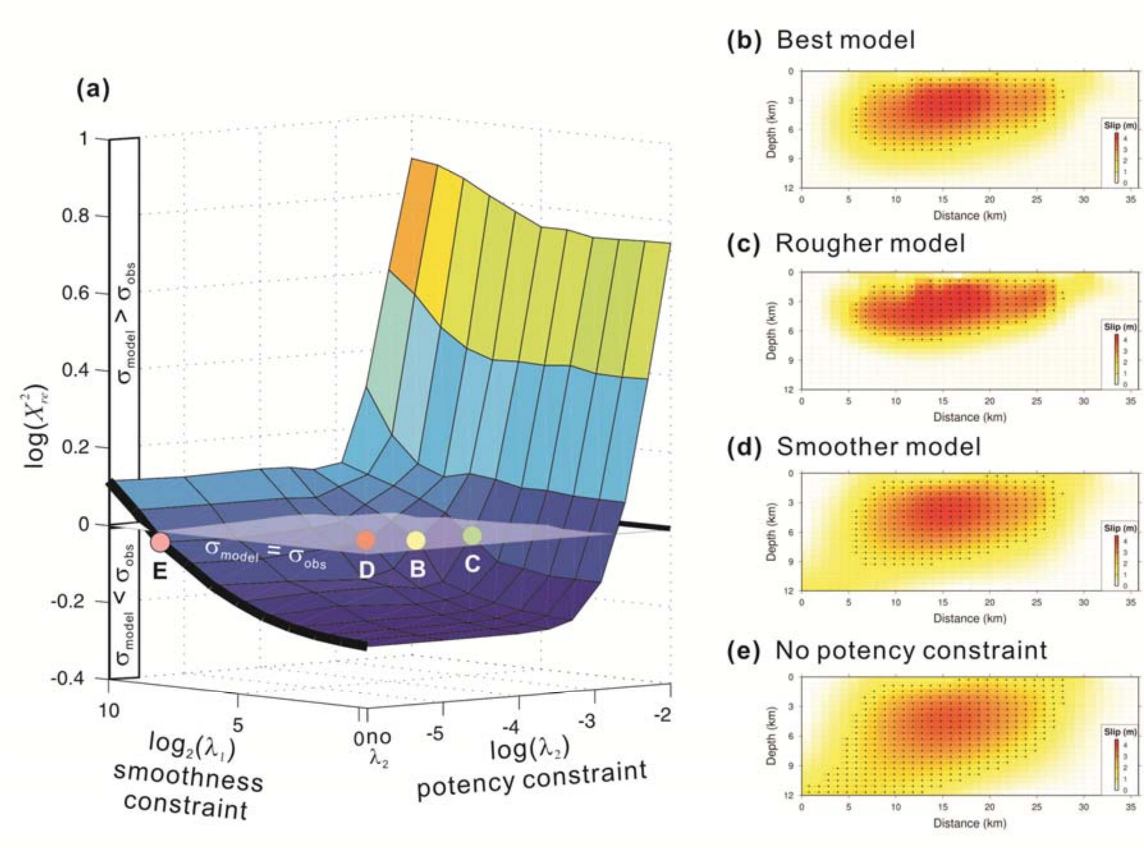

Figure 6. (a) The reduced chi-square (χ^2_{re}) plot as a function of the regularization weighting parameters, λ_1 (for model smoothness constraint) and λ_2 (for total potency constraint). (b)-(e) Different realizations of models. The best model is chosen based on the L-curve knees and on the proximity of χ^2_{re} values to unity.

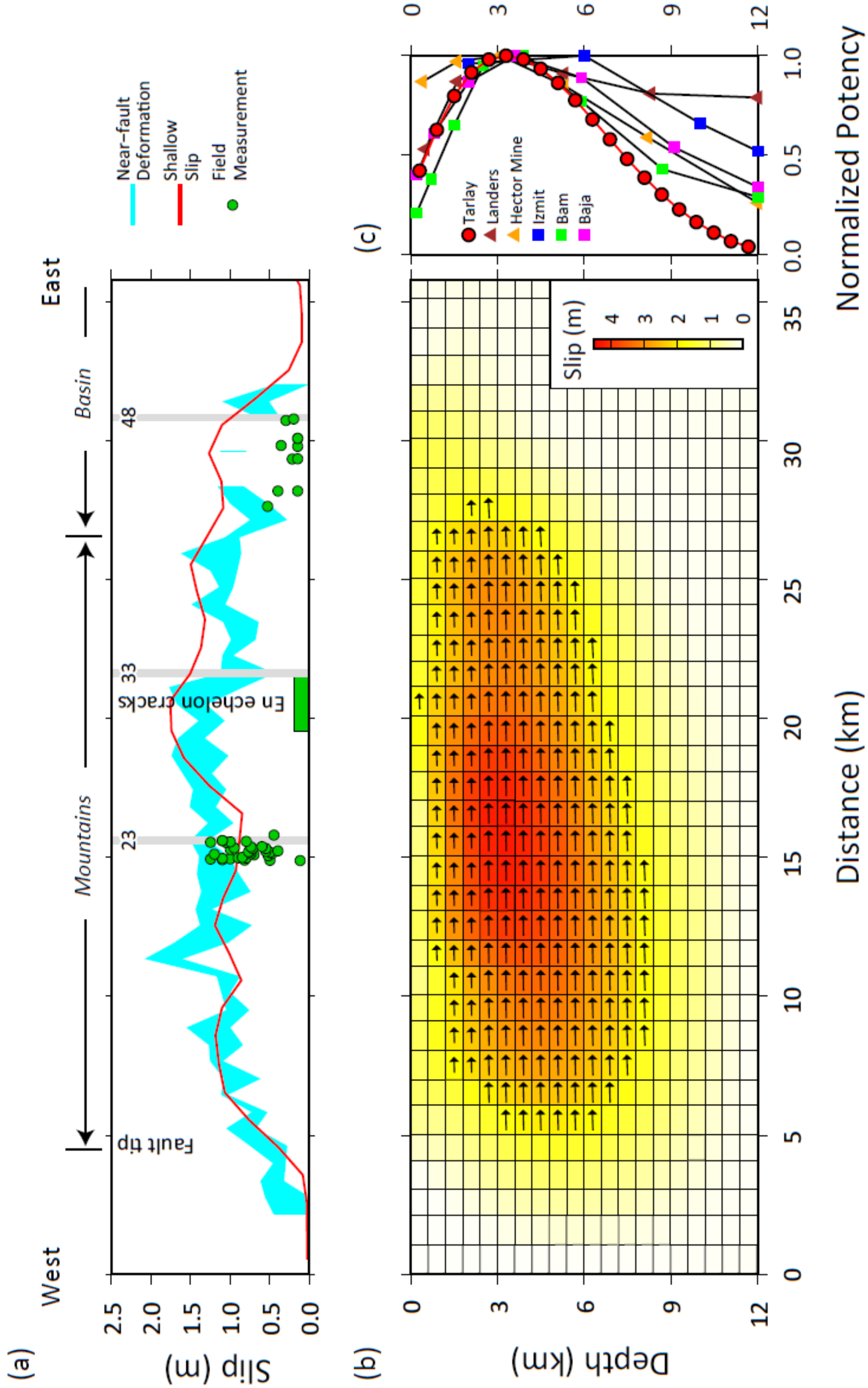
(a)
(b)
(c)
Slip (m)
Depth (km)
Distance (km)
Normalized Potency
West
East
Mountains
Basin
Fault tip
En echelon cracks
23
33
48
Near-fault Deformation
Shallow Slip
Field Measurement
Slip (m)
Tarlay
Landers
Hector Mine
Izmit
Bam
Baja

Figure 7. (a) Comparison between field measurements (green dots), the upper 600 m fault slip (red line), and the near-fault deformation measured from the AZO pixel tracking analysis (Cyan band; Fig. 4) along the Tarlay segment. This figure shows generally good match between the model result, the near-fault displacement and the field investigation result at the central part of the fault. To the east in the basin area, both the field measurements and the near-fault displacement are systematically smaller than the modeled shallow slip. (b) The distribution of fault-slip along the Tarlay segment. The maximum fault slip in our model is slightly larger than 4 m at 2.5 – 5 km depth, Most of the slip occurred shallower than 10-km at depth. (c) The comparison of the normalized slip potency from our preferred model (red dots) and other earthquake events (from Kaneko and Fialko, 2011). Slip potency of the Tarlay earthquake shows a depth dependence profile very similar to the Landers earthquake and the El Mayor-Cucapah earthquake: all three events reach their maximum slip potency at about 3 km at depth, and their potency gradients at shallow depth are also identical.

Table 1. ALOS PALSAR data used in this study.

	Path	Frame	Pre-quake date	Scene ID	Post-quake date	Scene ID
Ascending track	486	390	2011/02/16	ALPSRP269800390	2011/04/03	ALPSRP276510390
	486	400	2011/02/16	ALPSRP269800400	2011/04/03	ALPSRP276510400
Descending track	126	3200	2011/02/14	ALPSRP269433200	2011/04/01	ALPSRP276143200
	126	3210	2011/02/14	ALPSRP269433210	2011/04/01	ALPSRP276143210

Appendix 1

Supplementary material of chapter 2 Active Tectonics and Earthquake Potential of the Myanmar region

Table S1. Indian-Burma plate convergent rate along the northern Sunda megathrust from various plate rotation models

Model	Latitude	Longitude	Speed	Azimuth	N Vel.	E Vel.	Plate	Site	Vector (1) (Remove Sagaing fault motion)				Vector (2) (Remove S.F. and Yunan blk)				Vector (3) (Remove Spreading center motion)	
			mm/yr	(cw)	mm/yr	mm/yr	(reference)	Name	Min	Max	Azimuth		Min	Max	Azimuth		Average	Azimuth
MORVEL 2010	23° 30'	90° 30'	41.58	10.98°	40.82	7.92	IN(SU)	SHIL	**20.4**	**24.2**	**202.8**	**199.1**	**23.4**	**26.7**	**216.5**	**211.4**		
GSRM v1.2	23° 30'	90° 30'	33.22	6.16°	33.03	3.56	IN(SU)	SHIL	**11.6**	**15.4**	**197.9**	**193.3**	**14.6**	**17.8**	**220.9**	**212.5**		
CGPS 2004	23° 30'	90° 30'	26.05	7.02°	25.86	3.19	IN(SU)	SHIL	**5.0**	**8.5**	**219.6**	**202.1**	**10.0**	**12.1**	**247.2**	**229.5**		
REVEL 2000	23° 30'	90° 30'	29.65	8.27°	29.35	4.27	IN(SU)	SHIL	**8.5**	**12.1**	**210.2**	**200.6**	**12.6**	**15.3**	**234.4**	**222.1**		
Socquet 2006	23° 30'	90° 30'	35.43	10.46°	34.84	6.43	IN(SU)	SHIL	**14.4**	**18.0**	**206.6**	**200.9**	**17.9**	**20.9**	**224.1**	**216.4**		
MORVEL 2010	21° 15'	91° 15'	42.11	12.56°	41.1	9.15	IN(SU)	CHIT	**21.2**	**24.8**	**205.6**	**201.6**	**24.4**	**27.6**	**218.4**	**213.3**		
GSRM v1.2	21° 15'	91° 15'	33.67	8.13°	33.33	4.76	IN(SU)	CHIT	**12.3**	**16.1**	**202.8**	**197.2**	**15.6**	**18.7**	**223.5**	**215.1**		
CGPS 2004	21° 15'	91° 15'	26.41	8.96°	26.09	4.11	IN(SU)	CHIT	**5.8**	**9.1**	**225.1**	**206.9**	**10.9**	**12.9**	**248.0**	**231.3**		

Model	Latitude	Longitude	Speed	Azimuth	N Vel.	E Vel.	Plate	Site	Vector (1) (Remove Sagaing fault motion)				Vector (2) (Remove S.F. and Yunan blk)				Vector (3) (Remove Spreading center motion)	
			mm/yr	(cw)	mm/yr	mm/yr	(reference)	Name	Min	Max	Azimuth		Min	Max	Azimuth		Average	Azimuth
REVEL 2000	21° 15'	91° 15'	30.21	10.65°	29.69	5.58	IN(SU)	CHIT	**9.5**	**13.0**	**216.0**	**205.5**	**13.9**	**16.5**	**236.4**	**224.7**		
Socquet 2006	21° 15'	91° 15'	35.83	11.93°	35.06	7.41	IN(SU)	CHIT	**15.0**	**18.6**	**209.6**	**203.5**	**18.7**	**21.7**	**225.8**	**218.2**		
MORVEL 2010	19° 30'	92° 30'	42.79	13.84°	41.55	10.24	IN(SU)	SITW	**22.1**	**25.7**	**207.6**	**203.5**						
GSRM v1.2	19° 30’	92° 30'	34.32	9.73°	33.82	5.8	IN(SU)	SITW	**13.2**	**16.8**	**206.1**	**200.1**						
CGPS 2004	19° 30’	92° 30’	26.92	10.53°	26.46	4.92	IN(SU)	SITW	**6.6**	**9.8**	**227.8**	**210.2**						
REVEL 2000	19° 30’	92° 30’	30.97	12.49°	30.24	6.7	IN(SU)	SITW	**10.6**	**14.0**	**219.1**	**208.7**						
Socquet 2006	19° 30’	92° 30'	36.36	13.16°	35.41	8.28	IN(SU)	SITW	**15.8**	**19.3**	**211.7**	**205.4**						
MORVEL 2010	18°	93° 30'	43.34	14.84°	41.89	11.1	IN(SU)	RAMR	**22.8**	**26.3**	**209.2**	**204.9**						
GSRM v1.2	18°	93° 30'	34.84	10.99°	34.2	6.64	IN(SU)	RAMR	**13.9**	**17.5**	**208.6**	**202.3**						

Model	Latitude	Longitude	Speed	Azimuth	N Vel.	E Vel.	Plate	Site	Vector (1) (Remove Sagaing fault motion)				Vector (2) (Remove S.F. and Yunan blk)			Vector (3) (Remove Spreading center motion)	
			mm/yr	(cw)	mm/yr	mm/yr	(reference)	Name	Min	Max	Azimuth		Min	Max	Azimuth	Average	Azimuth
CGPS 2004	18°	93° 30'	27.33	11.76°	26.75	5.57	IN(SU)	RAMR	**7.3**	**10.4**	**229.5**	**212.5**					
REVEL 2000	18°	93° 30'	31.61	13.94°	30.67	7.61	IN(SU)	RAMR	**11.5**	**14.8**	**221.3**	**211.0**					
Socquet 2006	18°	93° 30'	36.79	14.11°	35.68	8.97	IN(SU)	RAMR	**16.4**	**19.8**	**213.3**	**206.9**					
MORVEL 2010	15°	93° 6'	43.52	16.35°	41.76	12.25	IN(SU)	FOUL	**23.2**	**26.7**	**211.8**	**207.3**				**28.4**	**238.7**
GSRM v1.2	15°	93°6′	34.95	12.99°	34.06	7.86	IN(SU)	FOUL	**14.4**	**17.9**	**213.1**	**206.1**				**21.1**	**250.4**
CGPS 2004	15°	93°6′	27.42	13.71°	26.64	6.5	IN(SU)	FOUL	**8.0**	**10.8**	**234.5**	**217.0**				**18.5**	**271.1**
REVEL 2000	15°	93°6′	31.81	16.46°	30.51	9.01	IN(SU)	FOUL	**12.4**	**15.4**	**226.6**	**215.8**				**21.3**	**260.5**
Socquet 2006	15°	93°6′	36.91	15.49°	35.57	9.86	IN(SU)	FOUL	**16.8**	**20.1**	**216.0**	**209.3**				**23.5**	**248.6**
MORVEL 2010	12° N	92°	43.46	17.81°	41.38	13.29	IN(SU)	ANDM	**23.5**	**26.9**	**214.4**	**209.6**				**29.1**	**240.4**

Model	Latitude	Longitude	Speed	Azimuth	N Vel.	E Vel.	Plate	Site	Vector (1) (Remove Sagaing fault motion)				Vector (2) (Remove S.F. and Yunan blk)			Vector (3) (Remove Spreading center motion)	
			mm/yr	(cw)	mm/yr	mm/yr	(reference)	Name	Min	Max	Azimuth		Min	Max	Azimuth	Average	Azimuth
GSRM v1.2	12° N	92°	34.82	14.96°	33.64	8.99	IN(SU)	ANDM	**14.7**	**18.0**	**217.7**	**209.9**				**22.0**	**252.4**
CGPS 2004	12° N	92°	27.33	15.64°	26.32	7.37	IN(SU)	ANDM	**8.5**	**11.1**	**239.6**	**221.5**				**19.4**	**272.0**
REVEL 2000	12° N	92°	31.76	18.99°	30.03	10.33	IN(SU)	ANDM	**13.1**	**15.9**	**232.1**	**220.7**				**22.5**	**262.3**
Socquet 2006	12° N	92°	36.85	16.80°	35.28	10.65	IN(SU)	ANDM	**17.0**	**20.3**	**218.7**	**211.6**				**24.1**	**195.4**

1. The Sagaing fault velocity is 18-22 mm/yr northward. 2. The Yunnan block moves 6 mm/yr westward. 3. The opening rate of the Andaman Sea spreading center is 30 mm/yr along 335°

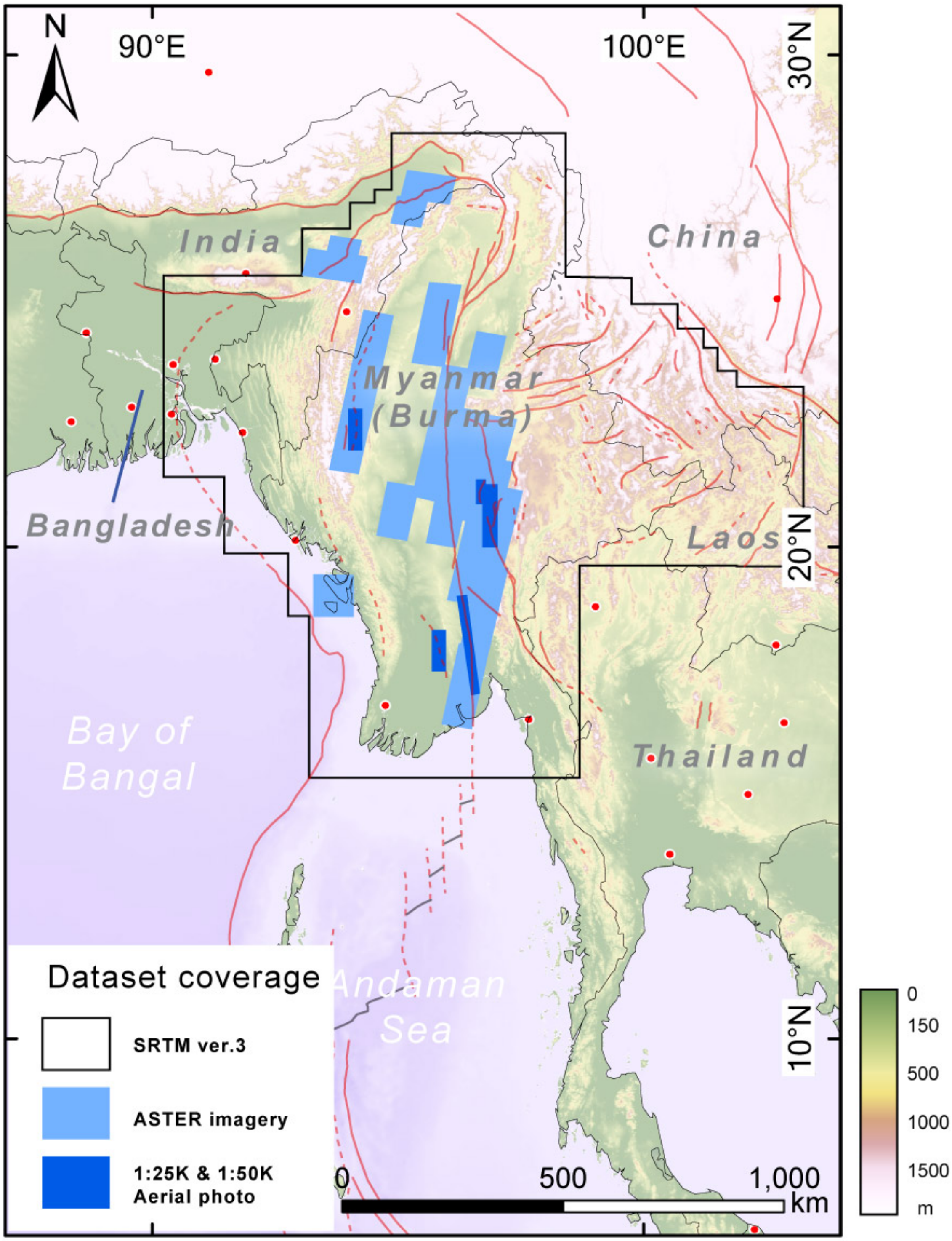

Fig. S1 The coverage map of the remote sensing dataset that used in this study.
We also used the Landsat ETM+ imagery that its cover area is identical to the SRTM digital elevation model.

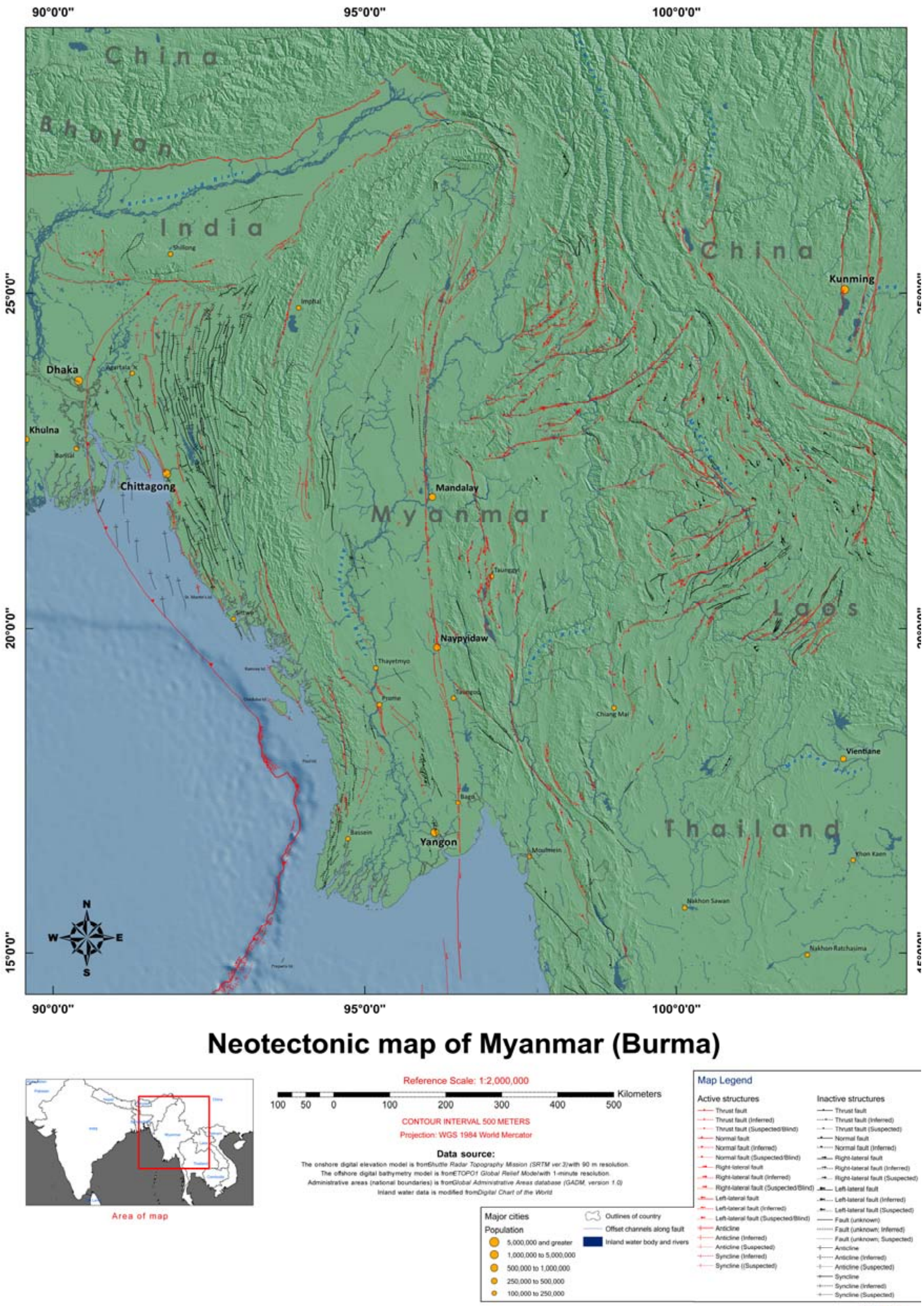

Fig. S2. Neotectonic map of Myanmar (Burma)

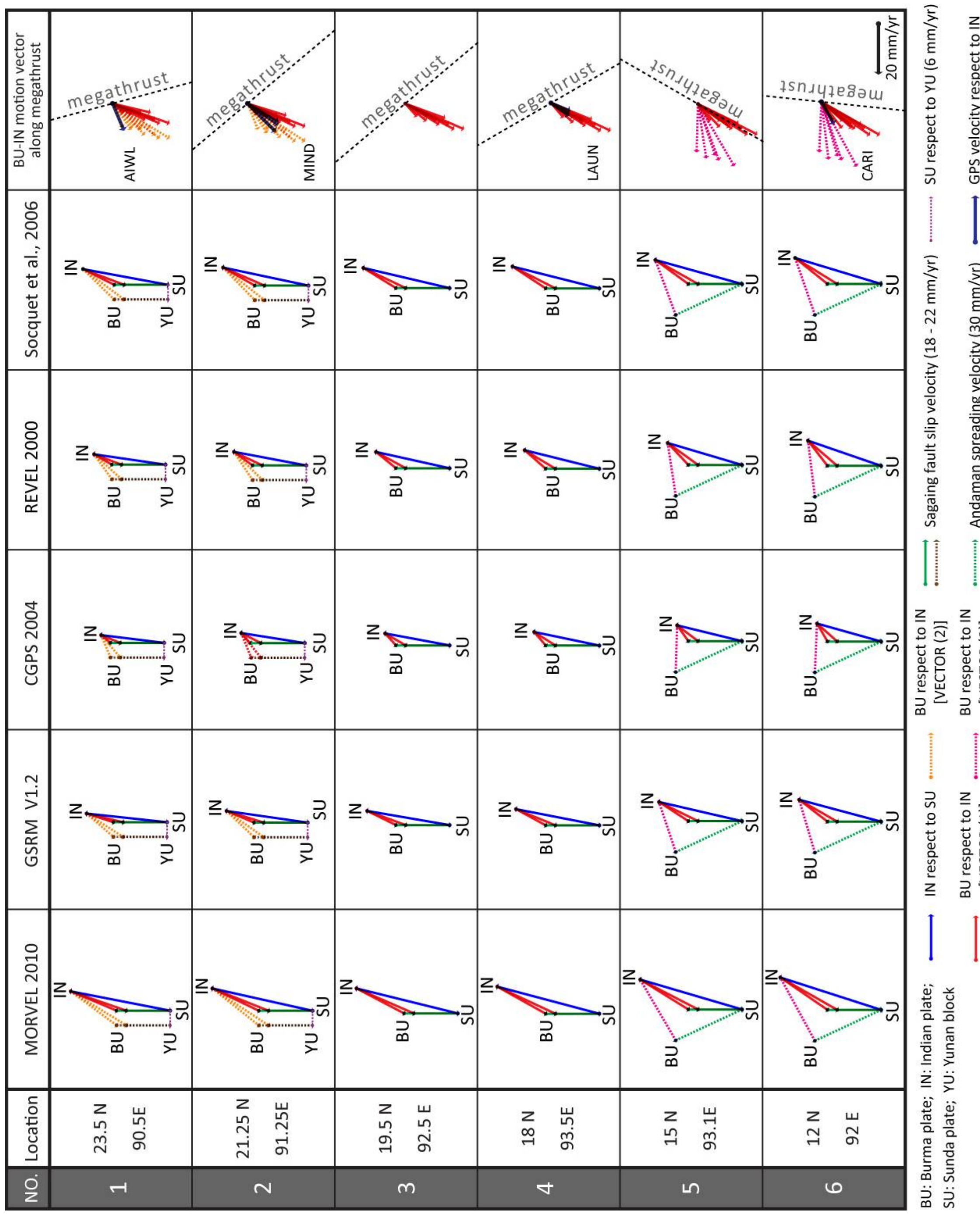

Fig. S3 The plate motion vector diagram along the western Myanmar coast

Appendix 2

Supplementary material of chapter 3 Earthquakes and slip rate of the Southern Sagaing fault: insights from an offset ancient fort-wall, Lower Myanmar (Burma)

Table S1. Stories of the May 1930 earthquake from local villagers near the city of Bago (Pegu)

Date	Location	Name (age)	Story of earthquake from villager	Note
Apr-8th-2008	Sangdi N17.303 E96.510	U Thien Moun (95)	Ground cracks opened around and south of his village. He traced these ground fractures to another village "Kyad-Pa-Gan," 5 miles south of his village (Sangdi). These fractures ran though Kyad-Pa-Gan village and even further south. He remembers the structure of the old monastery building was displaced 1 to 2 feet in the Pegu earthquake. The sense of displacement is right-lateral.	
July-31st-2008	Kyaikpadainga-ale N17.226 E96.513	U Thaung (88)	He remembered there was an earthquake when he was 5-6 years old in the afternoon or evening of a summer day. There were ground cracks around his village, especially east of the village. He remembers these cracks openned 10-15cm wide, and were 6-10 meters long. No sand and water came out of these cracks.	
Aug-1st-2008	Tawa N17.219 E96.498	U Dama nanda (66)	His master (who would be 88 yrs old, if alive) told him there was an earthquake when he was about 5 yrs old. During the earthquake, ground cracks formed around the village. His master also saw sand blow out with water around the village during the earthquake. The ground cracks were especially abundant west of the village. The ground cracks were about 2 meters wide, next to the Pegu river, west of the village.	

Date	Location	Name (age)	Story of earthquake from villager	Note
Aug-1st-2008	Tawa N17.219 E96.498	Daw Tin Myunt (88)	When she was 10 yrs old, a big earthquake hit her village. Her parents told her that four brick buildings in the village collapsed. She did not notice the ground cracks near the village, but heard from other villagers about those cracks.	
Aug-1st-2008	Kyaikme N17.203 E96.517	U Thuzata (74)	He heard from his relatives a big earthquake struck the village 4 yrs before he was born. During the earthquake, nobody could stand on the ground. The ground wave was easy to see. After the earthquake, the canal in the village became shallower than before. The elevation of village also became higher after the earthquake. Fences were offset inside the village. He also heard from his aunt that cracks opened west of his village. The cracks could be traced all the way to Sangdi and Bago after the earthquake. These cracks were not continuous. His relatives told him that other cracks opened west of Zayaungbin and around Tawa (west of his village).	The remaining of the open fissure is in Table S2-D. The fault trace is in Table S2-E
Aug-1st-2008	Makainggyi N17.174 E96.521	U Ba Than (81)	The earthquake happened when he was 3 yrs old. He claimed that water blew up from a small crack north of his village during the earthquake.	
Aug-2nd-2008	Payale N17.509 E96.533	Daw Phwa Chit (97)	She remembered that a big earthquake hit her village when she was 17-18 yrs old, when the rice field was dry. There were ground cracks in the paddy field northwest of the village after the earthquake. The ground cracks were long and narrow, and water flowed out from these cracks. People could use small cups to get the water from the cracks. She did not notice any damage to the railroad and car track near her village	

Date	Location	Name (age)	Story of earthquake from villager	Note
Aug-2nd-2008	Thabyeyo N17.502 E96.501	U Pan Nait Sa (85)	He remembered there was an earthquake when he was 3 yrs old, during an evening in early May. He heard from his parents that there some ground cracks appeared northeast of the village during the earthquake. Water and sand ejected from these cracks, but not very high. The orientation of these cracks was N-S, and they were continuous. The day after the earthquake, he and his friend checked these cracks from his village to the ancient fortress. The cracks extended both northward and southward from his village. A ground crack passed through the main road south of the ancient fortress, and extended further south, but he did not notice any offset on the main road across the ground crack	
Aug-2nd-2008	Western Shwedan village N17.438 E96.500	U Win Sein (76)	He heard from his father that the railroad was tilted after the earthquake south of Shweden village. The rail was tilted to west near the mile-67 marker. There was no bending and twisting of the rail, just tilting.	The displaced railroad embankment is in Table S2 A
Aug-3rd-2008	Village west of Payagyi N17.479 E96.491	U Soe Tim (82)	He heard from his parents that ground cracks appeared SE of the village after the 1930 Pegu earthquake. He also heard from his parents that the wall of the Payagyi ancient fortress was broken during the earthquake. In the subsequent rainy season, water inside the ancient fortress was able to flow out through the broken wall. There were 5 bridges along the main road from Payagyi to his village. Only the third bridge, south of the ancient fortress failed during the earthquake.	

Date	Location	Name (age)	Story of earthquake from villager	Note
Aug-3rd-2008	Payagyi N17.477 E96.525	U Tint Mon Lay (86)	He was about 11 yrs old when earthquake occurred. He noticed a ground crack appeared near his house. Sand and water blew out from the crack about 1 meter high during the earthquake. The ox cart parked near his house moved 2-3 meters to the east during the earthquake because of the earthquake shacking. His parents told him the earthquake in 1930 was stronger at Payagyi than the earthquake in 1917	
Aug-3rd-2008	Awaing-Ywahuang N17.382 E96.501	Daw Kywe May (85)	She claimed she was 6 yrs old when the earthquake happened. She was in Bago during the earthquake. Her father did not notice any damage on the road, which is a dirt-road NE of their village. Her parents also mentioned there were ground cracks near the village, especially west of the village. Her parents also saw the ox cart had fallen into the crack; the crack was more than 2 feet deep. She did not see the ox cart herself, but heard some villagers asking “who’s ox cart fell into the crack” after the earthquake. Her parents also told her that the earthquake in 1930 was stronger than the earthquake in 1917.	

Date	Location	Name (age)	Story of earthquake from villager	Note
Aug-3rd-2008	Awaing-Ywahuang N17.382 E96.501	U Pwa (82)	He was 2 yrs old then the earthquake happened. He father told him that NE-SW-trending ground cracks appeared after the 1930 earthquake east of the village. There were also a lot of ground cracks SW of the village near the Pegu river. His father also claimed that some paddy field boundaries were offset right laterally across the ground crack east of his village. These ground cracks were later connected by excavation to make the canal in the field. He also heard about the 1917 earthquake from his parents. They told him that ground cracks appeared SW of the village, near the Pegu river. Some water blew out from the crack. His parents also claimed that the ground cracks in 1930 were not as numerous as the ground cracks in 1917. They also claimed that the intensity of 1930 earthquake was stronger than the intensity of the 1917 earthquake.	The offset paddy field is in Table S2 B
Aug-3rd-2008	Kale N17.367 E96.511	U Ngwe Maung (92)	He heard from others that the rail was bent between Kale and Pegu but did not check it by himself. Because of the earthquake, one paddy field became two paddy fields. Some water with sand was ejected out from the ground cracks west of the village. He remembers the land west of the crack moved down in 1930.	

Table S2. Field photographs of small offsets along the Sagaing fault

Photographs were taken in Summer 2008

A

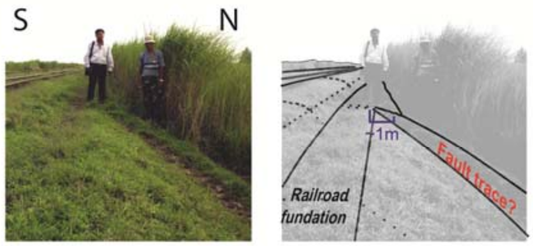

Displaced railroad embankment south of the Shwedan village, near the Mileage marker 67 on the railway. (N17.42817 E96.50440)

B

Right-lateral offset (~ 2 m) of a paddy field boundary. Local famer (U Pwa) claimed the channel between the fields (not visible) was the ground fissure of 1930 earthquake, and separated one paddy field into two in 1930 earthquake. (N17.37892 E96.50408)

C

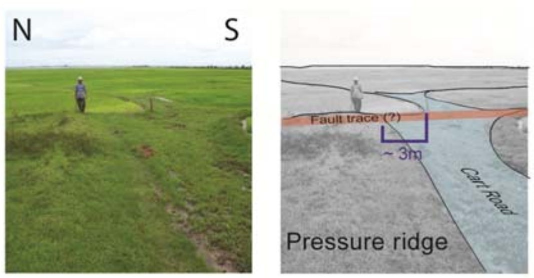

Right-lateral offset (~ 3 m) of a cart road, 7 km south of Bago. View to the east (N17.26254 E96.51290)

D

“Earthquake crack creek” (Open fissure) south of Kyaikme village. Local villager claims the fissure opened during 1930 earthquake. It was widened by lateral erosion after the earthquake (N17.19751 E96.51411)

E

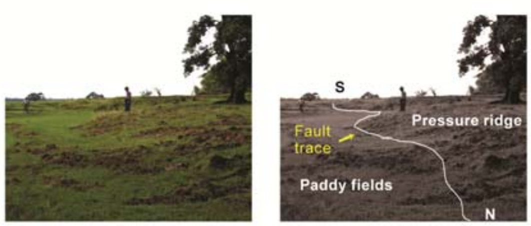

West-facing fault scarp ~10 cm to ~80 cm high bounding the western margin of a N-S trending pressure ridge, south of Kyaikme village. (N17.19639 E96.51407)

Table S3. Original description of the temporary palace near the Payagyi pagoda from U Kala's Maha-ya-zawin-gyi ("Great Chronicle")

Original text (in Red box)	**Ch:] 25-Preparing/Placing Treasure Chest or Reverend Pie for Mahavizara Zedi Stupa 45** တွဲ၊] ၂၅-မဟာဝိဇယစေတီဌာပနာခြင်း ၄၅ သုဒဿန နတ်လမ်းကဲ့သို့ အံ့ဩဖွယ်သရဲ့သော ခရီးကို တလိုင်း, မြန်မာ,ရှမ်း, ကုလား,သူဌေး,သူကြွယ်,အမှူးအမတ်,ဆွေတော်,မျိုးတော်, မင်းညီမင်းသား အပေါင်းတို့သည် အထူးထူး အပြားပြားသော တန်ဆာတို့ကို ဆင်ယင် ဝတ်စားကုန်လျက် ကြီးစွာသော သဘင်ဖတော်ကိုခံ၍ ကောင်းမှုတော်သို့ ပို့ရ သည်။ ၎င်း သက္ကရာဇ် (၉၃၈)ကိုးရာ့သုံးဆယ့်ရှစ်ခုနှစ် ပြာသိုလဆန်း ခြောက် ရက် တနင်းလာနေ့ ကောင်းမှုတော် မဟာဝိဇယစေတီ အနောက်တွင် သာယာလှစွာသော သဘင်တဲတော် ဆောက်စေ၍ သဘင်နန်းတော်၌ နေ တော်မူသည်၊ ၎င်းနေ့ မဟာဥပရာဇာ အစရှိသော ညီတော်, သားတော်, မှူးတော်,မတ်တော်, သူဌေးသူကြွယ် အပေါင်းတို့ လက်ဆောင်တော် ဆက် သည်၊ ထိုလက်ဆောင်တော်ကို ကောင်းမှုတော် မဟာဝိဇယ စေတီတွင် သုဓမ္မာစရပ်ကို ရွှေထည့်စရာလှူတော်မူသည်၊ ပြာသိုလပြည့်ကျော် ၁-ရက်နေ့ ကောင်းမှုတော်ကို ဒုတိယ ဌာပနာတော်မူသည်၊ ၎င်း ပြာသိုလပြည့်ကျော် ဆယ့်နှစ်ရက်တနင်းလာနေ့ တတိယဌာပနာတော်မူသည်၊ယင်းသောခါ သဘင် တဲတော်ကသည်ကောင်းမှုတော်သို့ ညီတော်,သားတော်,မှူးတော်,မတ်တော်, ကိုယ်လုပ်မောင်းမ အပေါင်းနှင့် မွေးတော် ခတ်တော်တို့ကို ကိုယ်တိုင်တော် ပို့ရသည်၊ ယင်းသည့်နေ့ပင် ကောင်းမှုတော် ရွှေထည့်စရာ စားတော်ခေါ် သည့် ကွမ်းခွက်,လက်ဘက်အိုး,တကောင်းဖိုး,သောက်တော်မူသော ဖလား နှင့်တကွ ရွှေတဆယ့် သုံးပိဿာခုနစ်ဆယ်ကို ' မျက်ပါးခတ်ပြီးလျှင် သိဒ် ရာဇာ, ငဆွေညို, ငရဲထောင်တို့နှင့် ဆရာတော် နန္ဒသာရ သာသနဂုရုကို ကြပ်မ၍ ရွှေထည့်ရသည်။
English Translation by Soe Thrua Tun after Jon Fernquest[1]	… Within the year 938 (1576 or 1574) on the 6th waning moon of Pyatho monday on the west (back) of Kaunmudo Mahawizaya pagoda *(Payagyi pagoda)*, by building a temporary tent for celebrating the feast the king stayed there in a temporary palace constructed for his enjoyment. …
1. The original English translation is from Jon Fernquest's webpage. (http://burmesehistoricalchronicle.blogspot.com/)	

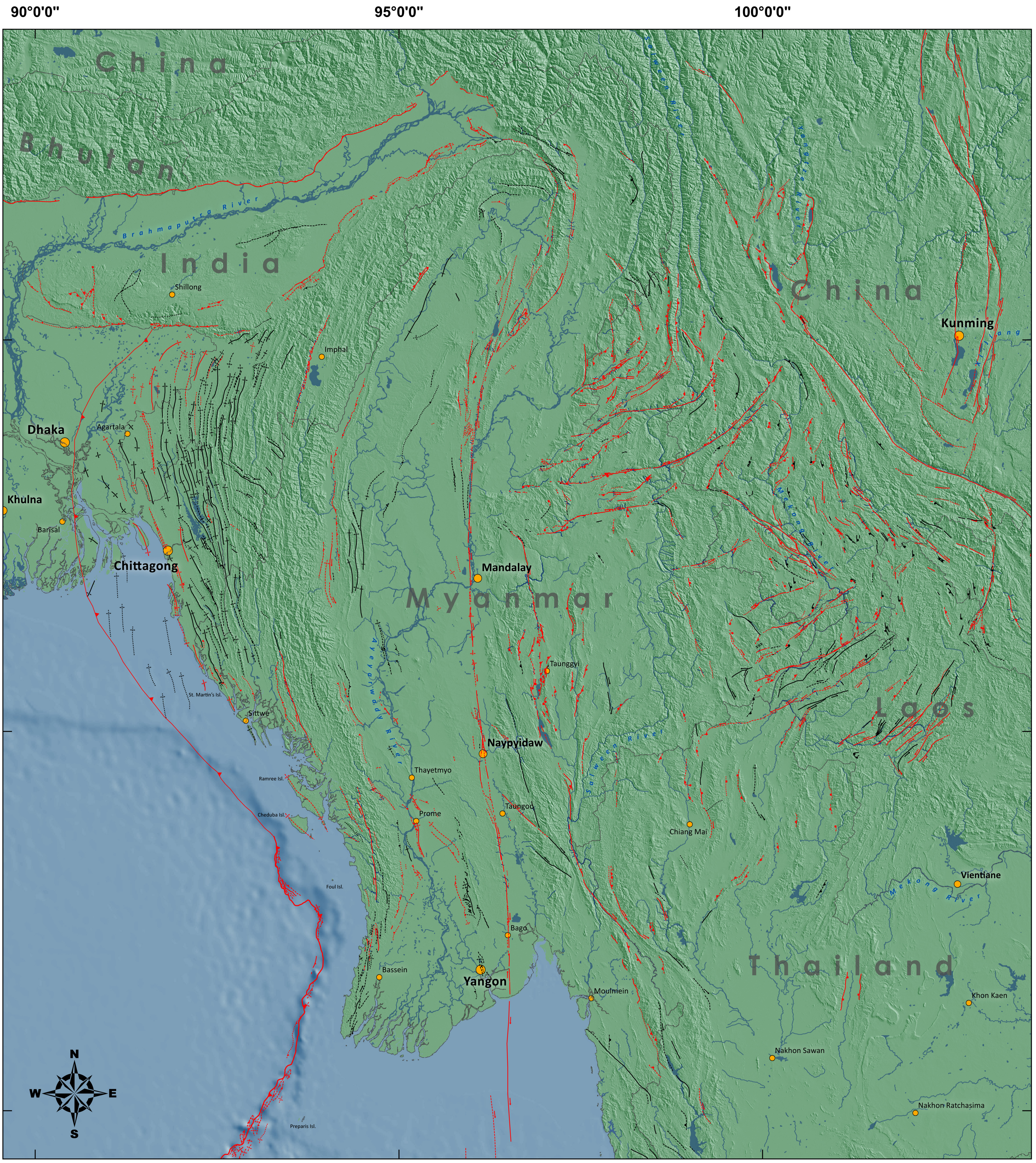

Neotectonic map of Myanmar (Burma)

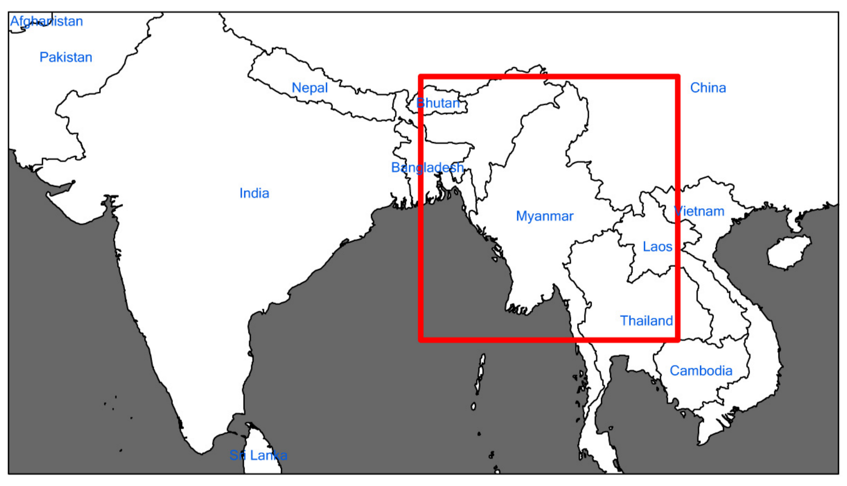

Area of map

Reference Scale: 1:2,000,000

100 50 0 100 200 300 400 500 Kilometers

CONTOUR INTERVAL 500 METERS

Projection: WGS 1984 World Mercator

Data source:

The onshore digital elevation model is from *Shuttle Radar Topography Mission (SRTM ver.3)* with 90 m resolution.
The offshore digital bathymetry model is from *ETOPO1 Global Relief Model* with 1-minute resolution.
Administrative areas (national boundaries) is from *Global Administrative Areas database (GADM, version 1.0)*
Inland water data is modified from *Digital Chart of the World*

Major cities

Population

- 5,000,000 and greater
- 1,000,000 to 5,000,000
- 500,000 to 1,000,000
- 250,000 to 500,000
- 100,000 to 250,000

Outlines of country
Offset channels along fault
Inland water body and rivers

Map Legend

Active structures

- Thrust fault
- Thrust fault (Inferred)
- Thrust fault (Suspected/Blind)
- Normal fault
- Normal fault (Inferred)
- Normal fault (Suspected/Blind)
- Right-lateral fault
- Right-lateral fault (Inferred)
- Right-lateral fault (Suspected/Blind)
- Left-lateral fault
- Left-lateral fault (Inferred)
- Left-lateral fault (Suspected/Blind)
- Anticline
- Anticline (Inferred)
- Anticline (Suspected)
- Syncline (Inferred)
- Syncline ((Suspected)

Inactive structures

- Thrust fault
- Thrust fault (Inferred)
- Thrust fault (Suspected)
- Normal fault
- Normal fault (Inferred)
- Right-lateral fault
- Right-lateral fault (Inferred)
- Right-lateral fault (Suspected)
- Left-lateral fault
- Left-lateral fault (Inferred)
- Left-lateral fault (Suspected)
- Fault (unknown)
- Fault (unknown; Inferred)
- Fault (unknown; Suspected)
- Anticline
- Anticline (Inferred)
- Anticline (Suspected)
- Syncline
- Syncline (Inferred)
- Syncline (Suspected)

Date: 2013/5/1